Plasma Ignition in Underwater Gas Bubbles

by

Bradley S. Sommers

A dissertation submitted in partial fulfillment
of the requirements for the degree of
Doctor of Philosophy
(Nuclear Engineering and Radiological Sciences)
in The University of Michigan
2013

Doctoral Committee:

Associate Professor John E. Foster, Chair
Natalia Y. Babaeva, Research Scientist
Professor Brian E. Gilchrist
Professor Ronald M. Gilgenbach
Professor Mark J. Kushner

Success is the sum of small efforts, repeated day in and day out. - Robert Collier

To my friends and family, whose love and support are woven into every page of this book.

ACKNOWLEDGEMENTS

My advisor John Foster has been a wonderful mentor over the past six years. His practical knowledge is exceeded only by the positive energy he imparts on those around him. I would also like to thank my committee, which includes Ron Gilgenbach, Mark Kushner, Brian Gilchrist, and Natalia Babaeva. Their support and critical review helped craft my dissertation into its final form.

I am particularly lucky to have had such a strong source of funding during my studies. For this opportunity, I owe special thanks to the National Science Foundation and the Horace H. Rackham School of Graduate studies. I would also like to thank the Department of Nuclear Engineering for giving me the privilege of serving as a graduate student research assistant as well as a graduate student instructor. Both have been instrumental in my development.

Next, I would like to thank my colleagues, who have supported me throughout my time at Michigan. I would like to give a special thanks to Dr. Brandon Weatherford, Dr. Eric Gillman, Dr. Aimee Hubble, Ben Yee, Paul Cummings, Sarah Gucker, and Kapil Sawlani. Thank you all for your knowledge and friendship.

Finally, I would like to thank my friends and family, who have been behind me at every stage of my academic career. I will never forget the joy of seeing so many of you at my defense, providing love and support as you always do. Above all, I would like to thank my wife Staci, who is my best friend and greatest source of inspiration. Thank you, I love you.

TABLE OF CONTENTS

DEDICATION ii

ACKNOWLEDGEMENTS iii

LIST OF FIGURES viii

ABSTRACT xviii

CHAPTER

I. Introduction 1

1.1 Environmental Applications of Plasma Discharges 1
1.1.1 Industrial Waste Processing 4
1.1.2 Water Purification: Addressing a Global Epidemic . 6
1.2 Plasma Discharge Types 9
1.2.1 Direct Discharges 10
1.2.2 Indirect Discharges 14
1.3 Plasma Discharges in Gas Bubbles 18
1.3.1 The Electrode Attached Bubble Geometry 19
1.3.2 The Rising Bubble Stream Geometry 22
1.3.3 Physics of Bubble Discharges 23
1.3.4 Plasma in Isolated Bubbles 25
1.4 Dissertation Scope: Making Bubble Discharges Practical . . . 27

II. Theory 29

2.1 Introduction 29
2.2 Electrical Breakdown in Atmospheric Gases 29
2.2.1 Electron Swarm Parameters 31
2.2.2 Townsend Breakdown 35
2.2.3 Streamer Breakdown 36
2.2.4 Plasma Formation in an Isolated Bubble 38
2.3 Changing the Breakdown Conditions in a Bubble 41

2.3.1 Motivation . . . 41
2.3.2 The Shape Effect . . . 41
2.3.3 The Volume Effect . . . 44
2.4 Bubble Dynamics . . . 47
2.4.1 The Bubble at Equilibrium . . . 47
2.4.2 Radial Deformations of the Bubble . . . 48
2.4.3 General Deformation . . . 49
2.4.4 Bubble Damping . . . 52
2.4.5 Gas Diffusion at the Bubble Interface . . . 54
2.4.6 Methods of Achieving Bubble Deformation . . . 56
2.5 Bubble Deformation via Electric Fields . . . 57
2.6 An Example: The Dielectric Sphere in a Uniform Field . . . 59
2.6.1 Solution of the Electric Field . . . 59
2.6.2 Solution of the Electric Stress . . . 60
2.6.3 Net Body Force on Dielectrics . . . 62
2.6.4 Extension to Leaky Dielectrics . . . 63
2.7 A.C. Electric Fields: Coupling to Natural Bubble Modes . . . 64
2.8 Strategy Going Forward . . . 65

III. Experimental Approach . . . 66

3.1 Development of the Ultrasonic Levitation Cell . . . 66
3.1.1 Principles of Levitation: The Bjerknes Force . . . 66
3.1.2 Implementation of the Transducer . . . 71
3.1.3 Transducer Calibration . . . 72
3.1.4 Bubble Injection . . . 74
3.1.5 Other Issues . . . 77
3.2 Achieving Shape Distortion in Practice . . . 78
3.2.1 Electrode Design . . . 78
3.2.2 Coupling to the $l = 2$ Mode . . . 80
3.3 H.V. Sources I: Shape Distortion . . . 81
3.3.1 The Elgar A.C. Power Source . . . 81
3.3.2 The TREK Amplifier . . . 82
3.4 H.V. Sources II: Pulsing and Plasma Ignition . . . 84
3.4.1 The Suematsu Pulser . . . 84
3.4.2 Other Methods . . . 86
3.5 Imaging . . . 86
3.5.1 The Redlake Camera . . . 88
3.5.2 The PIMAX ICCD Camera . . . 88
3.5.3 Camera Lenses and Lighting . . . 90
3.5.4 Image Analysis . . . 91
3.6 Evaluating the Shape Effect . . . 93
3.7 Experimental Plan . . . 94

IV. Preliminary Experiments in Electrode-Attached Gas Bubbles 95

4.1 Overview . . . 95
4.2 Excitation of Bubble Oscillations by A.C. Electric Fields . . . 98
4.3 Properties of Streamers in Electrode Attached Bubbles . . . 99
4.4 Resonant Excitation of Surface Waves . . . 107
4.4.1 Capillary Waves . . . 107
4.4.2 Rayleigh-Taylor Instabilities at the Bubble Surface . 110
4.4.3 Capillary Waves Excited in the Point-to-Plane Geometry . . . 111
4.4.4 Capillary Waves Excited on a Thin Needle Tip . . . 114
4.4.5 Wave Coupling Between Bubbles . . . 116
4.4.6 Evaluating the Shape Effect in Capillary Waves . . 118

V. Nonlinear Distortion of Free Standing Gas Bubbles . . . 123

5.1 Operating Conditions . . . 125
5.2 Excitation of the $\ell = 2$ Mode . . . 126
5.3 Excitation of the $\ell = 4$ Mode . . . 131
5.4 Evaluating the Field Enhancement in Spherical Harmonic Deformations . . . 134
5.4.1 The Dielectric Ellipsoid: A Guide to Field Enhancement . . . 134
5.4.2 Electrostatic Simulation of the Field in Observed Bubbles . . . 137
5.4.3 Electrostatic Simulations in Pure Spherical Harmonic Modes . . . 141
5.5 Bubble Deformation Under Extreme Electric Fields . . . 146
5.5.1 Bubble Breakup . . . 147
5.5.2 Dependence of the Field Strength on Distortion . . 148
5.6 Evaluating the Volume Effect . . . 151

VI. Fundamental Discharge Processes in Gas Bubbles . . . 154

6.1 Experimental Approach . . . 156
6.1.1 Electrode Design . . . 157
6.1.2 Gas Types . . . 159
6.1.3 Imaging . . . 159
6.2 Summary of Observed Plasma Phenomena . . . 160
6.2.1 The Multiphase Streamer . . . 163
6.2.2 IV Characteristic of the Multiphase Streamer . . . 167
6.3 ICCD Imaging of the Multiphase Streamer . . . 168
6.3.1 Early Timescales: Streamer Formation and Bubble Impact . . . 170
6.3.2 Characterization of Bubble Plasma . . . 173
6.3.3 Late Timescales: Fluid Motion and Instability . . . 176

6.4 Plasma Ignition in Isolated Bubbles 182
6.4.1 ICCD Imaging of Ignition in Isolated Bubbles . . . 182
6.4.2 Estimating the Electric Field and Ionization Coefficient in an Isolated Bubble 187

VII. Plasma Ignition in Deformed Gas Bubbles 193

7.1 Experimental Overview 193
7.2 Plasma Ignition Using a Single Source 194
7.2.1 Experimental Results 194
7.3 Plasma Ignition Using a Dual Source 199
7.3.1 Experimental Approach 199
7.3.2 Results 200
7.4 Simulation of the Electric Field Inside Deformed Bubbles . . 203

VIII. Conclusion 209

8.1 Overview of Research 209
8.2 Towards a Practical Plasma Reactor 212
8.2.1 Source of Bubble Deformation 212
8.2.2 Optimal Deformation Type 213
8.2.3 Geometry 214
8.3 Future Work 216

BIBLIOGRAPHY 218

LIST OF FIGURES

Figure

1.1 Ignition of plasma in the dye filled water leads to the direct injection of reactive species capable of deactivating the dye. 5

1.2 Local water sources, particularly those in underdeveloped countries, illustrate the need for clean, portable water treatment systems. . . . 7

1.3 A simple scheme for a portable, point of use water treatment system utilizing a plasma discharge. 8

1.4 Direct discharge modes in increasing order of spatial extent: (a) corona, (b) streamer, (c) spark. 12

1.5 An indirect discharge is excited in a nearby gas in the vicinity of the target liquid. The four most prevalent approaches are (a) the surface discharge (b) the gliding arc, (c) contact glow discharge electrolysis, and (d) the dielectric barrier discharge. 15

1.6 In the electrode attached reactor geometry, the bubble is placed in contact with the electrode. The reactive products form along the walls of the bubble and diffuse out into the liquid volume. 20

1.7 In the rising streamer reactor geometry, the bubbles rise up in between the electrodes. During ideal operation, the plasma forms in isolated bubbles. However, in reality, the majority of excitation occurs in bubbles that become attached to the wall. 23

2.1 A survey of reduced ionization coefficients for noble gases (Ar, He) and electronegative gases (H_2O, O_2, and air). All data taken from Dutton [92]. 34

2.2 The reduced attachment coefficient for oxygen, the primary source of attachment in ambient air. At low E/N, η is dominated by three body attachment, while at higher E/N it becomes dominated by two body dissociative attachment. Data taken from Dutton [92] and Naidu [94]. 34

2.3 A model suggested by Raju [98] for estimating the apparent ionization coefficient in air and helium over the range 0-200 Td. For this case, λ is calculated at 1 atm. 40

2.4 A simple illustration of the shape effect. Changing the curvature of the dielectric boundary changes the distribution of the applied electric field inside the bubble. 43

2.5 A simple illustration of the volume effect. As the bubble expands, its internal pressure and number density both decrease. This expansion must be faster than the diffusion of dissolved gas from the liquid. . 45

2.6 The spherical coordinate system is a natural fit for characterizing bubble shape deformation. In this dissertation, most cases of interest are azimuthally symmetric and thus do not depend on the angle ϕ. . 50

2.7 The volume mode, f_0 and first three shape modes, f_2, f_4, f_6 as a function of radius for gas bubbles in water. All frequencies decrease with increasing radii. 53

2.8 Spherical harmonic perturbations of the unit sphere for the $l = 2$ mode (top row) and the $l = 4$ mode (bottom row). At large negative values, both modes undergo severe contraction of the bubble boundary onto itself. 53

2.9 The diffusion of gas into and out of a sphere with initial concentration, c_0 inside and constant concentration, c_∞ at the boundary. For times large relative to the diffusion time, t_{diff}, the concentration approaches c_∞ everywhere inside the bubble. 56

2.10 Under an external uniform field, the bubble is stretched vertically. Analysis of the electrostatic stress shows that the highest pressure occurs at the bubble's sides, pushing it inward. 61

3.1 The piezoelectric cell used to suspend gas bubbles in an ultrasonic acoustic field. The dimensions are chosen to excite a rectangular standing mode of the type [1,1,2]. The bubble is trapped at the vertical node by the Bjerknes forces. 68

3.2 (a) When the transducer surface is flat, the horizontal pressure field creates an unstable equilibrium. (b) The trapping field is stabilized by the addition of the spiked piezo-coupling horn. 71

3.3 (a) The impedance of the piezoelectric transducer is minimized at its natural resonance. (b) This corresponds closely to the point at which the absorbed power is maximized. Using this calibration, the operating point was chosen to be 26.4 kHz. 74

3.4 The helium injector is used to inject helium bubbles directly into the node of the ultrasonic acoustic field. Gas injection is precisely controlled using a solenoid valve. 75

3.5 (a) A close up view of the bubble held in stable levitation. (b) The electrode arms held in position around the bubble. (c) The piezo-cell along with the electrode arms mounted on a 3-D translation stage. . 79

3.6 The primary electrode types used to drive shape distortions and ignite plasma in the bubble. 80

3.7 The Elgar A.C. power supply (bottom) and the high voltage transformer (top) used to drive bubble oscillations. 83

3.8 The electrical circuit used to deliver voltage from the Elgar power supply to the levitation cell. 83

3.9 The TREK H.V. amplifier provides higher voltage and greater waveform control relative to the Elgar system. All input signals are provided by the Agilent arbitrary function generator. 85

3.10 The electrical circuit used to deliver high voltage signals from the TREK supply to the submerged electrodes. 85

3.11 The 3 module Suematsu system was the primary ignition mechanism for plasma in the levitation cell. 87

3.12 Two example pulses generated by the Suematsu pulser. (a) For a 500 ohm load, the pulser is perfectly matched and suffers no overshoot. (b) For an open load, a secondary negative reflection pulse is ignited. 87

3.13 The cameras and lenses used to image bubble physics. The high speed camera (top left) was used primarily to capture fluid and bubble motion ($\sim$ 0.1-1 ms) while the ICCD camera (bottom left) was used to capture plasma phenomena (10-1000 ns). Each camera was used with one of two lenses. The macro lens (top right) provided adjustable zoom and focus to cover a wide range of phenomena, while the telescoping lens (bottom right) was used to image very small (up to 10x zoom) phenomena. 89

3.14 (a) A raw image taken with the Redlake camera. (b) The image after thresholding. (c) Discrete data points of the boundary obtained by applying the edge detection algorithm. 92

4.1 Injected bubbles pass between the electrodes and become trapped on the surface of the threaded rod, which is biased at high voltage. . . 97

4.2 Periodic bubble driving at 50 Hz, 1.6 kV, illustrates the maximum and minimum deformation of the bubble (top) under the force of the applied field. Periodic bubble driving at the same conditions (bottom) can be accompanied by plasma streamers. These streamers occur predominantly in the positive phase of the applied voltage . . 100

4.3 Discharge characteristics for a 100 Hz signal driving bubble deformation and igniting streamers. Distortion of the voltage signal is caused by both dielectric breakdown as well as the limitations of the high voltage transformer. 101

4.4 IV traces for bubble plasma produced by the Suematsu pulser with a 1 μs pulse length. Observation of the current spikes is accompanied by a slight voltage dip. 103

4.5 (Top) Plasma streamers ignited in bubbles at different pulse frequencies. The effect of higher pulse rate is to increase the average stress on the bubble, thus resulting in higher deflection of the bubble surface.(Bottom) Model of electron density growth of the streamer as its propagates along a smooth bubble surface and a perturbed bubble surface. Results are taken from Sommers [108]. 104

4.6 Spectra observed from plasma forming in the attached gas bubble confirms the production of reactive species such as OH. 108

4.7 Relaxation of the perturbed bubble surface in the aftermath of a wall hugging streamer. Eventually, (t $>$ 10 ms) the wave is damped by viscous forces in the water. 108

4.8 A single oscillation period illustrating the excitation of capillary waves on the surface of the bubble. Pulses are applied at 500 Hz and 12 kV. 111

4.9 The evolution of capillary wave amplitude over N pulse cycles. Eventually the wave growth reaches a steady state amplitude. 112

4.10 Capillary waves excited on a needle electrode using a single 1 μs, 12 kV pulse from the Suematsu supply. 115

4.11 A nearby bubble undergoes capillary wave oscillations communicated by the attached bubble. Times are relative to streamer excitation. . 117

4.12 Wave coupling can be extended to bubbles up to 2 cm away from the original attached bubble. The excitation of nearby bubbles spreads in time, starting at bubble #1 and eventually reaching bubble #3. . 117

4.13 Simulation of the electric field enhancement factor, G, in cases where the wave amplitude is varied. The wavenumber is held constant at n = 20. 120

4.14 Simulation of the electric field enhancement factor, G, in cases where the wavenumber, n is varied. The amplitude is held constant at a = 0.10. 120

5.1 (a) Mesh plate electrodes provide an approximately uniform field to drive the suspended gas bubbles. (b) A bubble levitating in between the mesh electrodes. The cross hatching on the mesh is visible. . . . 125

5.2 The applied voltage, current and normalized electric field pressure used to drive $\ell = 2$ mode oscillations of the levitated bubble in case 1. 128

5.3 A typical cycle of the $\ell = 2$ mode beginning at t = 12.48 ms. The equilibrium bubble diameter is 0.43 mm. 128

5.4 Shape mode analysis for a bubble oscillating in the $l = 2$ mode. The left column shows even coefficients, from top to bottom, (a) b_2, (b) b_4, and (c) b_6. The right column shows (d) odd coefficients b_1, b_3, b_5, (e) volume mode coefficient b_0 and (f) the normalized volume. . . . 129

5.5 The applied voltage, current and normalized electric field pressure used to drive $\ell = 4$ mode oscillations of the levitated bubble in case 2. 132

5.6 A typical cycle of the $\ell = 4$ mode beginning at t = 15.40 ms. The equilibrium bubble diameter is 0.65 mm. 132

5.7 Shape mode analysis for a bubble oscillating in the $l = 4$ mode. The left column shows even coefficients, from top to bottom, (a) b_2, (b) b_4, and (c) b_6. The right column shows (d) odd coefficients b_1, b_3, b_5, (e) volume mode coefficient b_0 and (f) the normalized volume. . . . 133

5.8 The electric field enhancement inside an axisymmetric ellipsoid air bubble. The quantities c and a represent the dimensions parallel and perpendicular to the field respectively. From left to right, the displayed shapes represent $c/a = 0.1, 1, 10$. 138

5.9 Four examples illustrating large excitation of the two dominant modes, (a) b_2 = -0.424, (b) b_2 = 0.683, (c) b_4= -0.101 and (d) b_4= 0.067. The simulated field was oriented as shown. 139

5.10 The enhancement factor G calculated for the four characteristic images in Figure 5.9. The value $G_0 = 1.5$ (in green) corresponds to the enhancement in an unperturbed sphere. Labels indicate the value of G at the boundary between two colors. 140

5.11 Contour maps showing the enhancement factor of the applied electric field in log scale. The field is enhanced substantially in areas where the bubble is compressed in the direction of the applied field. 143

5.12 Axial profile of the field enhancement factor, G, inside a gas bubble subjected to excitations of the (a) $\ell = 2$ mode and (b) $\ell = 4$ mode. The coefficient value, b_2 or b_4, is labeled beside each curve. 144

5.13 The ionization product, M calculated in 1 mm air bubbles for hypothetical values of the electric field strength. The integral is taken along the centerline of bubbles deformed by the $l = 2$ mode (left) and $l = 4$ mode (right). The mode coefficient is labeled beside each line. 144

5.14 A bubble stretches under the action of a uniform electric field, with amplitude 25 kV/cm. The field is generated by a pair parallel plate electrodes placed above and below the levitated bubble. 148

5.15 The normalized deformation in the direction of the applied electric field as a function of the Weber number 150

5.16 The effect of increasing the strength of the electric field acting on a levitated bubble. As the amplitude increases, the bubble's sides narrow up to a critical point beyond which it is separated into two fragments. 150

6.1 Submerged gas bubbles can extend the plasma deep into the liquid via two different mechanisms: (1) A liquid streamer is sustained by passing through a chain of gas bubbles (2) The plasma is ignited solely in the volume of the gas. This plasma can hop to other bubbles through either the release of resonant photons or the coupling of the streamer field to a nearby bubble. 156

6.2 The electrode geometry as observed by a 500 nsec gated ICCD image. A faint backlight brings the geometry just above the ICCD noise level but not too high to drown out plasma emission resulting from the pulse. The small light spot at the center of the bubble represents the focused image of the backlight. 158

6.3 The liquid streamer appears at small voltages and large gap separation. Both images are shown in the ICCD intensity scale 590-700 counts 162

6.4 The spark appears at large voltages and small gap separation. It is marked by a (a) characteristic prestreamer channel that forms before the spark. When the spark is ignited, (b) the emission is up to 50 times more intense than the liquid streamer. (c) In cases where the bubble is in the electrode gap, the spark is easier to ignite and can travel through the bubble. 162

6.5 The streamer bubble interaction, as captured by the high speed camera at 5000 frames s^{-1}. Upon making contact, the streamer imparts energy to the bubble, resulting in extreme destabilization of the bubble's shape. 164

6.6 A spark ignited between the two electrodes travels through the attached bubble. In the aftermath, a distinct track mark is left on the bubble surface. The Suematsu is pulsed at 12 kV, 750 Hz. The capture rate is 5000 frames s^{-1}. 166

6.7 Another example of the streamer bubble interaction more clearly shows the streamer channel evolution over time as well as the tendency of the streamer to find the bubble. The camera frame rate is 5000 frames s^{-1}. 167

6.8 Typical voltage and current traces for the streamer bubble interaction. The voltage drop is characteristic of a dielectric barrier discharge. The time scale displayed is relative to the oscilloscope trigger. 169

6.9 Evolution of the multiphase streamer within 2 μs of the breakdown event. The bubble glow becomes visible following the relaxation of the streamer channel. All images are shown in the ICCD intensity scale 590-700 counts. 170

6.10 ICCD images of the streamer making contact with the bubble, with 50 ns exposure. Below each image is a line profile of the emission intensity captured by the ICCD. The connection of the streamer to the bubble is marked by a dramatic increase in emission. 172

6.11 Bubble plasma in the aftermath of the streamer. The top row shows a comparison between air bubbles (left) and helium bubbles (right). The second row shows images taken with the He filter (590 nm), indicating the presence of helium in the bubbles. The bottom row shows plasma excitation in small bubbles (left) and large bubbles (right). All cases were taken at 13.6 kV and 500 ns exposure. 174

6.12 Evolution of the fluid boundary in the aftermath of the streamer impact. The conical wave front expands outward from a point that is directly across from the streamer impact location. 177

6.13 The fluid explosion length,Δx, was measured relative to the equilibrium diameter of the bubble, d_0. 179

6.14 The extent of the exploding boundary as a function of time following the breakdown event. Average bubble diameters were 0.5 mm, 1.3 mm, 1.8 mm, and 2.4 mm. 180

6.15 The explosion start time as a function of the equilibrium diameter. The larger the bubble, the longer the delay until the fluid boundary begins to explode outward. 180

6.16 The response of the bubble boundary at early times closely resembles a surface wave, which is distinct from the conical wave front observed at later times. 181

6.17 The excitation of plasma in a helium bubble contaminated with air for five cases: (a) a control bubble not driven by any pulse, (b) A 12 kV pulse, (c) a 11.5 kV pulse (d) two examples of plasma excitation at 13.6 kV with the backlight turned off. 184

6.18 The excitation of plasma in an air bubble. In this case, plasma is excited only when the bubble is extremely close to the electrode tip. 186

6.19 The excitation of plasma in a detached helium bubble under a 50 Hz, 12 kV pulsed voltage signal. Both rows are displayed in the ICCD intensity scale 590-700 counts. 186

6.20 2-D maps of the apparent ionization coefficient, λ, for (a) air bubbles and (b) helium bubbles. All values are shown in units of cm^{-1}. The ionization product, M, calculated using equation 2.12, is displayed in each bubble. 189

6.21 The dependence of λ on the size of the bubble for three different air bubbles. The total ionization product becomes sensitive to the bubble diameter, d when the attenuation length of λ is comparable to the size of the bubble. 191

6.22 The ionization product, M and the voltage drop across the bubble for different bubble sizes of air bubbles along with the single case for helium. In the case of helium, the bubble radius is 0.75 mm. 192

7.1 The modified wire-plane geometry used to drive and ignite a single bubble. The molybdenum wire electrode tip is not nearly as sharp as the syringe needle. 195

7.2 A single 1 ms electric pulse is applied to a levitated bubble. The bubble first distorts in response to the field and then aids in the ignition of an arc. The applied +voltage is 11.2 kV. 196

7.3 An initially attached bubble is pulled off the electrode, eventually aiding in the ignition of a spark across the electrodes. The applied voltage is 11.2 kV. 197

7.4 Following the elongation of the bubble by the applied field, small amplitude waves are spontaneously excited on the bubble surface. This phenomenon could be a result of plasma ignition in the bubble. 198

7.5 Dual voltage traces for the drive voltage (provided by the TREK) and the pulse voltage (provided by the Suematsu). The drive electrode stretches the bubble into the $l = 2$ mode, while the needle electrode pulses the bubble. 200

7.6 The bubble is stretched in response to the drive field. At 700 us, the pulse voltage is triggered, resulting a bridging streamer. 202

7.7 In certain cases, the bridging streamer appears to originate from the bubble, rather than from the needle electrode. 204

7.8 The bridging streamer splits the bubble into two separate fragments. 204

7.9 An arc bridges the needle and ground plate. Secondary streamers travel instead to the bubble (or vice versa). 205

7.10 2D Maxwell simulations of the electric field for both the spherical control bubble and the deformed ellipsoid bubble. (Top row): the simulated geometry along with the image that each is modeled after. (Middle row): the magnitude of the electric field shown in kV cm^{-1}. Dashed lines correspond to the integration path used to calculate M. (Bottom row): the electric field vectors in and around each bubble. 207

8.1 A simplified diagram illustrating the practical application of the shape effect. The injected bubbles float upward into the acoustic sound field, which excites capillary wave oscillations. The electrodes are then pulsed to ignite plasma in the volume of the bubble. 215

ABSTRACT

Plasma Ignition in Underwater Gas Bubbles

by

Bradley S. Sommers

Chair: John E. Foster

The ignition of plasma in underwater gas bubbles is a promising method of injecting chemically reactive species into liquids for applications in environmental remediation. To date, these studies have been limited to bubbles attached to the surface of the electrode. This dissertation proposes that plasma can be ignited in bubbles that are separated from the electrode by first deforming the shape of the bubble's dielectric boundary. This approach exploits a phenomenon termed the shape effect, in which the distortion of the dielectric boundary distorts and enhances the applied electric field in the volume of the bubble. The purpose of this dissertation was two-fold: (1) to demonstrate the shape effect by exciting strong deformations in underwater bubbles, and (2) investigate the fundamental mechanisms responsible for plasma formation in isolated bubbles. To accomplish this goal, an experimental apparatus was developed, capable of confining the bubble, deforming the shape of the bubble, and igniting plasma within the bubble interior. The apparatus utilizes ultrasonic acoustic standing waves to trap the bubble at a fixed position underwater and apply electric fields using electrodes that are mounted on a 3-D translation stage.

In general, it was observed that electric fields in the range 10-25 kV cm^{-1} were

capable of exciting bubbles into a wide variety of nonlinear deformations, including resonant capillary waves on the bubble surface, spherical harmonic perturbations, and in some cases the complete breakup of the bubble into multiple fragments. Simulations of the electric field in these deformed bubbles indicate that the enhancement of the applied field could be as large as a factor of 10. It was determined that the critical field for the destabilization and breakup of the bubble is approximately 25 kV cm^{-1}. A thorough investigation of fundamental discharge mechanisms in bubble filled liquids was also undertaken. It was shown that in a specific range of voltage and electrode geometry, a new type of streamer is observed that travels through the both liquid and the bubble gas. The interaction of the liquid streamer with the bubble was observed to result not only in the ignition of plasma in the bubble, but also to an explosion of the fluid boundary occurring in the aftermath of the streamer impact. Under careful adjustment of the operating conditions, the plasma could actually be confined to the bubble when driven by a 12 kV, 1 μs positive pulse. It was further observed that this isolated bubble plasma could be ignited much easier using a repetitively pulsed voltage source.

CHAPTER I

Introduction

This dissertation constitutes a fundamental investigation of plasma formation in underwater gas bubbles. This research is motivated by the potential utilization of liquid plasma discharges for applications in water purification and industrial waste processing. We begin with a review of recent efforts to use plasma discharges to replace conventional purification approaches and highlight the current limitations of such approaches. These limitations illustrate the growing need for a more balanced and sophisticated approach to producing plasma in liquids. At the foundation of this advance is a better understanding of the formation of plasma discharges in and around liquid water.

1.1 Environmental Applications of Plasma Discharges

The generation of electrical discharges in liquids, such as water, can be used to produce a variety of chemically reactive products, among which include free radicals, ions, high energy electrons, UV light, and shock waves [1, 2, 3]. The combined action of these products comprises an advanced oxidation process (AOP). AOPs can be applied to engineering problems ranging from the decomposition of volatile organic compounds (VOC) and dyes in industrial waste to the development of point-of-use water purification [1, 3, 4, 5, 6]. The plasma can be produced directly in or near the

liquid, allowing one to produce the relevant radical chemistry directly in the targeted medium without the need for long term storage or preprocessing.

Among the relevant chemical products generated in water plasma are H_2O_2, $O^{\bullet}$, $OH^{\bullet}$, $HO_2^{\bullet}$, O_3^*, e^-, O_2^-, O^-, O_2^+ [2]. These products share among them a high oxidation potential, lending them a degree of strong of reactivity with organic compounds. The product, ozone (O_3), is a radical species already in use worldwide for the purpose of water purification [5, 7]. The most substantial contributor to reactivity in atmospheric plasma sources, however, is believed to be OH [1], due to its high oxidation potential. The rate constant, k, for reactions between OH and organic compounds, for example, is of order 10^9 M^{-1} s^{-1} compared with ozone, which is in the range $10^{-2} - 10^4$ M^{-1} s^{-1} [5].

The excitation of liquid and gas molecules by plasma electrons can also lead to the production of UV radiation by the process of molecular relaxation. The discharge emission is typically in the near UV region (230 nm $< \lambda <$ 300 nm) [1], which is well known to be hazardous to bacteria. Finally, the intense energy density of many of these discharges also results in the excitation of shock waves and ultrasonic waves, which form another avenue for both biological deactivation and enhanced chemical reactivity [3].

Table 1.1 shows a list of the essential reactions involved in the production of reactive species by plasma discharges. The key mechanism is the production of high energy electrons, which provide the necessary activation energy for many of the chemical reactions. The primary reactions, which include excitation, dissociation, electron

Ionization:	$e^{-*} + A \rightarrow 2e^- + A^+$
Dissociation:	$e^{-*} + A_2 \rightarrow 2A^{\bullet} + e^-$
Excitation:	$e^{-*} + A \rightarrow A^* + e^-$
Electron Capture:	$e^{-*} + A + B \rightarrow A^- + B$

Table 1.1: Essential reactions involved in the production of reactive species in a plasma.

capture, and ionization, provide the starting point for a set of chain reactions that generate reactive species. In each case, A^* represents a particle in an excited state, while $A^\bullet$ represents a free radical. For plasma excited in atmospheric gas, the average electron energy is 1-10 eV, which favors the excitation of N_2 into the excited state $N_2(A^3\Sigma)$. Excited nitrogen can react with diatomic oxygen to produce the oxygen radical, $O^\bullet$ [3],

$$N_2^*(A^3\Sigma) + O_2 \rightarrow N_2 + 2O^\bullet \tag{1.1}$$

This oxygen radical provides the primary pathway for the production of ozone, O_3, though it is itself highly reactive with organic compounds. The oxygen radical can also be produced through impact ionization resulting from collisions between high energy electrons and diatomic oxygen.

For plasma discharges occurring exclusively in water, the reactant A takes the form of H_2O. In this case, dissociation plays an important role in producing the reactive radicals $OH^\bullet$ and $O^\bullet$. Another highly reactive product, H_2O_2, is formed from secondary recombination reactions. The deactivation of organic compounds by OH proceeds through one of two mechanisms, abstraction or addition [8]. In abstraction, the hydroxyl atom removes (or abstracts) a hydrogen atom from the organic compound while in the case of addition, the hydroxyl adds itself to the compound. In both cases, the hydroxyl radical, OH, attacks a hydrogen atom, H, in the organic compound, converting it to a highly reactive radical. This process typically results in a cascade of reactions that eventually convert the compound into harmless constituents. For an organic compound, RH, the most basic abstraction process typically

proceeds as follows [5],

$$\begin{aligned} RH + OH^{\bullet} &\rightarrow H_2O + R^{\bullet} \\ 2OH^{\bullet} &\rightarrow H_2O_2 \\ R^{\bullet} + H_2O_2 &\rightarrow ROH + OH^{\bullet} \\ R^{\bullet} + O_2 &\rightarrow ROO^{\bullet} \\ ROO + RH &\rightarrow ROOH + R \end{aligned} \tag{1.2}$$

Here the notation, $R^{\bullet}$, indicates that the compound, R, is a free radical. As an example, the deactivation of methanol, CH_3OH, results in the production of CO_2 and H_2O, two compounds that are less environmentally impactful. The mechanism for radical production described above indicates that the production of atmospheric plasma in liquids may provide a promising solution to applications requiring the reactive chemistry associated with O_3 and OH. The following sections provide a concise overview of some particular applications where plasma reactors have already shown promise.

1.1.1 Industrial Waste Processing

A wide range of industrial processing applications utilize water as a reagent or solvent, thus requiring a processing scheme that is compatible with a liquid environment [9]. The energy required to drive these reactions in-situ is usually supplied by heating the liquid medium. This is accompanied by substantial waste energy in the form of heat loss, which reduces the overall efficiency of the process. Cases requiring very high temperatures bring with them extra safety protocols and complex apparatus, which add additional cost and inefficiency. Non-equilibrium plasmas offer a promising alternative to this approach because they are capable of providing adequate activation energy without the need to elevate the reaction medium to high temperature [2, 8]. In addition to increasing energy efficiency, this approach also

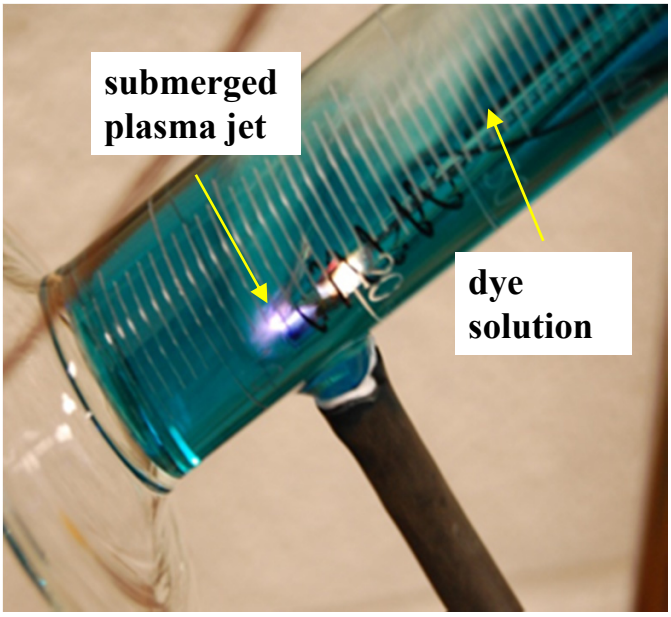

Figure 1.1: Ignition of plasma in the dye filled water leads to the direct injection of reactive species capable of deactivating the dye.

extends the set of possible reactions to those that require high activation energies but have products that would not survive high temperatures. Furthermore, the ability to control the energy distribution of plasma electrons using the applied voltage and gas flow allows one to specifically tailor the plasma to the specific application. Because of this versatility, atmospheric plasma sources have been investigated in a variety of liquid processing applications, including hydrocarbons [10], polymers [11], and nanomaterials [12]. In each of these cases, plasma sources have shown specific advantages over conventional processing technologies [8]. Among the most popular applications of atmospheric plasma sources to industrial processing is the treatment of industrial dyes, which account for nearly 20% of industrial water pollution [13]. This amounts to approximately one million kilograms of dye waste deposited into rivers and streams [14, 15]. Many of these dyes are carcinogenic. Others can become carcinogenic when metabolized by microorganisms and can also be toxic to local aquatic

life [13]. Traditional water treatment methods cannot remove such dyes due in large part to their inherent resistance to fading and the sheer volume of dye types [16]. Advanced oxidation processes, in conventional applications, have been investigated for water decolorization [17]. Since plasma produces a host of advanced oxidation products, they have also been investigated for water decolorization [18]. Plasmas are capable of reducing dyes into much simpler products (carbon dioxide, water, and inorganic intermediates). This process, known as mineralization, depends heavily on the OH radical, which is produced in abundance by plasma discharges. A plasma based processing scheme could be used to completely remove dyes from wastewater, allowing factories to recycle spent water streams. Plasma-based degradation of organic dyes in solution using plasma sources has been demonstrated in a number of studies [19, 20, 21, 22, 23, 24].

1.1.2 Water Purification: Addressing a Global Epidemic

Perhaps the most significant contribution plasma reactors can make to environmental mitigation is the preservation of affordable access to safe drinking water. Water sources across the globe are under the constant threat of contamination from agricultural runoff and industrial waste [1, 6, 5, 4, 10]. Nearly 80% of all childhood deaths worldwide are due to water-borne illness [25]. Increasing industrialization requires intensive water treatment protocols, designed to ensure that harmful chemicals and pathogens are reduced to levels that do not impact health. In underdeveloped countries with limited water resources, the need for waste regulation and modernized treatment facilities is great [26, 27]. In such regions, water quality imposes severe socio-economic forces on the indigenous population.

The direct transplant of advanced water treatment facilities from the developed world to the developing (or underdeveloped) world is very difficult due not only to the lack of economic resources but also to the lack of necessary infrastructure. This

Figure 1.2: Local water sources, particularly those in underdeveloped countries, illustrate the need for clean, portable water treatment systems.

includes resources such as reliable waterworks and electrical power. Water sources in these locations may also be highly localized, such as that shown in Figure 1.2.

In large part, then, it is the need for a portable, point-of-use water treatment system that is not only efficient but also free from the requirements of specialized infrastructure that motivates the development of plasma-based reactors. An idealized point-of-use system is depicted in Figure 1.3. Here contaminated water is extracted from the source (e.g. a local pond or stream) via pump. The source water is processed as it passes through the system, resulting in the expulsion of clean water into a receptacle. Such a system could make a dramatic improvement in water quality and health in underdeveloped countries.

The conventional approach to portable water treatment relies largely on the removal of harmful particles by filtering. Devices utilizing this method require frequent filter replacement due to contamination, particularly when operating in particulate and chemical-rich environments. This leads to reduced throughput and after pro-

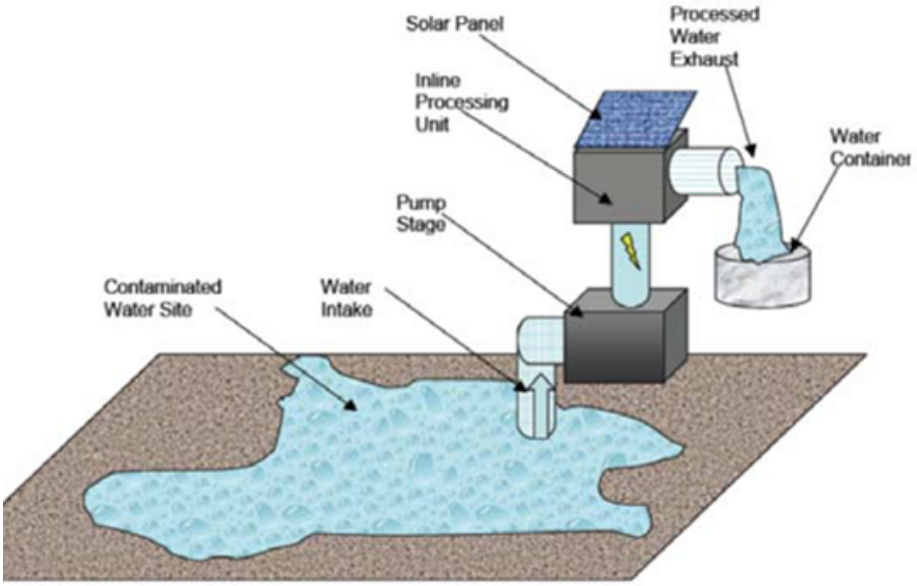

Figure 1.3: A simple scheme for a portable, point of use water treatment system utilizing a plasma discharge.

longed use to microbial contamination, thus turning the filter itself into a health hazard [28, 29]. Another limitation in these devices is the inability to remove certain classes of cysts and viral particles that are responsible for water borne illnesses.[30].

The use of chemical methods commonly associated with systems in the developed world, such as chlorine, have severe limitations when transplanted into portable treatment strategies, even in developed countries. Reactions of chlorine with organic matter in water produce trihalomethanes [31], which are carcinogenic and have been linked specifically to bladder cancer[32]. Bacteria and viral particles cannot develop a resistance to plasma AOPs because the process constitutes direct chemical oxidation of the microbial structure itself, including destruction of the cell membrane and cell wall [33]. OH radicals from the plasma can also diffuse into the cell, destroying or disrupting cell components, including enzymes and protein synthesis. Chlorination in rural and underdeveloped areas also raises a practical issue due to the difficulty in storing large tanks of chemicals. The promise of a plasma-based treatment source lies in its ability to produce on demand reactive products to address the wide variety

of biological and chemical materials that are dissolved in the contaminated water. Accomplishing this task without the need for long term storage of chemicals for large facilities makes plasma sources particularly attractive for the point-of-use water treatment system suggested above. The energy cost for cleaning water with plasma has been estimated to be as low as 10^{-4} kWh l^{-1}. [1]. More recently, it has been demonstrated that plasma-based methods of producing peroxide in liquid state are also competitive with conventional methods from an energy cost standpoint [34].

The list of contaminants that have been treated using plasma sources is long and diverse. Among these include, bacteria [35], viruses [36], pesticides [37], industrial dyes [38], and even pharmaceuticals [39]. Plasmas can also aid in more aesthetic effects, such as the removal of color, odor, and suspended materials. An extensive list of known reaction products can be found in Locke [2] and Malik [3]. A review of particular case studies utilizing the treatment of water by plasma can be found in Foster [8].

1.2 Plasma Discharge Types

Atmospheric plasma discharges have been studied in a wide variety of geometries and voltage sources. Locke [2] and Sato [40] have written thorough reviews, containing many of the same devices highlighted in this dissertation. Bruggeman [41] has written a review specifically for atmospheric discharges produced in or near liquids. Typically plasma discharges in liquid applications can be divided into two groups: (1) direct discharges, in which plasma is excited directly in the treated liquid, and (2) indirect discharges, in which the plasma is excited in a gas near the liquid surface. These can be further distinguished by the type of voltage used to excite the plasma: including direct current (D.C.), alternating current (A.C.), or pulsed discharges, in which the voltage is applied for durations down to $\sim$10 ns. In some cases, the plasma can be generated using travelling wave radiation sources, such as radiofrequency [42]

or microwave [43]. The following is a review of direct and indirect discharges, highlighting the different approaches taken to generate reactive species as well as the advantages (or disadvantages) of each approach.

1.2.1 Direct Discharges

Direct discharges are plasma sources generated directly inside the target liquid. [44, 45, 46]. This includes both direct ionization of the liquid as well as vaporization of the liquid in the vicinity of the electrode. Current understanding of liquid plasma is much less advanced than gas plasma due in large part to the increased complexity of the discharge mechanisms and propagation. A comprehensive review can be found in Joshi [47] and Kolb [48]. The conventional view of electron bombardment, for example, cannot fully explain ionization in liquids due to the large densities in fluids, (up to 10^6 higher than gases), which result in high collisionality and consequently electron energies far below the ionization potential [49]. Additionally, the chemical properties of polar liquids, such as water, lead to the quick solvation of electrons into the liquid solution ($\sim$10 psec) [50]. As a result, the primary charge carriers are positive and negative ions. In liquids containing dissolved gas, such as ambient water, it is believed that formation or preexistence of microbubbles is critical to the startup of the discharge [51, 52, 53], although Starikovskiy [54] has offered evidence that plasma can be excited directly in the liquid (without a gas discharge), as long as the pulse is sufficiently short.

An alternative explanation for ignition in liquids has been given by Lewis [55]. In this model, the intense electric field at the electrode-liquid boundary acts to electromechanically tear open the surrounding liquid, leading to gas pockets where plasma is ignited, thereby recreating the large electric fields at the electrode surface. This process leads to the gradual "unzipping" of the liquid medium allowing a gaseous plasma to propagate behind it. The gas pockets are believed to be initiated by the

transfer of vibrational phonon energy from the electrode to the liquid.

Overall, the precise mechanism of liquid breakdown is still debated. The propagation of the liquid plasma can be best modeled as a streamer discharge, similar in many ways to its gas counterpart [47]. Water has a large dielectric strength ($\varepsilon = 81$) and requires a larger electric field strength to excite plasma ($E_{holdoff} > 1$ MV cm^{-1}). This typically leads to higher power densities compared to gas discharges.

1.2.1.1 Types

Direct discharges fall under two primary modes of operation: the pulsed corona discharge (PCD) [45] and the pulsed spark discharge (SD) [46]. In a corona discharge, illustrated in Figure 1.4(a), the plasma is confined near the surface of a single electrode and does not make contact with the opposing electrode [3]. Often, this corona is a result of vaporization occurring at the electrode surface. Often the corona can evolve into a liquid streamer, shown in Figure 1.4(b), extending farther out into the reactor volume. If the voltage becomes large enough and the electrodes are sufficiently close, the plasma can make contact with the other electrode, resulting in a low conductivity plasma channel known as a spark. This is shown in Figure 1.4(c). The temperature in this plasma channel may reach 14,000−50,000 K with the plasma strongly emitting both emitting UV radiation and intense shock waves [38]. These factors tend to contribute to the higher rate of radical production in spark discharges. The downside is that a large amount of energy is spent raising the temperature of the water, leading to energy waste. This temperature increase is provided by the large current transported through the conductive channel. For comparison, pulsed corona discharges use about 1 J per pulse with a pulse frequency in the range 10^2−10^3 Hz while spark discharges use closer to 1 kJ per pulse with a pulse rate of 10^{-2}−10^{-3} Hz. [56]. The voltages required to ignite plasma directly in the liquid is in the range 10-100 kV depending on the sharpness of the electrode and the electrode gap

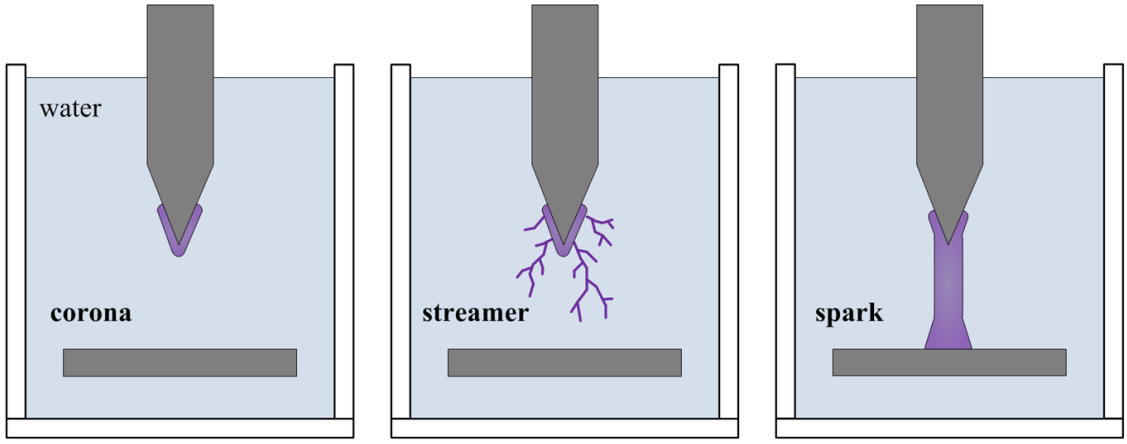

Figure 1.4: Direct discharge modes in increasing order of spatial extent: (a) corona, (b) streamer, (c) spark.

spacing. The key parameter is the critical electric field for breakdown, which is typically ∼1 MV cm^{-1}. In cases where the pulse length exceeds ∼100 ns, Joule heating and electrostatic stress can result in small voids or micro bubbles near the electrode surface [49]. These local gas pockets can reduce the electric field required for breakdown. The pulse length in most devices is very short, in the range 10-1000 ns, which minimizes thermal heating of the liquid.

1.2.1.2 Current Research and Issues

Despite their complexity, underwater discharges were among the first reactors proposed for plasma processing applications. A complete review of such approaches is given by Locke [2]. Large volume discharges in water have been demonstrated as a means to destroy organic compounds, including representative organic dyes [57, 58]. A comparative study of the relative efficiency of various discharge approaches has been carried out by Malik [59]. It was found that the approach with the highest energy efficiency is the pulsed spark discharge with oxygen gas bubbled through the apparatus. This dissolved oxygen is believed to decrease the voltage required for breakdown and enhance the direction conversion of O_2 into ozone O_3. The effect of

pulsed plasma on E. coli bacteria in river water has been demonstrated by Dors et al. [60], achieving up to 99.8% deactivation from a 56 kV pulsed corona discharge. Similar deactivation studies have been reported [21, 22, 23].

These results indicate a promising start in the development of viable plasma liquid reactors. However, there are a number of issues limiting the viability of direct discharges. Primary, among them is the large breakdown strengths associated with dielectric liquids. Water, for example, has a breakdown field of approximately 1 MV/cm [47]. Such high fields require extreme electrode geometries to effectively ignite plasma [2]. This usually takes the form of high curvature needle tips or small electrode gaps, neither of which is suited for processing large volumes of liquid. These conditions also lead to large energy densities, resulting in low electrical efficiency and erosion of the electrode [61]. An investigation of erosion dynamics in pulsed discharges by Goryachev [62] indicates that erosion proceeds largely through the current heating and subsequent boiling of the surface. In particular, it was observed that two factors dramatically increased the erosion rate: (1) an increase in pulse length, which provided more time for the electrode surface to reach its boiling point, and (2) an increase in the sharpness (or curvature) of the electrode, which concentrated the electric field and hence current density locally, thus leading to higher energy deposition. For practical considerations, the erosion of the electrode material not only contaminates the processing material but also leads to a change in the discharge performance as the electrode geometry continually changes.

Another issue that arises in designing practical devices is water conductivity, which has a strong influence on the excitation of direct discharges. In pulsed corona discharges, an increase in the conductivity (when changing from deionized water to tap water for example) results in a decrease in the radical production efficiency [2]. This is due to the ability of free charge to move around and shield out the applied field. In addition, a larger conductivity results in larger Joule heating of the liquid, which

may limit the energy available to drive radical chemistry. The conductivity issue is especially important for applications in liquid processing because most "real world" liquids are contaminated with metal ions and thus have high conductivity [63].

1.2.2 Indirect Discharges

The current limitations of direct discharges stand as a barrier to the practical realization of water plasma reactors. It is possible to avoid many of these shortcomings by producing the plasma in a gas phase discharge in close proximity to the liquid. The radicals and excited species can then be transported into the liquid by convection or diffusion. The most basic way of implementing this approach is to place the pulsed electrode immediately outside the surface of the liquid as is shown in Figure 1.5(a). Often the ground electrode is submerged in the water. This geometry is usually called a surface discharge and is typically just a corona or streamer formed in the ambient air above the liquid. Malik observed, in his review of discharge efficiency[59], that surface discharges have much higher energy efficiency relative to any direct discharge, but unfortunately have considerably less mass yield for reactive products. For a surface discharge placed over a thin liquid film, the efficiency was nearly 2000 times larger than the typical direct discharge. However, the thinness of the liquid film severely limits the maximum processing rate of the discharge.

This design illustrates a consistent theme pervading the literature on liquid plasma sources: indirect discharges expend less energy but produce fewer radicals and hence achieve lower reactivity. The following sections provide an overview of the most prominent approaches to indirect discharges; a thorough review can be found in Bruggeman and Leys [41].

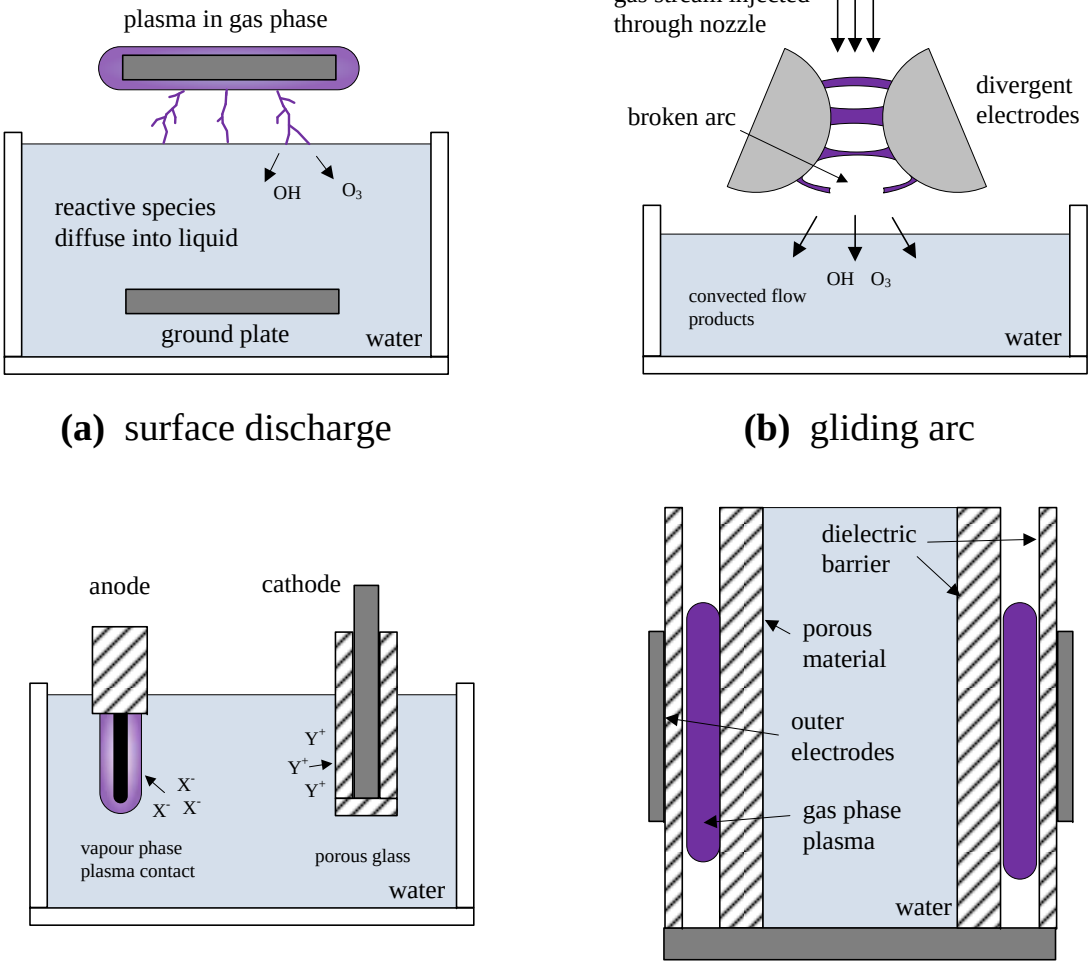

Figure 1.5: An indirect discharge is excited in a nearby gas in the vicinity of the target liquid. The four most prevalent approaches are (a) the surface discharge (b) the gliding arc, (c) contact glow discharge electrolysis, and (d) the dielectric barrier discharge.

1.2.2.1 Dielectric Barrier Discharges

In a dielectric barrier discharge, plasma is formed in an electrode gap where one or both of the electrodes are isolated with a dielectric material [64, 7, 65]. This dielectric material prevents large currents from flowing between the electrodes and hence prevents runaway current, thus preventing appreciable gas heating. Typical electrode voltages are 15 kV. The electron density in these streamer discharges reaches up to 10^{14} cm^{-3} with electron energies in the range 1-10 eV [7]. The implementation of a dielectric barrier discharge to a processing reactor can be accomplished in a number of ways. The most direct method is to simply ignite the DBD above the liquid much in the same way as done in the surface discharge. However, in this geometry it is difficult to maximize treatment area. A more clever approach is shown in Figure 1.5 [64]. In this case, the dielectric boundary is formed by a porous material in contact with the liquid. This porous material allows the transmission of reaction products into the liquid without allowing the two phases (gas and liquid) to mix. Hence one can ignite an energy efficient discharge on one side and maximize the treatment area on the other.

Another approach used to increase the exposure area of the plasma to the liquid is the submerged DBD plasma jet. This design features a coaxial electrode geometry with a thin glass tube forming the dielectric. The gas is fed through the tube and is ignited at the tube outlet. In this geometry, the injection of gas through the central tube preserves a small volume of gas at the jet outlet where plasma can be formed, thus allowing plasma to form in the tube gas and not in the liquid. A D.C. powered plasma jet, developed by Liu et al. [66], has demonstrated effective inactivation of the S. aureus bacteria. Foster [67, 68] has developed an underwater jet powered by A.C. voltage at 1-5 kHz. Decomposition of methylene blue up to 93 % concentration has been achieved for processing times under 7 minutes.

1.2.2.2 Contact Glow Discharge Electrolysis

Contact glow discharge electrolysis (CGDE) is an extension of normal electrolysis [69, 19, 70, 71, 72, 73]. When the voltage between the anode and cathode becomes large enough, a plasma forms within the thin layer of vapor surrounding the liquid. This results in a significant reduction in the current through the electrolytic solution. More importantly, it allows a substantial increase in the chemical yield far beyond the so called Faraday value, which is an inherent limit in the reaction rate of normal electrolysis. It is believed that this phenomenon is due to the production of reactive species resulting from collisions between neutral particles and high energy ions as they are accelerated (to as high as 100 eV) through the plasma sheath [74]. The evolution of the plasma sheath has been determined to be a combination of Joule heating through the solution and hydrodynamic instabilities at the electrode surface. The use of CGDE to produce a plasma reactor would allow the production of relevant radicals directly in the volume of water without the need to produce a direct liquid breakdown. The typical operating voltage for CGDE devices is 0.5-1.5 kV. Early processing experiments with CGDE, such as that done by Harada [73], involved synthesis of organic compounds, amino acids in particular, in aqueous solution. The first decomposition experiments were done by Sharma [37] on the pesticide Pentachlorophenol (PCP). In this experiment high level decomposition was achieved, reducing a solution of 50 ppm down to under 0.01 ppm in 30 minutes. More recently, Jin et al. [19] demonstrated the decomposition of acid orange 7.

1.2.2.3 Gliding Arc Discharges

The gliding arc discharge is a transient plasma source produced between two curved electrodes with the so called diverging geometry [75, 76, 77, 78, 79, 80]. A diagram of the most basic design is shown in Figure1.5 (b). A gas nozzle is placed directly above the electrode system and used to inject gas between the electrodes. A

plasma arc, composed of the injected gas, is then produced between the electrodes near the point of closest inter-electrode separation. The forced convection of the injected gas stream carries the arc downward in the direction of increasing electrode separation. Eventually the arc becomes disconnected and the plasma cools, thus preventing excessive thermal heating of the gas stream. The net result of this process is the convective transport of reactive species (produced by the plasma) directly into the liquid surface.

Typically, the operating voltage on the electrodes is 10-15 kV, with discharge powers in the range 100-700 W. Demonstrations of contaminant decomposition in liquid water have been performed by Czernichowski [76]. However, the reactivity is limited by the low exposure area of the plasma to the liquid surface. One method of increasing the exposure area is to inject the treated liquid as a vapor spray through the gliding arc reactor geometry, as done by Burlica [75]. In this geometry, gliding arc discharges have been found to produce energy efficiencies up to 400 times higher than the standard (direct) pulsed corona discharge [75], particularly when the arc is produced by a pulsed voltage source. Demonstrations of gliding arc discharges placed above liquids (see Figure 1.5(b)), however, have yielded lower efficiencies, closer to a direct, underwater discharge [59]. The primary limitation of this approach is a decrease in processing rate since the treated liquid must be vaporized and injected through the small electrode gap ($\sim$5 mm) of the arc geometry.

1.3 Plasma Discharges in Gas Bubbles

The design and evaluation of plasma devices for applications in the liquid medium is dictated by the need to (1) ignite plasma efficiently in a gas phase discharge and (2) transport reaction products efficiently into the liquid. It is clear that due to the desired transport of short-lived radicals into the liquid, the gas phase plasma must be as close to the liquid as possible. A natural approach to improve the exposure area

of the gas phase plasma to the contaminated liquid is to produce the plasma in gas bubbles that are distributed throughout the liquid volume. This approach represents a marriage between the efficient plasma production of the indirect discharge, and the direct exposure of radicals and high reaction rate associated with the direct discharge. Ideally, the plasma would be evenly distributed throughout a multitude of bubbles in order to maximize the reaction area.

The following sections provide a detailed look at different approaches that utilize plasma formation in bubbles to inject chemical reactivity into water. As is true of all indirect discharges, the bubble gas represents a lower breakdown voltage medium in which plasma can be ignited to feed reaction products into the liquid medium. The key design goal is to exploit the presence of the bubbles to increase the plasma exposure to the liquid and hence increase the amount of reactivity.

1.3.1 The Electrode Attached Bubble Geometry

The most common approach to bubble plasma reactors features the electrode attached bubble geometry, shown in Figure 1.6. In this approach, bubbles are in direct contact with the high voltage electrode responsible for igniting the plasma discharge. The bubble can be injected using a syringe, by agitation using a piezoelectric valve, or by fast injection using a solenoid valve. This latter option allows precise control over the bubble size, which is a property that directly affects not only the reaction area of the plasma but also the physics of plasma formation. The high voltage electrode may function as the injection needle−as in the case of Shih [81]−or it may simply be positioned near the injection point−as in the case of Gershman [82]. The grounded electrode is typically a plate, located across from the gas injection inlet, separated by a body of water. The reactor may use a single bubble, resting at the gas inlet, or a constant flow rate of bubbles. This is often established when the inlet pressure feeds gas into the bubble until it is too large to retain contact and floats away, resulting in

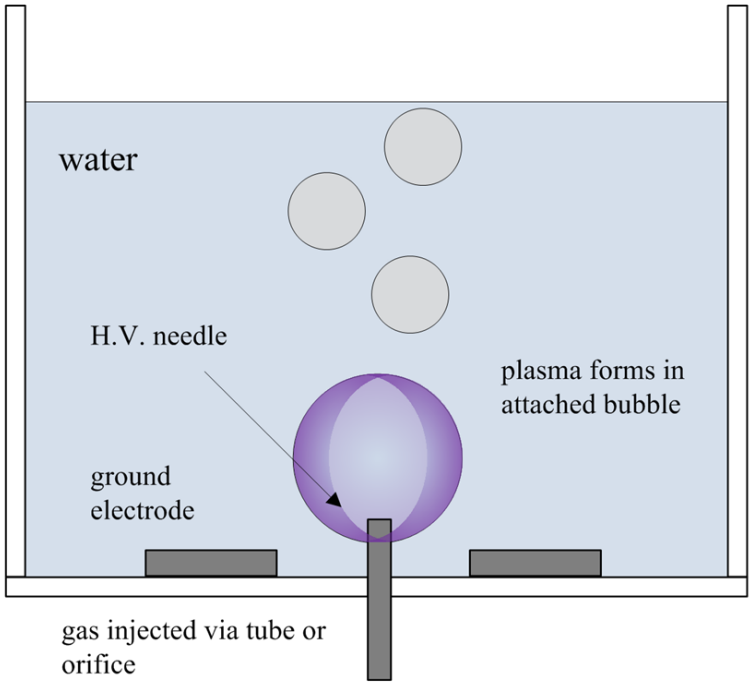

Figure 1.6: In the electrode attached reactor geometry, the bubble is placed in contact with the electrode. The reactive products form along the walls of the bubble and diffuse out into the liquid volume.

the growth of the next bubble. The bubble may also be expelled from needle by the discharge itself, either by heating or simply the high electric stress, resulting in a slow consistent flow of bubbles. A more detailed look at the physics of these discharges and the influence of gas type is provided in section 1.3.3.

Among the most detailed investigations of this discharge type was done by Gershman [82]. In this design, a single bubble, 2-8 mm in diameter, was injected through a 0.5 mm needle tip, which also formed the negative high voltage electrode. The bubble was pulsed at 3-15 kV with a pulse length of 1 us and a rise time of 100-200 ns. The pulse was delivered through a Blumlein pulse forming line. The positive ground plate electrode was held 5-10 mm across from needle in water, which was deionized. It was determined using high speed light measurements (with a photomultiplier tube) and current measurements that over the course of the pulse, multiple discharges occurred and that each took place over the span of approximately 10 ns-with a 50-80 ns decay.

This was found to be consistent with the transit time of an electron avalanche across the bubble diameter, indicating that the plasma was a streamer occurring in the volume of the bubble. It was observed that two factors decreased the time delay before plasma formation (1) increasing the voltage and (2) decreasing the bubble diameter. Furthermore, it was observed that there existed a minimum voltage beneath which the plasma would not ignite reliably. A 2 mm bubble for example, required at least 4 kV for breakdown. Use of the 309 nm OH filter confirmed the production OH radicals following ignition of the discharge.

Shih and Locke [81] developed a similar device that featured an injection port separate from the high voltage needle with continuous injection of bubbles into the device. After injection, the bubbles rose along the length of the needle, during which time plasma is ignited within. The high flow rate of these bubbles produced an effective gas "cloud" around the needle, feeding discharge products into the liquid medium. In this case, argon was the feed gas at 500 mL/min. Voltage was supplied at 35-55 kV pulses with 200 ns rise time and 200-300 ns pulse length. In this study, greater attention was paid to the power input and radical generation rates, in order to evaluate the discharge as a potential reactor. A second discharge geometry featuring a direct ignition of the liquid with the high voltage needle was also investigated for comparison with the bubble discharge. It was observed that the bubble discharge had lower power input and lower electrode erosion but that it had considerably lower mass yield of reactive radicals (g/kWh) compared to the direct discharge. This was explained by the observation that in the case of the direct streamer discharge, the contact area between the liquid and plasma was maximized, whereas in the case of the bubble discharge, most of the discharge was taking place deep within the volume of the bubble near the needle, thus restricting the transport of the radicals into the volume of the water.

1.3.2 The Rising Bubble Stream Geometry

An alternative to the electrode attached geometry is to inject the bubbles as a rising stream that travels between the electrodes, such as that done by Miichi et al. [83, 84]. This approach represents an attempt to extend the plasma farther into the volume of the water and produce a reactor with true "in-volume" processing capability. A simplified scheme for this reactor type is shown in Figure 1.7. In this approach, bubbles are injected at the bottom of the cell and are allowed to float upward between the electrodes. The bubbles are injected in sufficient density and proximity to the electrode that plasma can be ignited directly inside them. The average bubble size was calculated to be 1.5 mm and the average steady state number of bubbles was approximately 2000 within the active region. The electrodes were set 5 mm apart and powered with 13-18 kV pulses that had a 100 ns rise time and a 200 ns pulse length. Production of OH radicals was confirmed via spectroscopy, and ozone levels of up to 300 ppm were produced directly above the water, with mass yields up to 40 gO_3/kWh, considerably lower than the typical direct discharge. An important factor in performance was proper coupling of the energy input to the bubble flow rate. If the bubble flow rate was too large, then many bubbles in the stream would not undergo breakdown and hence not participate in radical production. If the flow rate was too low, then the processing rate would not be practical. The former situation is also undesirable because bunching of the bubbles can result in spark discharges across the electrode gap, which result in large, inefficient energy input the liquid. Because these tests were focused on demonstrating the efficacy in producing radicals, little effort was put into determining the exact nature of the discharge. It is unclear if the rising bubbles need to be attached to the electrodes for plasma ignition to occur. If so, is what is minimum voltage required to restrict the plasma to only the isolated bubble? This leaves a number of open ended questions related to the physical origin of bubble discharges to be addressed in future work.

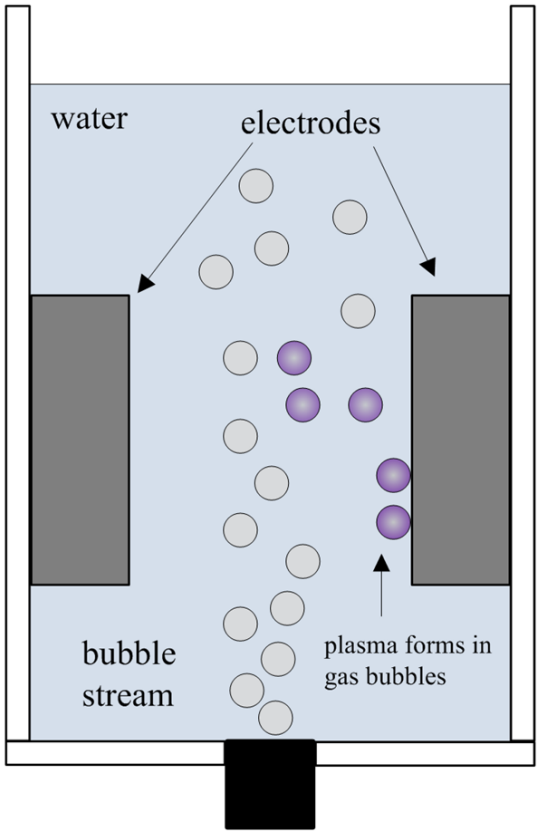

Figure 1.7: In the rising streamer reactor geometry, the bubbles rise up in between the electrodes. During ideal operation, the plasma forms in isolated bubbles. However, in reality, the majority of excitation occurs in bubbles that become attached to the wall.

1.3.3 Physics of Bubble Discharges

The approaches reviewed thus far have yielded a number of promising results that suggest bubble plasmas offer a realistic approach to mitigating environmental hazards, specifically in their ability to improve energy efficiency and electrode wear relative to direct discharges. Detailed studies of the discharge physics have been done by Sato [40] and Tachibana [85]. In the former case, the H.V. needle was replaced by a plate beneath the gas flow injector. Discharges in different feed gases were compared between argon, helium and oxygen and time resolved using a high speed ICCD camera. It was observed that in general, the discharge begins at the base of the bubble and travels up through the bubble along the bubble wall. In argon and helium,

the discharge was observed to be more uniform. For the specific case of helium, the discharge represented a single dense channel travelling vertically through the volume of the bubble.

A similar study in determining the role of gas type on discharge properties was performed by Tachibana [85]. In this case, applied voltages were 15 kV. It was observed that in the case of molecular gases, such as oxygen and nitrogen, the discharge was filamentary and produced a noticeable perturbation on the bubble surface in the immediate aftermath of the streamer. For rare gases, such as helium and neon, the discharge was constrained to a single channel and produced a more diffuse glow. Rather than initiating surface waves, the streamers were observed to produce a substantial perturbation on the top of the bubble. A single central channel streamer is observed immediately before this. To explain the difference in streamer propagation observed in different gases, the authors offer the following explanation: rare gases, such as helium and neon, have ionization coefficients that are less sensitive to changes in the reduced field. Therefore, ionization need not take place at the fluid boundary where the field enhancement is largest. Furthermore, once the discharge is initiated in a straight path for these rare gases, the streamer field becomes the dominant source of ionization causing it to continue on its path straight. Rare gases also have shorter photon mean free paths, making ionization along the axial channel more likely.

Tachibana also used bandpass optical filters to measure the gas dependence and position dependence of various emission lines. It was observed that at the boundary of the bubble where the streamer channel is most intense, the dominant line is the hydrogen alpha, H_α, while the emission from the volume of the bubble was largely due to the specific gas. Furthermore, the intensity of both OH and H_α was approximately a factor of 4 larger in the case of helium and neon compared to nitrogen and oxygen.

A computational investigation of streamer formation in gas bubbles surrounded by dielectric liquids was performed by Babaeva and Kushner [86]. The model used

in this work, *nonPDPSIM*, is a plasma hydrodynamics model in which continuity, momentum, and energy equations are solved for charged and neutral species while the Poisson's equation is used to solve for the electric potential. A full description of the code is found in [87]. In this study, it was determined that the permittivity of the surrounding liquid played a critical role in determining the propagation of the streamer through the bubble. In particular, as the permittivity rises, the tendency of the streamer to hug the boundary of the bubble increases. In the cases of water, where the relative permittivity is 80, the streamer travels exclusively along the surface. All simulations were done for humid air, so it is unclear what further effect the gas type has on this process. The reason streamers tend to hug the surfaces of the bubble in dielectric liquids is due to the refraction of the applied electric field at the boundary of the bubble, where the permittivity changes drastically. The distortion of such fields, as we shall see, plays an integral role in the design and characterization of a geometry capable of producing plasma in bubbles. It was also observed that increasing the conductivity of the liquid also increased the tendency of the discharge to propagate along the surface. This is again due to distortion of the field. In a conductor, negative charges move in the vicinity of the boundary in an attempt to cancel the applied field. This results in the regions of high field strength being pushed inside the bubble and hence increases the field at the boundary.

1.3.4 Plasma in Isolated Bubbles

Up to this point, practical realizations of plasma occurring in bubbles have been limited to surface discharges, in which the bubble is attached to the high voltage electrode. Such surface discharges appear to offer little improvement to the processing rate, or throughput problem, compared with the other indirect discharges reviewed so far. Ideally, it is preferable to produce plasma in an array of gas bubbles that are extended throughout the processing volume. The ability to extend the reaction

volume of the plasma would go a long way towards solving the throughput problem. In this case, the reaction products could be produced anywhere within the volume of the liquid, dependent largely on the location and relative density of the active bubbles. As a result, transport of reactive species into the liquid would be restricted only by the penetration depth of the local bubble surface. This effect could be improved by increasing the density of air bubbles in the liquid, which under sufficient proximity may even be able to support the hopping of plasma streamers bubble to bubble, as shown by Kushner and Babaeva [88]. It is quite clear, therefore, that successful ignition of plasma in isolated bubbles is a critical step in making bubble discharges (and all liquid discharges) a viable option as a source of environmental mitigation.

Plasma ignition in isolated bubbles, however, is quite difficult. One reason is the high permittivity of the surrounding water, which prevents the applied electric field from penetrating far into the liquid medium [49]. The electric field in an isolated bubble will therefore be severely depressed from its value at the electrode. The most important reason is the absence of a conducting surface in the proximity of the volume. A conducting surface provides a source of secondary electrons via ion impact and also through field emission [89]. These secondary electrons may play a crucial role in seeding the discharge and thus reducing the voltage required for breakdown. The electrode surface also provides indirect field enhancement from the inevitable asperities associated with manufacturing.

Perhaps, the closest experimental case of plasma in an isolated bubbles comes from Bruggeman [90], who investigated plasma formation in capillary bubbles. In this work, air bubbles were trapped underwater between the edges of a thin Pyrex tube 1.1 mm in inner diameter. Two opposing electrodes were submerged in the water far away from the bubble on either side. The applied voltage was 9 kV. The exciting electrodes were placed in the water, far away from the bubble. Bruggeman observed surface discharges occurring on the boundary between the bubble and glass. These

were explained as a result due to field enhancement at the dielectric glass surface, which resulting in corona like discharges that were incapable of developing into full streamers, due in part because, at 26 kV cm^{-1}, the attachment rate was higher than the ionization rate.

Simulations done by Babaeva and Kushner [88] have provided a glimpse into the physics of plasma formation in isolated bubbles. This work investigated the formation of streamer in the presence of bubbles of lower density than their ambient. This density variation served to simulate the difference in breakdown conditions between air and water through density alone. Overall it was observed, that the presence of low density bubbles strongly influenced the propagation of the streamer and in some cases resulted in the isolated ignition of plasma inside the bubbles. Moreover, these seed plasma were observed to evolve into both cathode and anode directed streamers in the liquid, depending on the conditions. These simulations give a preliminary indication of the effect that bubbles have on breakdown and the ability to seed isolated plasma directly in the bubbles. It is clear, however, that the presence of liquid presents a degree of complexity that is not captured by simply altering the gas density. For example, these simulations did not account for any permittivity change between the bubbles and background. Moreover, as a result, the effect of molecular cohesion was not included in determining streamer breakdown or electron solvation/attachment.

1.4 Dissertation Scope: Making Bubble Discharges Practical

It appears that the key factor in achieving plasma ignition in isolated bubbles is to find an approach that will compensate for the increasingly difficult breakdown conditions observed in changing from attached bubbles to isolated bubbles. As discussed in Section 1.3.4, these difficulties arise from two primary issues: (1) the absence of secondary electrode effects and (2) the attenuation of the applied field far into the reactor volume. The overarching purpose of this dissertation is to present an approach

that is capable of altering the breakdown conditions inside the bubble. A secondary goal of this work is to further characterize the physical understanding of plasma ignition and evolution in bubbles. The focus of contemporary literature, until now, has been on the experimental demonstration of plasma bubble reactors, with little attention paid to the characterization of fundamental discharge physics. A better understanding of the mechanisms behind plasma formation in and near the gas liquid boundary is critical not only for the practical design of liquid plasma reactors but also for the current understanding of plasma formation in liquids.

CHAPTER II

Theory

2.1 Introduction

A complete characterization of plasma formation in underwater gas bubbles covers a wide range of disciplines including gas discharge physics, fluid mechanics, and electrodynamics. This chapter provides a concise introduction to each of these areas, beginning with a review of plasma ignition in atmospheric sources. This review establishes the necessary foundation to introduce the central hypothesis of this work, that altering the shape of underwater gas bubbles can be used to alter the primary factors that determine plasma formation, including the electric field and the gas pressure. Following the statement of the hypothesis, a review of bubble dynamics is given, including a description of the behavior of bubbles under the action of electric fields. Finally, the chapter ends with an example of the dielectric sphere, which illustrates how many of the tools presented here can be used to analyze discharge physics inside a bubble.

2.2 Electrical Breakdown in Atmospheric Gases

Electrical breakdown in gases arises from the development of electron avalanches under the action of an applied electric field. The growth of an avalanche (or swarm

as it is often called) is influenced by a variety of ionization processes, including electron impact ionization, photoionization, dissociative ionization and Penning ionization [89]. Electrons can be lost from the avalanche as well, through multiple processes such as attachment, recombination, and diffusion. In general, the evolution of the electron energy distribution, $f(v)$, in the electron avalanche is determined by the Boltzmann equation [91],

$$\frac{\partial f}{\partial t} + \mathbf{v} \cdot \nabla f + \frac{\mathbf{F}}{m} \cdot \frac{\partial f}{\partial \mathbf{v}} = \left(\frac{\partial f}{\partial t}\right)_{coll} \tag{2.1}$$

Here, the term $\mathbf{F}$ represents the external force acting on the electron, in this case the applied electric field. The term on the right hand side of the equation represents the change in $f(v)$ due to collisions. At equilibrium, many properties of the electron, including the mean electron energy, v_e, and the electron energy distribution function, $f(v)$, can be characterized by a quantity called the reduced electric field [92], which is defined as the applied field strength E divided by the neutral gas density N. The reduced field is typically stated in units of Townsend (Td) with the conversion, 1 Td $= 10^{-17}$ V cm^2. The rate constants for many of the gain and loss processes occurring in the avalanche can be expressed as the number of reactions occurring per unit distance traveled by the electrons. Many of these parameters have been measured and tabulated extensively [93, 94, 95, 96, 97, 92, 98]. Although most atmospheric plasma sources are fundamentally nonequilibrium in nature [99], the use of these well-characterized swarm parameters can provide a useful diagnostic in predicting the evolution of plasma in this work. The following sections provide an overview of the basic electron swarm parameters used throughout this work.

2.2.1 Electron Swarm Parameters

The number of electron-ion pairs created per unit length through the process of electron impact ionization of neutrals is denoted by the letter α. This is historically referred to as the first Townsend coefficient. A formal definition can be written in terms of the ionization cross section $\sigma_i(v)$, neutral particle density N, electron drift velocity v_d, and electron energy distribution, $f(v)$,

$$\alpha = \frac{N}{v_d} \int \sigma_i(v) v f(v)\ \mathrm{d}v \quad \left[\mathrm{cm}^{-1}\right] \tag{2.2}$$

Obtaining an analytical form of α is complicated by the fact that collisions define the energy distribution, which reciprocally determines the collision rate. One can simplify this analysis by assuming that the swarm is in equilibrium with the applied field [92]. Townsend was the first to derive a semi empirical form with this approach, obtaining an expression for α written in terms of the reduced field E/N [100],

$$\frac{\alpha}{N} = F \exp\Big(- \frac{G}{E/N} \Big) \quad \left[\mathrm{cm}^{2}\right] \tag{2.3}$$

The parameters F and G can be estimated by experimental measurements of α or can also be estimated by assuming a simple form for the electron distribution function [101]. The form of α given by equation 2.3 provides a good approximation over the range 50-200 Td, in air for example, but becomes less accurate at high values of E/N due to the presence of high energy electrons in the tail of the energy distribution. According to equation 2.3, the first Townsend coefficient is determined primarily by the electric field and neutral gas density through the reduced field E/N.

Figure 2.1 shows the ionization coefficient for a variety of relevant gases. All data is taken from the review by Dutton [92]. Typically, the noble gases have higher α than the electronegative gases. At a value of 100 Td (25 kV cm^{-1} at 1 atm), for example,

the ionization rate for helium is larger than air by a factor of nearly 600. As the reduced field is increased above 1000 Td, however, all values of α converge toward one another. The reason for the disparity in α among different gases, especially those with similar ionization potentials, is due to the multitude of other processes affecting the electron swarm as it evolves under the applied electric field. In electronegative gases such as oxygen and water vapor, electrons can be removed from the swarm through electron attachment, a process by which the electron becomes attached to a neutral molecule. An electron lost from the avalanche in this manner can no longer take part in ionization reactions and thus represents a loss mechanism. One can define the attachment coefficient in an analogous manner to α, as the number of attachments occurring per unit distance. It is often denoted by the letter η. In general, there are four different reactions through which attachment can occur.

1.) radiative attachment: An atom absorbs an electron and the excess energy is emitted as a photon with frequency ν.

$$A + e \rightarrow A^- + h\nu \tag{2.4}$$

2.) dissociative attachment: A molecule, AB dissociates into its constituents, with one of the atoms absorbing an electron.

$$AB + e \rightarrow A^- + B \tag{2.5}$$

3.) three-body attachment Two atoms and an electron simultaneously collide, resulting in the attachment of the electron to A or B.

$$A + B + e \rightarrow A^- + B \tag{2.6}$$

4.) dissociation into ions: The molecule, AB collides with an electron, dissociating into its constituent parts.

$$AB + e \rightarrow A^- + B^+ + e \tag{2.7}$$

In atmospheric discharges, dissociative attachment and three body attachment are the two dominant processes [92]. Furthermore, in three body attachment, $\eta \propto N^2$, which is due to the requirement of two neutral gas particles for the reaction to take place. In contrast, for dissociative attachment, $\eta \propto N$. These relationships indicate that three body attachment should dominate at high levels of N while dissociative attachment should dominate at lower values of N.

Figure 2.2 shows experimentally obtained values of η for oxygen, tabulated from two sources, Dutton [92] (for low E/N) and Naidu [94] (for high E/N). Like the ionization coefficient, the attachment coefficient is shown in reduced form as η/N. At low values of E/N, the quantity η/N, is sensitive to changes in density due to the dominance of three body attachment. However, at sufficiently high values of the reduced field ($E/N \sim 30$ Td), the quantity η/N becomes independent of density. Measurement of η above 100 Td is difficult in any gas due to the dominance of ionization [89].

Another process observed in electronegative gases is detachment, the liberation of an electron from a negative atom or molecule. As a result, it represents a gain process that contributes to the electron swarm. Like the other coefficients, the detachment coefficient, δ, is often defined in reduced form, as δ/N. Although detachment is expected to play a significant role in avalanche development, it will be ignored in this work. The error in neglecting detachment is not great since the measurements of δ/N in the range 100-140 Td are of order 10^{-19} cm^2 in air. [92]. Looking at Figures 2.1 and 2.2, this is relatively small compared to the other coefficients defined thus far.

The collective action of gain and loss mechanisms in electronegative gases is represented by a quantity, λ, often referred to as the "apparent" ionization coefficient

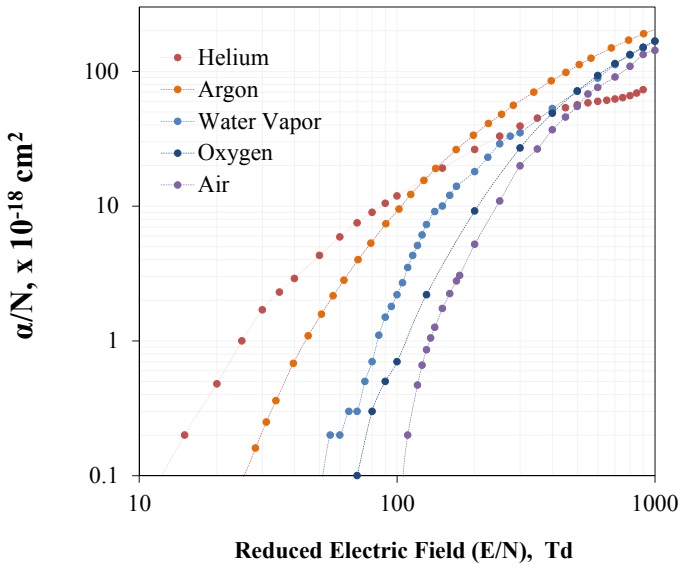

Figure 2.1: A survey of reduced ionization coefficients for noble gases (Ar, He) and electronegative gases (H_2O, O_2, and air). All data taken from Dutton [92].

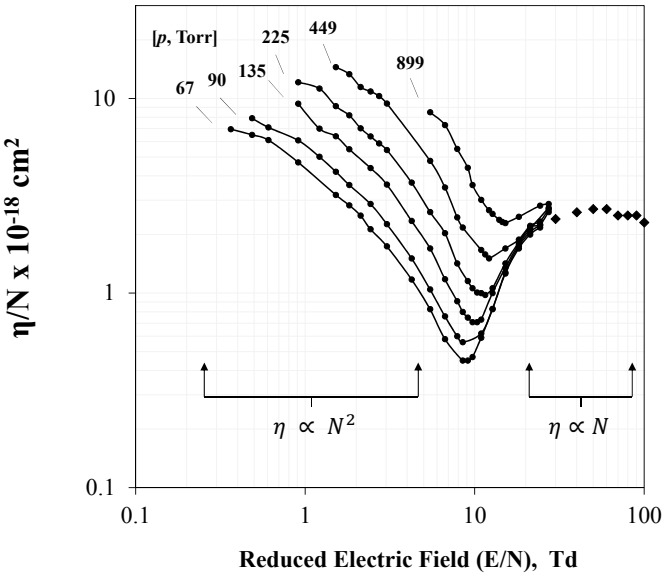

Figure 2.2: The reduced attachment coefficient for oxygen, the primary source of attachment in ambient air. At low E/N, η is dominated by three body attachment, while at higher E/N it becomes dominated by two body dissociative attachment. Data taken from Dutton [92] and Naidu [94].

[92]. In reality, experimentally obtained values of α for electronegative gases, including those in Figure 2.1, more accurately reflect the apparent ionization coefficient [92] due to the difficulty in separating each process experimentally. Methods of separating ionization from attachment do exist, but not at large values of the reduced field [92]. The apparent ionization coefficient is convenient for the analysis of plasma formation in bubbles since it measures the net ionization occurring in the bubble, which can be used to predict when breakdown will occur. A relation for both the electron swarm growth and apparent ionization coefficient, after taking into account all swarm processes, can be derived, but is rather complex [92]. Under the conditions that only ionization and attachment are important, the form of λ can be reduced to,

$$\lambda(\mathbf{x}) = \alpha(\mathbf{x}) - \eta(\mathbf{x}) \tag{2.8}$$

Here the spatial dependence of the swarm parameters is explicitly stated. This results from the spatial dependence of the applied field, E. This

In this work avalanche growth will be assumed to be a balance between impact ionization and attachment, with the apparent ionization coefficient $\lambda = \alpha - \eta$ determining whether the avalanche is growing or subsiding.

2.2.2 Townsend Breakdown

Electrical breakdown usually takes place in the presence of conducting electrodes, which contribute to the ionization process. During avalanche formation, ions created in the avalanche are accelerated back to the cathode by the applied field, where they collide with the surface. A fraction, γ, of these collisions each result in the liberation of an electron from the surface, which is accelerated by the field and contributes to the electron swarm. The variable γ is known as the second Townsend coefficient. More generally, γ contains contributions of secondary electron emission due to a host

of processes, including photon and metastable interactions with the cathode surface [89]. The electron swarm density at a distance x from the cathode can be written in terms of the swarm parameters, α, η, and γ, as [89],

$$n(x) = \frac{n_0 e^{(\alpha-\eta)x}}{1-\gamma\left(e^{(\alpha-\eta)x}-1\right)} \tag{2.9}$$

The basic Townsend breakdown criterion can be derived by setting the denominator equal to zero, which corresponds to the condition that the avalanche current (or density) grows to infinity. For a position dependent electric field (and hence position dependent α and η), this breakdown condition can be stated as [98],

$$\int_0^d (\alpha-\eta)\mathrm{d}x = \ln\left[\frac{1}{\gamma}+1\right] \tag{2.10}$$

In this case, d is the electrode gap spacing. Equation 2.10 states that breakdown is likely to occur if either the secondary electron yield or the integral of the apparent ionization coefficient are sufficiently large.

2.2.3 Streamer Breakdown

Under certain conditions, the Townsend criterion is difficult to satisfy. Typically this occurs when the product of the pressure and gap distance pd is very large ($d >$ 5 cm at 1 atm) [89]. In other cases, it may be that the conditions in equation 2.10 cannot be satisfied. This can occur in electronegative gases with high values of η or in cases with extremely low γ [99]. The latter case is common among electrodes that are covered by an insulating material, such as water. In its liquid phase, water has a substantially higher effective work function (8.7-8.9 eV) compared to conventional metals, which are in the 2-4 eV range [102, 103]. As a result, the secondary electron yield due to both ion bombardment and field emission is expected to be relatively

low.

Achieving electrical breakdown in these scenarios requires higher values of the reduced field, E/N, which often leads to an entirely different breakdown mechanism known as the streamer discharge [89]. The avalanche to streamer transition occurs when the electric field at the avalanche head becomes comparable to the applied electric field [89]. Under these conditions, the avalanche becomes self-sustaining. The field at the tip of the streamer is a result of charge accumulation produced by ionization in the avalanche. This charge becomes separated due to the highly mobile electrons, which are quickly accelerated by the applied field, leaving the low mobility ions behind. Meek first derived a condition for streamer formation by modeling the avalanche as a growing ball of charge with radius $r(x)$ [104]. After a distance, x_s, this ball of charge will grow large enough to generate a field, E_s equal to the applied field, E_0. This condition can be written in the following form,

$$E_a = E_0 = \frac{e}{4\pi\epsilon_0 r^2}\exp\Big[\alpha\Big(\frac{E_0}{N}\Big)\cdot x_s\Big] \tag{2.11}$$

It has been estimated that the critical avalanche growth required for streamer self-sustainment corresponds to $\exp(\alpha x) \sim 10^8$, which corresponds to $\alpha x \sim 20$ [104]. The second statement is commonly known as the "Meek condition". In conventional atmospheric discharges, the electric field, E_0, required to satisfy this condition is large enough such that $\alpha \gg \eta$ [89]. However, in the general case, the condition $\lambda x \sim 20$, which takes into account losses due to attachment, is more accurate.

The excitation rate in the streamer head is also large enough to generate a substantial photon flux, which provides an additional source of ionization [99]. These photons propagate out from the head of the streamer and ionize neutral particles. The resulting electron-ion pars then build secondary avalanches under the action of the field, which feed into the primary streamer avalanche. The body of the streamer

can be divided into two regions, 1) the streamer head, and 2) the passive region [91]. The streamer head is a region of intense electric field strength where ionization and photon emission occur [48]. Behind the streamer head is a residual quasineutral plasma called the passive region. Due to the high charge density, the passive region is very conductive and hence has very low electric field. In this region, $\alpha - \eta < 0$ such that the electron density is no longer growing. Streamer propagation is controlled largely by ionization occurring over a very small scale where the electric field is most intense. For this reason, the body of the streamer is narrow, usually well below 1 mm [89].

In some cases, the local electric field is sufficiently high to create substantial ionization but not over a scale long enough to transition to a streamer. In this case the plasma will take the form of a corona discharge. This typically occurs in geometries with highly nonuniform fields. [89, 105].

2.2.4 Plasma Formation in an Isolated Bubble

The previous sections provide a basic physical mechanism with which to evaluate and predict plasma formation in isolated, underwater gas bubbles. Under this assumption, the applied electric field will result in position dependent swarm parameters inside the bubble, $\alpha(\mathbf{x})$, $\eta(\mathbf{x})$. These conditions may or may not lead to the transition of an electron avalanche to a plasma streamer.

One factor that tends to complicate this process is the isolation of the bubble from the electrode surface. This separation tends to impede plasma formation in two ways: (1) the low γ of the water surface decreases the contribution of secondary electrons to the swarm and (2) the geometric attenuation of the electric field over the electrode-bubble gap decreases the reduced field in the bubble. In such cases, the apparent ionization coefficient, $\lambda = \alpha - \eta$ is very low or less than zero. As a result, plasma formation is not possible. Another key parameter in predicting plasma

formation in bubbles is the bubble diameter, which forms the effective electrode gap d. If the diameter is too small, then the Meek condition ($\lambda d \sim 20$), in particular, cannot be satisfied. This suggests that yet an additional requirement for breakdown in a bubble is a sufficiently large bubble diameter.

The integral of the apparent ionization coefficient on the left hand side of equation 2.10 provides a useful figure of merit in predicting the tendency to form plasma at atmospheric pressure. In this dissertation it will be termed the *ionization product*,

$$M = \int_{\ell} (\alpha - \eta)\ \mathrm{d}\mathbf{x} \qquad \text{(Ionization Product)} \tag{2.12}$$

Here, the variable ℓ represents the path of integration. The quantity $\exp(M)$ represents the net number of charged particles created by the swarm as it traverses the total electrode gap, d along the path ℓ. In the case of a bubble, d is the bubble diameter. It has already been shown that the condition $M = \ln\left[\frac{1}{\gamma} + 1\right]$ represents the Townsend condition for breakdown, while the condition $M \sim 20$ represents the approximate requirement for streamer formation. In general, though, the condition, $M \gg 1$ indicates that ionization will be substantial [89].

Correctly predicting swarm evolution in an underwater gas bubble is further complicated by the presence of water vapor, which provides an additional source of both ionization and attachment. The measurement of η in water vapor is not nearly as well characterized as in other gases such as oxygen. Tabulated values from Dutton, [92], indicate that η can be assumed to be approximately constant in the range of E/N = 50-150 Td. In this range, $\eta/N \sim 5 \cdot 10^{-18}$ cm^2, which corresponds to $\eta \sim 100$ cm^{-1} at 1 atm. This is comparable to the values of η for oxygen under the same conditions. However, for a submerged bubble at standard temperature and pressure, the vapor pressure of water is 23 Torr [106]. Under these conditions, the ratio of oxygen molecules to water vapor molecules is 154:23. Thus, there are about 6.7 times more

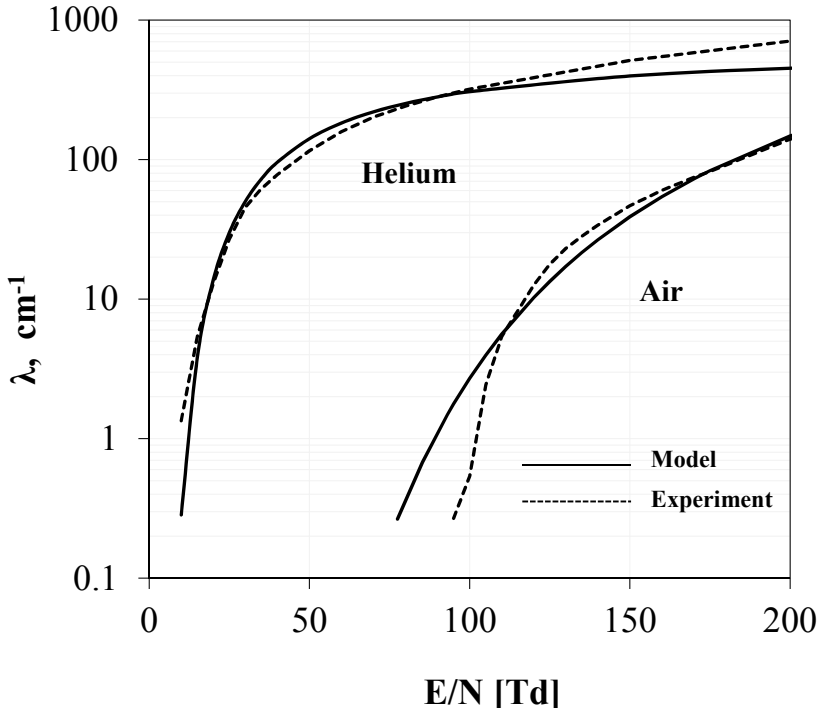

Figure 2.3: A model suggested by Raju [98] for estimating the apparent ionization coefficient in air and helium over the range 0-200 Td. For this case, λ is calculated at 1 atm.

oxygen targets than water vapor targets. As a result, the attachment effects due to oxygen will dominate those due to water vapor. This assumption will not necessarily hold if the water temperature is increased, which would increase the partial pressure of water vapor [106].

The above discussion indicates that the semiempirical form of the ionization coefficient given in equation 2.3 should provide a suitable approximation to the apparent ionization coefficient for both air and helium. If the theoretical form of λ given in equation 2.3 agrees with the tabulated values over a given range of reduced fields, then it will serve a good model of predicting plasma formation in bubbles. Figure 2.3 shows two theoretical forms for λ_{air} and λ_{He} as suggested by Raju [98]. In the case of air, the coefficients $F = 3 \cdot 10^{-16}$ cm^2 and $G = 800$ Td are used while in the case of helium, $F = 0.7 \cdot 10^{-16}$ cm^2 and $G = 77.6$ Td. These values fit the experimental values closely over the range 0-200 Td. Above values of 300 Td, the model and experiment

begin to diverge greatly. However, the model will still serve the purposes of analysis in this work because it is the plasma initiation at moderate values of reduced field that are of interest.

2.3 Changing the Breakdown Conditions in a Bubble

2.3.1 Motivation

It appears from the discussion of atmospheric discharges thus far, that a critical step in achieving plasma formation in an isolated bubble is to substantially increase the reduced electric field strength inside the bubble. The purpose of this dissertation is to investigate strategies to address this issue and develop a general guide for igniting plasma in an isolated bubble. The fundamental principle behind this approach is the observation that gas bubbles are not rigid objects, but can be stretched, distorted, torn apart, and carefully excited into a wide variety of deformations. In the following sections, we will show that there are two ways to exploit this property in a manner that will increase the reduced field, E/N within the bubble: (1) *the shape effect*, in which changing the surface curvature of the bubble's dielectric boundary enhances the electric field in the gas and (2) *the volume effect*, in which increasing the volume of the bubble decreases the pressure, and hence decreases the density. Both effects act together to increase the reduced field E/N inside the bubble.

2.3.2 The Shape Effect

The enhancement of the applied electric field at the boundary of two dielectric media is a well known phenomena [107]. A prime example is the observation of wall hugging streamers in electrode-attached bubbles, as discussed in Chapter 1 [108, 86]. Field enhancement is primarily the consequence of the change in polarization between two dielectric media. For linear dielectrics, the induced polarization, which represents

the resulting dipole moment per unit volume, is given by,

$$\mathbf{P} = (\epsilon - \epsilon_0)\mathbf{E} \tag{2.13}$$

At the boundary between the two materials of different permittivity, say ϵ_1 and ϵ_2, the polarization will produce a surface bound charge, σ_b given by,

$$\sigma_b = (\mathbf{P}_2 - \mathbf{P}_1) \cdot \mathbf{n} = (\epsilon_2 - \epsilon_1)\mathbf{E} \cdot \mathbf{n} \tag{2.14}$$

Here $\mathbf{n}$ is the unit normal to the surface. It is clear from equation 2.14 that the sign and strength of the induced charge is determined by the relative strength of the two permittivities. If the two surfaces are air and water, then $\epsilon_1 \approx \epsilon_0$ and $\epsilon_2/\epsilon_0 \approx 80$. In this case, σ_b is largely due to the polarization of the water. The induced field in the air will be much larger than that in the water because the water is a stronger dielectric and hence acts to cancel out (partially) the applied field. The field in the gas, in contrast, will be enhanced. Suppose now that, the surface is bent upward, resulting in a curved point that faces into the gas. The induced charge is now bunched up closer together, resulting in an effectively larger surface charge density. The induced field due to this higher charge density will be larger. Thus, increasing the curvature of the surface leads to an enhancement of the field. It can be shown that bending the surface in the opposite direction, away from the gas results in a decrease in the field [107].

Another way to understand the shape effect is by viewing the dielectric boundary as a change in the refractive index. In this case, the angle of the electric field through the boundary will change depending on the ratio of the two permittivities via Snell's law. The angle of the electric field relative to the surface normal, $\mathbf{n}$, each material,

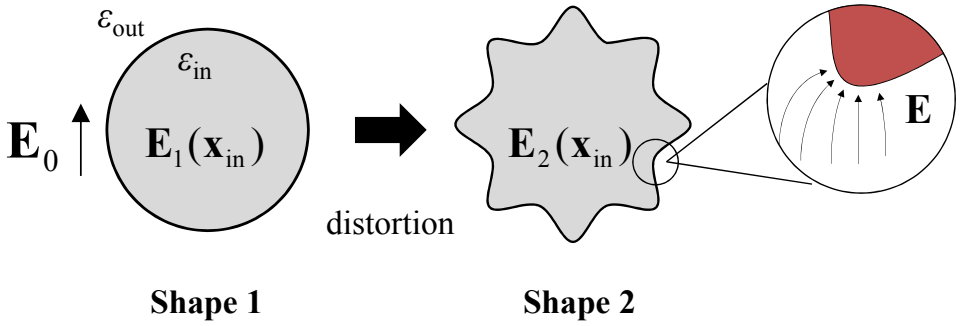

Figure 2.4: A simple illustration of the shape effect. Changing the curvature of the dielectric boundary changes the distribution of the applied electric field inside the bubble.

given by θ_1 and θ_2, will depend on the ratio of permittivities by,

$$\frac{\tan\theta_1}{\tan\theta_2} = \frac{\epsilon_2}{\epsilon_1} \tag{2.15}$$

This equation shows that materials with large changes in permittivity produce sharp bending of the electric field across the surface. The absence of free charge inside the bubble requires that the "bent" displacement field $\mathbf{D}$ be divergenceless. To satisfy this condition, the field strength must increase or decrease depending on the direction of the bending. As a result, the field is effectively focused by the dielectric, essentially refracted or pushed into regions of smaller permittivity.

The shape of the boundary ultimately determines to what degree the applied field is distorted or amplified. This concept can be extended to the geometry of a gas bubble in a straightforward manner. If a uniform field, $\mathbf{E}_0$, is applied across the body of the bubble and the resultant field in the bubble is $\mathbf{E}_1(\mathbf{x})$, then the enhancement of the electric field inside the bubble can be written,

$$G(\mathbf{x}) = \frac{\left|\mathbf{E}(\mathbf{x})\right|}{\left|\mathbf{E}_0\right|} \qquad \text{(field enhancement factor)} \tag{2.16}$$

The enhancement factor, G, represents a simple way of measuring the severity of field enhancement in the bubble. It will be shown in several examples throughout this work that often G is independent of the applied field and can be much greater than one in cases where the curvature of the surface is extreme [107]. If a gas bubble can be deformed to a shape specifically designed to maximize the enhancement of the applied field, then plasma ignition within the bubble gas can be achieved at reduced voltages. This is the *the shape effect*. In the simple case of a spherical bubble, it can be shown that the field enhancement in the bubble is uniform and proportional to the applied field, $\mathbf{E}_0$,

$$\mathbf{E}_1 \approx \frac{3}{2}\mathbf{E}_0 \tag{2.17}$$

This example will be discussed in detail in Section 2.6.

2.3.3 The Volume Effect

The second method that can be used to alter the reduced field in the bubble is to vary the neutral density, N. At high density, the electron-neutral collision mean free path is too small for electrons to gain energy comparable to the ionization energy. Conversely, at low pressure, the scarcity of neutral targets limits the ionization rate [91]. At atmospheric pressure, the former effect dominates, such that any decrease in pressure generally leads to an increase in the ionization rate [109]. In the context of a gas bubble, the pressure is as equally important as the magnitude of the electric field in determining the probability of breakdown.

The volume of the bubble can be altered under the force of a sufficiently strong external pressure. Sudden, nonlinear changes in the bubble pressure have been studied extensively, both experimentally [110] and theoretically [111]. If the bubble expansion occurs rapidly enough, the gas pressure will be temporarily reduced below atmosphere. Depending on the equation of state assumed during this process, the decrease in pressure will result in a decrease in neutral gas density. The resulting den-

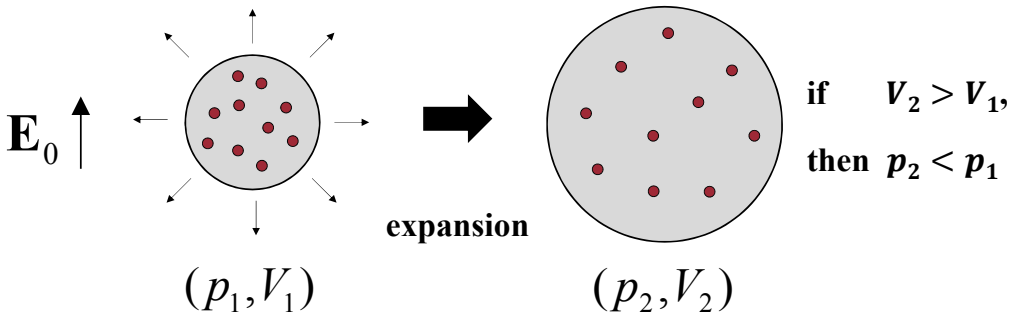

Figure 2.5: A simple illustration of the volume effect. As the bubble expands, its internal pressure and number density both decrease. This expansion must be faster than the diffusion of dissolved gas from the liquid.

sity decrease will tend to lower the strength of the electric field required for electrical breakdown [109]. This is termed *the volume effect* and can serve as an additional mechanism to facilitate plasma formation within the bubble. The pressure change resulting from the expansion or contraction of the bubble will be determined by the appropriate equation of state. In cases where the volume changes slowly compared to heat diffusion, then the expansion will be isothermal and the pressure change will satisfy $p \sim 1/V$ according to the ideal gas law [112]. In the other extreme, the bubble motion will occur faster than heat diffusion. In this case, the expansion will be adiabatic and the evolution of pressure and volume between any two states 1 and 2 will be determined by,

$$p_1 V_1^{\kappa} = p_2 V_2^{\kappa} \qquad \text{(adiabatic expansion)} \tag{2.18}$$

The exponent κ, known as the adiabatic index, is equal to the ratio of the specific heats,

$$\kappa = \frac{C_p}{C_V} = \frac{a+2}{a} \tag{2.19}$$

In equation 2.19, a is the number of degrees of freedom of the gas molecule. For

diatomic molecules like nitrogen and oxygen, which are the main components of air, $\kappa = 7/5$. A volume expansion of 20%, in this case, would lead to a pressure decrease of 23%. At atmosphere, this corresponds to a pressure reduction to 585 Torr.

The evolution of the bubble pressure during expansion and contraction is unfortunately not this simple. If there is a gas dissolved in the liquid, as is true in ambient environments, a gradient in the pressure between the bubble gas and the fluid will cause mass diffusion between the two media. This will counteract the desired effect and eventually return the bubble to atmospheric pressure. The timescale for this mass relaxation process is determined by the diffusion rate of the particular gas within the liquid. Thus, an additional criterion for igniting plasma in the deformed bubble is that the combined process of deformation and ignition must occur faster than the mass diffusion time of the dissolved gas. The case of adiabatic expansion is perhaps more preferable for this application since it represents a relatively fast change in conditions. The characteristic diffusion time of the dissolved gas is determined by the diffusivity, D of the gas dissolved in the liquid [112]. For an air bubble submerged in water at standard temperature and pressure, the diffusivity, D_{air} is 0.282 cm^2 s^{-1} [113]. The characteristic diffusion time, t_{diff}, for diffusion into the bubble will be [112],

$$t_{diff} \sim \frac{R_0^2}{D_{air}} \tag{2.20}$$

For a bubble of radius $R_0 = 1$ mm, $\tau_{diff} \sim 35$ ms. If the bubble is expected to sustain a significant pressure drop, all motion must occur much faster than this timescale. A more detailed discussion of mass diffusion across the bubble boundary can be found in Section 2.4.5.

2.4 Bubble Dynamics

The previous section illustrates the substantial impact that shape deformation can have on the breakdown conditions in a gas bubble. The following section provides an overview of the governing equations relevant to the study of the bubble's shape and dynamics. This discussion will illustrate the specific factors that influence the ability to distort and excite the bubble's shape.

2.4.1 The Bubble at Equilibrium

The underwater bubble is composed of a gas cavity surrounded by a highly polar and cohesive liquid, water. The equilibrium state of the bubble is determined by a balance between forces pushing outward against the liquid boundary (the internal gas pressure p_g and vapor pressure p_v) and forces pushing inward (the pressure of the surrounding liquid, p_0 and the surface tension p_s) [114]. The internal gas pressure can be written in terms of the other forces as,

$$p_g = p_0 + p_s - p_v \tag{2.21}$$

The surface tension pressure, p_s results from the cohesion of the liquid molecules at the fluid boundary [114]. When the fluid surface is bent inward as in the case of an air bubble, the net force on a surface molecule is in the direction of its nearest neighbors along the surface. In the case of a sphere, the components of the force parallel to the surface cancel out, resulting in a net force that acts radially inward and attempts to straighten the bubble surface. For a general perturbation of the fluid surface, the surface tension pressure is proportional to the mean curvature of the surface, which can also be written as the divergence of the local unit vector normal to the surface [115],

$$p_s = \gamma \nabla \cdot \mathbf{n} \tag{2.22}$$

The surface tension constant, γ, is a function of the interface material and temperature [116]. From this relation, one can conclude that surface tension becomes more intense as the curvature of the bubble sharpens. This effect resists any bending and tends to smooth out the surface in an attempt to restore it to spherical equilibrium. At this equilibrium condition, the surface tension pressure can be expressed as a function of the bubble radius, R_0 [114],

$$p_s = \frac{\gamma}{2R_0} \tag{2.23}$$

At ambient temperature, the surface tension pressure and vapor pressure (see Section 2.2.4) are considerably less than the ambient pressure of the liquid, leading to the condition $p_g \approx p_0$ [114].

2.4.2 Radial Deformations of the Bubble

Consider now the case in which the bubble undergoes deformations that are purely radial, that is, $\mathbf{r} = R(t)$. In practice, these deformations can result from an incident travelling pressure wave with wavelength much longer than the bubble radius [114]. In this case, the pressure field around the bubble is nearly uniform, but still time varying. The pressure gradient is zero in the fluid volume but experiences a jump at the bubble boundary, where it is purely radial. The dynamics of bubbles in these long wavelength fields is of particular interest in ultrasonic cleaning applications [117]. In this dissertation, they represent the most basic method of achieving the volume effect. A general equation describing purely radial deformations was first formulated by Rayleigh and Plesset [118]. It can be derived by solving the Navier Stokes equation in the surrounding fluid, while assuming that the fluid is both incompressible and obeys an equation of state (e.g. adiabaticity). Under the action of a time varying (but uniform) external pressure $p(t)$, the radius $R(t)$ will be determined by a stress

balance at the bubble surface,

$$\underset{(1)}{\frac{3}{2}\rho\dot{R}^2 + \rho\ddot{R}R} = \underset{(2)}{p_g\Big(\Big(\frac{R_0}{R}\Big)^{3\kappa} - 1\Big)} \underset{(3)}{- (p_0 + p_1(t))} \underset{(4)}{+ 2\gamma\Big(\frac{1}{R_0} - \frac{1}{R}\Big)} \underset{(5)}{- \frac{4\mu\dot{R}}{R}} \tag{2.24}$$

Here ρ, p_g, and κ represent the liquid density, equilibrium gas pressure, and adiabatic index respectively. The left hand side (term (1)) of equation 2.24 represents the convective derivative of the expanding fluid surface. The terms on the right hand side represent contributions from the (2) volume expansion, (3) driving pressure, (4) surface tension and (5) viscosity respectively. The quantity μ is the viscosity of the liquid. For small, viscosity free deformations, equation 2.24 can be linearized and reduced to the equation of a forced harmonic oscillator [114]. For a sinusoidal driving pressure of the form, $p(t) = p_0 + p_1 \sin\omega t$, equation 2.24 is simplified to,

$$\frac{d^2R(t)}{dt^2} + \omega_0^2 R(t) = \Big(\frac{p_1}{\rho R_0}\Big)\sin\omega t \tag{2.25}$$

The associated natural frequency, ω_0, is often referred to as the volume mode or breathing mode [114]. It can be expressed as,

$$\omega_0^2 = \frac{1}{\rho R_0^2}\Big[3\kappa\Big(p_0 + \frac{2\gamma}{R_0}\Big) - \frac{2\gamma}{R_0}\Big] \tag{2.26}$$

The frequency, ω_0, represents the natural resonance of the radial deformation of the bubble. In order to maximize the amplitude of the radial deformation, and hence the volume deformation, the bubble should be driven at the frequency, ω_0.

2.4.3 General Deformation

In general, the deformation of the bubble shape will not be purely radial. Assuming the fluid boundary maintains its composition, the bubble shape can be modeled

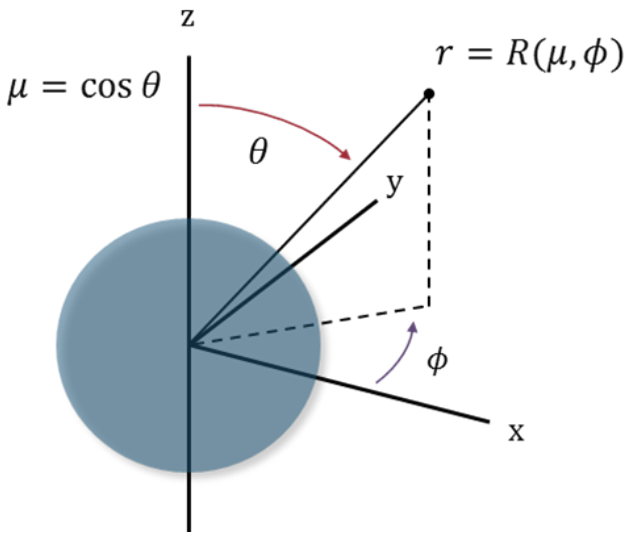

Figure 2.6: The spherical coordinate system is a natural fit for characterizing bubble shape deformation. In this dissertation, most cases of interest are azimuthally symmetric and thus do not depend on the angle ϕ.

as a surface in $\mathbb{R}^3$. Typically, this surface is parameterized in the spherical coordinate system (r, θ, ϕ), as illustrated in Figure 2.6. In this definition, r is the radial distance from the origin, θ is the polar angle, which rotates vertically from the positive z axis to the negative z axis, and ϕ is the azimuthal angle, which rotates from 0 to 2π in the x-y plane. The time dependent radius $R(t)$ can be solved as a function of the angular coordinates θ and ϕ by expanding it as a superposition of spherical harmonics, Y_0^n [114],

$$R(\theta, \phi, t) = R_0\Big(1 + \sum_{n=0}^{\infty} a_n(t) Y_0^n(\theta, \phi)\Big) \tag{2.27}$$

The coefficient, $a_n(t)$ represents the time dependent contribution of each harmonic component, Y_0^n. In the case of axisymmetric deformation (no ϕ dependence), we can expand instead in terms of the Legendre polynomials, P_l, using a different set of coefficients, b_l,

$$R(\mu, t) = R_0\Big(1 + \sum_{l=0}^{\infty} b_l(t) P_l(\mu)\Big) \tag{2.28}$$

In equation 2.28, μ represents $\cos(\theta)$. For most cases presented in this work, bubble deformation will be approximately axisymmetric. The coefficients, $b_l(t)$ can be solved by integrating against the corresponding Legendre polynomial [119],

$$b_l(t) = \begin{cases} \left(\frac{1}{2R_0}\right) \int_{-1}^{1} R(\mu, t) d\mu - 1, & l = 0 \\ \left(\frac{1}{R_0}\right) \int_{-1}^{1} R(\mu, t) P_l(\mu) d\mu, & l \geq 1 \end{cases} \tag{2.29}$$

For small amplitude oscillations about R_0, linear perturbation analysis can be used to show that for each mode, $P_l(\mu)$, there is a characteristic frequency f_l that corresponds to a 1st order oscillation about equilibrium [120]. In the linear case, these modes are decoupled and each amplitude, $b_l(t)$, oscillates at the characteristic frequency $\omega_l = 2\pi f_l$,

$$b_l(t) \sim \exp\left(i\omega_l t\right) \tag{2.30}$$

The lowest coefficient, b_0 is simply the volume mode frequency, ω_0, already derived in the previous section. It represents a shape preserving oscillation of the bubble radius. The remaining modes ($l \geq 2$) represent volume preserving perturbations of the Legendre polynomial $P_l(\mu)$, each with a characteristic frequency given by [114],

$$f_l = \frac{1}{2\pi} \sqrt{(l+2)(l+1)(l-1)\frac{\gamma}{\rho R_0^3}} \qquad l \geq 2 \tag{2.31}$$

These modes are referred to as shape oscillations and represent volume conserving oscillations of the bubble shape. For these modes, surface tension is the primary restoring force. Looking at equation 2.31, one may wonder why solutions do not exist for $l = 1$. In this case, the Legendre polynomial is given by $P_l(\theta) = \mu$. This is simply the z component of the surface, and therefore the term $b_1(t)P_l$ is simply the addition of every point of the surface by $b_1(t)$. Hence, we see that the first order mode is simply a translation back and forth in the z direction. If we assume the bubble has no net

drift, then b_1 must be zero. In the case of a driven bubble, this assumption simply means that the net force on the bubble is zero. If a physical constraint is added to the surface, as Theisen et al have done [121], then the mode f_1 becomes nonzero.

To summarize, the "volume" mode represents a shape preserving oscillation of the volume, while the "shape" modes represent volume preserving oscillations of the shape. It is clear that volume mode oscillations will be important for investigating the volume effect while shape oscillations will be important for investigating the shape effect. The general motion of the bubble is a superposition of these modes. For reference, Figure 2.7 shows the volume mode as well as the first three even modes as a function of radius. For a 1 mm radius bubble, $f_0 \sim 2.75$ kHz. At this point, the first few even modes are ∼150 Hz, 400 Hz, and 715 Hz respectively. For sufficiently high values of l, the shape mode frequency will eventually become larger than the volume mode frequency. For the lower order modes investigated in this work, the shape modes will be lower in frequency than the volume mode. Figure 2.8 shows the shapes for the first two even shape modes, $l = 2$ and $l = 4$. Throughout this work, the $l = 2$ and $l = 4$ modes will be referred to as the "dipole" mode and the "quadrapole" mode respectively. These names are primarily derived from the symmetry in the driving pressure field used to excite them, which is explained in more detail in Section 2.5.

2.4.4 Bubble Damping

Bubble oscillations undergo energy damping (i.e. energy loss) in a manner analogous to a damped harmonic oscillator. In general, the oscillating bubble loses energy by three primary mechanisms: (1) *viscous damping*, in which the moving fluid boundary does work against the viscous forces in the fluid, (2) *thermal damping*, in which the bubble gas produces heat energy during motion and diffuses it out into the fluid, and (3) *radiation damping*, in which the vibrating bubble radiates acoustic energy in the form of pressure waves [114]. In the case of volume mode oscillations, the three

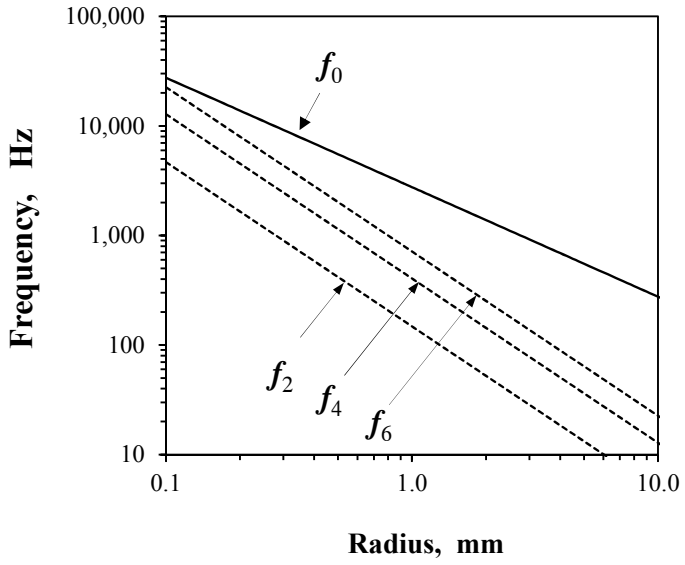

Figure 2.7: The volume mode, f_0 and first three shape modes, f_2, f_4, f_6 as a function of radius for gas bubbles in water. All frequencies decrease with increasing radii.

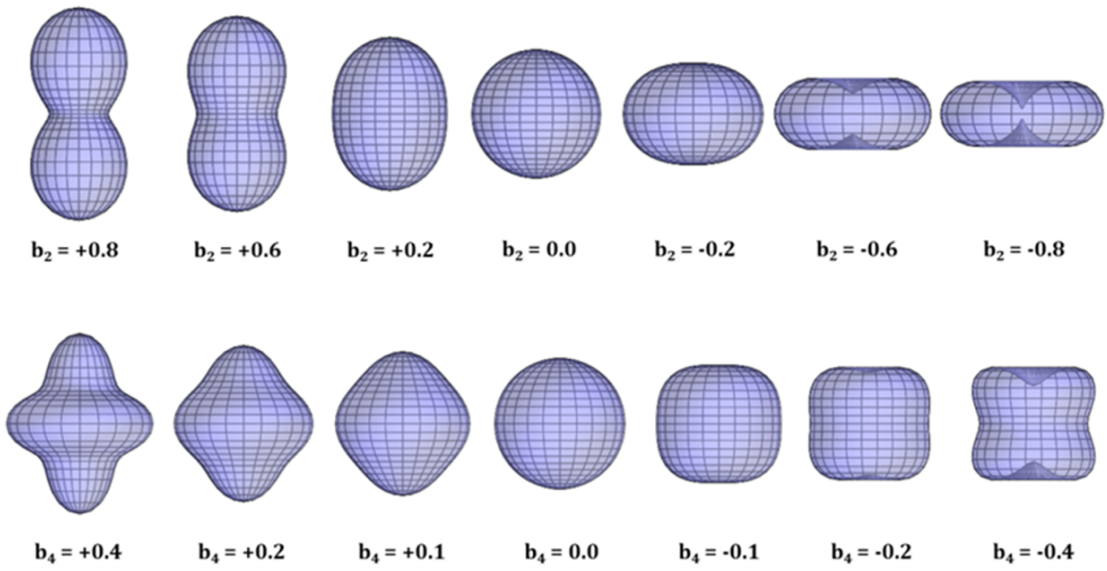

Figure 2.8: Spherical harmonic perturbations of the unit sphere for the $l = 2$ mode (top row) and the $l = 4$ mode (bottom row). At large negative values, both modes undergo severe contraction of the bubble boundary onto itself.

damping terms can be combined into one effective damping constant, δ_{tot}, which represents the inverse of the quality factor, Q, of the oscillations. In general, it can also be expressed as the ratio of the decay time constant, β $[s^{-1}]$, to the volume mode resonance frequency, ω_0,

$$\delta_{tot} = \frac{1}{Q} \approx \frac{2\beta}{\omega_0} \tag{2.32}$$

For bubbles in the 1 mm range, the total damping constant, δ_{tot}, is approximately 0.05 and is largely dominated by thermal damping [114]. This corresponds to a decay rate of 0.5 ms^{-1}, or a characteristic decay time of 2 ms.

Shape mode oscillations, in contrast, are more sensitive to viscous forces acting on the evolving surface [122]. In addition, for constant volume oscillations, no thermodynamic work is done compressing and rarifying the bubble volume. As a result, thermal damping due to the heating of the gas bubble is not prevalent [114]. In these cases, viscosity becomes the dominant source of damping. Lamb has derived a special form of the decay constant, β_l, corresponding to the shape mode, f_l [122],

$$\beta_l = (l+2)(2l+1)\frac{\mu}{\rho R_0^2} \tag{2.33}$$

This result shows that larger bubbles have a smaller decay rate. As an example, the decay rate of the $l = 2$ mode for a 1 mm bubble is approximately 0.1 ms^{-1}, which gives a characteristic decay time of 10 ms.

2.4.5 Gas Diffusion at the Bubble Interface

As the bubble expands, contracts, and oscillates, gas particles may be transported across the gas-liquid boundary. This mass diffusion is typically driven by a gradient in either the gas pressure (as in the case of the volume mode oscillations) or a gradient in the particle density. The latter case can arise when the species in the injected bubble differs from the species dissolved in the liquid. In this work, for example,

bubbles of different composition will be injected into the liquid medium. Over time, these particles will diffuse into the liquid medium and be lost from the bubble. As the gas is lost from the bubble, it is consistently replaced by dissolved gas in the liquid. Eventually, the gas in the bubble will be completely replaced with the gas in the dissolved liquid, in most cases a combination of oxygen and water vapor [112].

The diffusion of gas particles between media, is characterized by the diffusion coefficient, D, which has units of $\mathrm{cm}^2\ \mathrm{s}^{-1}$. The interchange of gas particles between the bubble and liquid can be estimated by solving the diffusion equation inside a spherical bubble. A solution for the case of a sphere be found in Crank [123]. A tractable solution can be obtained by assuming the following: the concentration of the injected species inside the sphere is initially c_0 and the concentration at the surface ($r = R_0$) is held constant at c_∞. In the case where the injected species is a noble gas, such as helium, this boundary condition takes the form, $c_\infty = 0$. This condition has the physical interpretation that the bubble diffuses out of the bubble quickly and does not linger very long in the vicinity of the bubble surface. With this approximation, the concentration, $c(r,t)$ inside the bubble can be written as [123],

$$\begin{gathered}\Delta\%c = \frac{c(\xi,\tau) - c_0}{c_\infty - c_0} = 1 + 2\sum_{n=1}^{\infty} \frac{(-1)^n}{n} \frac{\sin(n\pi\xi)}{\pi\xi} e^{-n^2\pi^2\tau} \\ \xi = \frac{r}{R_0} \qquad\qquad \tau = \frac{D}{R_0^2} t\end{gathered} \tag{2.34}$$

The variable, τ represents the time variable normalized by the diffusion time, $t_{diff} = R_0^2/D$. The solution of equation 2.34 for various times, τ, is shown in Figure 2.9. After a time, 0.3τ, the concentration in the bubble has reached 90% of the surface concentration. In the case of an injected gas species, this means that 90% of the injected species has left the bubble.

In Section 2.3.3, it was shown that the quick expansion of the bubble could be used to reduce the gas pressure in the bubble and hence reduce the electric field value

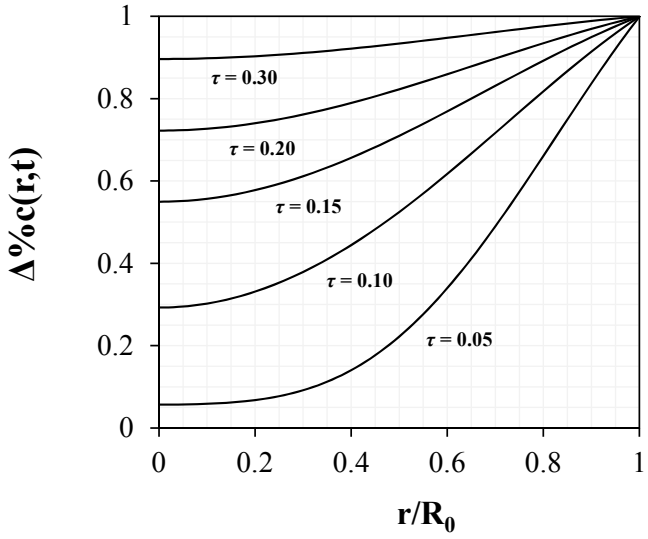

Figure 2.9: The diffusion of gas into and out of a sphere with initial concentration, c_0 inside and constant concentration, c_∞ at the boundary. For times large relative to the diffusion time, t_{diff}, the concentration approaches c_∞ everywhere inside the bubble.

required to achieve electrical breakdown. Let us now apply equation 2.34 to better understand the diffusion the processes occurring in this example. Suppose the bubble is expanded instantly to a volume V, such that the concentration of the gas falls to c_0 and the pressure falls to p. The pressure of the dissolved gas will be at the ambient pressure, p_∞ and thus we can assume so will the concentration. Figure 2.9 indicates that the dissolved gas will return to the bubble after approximately $\tau = 0.3$ or at a time that corresponds to 30% of the diffusion time. For the example used in Section 2.3.3, a 1 mm bubble being filled with air, this estimate corresponds to 10 msec.

2.4.6 Methods of Achieving Bubble Deformation

The most straightforward way to deform the shape of a bubble is by using an acoustic pressure field. A large body of work exists for investigating the use of sound fields to achieve both volume mode and shape mode oscillations [124, 125]. Typically this is achieved using an ultrasonic transducer to launch sound waves into the water

volume [114]. In this dissertation, however, a different approach is taken. Bubble deformations are instead achieved using electric fields, which act on the dielectric fluid surrounding the bubble. One advantage of this approach is that the driving electric field can also be used to initiate breakdown within the bubble. In addition, precise control of the shape, frequency and magnitude of the electric field are all straightforward for timescales associated with bubble oscillations ($\sim$1 kHz for mm sized bubbles). The following section serves as an introduction to the concept of electric field interactions in dielectric fluids, with a focus on the dynamics of gas bubbles.

2.5 Bubble Deformation via Electric Fields

The interaction between electric fields and dielectric fluids is known as electrohydrodynamics. In this model, the Navier-Stokes equations are modified to include the effect of the electric field stress acting on the fluid. Detailed reviews of the subject have been done by both Saville [116] and Melcher [126]. In general, the fluid is assumed to have both substantial permittivity and finite conductivity, which is summarized by the often used moniker, "leaky dielectric". The electromechanical stress is represented by the Maxwell stress tensor, $\mathbf{T}$, which in the electrostatic regime, is determined purely by the local electric field. In this case, the stress acts on electric charge but is assumed to couple with the dielectric medium either through the electromechanical spring forces of the chemical bonds (in the case of bound charge) or through the momentum transferring collisions associated with finite conductivity (in the case of free charge) [116]. For the purposes of this paper, the stress tensor can be thought of as a stress "acting" directly on the continuous media. In general, the dielectric fluid can have an inhomogeneous permittivity, $\epsilon(\mathbf{x})$, which is assumed to be the result of an inhomogeneous fluid density $\rho(\mathbf{x})$. In this case, the components of the stress tensor for any orthogonal coordinate system, can be represented using the

Kronecker delta, δ_{ij} by,

$$T_{ij} = \epsilon E_i E_j - \frac{1}{2}\delta_{ij}\epsilon\big(\mathbf{E}\cdot\mathbf{E}\big)\Big(1 - \frac{\rho}{\epsilon}\Big(\frac{\partial\epsilon}{\partial\rho}\Big)_T\Big) \tag{2.35}$$

A full derivation of equation 2.35 can be done using thermodynamics principles, as in the case of Landau [127], or using stress analysis mechanics, as in the case of Stratton [128]. If the medium has a homogenous permittivity, the gradient term in equation 2.35 is zero and $\mathbf{T}$ takes on the form usually presented in electrodynamics textbooks, such as Jackson [129]. Using the typical nomenclature of stress-strain theory, the resultant force per unit volume, $\mathbf{f}$ acting on a fluid can be found by simply taking the divergence of $\mathbf{T}$,

$$\mathbf{f} = \nabla\cdot\mathbf{T} \tag{2.36}$$

$$\mathbf{f} = -\frac{1}{2}\big|\mathbf{E}\big|^2\nabla\epsilon + \frac{1}{2}\nabla\Big(\big|\mathbf{E}\big|^2\rho\frac{\partial\epsilon}{\partial\rho}\Big) + \rho_e\mathbf{E} \tag{2.37}$$

We can obtain a more intuitive form of $\mathbf{f}$ by making two assumptions [55]: 1) the fluid is a tenuous dielectric, meaning, $\rho\big(\partial\epsilon/\partial\rho\big) \propto \epsilon$ and 2) the polarization is linear such that $\mathbf{P} = (\epsilon - \epsilon_0)\mathbf{E}$. The resulting force density in terms of the polarization $\mathbf{P}$ and free charge density ρ_e is,

$$\mathbf{f} = \big(\mathbf{P}\cdot\nabla\big)\mathbf{E} + \rho_e\mathbf{E} \tag{2.38}$$

From this view, the stress is simply a combination of 1) the dipole force (per unit volume) acting on the polarization derived bound charge, ρ_b and 2) the Coulomb force acting on the free charge density, ρ_e. In the case of a homogeneous dielectric medium, the volume bound charge is zero, $\rho_b = -\nabla\cdot\mathbf{P} = 0$. The bound charge is therefore restricted to the boundary where the surface charge density is $\sigma_b = \mathbf{P}\cdot\mathbf{n}$. As a result, electrical stress acts only at the interface between materials. The normal stress, p_n, and shear stress, τ_n, acting on a boundary with unit vector, $\mathbf{n}$, normal to

its surface are given by [128],

$$p_n = \mathbf{n} \cdot \big[\mathbf{T} \cdot \mathbf{n}\big] \qquad \text{(normal stress)} \tag{2.39}$$

$$\tau_n = \mathbf{t_i} \cdot \big[\mathbf{T} \cdot \mathbf{n}\big] \qquad \text{(shear stress)} \tag{2.40}$$

Here $\mathbf{t_i}$ is any vector lying in the plane perpendicular to $\mathbf{n}$. It is clear that the stress tensor can act in two different ways, 1) as a normal (or compressive) stress acting perpendicular to the surface of a body, and 2) as a shear stress acting parallel to the surface of the body.

2.6 An Example: The Dielectric Sphere in a Uniform Field

2.6.1 Solution of the Electric Field

To gain a physical understanding of electrohydrodynamic effects in practice, consider the example of a dielectric sphere. Suppose the sphere, having permittivity ϵ_1 is placed in another dielectric material with permittivity ϵ_2. Suppose that a uniform field $\mathbf{E}_0$ is applied in the z direction at an infinite distance. For now, assume that the conductivity of both areas is zero, such that ρ_e is zero. The presence of the sphere will distort the nominal field $\mathbf{E}_0$, resulting in a net field $\mathbf{E}_1$ inside the sphere and $\mathbf{E}_2$ outside the sphere. Both fields can be solved analytically by solving Maxwell's equations and using the usual boundary conditions at the dielectric interface [129],

$$\mathbf{E}_1(\mathbf{r}) = \frac{3}{q+2}\mathbf{E}_0 \quad \text{(inside)} \tag{2.41}$$

$$\mathbf{E}_2(\mathbf{r}) = \mathbf{E}_0 + \frac{q-1}{q+2}\Big(\frac{R_0}{r}\Big)^3\big(3(\mathbf{E}_0 \cdot \mathbf{r}) - \mathbf{E}_0\big) \quad \text{(outside)} \tag{2.42}$$

In this case, the quantity, $q = \epsilon_1/\epsilon_2$, is the ratio of the two permittivities. The field inside the sphere is uniform and proportional to the original field. Its magnitude is

enhanced (or depressed) depending on whether q is below (or above) unity. If the medium is water and the sphere is air, then $\epsilon_1 = \epsilon_0$ and $\epsilon_2 = 80\epsilon_0$, such that $q \sim 0$. In this case, the internal field of the sphere is enhanced by a factor of nearly 3/2. The field outside is a contribution from the original field plus the dipole field resulting from the polarization of the sphere. As expected, the contribution of the induced field to $\mathbf{E}_2$ tends to zero as $r \to 0$, (i.e. $\mathbf{E}_2 \to \mathbf{E}_0$). It can also be shown that $\mathbf{E}_1$, $\mathbf{E}_2$, and $\mathbf{P}$ are divergenceless. As a result, the volume bound charge is also zero. The only source of charge, therefore, comes from the net surface charge induced by the sphere and surrounding water. From the discussion in Section 2.3.2, it is clear that the liquid induced charge will dominate. The net surface charge can be solved as a function of the polar angle, in spherical coordinates,

$$\sigma_b = -3\Big(\frac{1-q}{q+2}\Big)\epsilon_0 E_0 \cos(\theta) \tag{2.43}$$

This surface charge is negative on the top hemisphere and positive on the bottom, generating a secondary field that reinforces $\mathbf{E}_0$ inside the bubble. This explains the field enhancement observed in equation 2.41.

2.6.2 Solution of the Electric Stress

Having obtained the electric field in the gas and the fluid, it is possible to calculate the electrostatic stress felt on the bubble using the Maxwell stress tensor, $\mathbf{T}$. The only surface charge present in this problem is the bound charge induced at the boundary between the bubble and liquid, which is given by equation 2.43. In the case of a sphere, the normal vector is purely radial (in the direction of $\mathbf{r}$). Hence the only relevant components of $\mathbf{T}$ are the normal stress, T_{rr}, and the two shear components, $T_{\theta r}$ and $T_{\phi r}$. Due to the azimuthal symmetry of the problem, $T_{\phi r} = 0$. That is, the stress acting in the azimuthal direction is zero. The two remaining components can

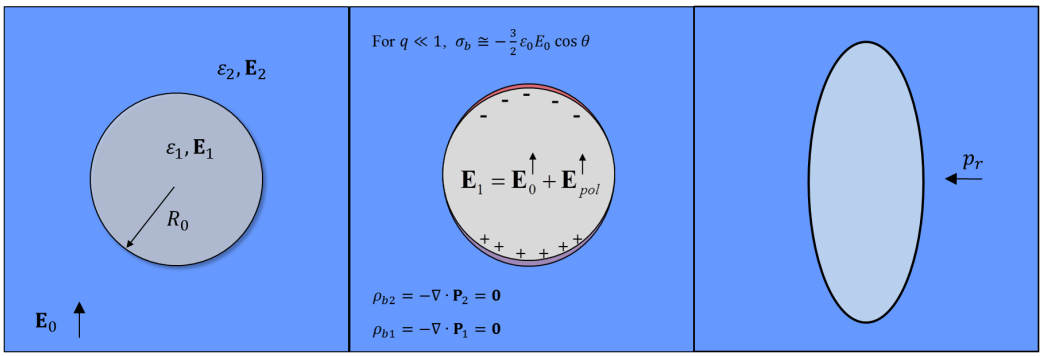

Figure 2.10: Under an external uniform field, the bubble is stretched vertically. Analysis of the electrostatic stress shows that the highest pressure occurs at the bubble's sides, pushing it inward.

be calculated by substituting the field relations into the stress tensor relation,

$$p_r = T_{rr} = -\frac{9}{8}\epsilon_2 \left|\mathbf{E}_0\right|^2 \sin(\theta)^2 \tag{2.44}$$

$$\tau_r = T_{\theta r} = 0 \tag{2.45}$$

In the case of the perfect dielectric sphere, the shear stress is zero everywhere. The only source of stress is an inward radial component, which is a function of the polar angle, θ, reaching its maximum at the equatorial plane ($\theta = \pi/2$). The stress, therefore, tends to squeeze in the bubble's sides harder than it pushes at the top and bottom. In the case that the bubble's volume is conserved, the equatorial stress will dominate, causing the top and bottom to expand outward. Vertical stretching of the bubble is a commonly observed phenomenon in literature [130, 131, 132, 52]. It has been observed that for a sufficiently large value of the electric field strength, the bubble will become destabilized. This can result in two scenarios: (1) the fission of the bubble into two separate fragments [132] or (2) the expulsion of small droplets from the vertical tips [130].

2.6.3 Net Body Force on Dielectrics

It is possible to calculate the net force acting on the sphere by integrating the stress tensor across the surface of the sphere.

$$\mathbf{F} = \oint_S \mathbf{T} \cdot \mathrm{d}\mathbf{a} \tag{2.46}$$

The solution to the radial stress, equation 2.44, has even symmetry about the equatorial plane ($\theta = 0$). Therefore, any net force resulting on the top half of the sphere will have an equal and opposite force acting on the bottom half. Hence, the net force on the body will be zero. It is clear that the strong distortion possible with a uniform field does not necessarily translate to a net force on the body. A general relation for the net force on a dielectric body has been derived by Pohl [133]. For a dielectric body with permittivity ϵ_1 resting in a second dielectric medium with permittivity ϵ_2, the net force is given by,

$$\mathbf{F} = \int_{body} \big(\mathbf{P} \cdot \nabla\big)\mathbf{E} \, \mathrm{d}\mathbf{x} \tag{2.47}$$

This is essentially the force density given by equation 2.38 integrated over the volume of the sphere. However, it was also shown by Pohl that in equation 2.46, the electric field, $\mathbf{E}$, under the integral sign is actually the original applied field in the *absence* of the dielectric body. An important consequence of this fact, is that in the case of a uniform field, for example, the term $\big(\mathbf{P} \cdot \nabla\big)\mathbf{E}$ will be zero. Therefore, any dielectric body placed in a uniform field, no matter what the shape, will have zero net force and hence zero net drift. A nonuniform field, on the other hand, will give rise to a net force on the body. This is known as dielectrophoresis [133]. As an example, it can be shown that a sphere placed in a slowly varying electric field undergoes a net

dielectrophoretic force given by,

$$\mathbf{F} = 2\pi R_0^3 \Big(\frac{q-1}{q+2}\Big) \nabla \Big(\big|\mathbf{E}(\mathbf{x})\big|^2 \Big) \tag{2.48}$$

Once again $\mathbf{E}(\mathbf{x})$ is the original, position dependent field strength in the absence of the sphere. The dielectrophoretic drift arises from a gradient in the polarization, $\mathbf{P}$ across the body of the dielectric. The gradient in polarization gives rise to a gradient in the electric stress, which scales as E^2.

It is clear from this analysis that any attempt to deform the bubble or excite oscillations on its surface may be accompanied by an unwanted drift. This drift may disrupt the bubble oscillations, particularly by pushing the bubble to a region of lower electric field strength. An exception to this rule occurs when the applied field has certain types of symmetry. In these cases, the net body force may cancel out to zero, as was the case in the example of the dielectric sphere placed in a uniform field. An example of this occurring in a nonuniform field is the case of the quadrapole electric field, as observed by Bellini [120]. In general, the above relations depend on the linearity of the dielectric medium. If the applied fields are sufficiently large ($\sim$1 MV cm^{-1}), then equations 2.13 and 2.43, which determine $\mathbf{P}$ and σ_b, will no longer hold.[129]. The induced electric field will therefore be different.

2.6.4 Extension to Leaky Dielectrics

In the case that both the fluid and bubble have finite conductivity, κ_1 and κ_2 respectively, then the resulting field and stress depend on the dimensionless product Rq [131], where R and q are defined as,

$$R = \frac{\kappa_2}{\kappa_1} \qquad q = \frac{\epsilon_1}{\epsilon_2} \tag{2.49}$$

In the case of a gas bubble submerged in water, $Rq \gg 1$, even though $q \ll 1$. This is due to the extremely low conductivity of the gas and therefore holds whether the water is from the tap or has been deionized. For a uniform D.C. field, the radial stress given in equation 2.44 remains approximately the same, but the shear stress is now given by [131],

$$T_{\theta r} = \frac{9}{4}\epsilon_1 \left|\mathbf{E}_0\right|^2 \sin(\theta)\cos(\theta) \tag{2.50}$$

This stress acts from the pole of the sphere toward the equator and therefore works to compress the sphere in a motion counter to the radial stress, which as seen in Figure 2.10, acts to stretch the bubble. It should be noted however, that the ratio of the shear stress (equation 2.50) to the radial stress (equation 2.44) is of order q, which is nearly zero ($\sim$1/80) in the case of an air bubble in water. In this case, the radial stress will always dominate.

2.7 A.C. Electric Fields: Coupling to Natural Bubble Modes

The discussion of electrohydrodynamics illustrates that electric fields can produce real hydrodynamic stress on dielectric liquids. The applied field will begin to distort the bubble surface when the field pressure becomes comparable to the surface tension of the bubble. The ratio of these two stresses is known as the electrical Weber number and is given by,

$$W_e = \frac{\varepsilon_0 \left|\mathbf{E}\right|^2 R_0}{\gamma} \tag{2.51}$$

The quantity, W_e provides a measure of how likely the surface is to be deformed. For reference, an electric field of 4.5 kV cm^{-1} acting on a 1.0 mm diameter bubble (in water) will yield $W_e \sim 1$. In general, the applied field can be used to deform the bubble into a variety of shapes, among which include the spherical harmonics. It is clear from Section 2.6 that a uniform field is especially useful for exciting the $l = 2$ mode deformation, and more generally that the geometry of the applied field

is critical in sculpting the subsequent deformation. The relationship between field geometry and mode excitation allows one to tailor the electrode geometry specifically to the desired mode. It is reasonable to expect that higher order spherical harmonics can be excited by introducing the appropriate symmetry of the mode. For the next highest even mode, $l = 4$, Bellini [120] has suggested that quadrapole symmetry is the optimal field geometry.

2.8 Strategy Going Forward

This chapter has reviewed a simple model for understanding plasma formation in gas bubbles and presented an hypothesis for altering the breakdown conditions within the bubble volume. This strategy depends on the complex interaction between the applied electric field and the dielectric boundary of the bubble surface. Having developed this strategy, it is now possible to present the experimental approach designed to demonstrate these principles and characterize, more generally, the fundamental processes underlying bubble discharge physics.

CHAPTER III

Experimental Approach

This chapter introduces the experimental device built specifically to examine the discharge physics of a single underwater gas bubble. This device is capable of deforming the shape of the bubble and igniting plasma within its interior, both through the use of an applied electric field. All testing reported in the following chapters was performed at the University of Michigan's Plasma Science and Technology Lab.

3.1 Development of the Ultrasonic Levitation Cell

3.1.1 Principles of Levitation: The Bjerknes Force

An individual gas bubble can be studied in a stable and controlled manner by trapping it in an ultrasonic standing wave. Acoustic levitation of bubbles has been used extensively in studies of fundamental bubble dynamics [110, 134] as well as sonoluminesence [135, 136]. The ultrasonic field can be excited in a variety of wave mode geometries, including spherical [137], cylindrical [138], and rectangular [139]. Spherical wave chambers are often used for basic sonoluminesence setups because the equilibrium trapping field is stable from all directions. As we shall see in the next section, this quality is difficult to achieve in other geometries. However, the low diagnostic accessibility of the spherical chamber (due to it being covered on all sides) renders it unfit for complex applications that require the insertion of electrodes and

other diagnostic equipment. The wave geometry chosen for this work was instead a 3-D rectangular wave mode geometry. A simplified schematic is shown in Figure 3.1. The acoustic standing wave is excited using a piezoelectric transducer composed of Lead Zirconium Titanate (PZT), which is manufactured by Channel Industries. It has the shape of a hollow cylinder with length 34 mm, inner diameter 34 mm, and wall thickness 5 mm. Every piezoelectric transducer is designed to have a mechanical resonance frequency, a condition at which the absorbed power into the element is maximized [117]. For a cylinder of this material and geometry, the mechanical resonance is 26.4 kHz. At this resonance, the hollow cylinder is excited in the "hoop mode" oscillation [117], which can be visualized as an axial compression accompanied by a radial expansion.

The levitation cell was designed to support a standing wave mode with frequency equal to that of the transducer resonance frequency. The resonant wave modes for a 3-D rectangular wave can be written in terms of the wavenumbers, n_i, the cell dimensions L_i, and the speed of sound in water c_s as,

$$f_s = \frac{c_s}{2}\sqrt{\left(\frac{n_x}{L_x}\right)^2 + \left(\frac{n_y}{L_y}\right)^2 + \left(\frac{n_z}{L_z}\right)^2} \tag{3.1}$$

The wavenumber, n_i, represents the number of half-wavelengths excited along the ith axis. The lowest wave mode, $n_i = 1$, corresponds to one half-wavelength, while $n_i = 2$ represents one full wavelength. In this device, the cell dimensions were chosen to sustain a three dimensional wave mode at frequency 26.4 kHz with wavenumbers of the form, $(n_x, n_y, n_z) = (1, 1, 2)$. This choice corresponds to half a wavelength in the lateral directions (x and y) and a one full wavelength in the axial direction (along z). The outer walls of the test cell were constructed from four 6.3 mm thick Plexiglas plates attached together using high strength, waterproof epoxy. The inner dimensions of the cell were 7 cm x 7 cm x 13 cm. The floor of the levitation volume

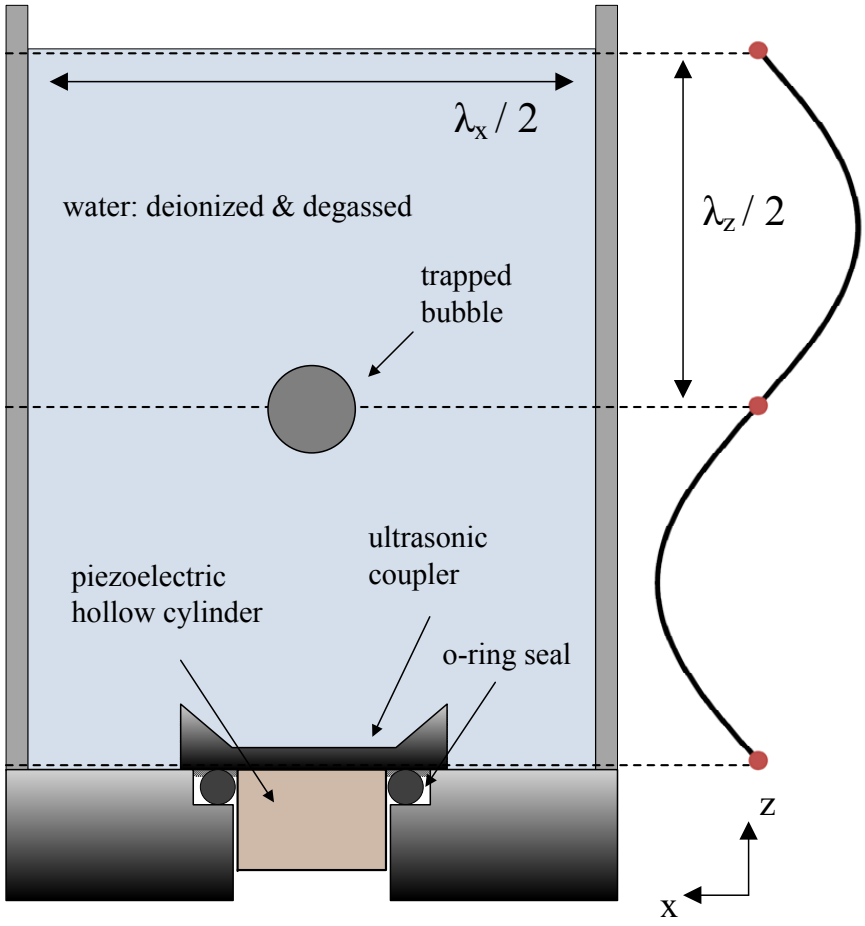

Figure 3.1: The piezoelectric cell used to suspend gas bubbles in an ultrasonic acoustic field. The dimensions are chosen to excite a rectangular standing mode of the type [1,1,2]. The bubble is trapped at the vertical node by the Bjerknes forces.

was formed by cutting a 45 mm hole into the center of a 7 cm x 7 cm square Plexiglas plate and attaching the plate to the inner walls of the chamber. The transducer was fed through the bottom of the hole and epoxied to the edges using the high strength epoxy. The total dimensions of the standing wave volume in this geometry were 7 cm x 7 cm x 7.3 cm.

The acoustic trapping force derives from small amplitude volume mode oscillations of the bubble, induced by the standing wave. If the acoustic wavelength is much larger than the bubble diameter, the acoustic force simply acts to compress and rarify the bubble volume, as described in Section 2.4.2. As the wavelength is decreased, the slight nonuniformity in the acoustic wave pushes (or pulls) the bubble in a nonuniform manner across its body, giving rise to a net force. The average of this force over a period of the sound field, $p(z,t)$, is known as the Bjerknes force [140] and is related to the bubble volume, $V(t)$ by,

$$F_b = \Big\langle V(t)\nabla p(z,t) \Big\rangle_{cycle} \tag{3.2}$$

Equation 3.2 represents the time averaged force acting on the bubble as it moves through the pressure gradient of the wave field. It can be shown that the bubble will travel up or down the pressure gradient depending on whether the acoustic frequency, f_s, is greater or less than the volume mode frequency, $f_0 = \omega_0/2\pi$ (see equation 2.26, Chapter 2). If $f_s > f_0$, the bubble will be pushed toward the nearest *node* in the standing wave, while if $f_s < f_0$, the bubble will be pushed toward the nearest *anti-node*. In these experiments, the typical bubble diameter is of order 1 mm, which yields a volume mode frequency of approximately 5 kHz. Since the volume mode frequency, f_0 is less than the sound field frequency, f_s, the bubbles in these experiments will be pushed toward the *nodes*.

Stable bubble levitation can be achieved when the Bjerknes force is large enough

to overcome the upward pull of buoyancy acting on the bubble. This buoyant force is simply the gravitational force density acting on the volume of water displaced by the bubble. For a liquid of density, ρ, with gravitational acceleration, g, the buoyant force acting on a bubble with volume, $V(t)$ is,

$$F_g = \rho g V(t) \tag{3.3}$$

The trapping condition can be obtained by setting $F_b = F_g$. The applied acoustic field can be written as a perturbation of the ambient pressure, p_0, in the z direction with wavelength, λ_z, and frequency, ω,

$$p(z,t) = p_0 + p_1 \sin(\omega t) \sin\left(\frac{2\pi z}{\lambda_z}\right) \tag{3.4}$$

It was shown in Chapter 2 that the response of the bubble for small enough driving fields can be approximated as a simple harmonic oscillator. An explicit relation for the Bjerknes force in this case is [140, 141],

$$F_b = \frac{1}{1-\omega^2/\omega_0^2}\left(\frac{2\pi^2 R_0^3 p_1^2}{3 p_0 \lambda_z}\right) \sin\left(\frac{2\pi z}{\lambda_z}\right) \tag{3.5}$$

By setting equation 3.5 equal to equation 3.3, one can solve for the wave pressure, p_1, necessary to overcome buoyancy. For a bubble of radius 1 mm, the minimum sound field amplitude corresponds to $p_1/p_0 \sim 0.5$. Thus the perturbing amplitude must be at least 50% of the ambient pressure and clearly corresponds to a nonlinear perturbation. In reality, the error from assuming linearity is substantially large. It can be shown that the actual pressure amplitude is considerably lower [141].

3.1.2 Implementation of the Transducer

The excitation of 3 independent degrees of freedom in the standing wave (i.e. x, y and z) presents a subtle difficulty in obtaining stable levitation. By definition, the nodes of the horizontal wave modes will give rise to a null in the vertical pressure profile, a point at which the contribution from the dynamic pressure will be given by $p_1(z,t) = 0$ for all z. A bubble pushed horizontally into this node will experience no Bjerknes force in the vertical direction, causing it to escape upward to the surface of the water. To obtain stable levitation, then, it is clear that the horizontal modes must not be allowed to have any nodes. The only wave modes satisfying this criterion are those with, $n_x = 1$ and $n_y = 1$, in which case both horizontal modes are excited at a half wavelength. In the absence of horizontal nodes, the bubble can still maintain equilibrium if it remains in the center of the sound field, a point where the Bjerknes force acts symmetrically in the horizontal plane, as shown below in Figure 3.2(a). However, this equilibrium is unstable because the bubble is resting at an antinode. Any perturbation of the bubble from its equilibrium will result in a nonzero Bjerknes

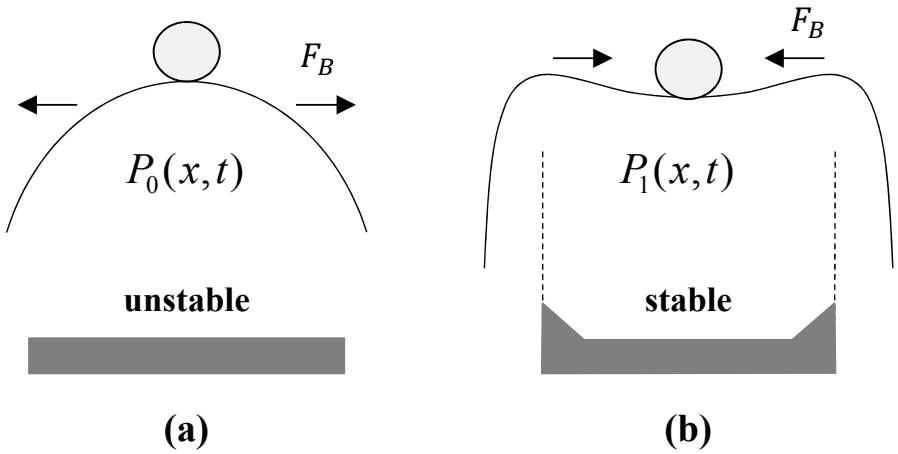

Figure 3.2: (a) When the transducer surface is flat, the horizontal pressure field creates an unstable equilibrium. (b) The trapping field is stabilized by the addition of the spiked piezo-coupling horn.

force that pushes the bubble away from the anti-node and toward the node, which in this case is the wall of the apparatus. Asaki [139] developed a method of removing this instability by attaching a metal coupling horn to the top of the cylindrical body of the transducer. This horn, shown in Figure 3.1, is machined with sharp edges on its outer diameter, resulting in local pressure spikes directly above the edges of the transducer. This perturbation is enough to transform the unstable pressure potential from a "hill" to a localized "valley", thus causing the bubble to be pushed back to the node whenever it is displaced from equilibrium. This effect is illustrated in Figure 3.2(b).

A metal coupling horn, similar to that employed by Asaki, was machined from an aluminum cylinder and affixed to the top of the hollow cylinder using epoxy. The horn protrudes into the standing wave volume, which unfortunately disturbs the standing wave condition set by equation 3.1. However, it was observed that the enhancements in the pressure field compensate for any disturbance to the standing wave resonance condition.

3.1.3 Transducer Calibration

Due to the large change in acoustic impedance in transitioning from water to air, the acoustic wave energy becomes trapped in the water [135]. Thus, the water surface acts as the top boundary of the standing wave. As a result, the exact standing wave frequency of the cell can be controlled by adjusting the water level in the cell. This adjustment was used to match the standing wave frequency, f_s, to the piezoelectric resonance frequency, f_p. The standard operating level was set at 5.4 cm. The electrodes used to excite the piezoelectric transducer were attached to the inner and outer walls of the cylinder using conducting epoxy. The sides of the cylinder were themselves covered, by the manufacturer, with a thin conducting film. The piezoelectric transducer was excited by a sinusoidal voltage signal first created by a function

generator (Instek) and amplified by a power amplifier (Teachspin SL100B). As the driving frequency is varied, both the amplitude, $\left|\tilde{I}(\omega)\right|$ and the phase, $\phi(\omega)$ of the current (relative to the voltage) will vary. The complex voltage and current of the transducer can be written [117],

$$\tilde{V}(\omega,t) = \left|\tilde{V}(\omega)\right| e^{i\omega t} \tag{3.6}$$

$$\tilde{I}(\omega,t) = \left|\tilde{I}(\omega)\right| e^{i\omega t - \phi(\omega)} \tag{3.7}$$

Here the frequency dependence of both amplitudes and as well as the phase are explicitly stated. This dependence is due to the complicated electromechanical properties of the piezoelectric transducer. The cycle average power absorbed by the transducer can be calculated [129],

$$P_{avg}(\omega) = \mathrm{Re} \int\limits_{cycle} \tilde{V}(\omega,t)\tilde{I}(\omega,t)dt = \frac{1}{2}\left|\tilde{V}(\omega)\right|\left|\tilde{I}(\omega)\right| \cos\phi \tag{3.8}$$

The term $\cos\phi$ is the frequency dependent power factor; it represents the fraction of the total power absorbed by the transducer. As the driving frequency approaches the resonance of the piezoelectric transducer, the relative phase, ϕ, approaches a minimum and the absorbed power is maximized. At the same time, the current through the transducer is also maximized, resulting in a minimum in the transducer impedance, $Z(\omega)$, which is defined as,

$$\left|Z(\omega)\right| = \frac{|\tilde{V}(\omega)|}{|\tilde{I}(\omega)|} \tag{3.9}$$

Figure 3.3 shows the average power and impedance of the transducer with the levitation cell operating at the resonant water level of 5.4 cm. At each frequency value, the voltage and current were monitored on a 70 MHz Tektronix TDS2004 oscilloscope. The current was measured using a model 6600 Pearson current transformer with 120 MHz bandwidth while the voltage was measured directly from the output of

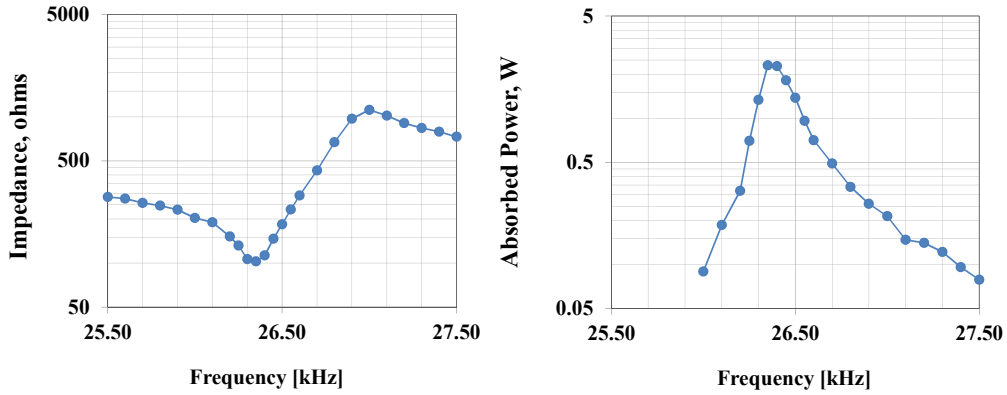

Figure 3.3: (a) The impedance of the piezoelectric transducer is minimized at its natural resonance. (b) This corresponds closely to the point at which the absorbed power is maximized. Using this calibration, the operating point was chosen to be 26.4 kHz.

the power amplifier. The relative phase between the voltage and current was obtained using the oscilloscope measurement function. The average power and impedance were then calculated using equations 3.8 and 3.9 respectively. The impedance curve obeys the characteristic "S" shape that is typically observed in piezoelectric circuit analysis [117]. The output of the function generator was 2-3 volts, giving rise to a typical amplitude of 40-60 V delivered across the transducer. The typical electrical current at resonance was 400-600 mA. Using the calibration shown in Figure 3.3, the standard operating frequency was chosen to be 26.4 kHz, which is consistent with mechanical resonance specified by the manufacturer.

3.1.4 Bubble Injection

Injected bubbles were composed of two different gases: ambient air and ultra-purity helium. In the case of air, bubbles were directly injected into the levitation cell using a 30 gauge (0.305 mm OD) insulin syringe. The levitation field was sufficiently strong that bubbles injected near the edges of the cell wall were pulled into the equilibrium trapping position. This enabled bubble injection even in cases where submerged electrodes prevented access to the node. Typical bubble sizes documented

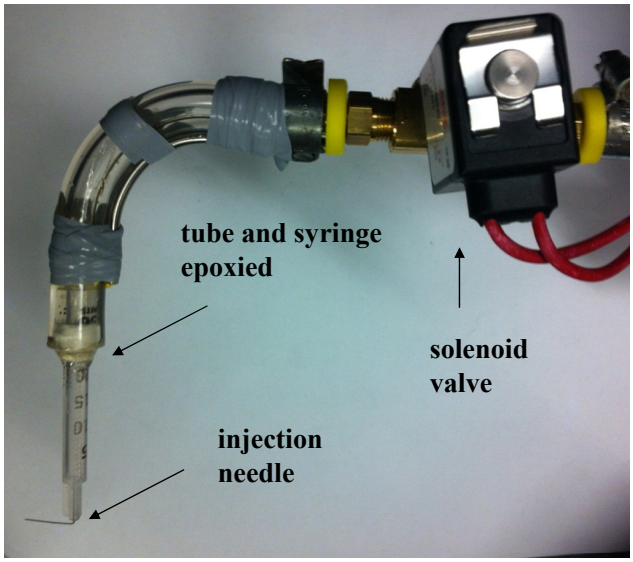

Figure 3.4: The helium injector is used to inject helium bubbles directly into the node of the ultrasonic acoustic field. Gas injection is precisely controlled using a solenoid valve.

ranged between 0.2−3 mm in diameter.

The injection of helium bubbles, in contrast, required a more sophisticated approach. The helium injector, shown in Figure 3.4, was composed of a solenoid valve placed in line with a syringe needle. The solenoid valve was pulsed on and off using a 1−5 ms pulse produced by a function generator. The input of the solenoid valve was connected to a helium gas cylinder through a vacuum sealed gas line. The output was epoxied (as shown) to the back of an insulin syringe tube such that the end output of the injector was the same 30 gauge needle used for the injection of air bubbles. The length of the solenoid opening pulse was used to control the size of the bubble injected from the needle. It was observed that for a small enough pulse, no bubble is injected, thus putting a lower bound on the size of helium bubbles that could be injected. Before each injection, helium in the tube downstream of the solenoid valve output was purged for 30 seconds in order to maximize the purity of the helium bubble being injected.

As discussed in Section 2.4.5, the gradient in the concentration between the injected bubble and the liquid will drive diffusion of helium out of the bubble. Typically, the injected bubble was allowed to sit 10-30 seconds before being pulsed. The diffusion coefficient for helium in water at room temperature, is, $D_{He} = 0.908$ cm^2 s^{-1}, which corresponds to a diffusion time of 11 ms [113]. After 10 seconds, therefore, the time is a factor of 900 larger than the diffusion time. Using the model introduced in Section 2.4.5 would suggest that the helium is completely removed from the bubble. However, this model overestimates the helium diffusion by assuming that the concentration at the boundary is held constant at $c_\infty = 0$. In reality, the helium is not instantly diffused out into the liquid body but remains in the vicinity of the bubble, providing a shielding effect for the helium still in the bubble. A better indicator of the true helium concentration in the bubble may be obtained using the model of the 2-D infinite slab. In this case, the helium is initially contained in a slab of thickness $2R_0$. For this slab, a solution without the restrictive boundary condition, $c(R,t) = c_\infty$ can be obtained. The concentration at the center of the bubble takes the form of the error function [123],

$$c(0,t) = c_0 \ \mathrm{erf}\Big(\frac{1}{\sqrt{4\tau}}\Big) \tag{3.10}$$

Using this model, the concentration falls to 1.9% of its initial value after 10 seconds ($\tau = 900$). From this model, it is clear that the helium bubble can be best described as an air-vapor bubble contaminated with helium. Despite this limitation, it is believed that the presence of helium may still have an effect on plasma formation in the bubble due to its large ionization coefficient, λ, as seen in Figure 2.1.

3.1.5 Other Issues

3.1.5.1 Degassing the Levitation Cell Water

The presence of dissolved oxygen in the levitation cell water presented an additional obstacle in achieving stable levitation. Air dissolved in the water functions as a parasitic load to the transducer, absorbing acoustic energy from the sound field, which results in cavitation of gas bubbles at the transducer surface. To reduce the concentration of dissolved oxygen, the cell water was first poured into a 500 mL Pyrex beaker and boiled on a Fischer Scientific hotplate for 1.5 hours. The water was then cooled in a cold water bath for 30 min before operation.

3.1.5.2 Minimizing Conductivity

The finite conductivity of the water in the cell presented a number of issues in operating the levitation cell and using high voltage power supplies. The metal coupling horn used to stabilize bubble trapping was observed to be in contact with the thin conducting plates on the sides of the cylinder. This provided a direct path to ground from the water. To remove this effect, it was necessary to insulate the surface of the metal coupling horn with a thin layer of non conducting epoxy. This was observed to dramatically reduce the electrical current escaping through the transducer. To minimize conduction current, all experiments were performed in deionized water, with an initial conductivity of 10 μS m^{-1}. The conductivity was monitored using an Omega PHH-60BMS conductivity meter. It remained below 20 μS m^{-1} throughout all testing performed in the levitation cell. With the modifications described above, levitation of air bubbles up to 5.0 mm in diameter were achieved. The axial pressure field in the levitation cell was also monitored using a submersible hydrophone.

3.2 Achieving Shape Distortion in Practice

3.2.1 Electrode Design

Much of this dissertation is focused on studying the effects of intense electric fields on gas bubbles. These fields can be applied to either drive deformation of bubble shape or excite plasma in the bubble volume. Accomplishing these goals requires the design of a robust electrode system that can be (1) submerged in the water, (2) precisely positioned near the bubble, and (3) biased to generate the range of electric field geometries and intensities required to both deform the bubble and ignite plasma. The approach taken in this work was to mount the electrode system on a 3-D translation system. The entire setup is shown in Figure 3.5, fitted with a pair of parallel plate electrodes as an example. This strategy allows the user to move the electrodes into place after stable levitation of the bubble has been achieved. Precise positioning of the electrodes relative to the bubble was achieved using an additional fine motion micrometer attached to the translation stage. Altogether, this allowed movement of the electrodes relative to both the bubble and each other.

Individual electrodes were attached to the translational mounting stage using a pair of "plug and play" snap in connectors. This allowed different electrode types to be easily switched in and out depending on the desired application. A few examples of different electrode types used are shown in Figure 3.6. These vary in shape, ranging from smooth, flat plate electrodes, which were used to excite uniform fields, all the way to sharp needle point electrodes, which were used to ignite plasma in the bubble. These electrode tips were constructed using 30 gauge (0.305 mm OD) syringe needles. Both the inside of the syringe and the electrode tube were filled with conducting epoxy in order to minimize the possibility of trapped air pockets. These air pockets result in parasitic discharges on the inside surface of the electrode, especially when submerged in water. Often, the size of the electrode would have to be changed to accommodate

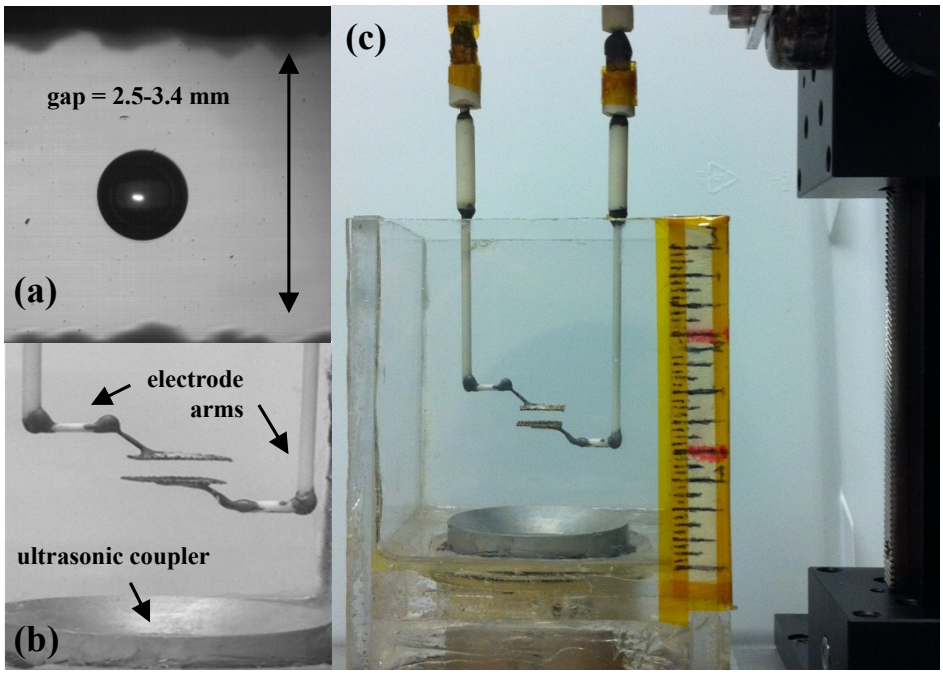

Figure 3.5: (a) A close up view of the bubble held in stable levitation. (b) The electrode arms held in position around the bubble. (c) The piezo-cell along with the electrode arms mounted on a 3-D translation stage.

a smaller surface area for collected current. For example, the circular plate electrodes shown in Figure 3.6(b) have diameter 4 mm while the square plate electrodes have diameter 10 mm. This size reduction was often necessary to sustain higher voltages in devices that have strict current limits (see Section 3.3). The downside to having smaller electrode sizes, however, was the decreased uniformity of the applied electric field.

One unsurprising result of submerging the electrodes near the bubble is that they interfere with the acoustic standing wave. When moving the electrodes too close to a trapped bubble, the bubble was observed to jump from its trapping point and attach to the electrode. Yet, in many cases, if the perturbation was small enough, the electrodes would only shift the bubble slightly. In some cases the bubble trapping was actually reinforced. This surprising observation was a result of the reflection of the acoustic waves off of the electrodes. In such cases, the pressure node actually became

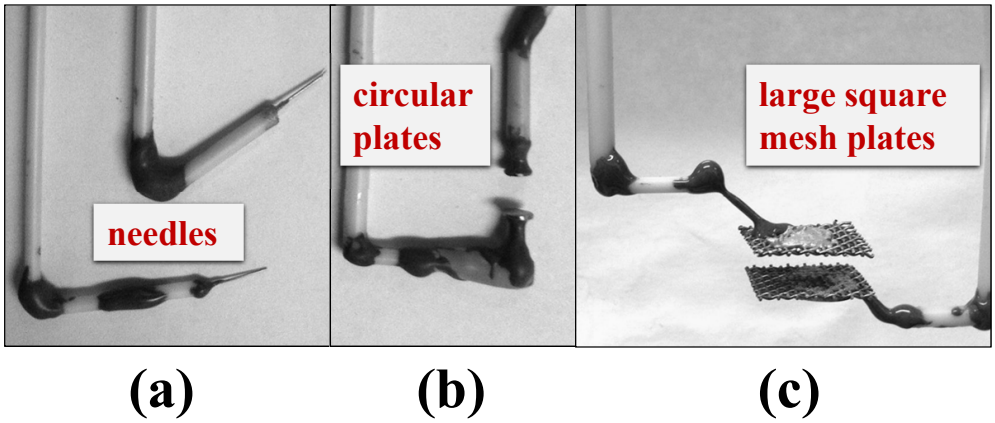

Figure 3.6: The primary electrode types used to drive shape distortions and ignite plasma in the bubble.

steeper, hence improving levitation stability. This is especially true in cases when the electrode is positioned directly above the bubble. This phenomenon is useful in practice. Upon trapping the bubble in the wake field of the overhanging electrode, it is possible to pull the bubble along with the translation stage, achieving small translations. This proved useful in imaging, for example, when trying to keep the bubble in focus.

3.2.2 Coupling to the $l = 2$ Mode

Section 2.6 in Chapter 2 demonstrates that excitation of the $\ell = 2$ shape mode requires the application of a uniform electric field. In this case, it is important that the electrode gap be smaller than the diameter. In the case that the electrodes are composed of mesh, like those shown in Figure 3.6(c), the uniformity condition must be expanded to include the condition that the mesh opening not be larger than the bubble diameter. The wire mesh shown in Figure 3.6(c) was composed of brass wire with 0.25 mm wire thickness and 0.75 mm wire spacing, yielding a transparency of 56%. Typical electrode gaps were varied between 2.5 and 3.4 mm. The use of mesh electrodes in some specific cases was chosen for three reasons: 1.)

the planar geometry provided an approximately uniform electric field within the gap, 2.) the reduced surface area minimized conduction current and 3.) the high physical transparency prevented acoustic disruption of the standing wave. In practice, it is possible to maintain stable levitation with a solid plate electrode scheme, but the bubble levitation was significantly less stable.

3.3 H.V. Sources I: Shape Distortion

Upon reviewing the discussion of bubble mode dynamics in Chapter 2, it is clear that optimal coupling to bubble resonance (or achieving distortion in general) requires electric fields that vary on timescales in the range 100-1000 Hz. This requirement places special constraints on the available power supplies to (1) achieve high enough electric fields to overcome the bubble's surface tension and (2) apply voltage for timescales long enough to couple to the natural modes of the bubble. For the first criteria, the concept of Weber number introduced in Section 2.7 indicates that fields must be at least 3-5 kV across a bubble of diameter $1-10$ mm. To accomplish these requirements, two different voltage supplies were used, each with its own advantages and limitations. The following sections give an overview of each supply. In most experiments, voltage signals were measured using a Tektronix P6015A high voltage probe and current signals were measured using a model 6600 Pearson current transformer coil, with a rise time of 5 ns and a bandwidth (-3 dB) of 120 MHz.

3.3.1 The Elgar A.C. Power Source

The first bubble driving scheme used was an A.C. power supply combined with a high voltage transformer. The A.C. power supply, shown in Figure 3.7, was an Elgar model 501SL, capable of producing 250 V A.C. signals in the range $50-5000$ Hz. The output of the Elgar was delivered to a Plasma Technics high voltage transformer, capable of producing voltages up to ± 5 kV and current up to ± 200 mA. The

transformer output was limited, however, to frequencies above 400 Hz. Operation below 400 Hz was possible but resulted in substantial distortion of the applied voltage signals. A circuit diagram illustrating typical operation of the Elgar transformer combination is shown in Figure 3.8. A 500 ohm ballast resistor was placed at the output of the transformer in order to prevent excessive current flow in the event that electrical breakdown occurred between the electrodes. Overall, the Elgar-transformer combination allowed a versatile method of probing bubble response due to an electric field over a wide range of frequencies. Its high current rating (200 mA) relative to other voltage sources (see the TREK supply below) allowed the use of large electrodes. This was particularly important in the case of generating very uniform fields, which required high aspect ratios for the electrodes used. In all cases, the low end of the transformer was held at ground. Hence for any experiment when electrodes were submerged, one of them was always held at ground potential.

3.3.2 The TREK Amplifier

A more sophisticated approach to exciting bubble oscillations was facilitated using the TREK 20/20C high voltage amplifier, shown in Figure 3.9. This amplifier is capable of $\pm$20 kV and $\pm$20 mA with a gain of 2000 V/V. The input to the TREK supply was provided by a 30 MHz arbitrary function generator (Agilent model 33521A). A simplified view of the circuit used is shown in Figure 3.10. Triggering was accomplished by leaving the TREK on and simply triggering the function generator with a delay generator. The ability to tailor the shape and duration of the voltage driving signals at such high voltage provided versatility in studying bubble deformation. The response time (or slew rate) of the TREK was 450 V/μs, resulting in a bandwidth of approximately 7.5 kHz. In addition, both the voltage and current being output by the TREK could be read directly from the TREK supply through low level outputs on its mainframe. The primary disadvantage of the TREK supply was its low current

Figure 3.7: The Elgar A.C. power supply (bottom) and the high voltage transformer (top) used to drive bubble oscillations.

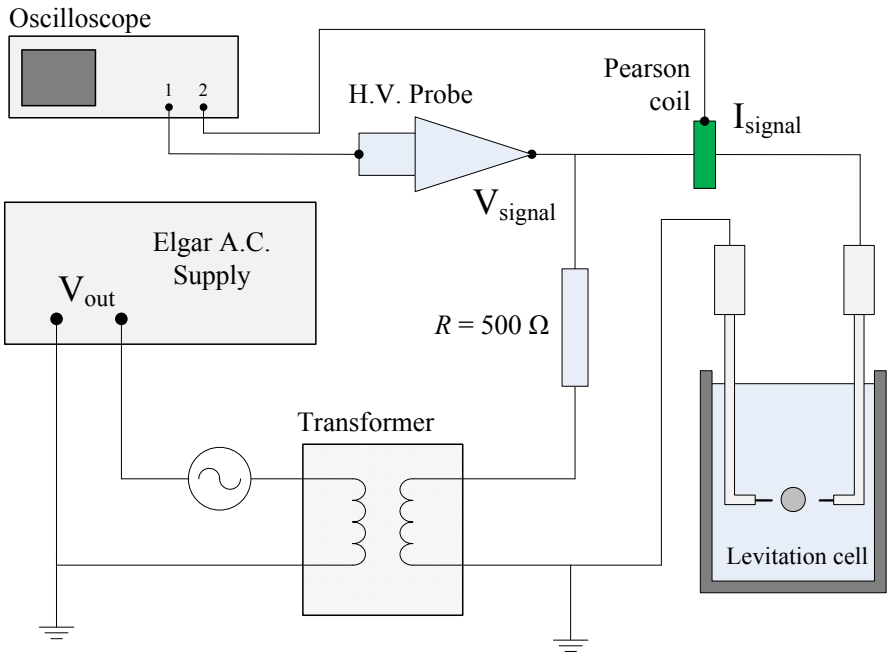

Figure 3.8: The electrical circuit used to deliver voltage from the Elgar power supply to the levitation cell.

rating ±20 mA, which not only limited the maximum available voltage in a given geometry, but also the electrode size and thus field uniformity achievable, as discussed at the beginning of Section 3.3.

3.4 H.V. Sources II: Pulsing and Plasma Ignition

The electric field timescales required to ignite plasma (∼10 ns−1 μs) [89] are significantly shorter than those required to drive shape distortions (see Section 3.3). At atmospheric pressure, the rise time of the applied pulse also has an impact on the evolution of the electron avalanche [89]. Thus, the supply used to ignite plasma should have a much shorter rise time and shorter pulse length compared to the driving supply. The following sections provide an overview of the different approaches used to ignite plasma in the levitated bubble.

3.4.1 The Suematsu Pulser

The primary voltage scheme used for plasma ignition was the MPC1300S high voltage microsecond pulser developed by Suematsu. It produces positive pulses up to +14 kV with a fixed pulse length of 1 μs and a rise time of 100 ns. The pulser is capable of a variable pulse frequency up to 2 kHz. A circuit diagram of the pulse transmission line is shown in Figure 3.11. The pulser itself consists of three different components: (1) a control unit, which is used to change the various pulse parameters (2) a charging unit, which produces an initial pulse in the range 0.4−1kV, and (3) an output unit, which produces the final output pulse. The pulser is optimized to deliver voltage to a 500 ohm load. An example of this is shown in Figure 3.12(a). However, in most practical applications, the pulser was used to drive an open load (one without plasma). In this case, the positive pulse suffered from substantial overshoot, giving rise to a negative reflection pulse that lasted for 1 μs after the first pulse. An example of this is seen in Figure 3.12(b). Though this pulse was undesirable, it often had little

Figure 3.9: The TREK H.V. amplifier provides higher voltage and greater waveform control relative to the Elgar system. All input signals are provided by the Agilent arbitrary function generator.

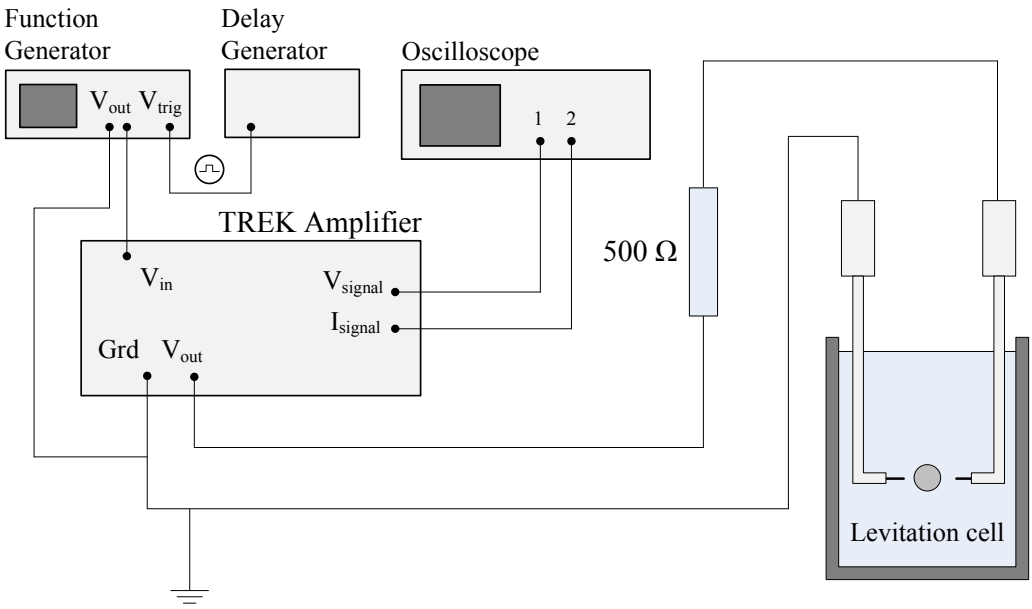

Figure 3.10: The electrical circuit used to deliver high voltage signals from the TREK supply to the submerged electrodes.

effect on the ability to accomplish the desired plasma ignition. Cases where it had a significant effect are noted throughout this work.

3.4.2 Other Methods

In some cases it was desirable to simultaneously drive shape oscillations and ignite plasma in the bubble (see Chapter 7). Due its short pulse length, the Suematsu pulser was incapable of delivering the electrohydrodynamic work necessary to alter the fluid of the bubble boundary. In such cases, an alternative ignition source was required. In other cases, voltages higher than 14 kV were required to initiate plasma ignition. In such scenarios, the TREK supply (capable of voltages up to $\pm$20 kV) was used to both drive the bubble and ignite plasma. In other cases, the TREK amplifier was used to provide D.C. pulses, with pulse lengths in the range 20$-$500 μs (see Chapter 7).

3.5 Imaging

High speed photography was the primary diagnostic technique used to characterize both bubble shape distortion and plasma formation within the bubble. Due to the multidisciplinary nature of processes occurring in the bubble, the timing and exposure requirements of all imaging were dependent on the phenomena being imaged. Bubble fluid motion and plasma evolution, in particular, occur over markedly different timescales. Typically, fluid motion occurs over the scale of $\sim$1 ms while plasma evolves over the scale of 1-100 ns [116]. As a result, different cameras and settings were required to capture different phenomena.

In this work, two cameras were used: (1) a Redlake high speed camera, which was primarily used to capture fluid motion, and (2) a high speed ICCD camera, which was used to capture plasma phenomena. Two types of lenses were used with each camera, (1) a macro lens used to capture general fluid phenomena, and (2) a

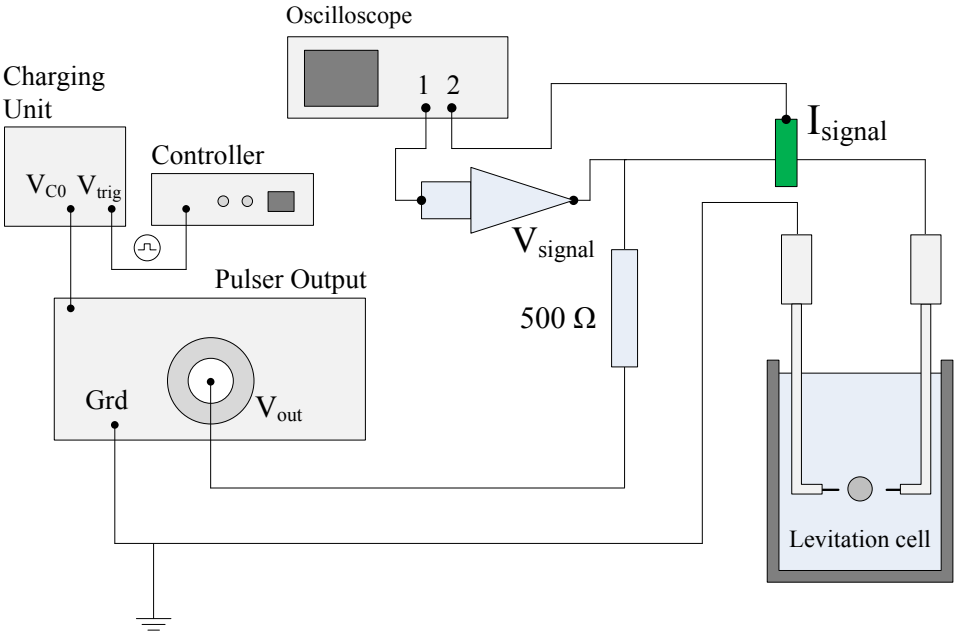

Figure 3.11: The 3 module Suematsu system was the primary ignition mechanism for plasma in the levitation cell.

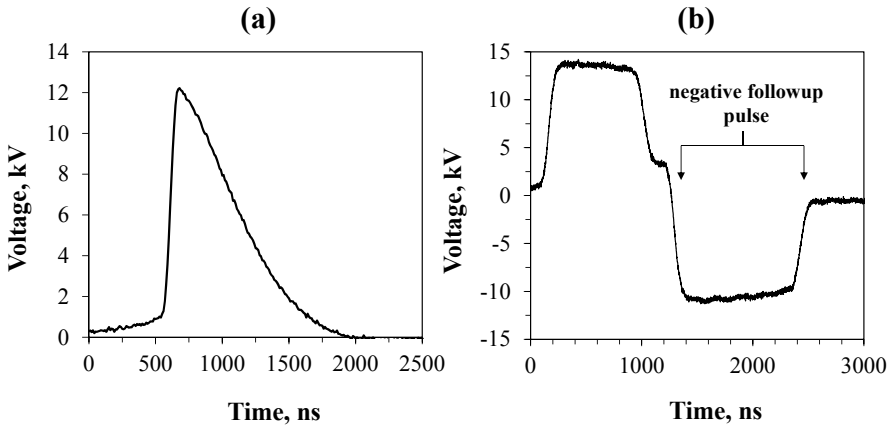

Figure 3.12: Two example pulses generated by the Suematsu pulser. (a) For a 500 ohm load, the pulser is perfectly matched and suffers no overshoot. (b) For an open load, a secondary negative reflection pulse is ignited.

high zoom telescoping lens that was used specifically for small scale phenomena ($\leq$ 2 mm). A photo of each camera, along with the different lenses used, is shown in Figure 3.13. Both cameras could be mounted on a 1-D translation stage in order to ensure clean focusing of the bubble image at all times. In addition, the lens mounts were both C mounts, allowing the use of any camera-lens combination depending on the application required. The following sections provide a more detailed description of each camera, as well as the lenses.

3.5.1 The Redlake Camera

The camera used to capture basic fluid phenomena was the Redlake high speed camera, which was capable of capturing images at up to 50,000 frames s^{-1} with a 512 x 512 array of CMOS sensors. Frames captured above 5130 frames s^{-1}, however, required a reduction in the region of interest. For typical bubble sizes ($\sim$ 1 mm), this placed an upper bound on the frame rate of approximately 31,500 frames s^{-1}. The typical frame rate used to capture fluid phenomena (bubble oscillations) was 5000 frames s^{-1} with an exposure time of 100 μs. The Redlake provided an ideal tool for imaging fluid processes, particularly bubble oscillations under the influence of an applied electric field.

3.5.2 The PIMAX ICCD Camera

The camera used primarily for imaging plasma phenomena was the PIMAX 3 ICCD, developed by Princeton Instruments. This camera is capable of high speed response (down to $\sim$1 ns) with exposure times down to 10 ns. The main limitation of using the PIMAX ICCD to image bubble phenomena is that the device is limited to single shot exposures. Though this limitation precludes time synchronized knowledge of multiple events occurring in a single bubble, it still allows us to obtain a solid qualitative understanding of plasma formation occurring in bubbles as well as an order

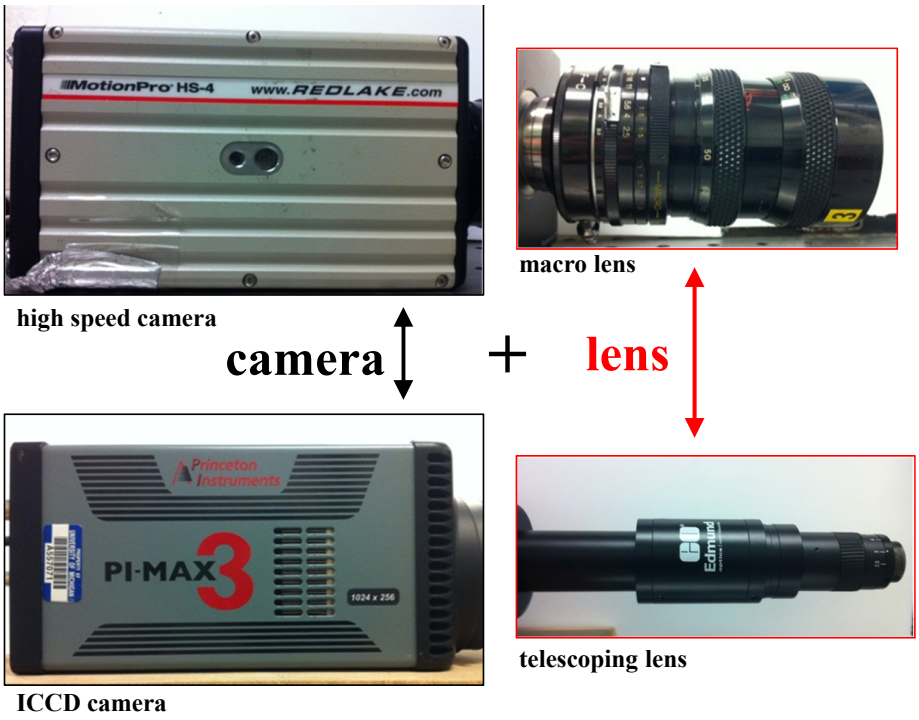

Figure 3.13: The cameras and lenses used to image bubble physics. The high speed camera (top left) was used primarily to capture fluid and bubble motion ($\sim$ 0.1-1 ms) while the ICCD camera (bottom left) was used to capture plasma phenomena (10-1000 ns). Each camera was used with one of two lenses. The macro lens (top right) provided adjustable zoom and focus to cover a wide range of phenomena, while the telescoping lens (bottom right) was used to image very small (up to 10x zoom) phenomena.

of magnitude estimate of important timescales. Insight into the time dependence of plasma events was accomplished by triggering the intensifier gate at a variable delay relative to the voltage pulse. This was set using a delay generator. The single shot limitation necessitated careful control of procedure in order to keep operating conditions consistent. Extreme care, therefore, was taken to develop a highly repeatable experimental setup. Among the most effective approaches used to accomplish this task was to clean the electrodes consistently in order to eliminate oxide layers forming in the aftermath of plasma formation.

3.5.3 Camera Lenses and Lighting

Each camera was capable of operating with two separate lenses, each equipped with a C-mount fitting. The first type of lens was a standard macro lens, capable of variable focal length and variable zoom up to a factor of 2X. This was the nominal lens used to image with the Redlake camera. In cases with objects requiring higher magnification, a long range telescoping lens from Edmund Optics was also used. This lens was capable of providing magnification in the range 2X-10X and was used primarily with the ICCD camera, particularly in the imaging of small scale plasma phenomena (< 2 mm). A precise calibration of the length scale for each picture was obtained by imaging an alumina tube of precisely known width. This was used to determine the length conversion in pixels/mm for an image taken at any zoom level.

All images were backlit with a standard 50 W tabletop lamp. In many cases, a white sheet of paper was placed between the backlight and the imaged object in order to provide a more diffuse and uniform low level source of light. The backlight was often necessary to view the boundary of the bubble during deformation. The dielectric boundary of the bubble presented a unique problem during this process. Often, the backlight was focused to the center of the bubble shape as it entered the lens, giving the false impression of plasma formation in the bubble. To minimize any

confusion, the backlight was turned off whenever possible, especially when the focus was solely on plasma phenomena. When such ambiguity exists in this dissertation, care will be taken to note the backlight and distinguish it from the plasma.

3.5.4 Image Analysis

It was shown in Section 2.4.3 that bubble oscillations can be naturally decomposed into the spectrum of spherical harmonic perturbations. If the applied electric field is axisymmetric, as in the case of a uniform field, then the electric stress felt by the bubble is also axisymmetric. Furthermore, any resulting deformation should also be axisymmetric. Under this assumption, the shape of the bubble can be characterized by capturing a 2D image of the bubble using high speed photography. In practice, the shape of the bubble was identified with relative ease by backlighting the levitating bubble with the 50 W lamp. An example of a raw image taken under these conditions is shown in Figure 3.14(a). For each image, the shape modes, defined by equation 2.31, were calculated using a computer program that utilizes Matlab's image processing toolbox [142]. The program first converts the 8-bit color image into a black and white image using a specified threshold. This conversion process had the effect of removing noise at the boundary of the bubble. The black and white image was then analyzed with an edge detection algorithm in order to obtain discrete data points for the coordinates of the bubble boundary. The boundary solving algorithm is built into the Matlab toolbox and is based on a canny edge detection method [142]. The number of boundary points for each image was approximately 100.

The discrete coordinates of the boundary were converted from rectangular coordinates (x_i, y_i) to azimuthally symmetric spherical coordinates (μ_i, r_i) by assuming that the vertical axis of the image corresponds to $\theta = 0$. In some cases, the bubble was observed to undergo small rotations during its motion. This was corrected by implementing a user feedback option into the Matlab program, in which the user could

analyze the boundary and input a small correction angle that produced axisymmetric results. The mode coefficients for each Legendre polynomial were then calculated by numerical integration of the discrete $R_i(\mu_i, t)$ data. Integration was performed numerically using the trapezoidal integration method. The resulting discrete form of 2.29 is,

$$b_l(t) = \begin{cases} \sum_{i=1}^{N-1} \frac{1}{4}\big(\mu_{i+1} - \mu_i\big)\big(R_{i+1} + R_i\big) - 1 & l = 0 \\ \sum_{i=1}^{N-1} \frac{1}{2}\big(\mu_{i+1} - \mu_i\big)\big(R_{i+1}P_l(\mu_{i+1}) + R_iP_l(\mu_i)\big) & l \geq 1 \end{cases} \tag{3.11}$$

The bubble volume was calculated by revolving the 2D image $R(\mu, t)$ around the axis of symmetry. The appropriate integral can be derived using the shell method for computing a surface of integration [143],

$$V(t) = \frac{2\pi}{3} \int_{-1}^{1} R^3(\mu, t)\ \mathrm{d}\mu \tag{3.12}$$

Image analysis provides a characterization of the various modes present during the shape distortion of the bubble. Using this approach, one can associate the observed excitation to one or more specific modes. It also provides a way to quantify the

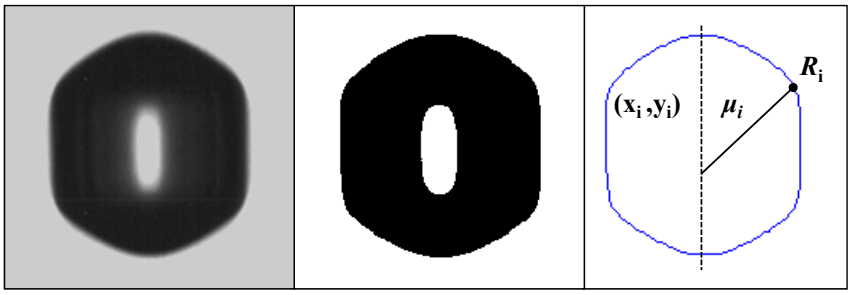

Figure 3.14: (a) A raw image taken with the Redlake camera. (b) The image after thresholding. (c) Discrete data points of the boundary obtained by applying the edge detection algorithm.

bubble deformation in response to a specific magnitude and geometry of electric field. For example, if it is desired to isolate or maximize a specific mode, one can vary the electrode geometry until the specific mode coefficient is maximized. In the case of the volume effect, shape analysis allows one to monitor the volume of the bubble as a function of time.

3.6 Evaluating the Shape Effect

The shape effect is influenced by the deformation of the boundary of the bubble and the gradient in permittivity between the water and air. Due to the slow timescales associated with the fluid motion of the bubble ($\sim$1 kHz), the evolution of the electric field can be considered quasistatic [116]. Thus, to good approximation, one can estimate the field enhancement occurring at any instant as that due to a D.C. electric field. In general, one can also assume the bubble is stationary but deformed to a shape matching an experimentally or theoretically determined shape. The evaluation of field enhancement can be further simplified by assuming that the applied field is uniform. In this case, the position dependent field enhancement factor, $G(\mathbf{x})$, defined in Chapter 2, can be used to evaluate the importance of the shape effect in each experimentally observed bubble shape. In such cases, the electric field enhancement within the bubble is given by,

$$G(\mathbf{x}) = \frac{\left|\mathbf{E}(\mathbf{x})\right|}{\left|\mathbf{E}_0\right|} \qquad \text{(field enhancement factor)} \tag{3.13}$$

Together, these approximations provide a simple, tractable way of evaluating the shape effect in bubble shapes observed by experiment; a method that is independent of the pulse length or rise time of the applied voltage. Even in the electrostatic regime, analytical solution of the electric field distortion occurring inside deformed bubbles is difficult to obtain. It is more practical to model the electric field numerically using

an electrostatic solver. The electrostatic solver used in this dissertation is the 2-D version of Maxwell [144]. The uniform field was created using a pair of electrodes above and below the bubble. The electrode diameter was set at 24 mm and the gap was set at 12 mm, giving an aspect ratio of 2:1. The bubble was placed at the center of the electrode gap with an unperturbed diameter of 1.0 mm. In the case of spherical harmonic shape distortion, the discrete boundary calculated using equation 3.11 was directly input into the Maxwell geometry. The electrostatic calculations provided by Maxwell serve as a diagnostic for evaluating the shape effect in deformed bubbles. Throughout this dissertation, these simulations will be used to investigate which types of deformations are most optimal for achieving the shape effect.

3.7 Experimental Plan

The apparatus introduced in this chapter is designed to accommodate a wide range of experiments focused on the fundamental physics of plasma formation in bubbles. The next four chapters comprise a detailed study of such phenomena. Insight gained from these experiments will form a general guide in the process of designing a liquid based plasma reactor. Chapter 4 begins with preliminary experiments performed on electrode attached bubbles. These experiments provide a basic introduction to the important issues in bubble discharge physics. The primary content of the remaining research focus can be split into goals: (1) The use of intense electric fields to achieve extreme shape distortion of levitating bubbles, as presented in Chapter 5 and (2) the use of intense electric fields to achieve plasma formation within isolated bubbles, as presented in Chapter 6. Finally, these approaches are combined in Chapter 7 to investigate plasma formation in deformed bubbles.

CHAPTER IV

Preliminary Experiments in Electrode-Attached Gas Bubbles

4.1 Overview

This chapter describes early experimental results focused on plasma excitation in electrode attached bubbles. These experiments represent an introduction to the use of electric fields to excite bubble shape deformations and ignite plasma within the bubble's volume. As discussed in Chapter 1, the excitation of streamers in electrode attached bubbles is a common approach in plasma based water purification schemes. Despite the practical limitations associated with the electrode attached bubble geometry, these experiments offer critical insight into the basic principles of bubble distortion and discharge physics. Overall, the preliminary experiments reviewed in this chapter had two goals: (1) demonstrate the viability of using electric fields to distort a bubble's shape and (2) investigate how these distortions affect the excitation of plasma within the bubble.

It will be shown that plasma streamers ignited in the bubble can substantially perturb the fluid boundary of the bubble. Under certain conditions, these fluid distortions are observed to grow to large amplitudes over the course of several oscillation cycles. At the heart of this nonlinear behavior is the dual relationship between the

applied field in the bubble and the fluid boundary: electric fields can be used to deform the dielectric boundary but the dielectric boundary can also distort the applied field. This has important consequences not only for the current understanding of discharge mechanisms in bubbles but also for the design of plasma based liquid purification schemes.

A diagram of the experimental setup used to investigate electrode attached bubbles is shown in Figure 4.1. The discharge cell is composed of a long glass tube with inner diameter 6 mm and relative permittivity equal to 4. The electrodes were designed to produce a point-to-plane geometry. The planar electrode, inserted through the top of the tube, was constructed from a 0.48 cm diameter threaded rod. The bottom surface of the rod was sanded to make it smooth and flat. The bottom electrode, which was fed through a side port near the bottom of the tube, was composed of a molybdenum wire 0.5 mm in diameter. The wire was covered using a high voltage insulator, with the top 1 cm of the wire tip exposed to the water. It was positioned on the centerline of the tube at a distance 4 mm below the threaded rod to achieve coaxial symmetry. The glass tube was filled with distilled water having conductivity equal to 0.7 μS cm^{-1}.

The applied electric field was generated using two different high voltage driving schemes. The first scheme used was the Elgar A.C. high voltage power supply, described in detail in Section 3.3.1. The Elgar high voltage transformer combination was used to produce voltage signals up to $\pm$5 kV with A.C. frequency in the range 100-1000 Hz. The use of such "slowly" varying A.C. signals allowed the bubbles to be excited near the typical range of resonance frequencies, as determined by equation 2.31. Under certain conditions, this voltage level was also large enough to ignite plasma in the bubble. The second voltage source, which was primarily used to excite plasma streamers, was the Suematsu high voltage pulse generator, also described in detail in Section 3.4.1. This supply was used to generate 12 kV pulses of 1 μs pulse

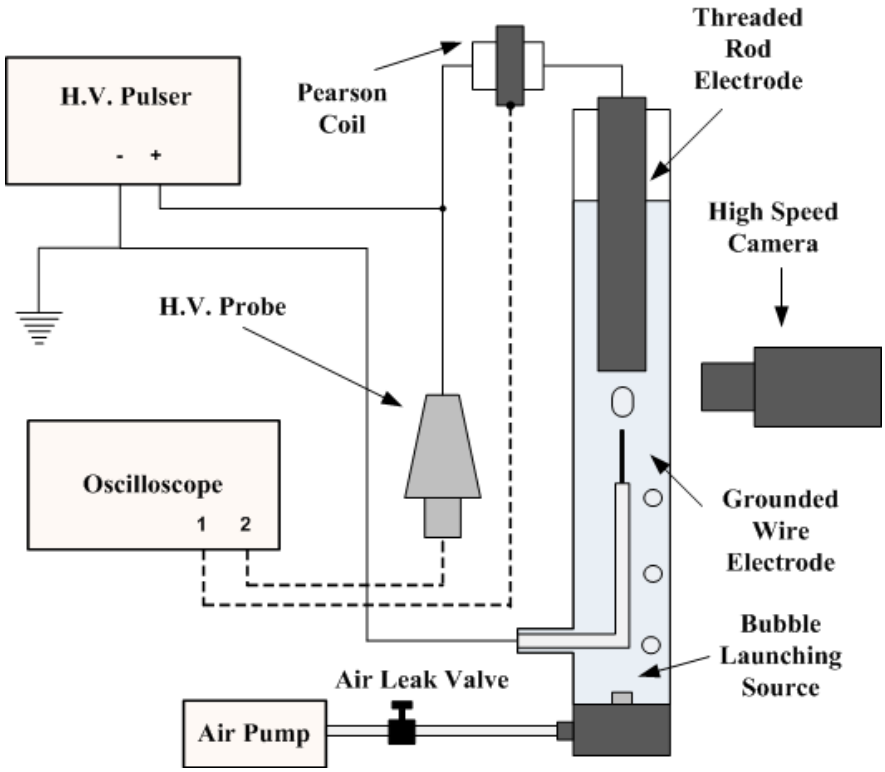

Figure 4.1: Injected bubbles pass between the electrodes and become trapped on the surface of the threaded rod, which is biased at high voltage.

length and 100 ns rise time. The Suematsu supply is capable of pulse frequency up to 2 kHz, but was generally operated at less than 750 Hz.

Bubbles were injected into the glass cell through the bottom port of the glass tube. An air pump was used to inject ambient air through a small channel at the bottom of the cell. This channel was filled with quartz crystals to prevent back flow of the water out of tube. Bubble formation was achieved by forcing air between the crystals and into the bottom of the tube. The bubbles could be biased as they passed through the electrode gap, but were typically trapped on the surface of the top electrode. Typical bubbles were 1 to 3 mm in radius.

Voltage and current signals were measured on a 500 MHz oscilloscope using a Tektronix P6015A high voltage probe and a 6600 Pearson current transformer coil. Imaging was performed using the Redlake high speed camera operating at an acquisition rate of 5000 frames s^{-1}. Unless stated otherwise, the exposure time per frame was 198 μs. A 50 Watt lamp was used to provide a backlight for bubble imaging. A thin piece of white paper was placed in between the light and the imaged tube in order to provide a uniform, low level of light, well suited to imaging both fluid motion and plasma ignition.

4.2 Excitation of Bubble Oscillations by A.C. Electric Fields

The first experiment conducted in this setup was a simple demonstration of bubble oscillations using the Elgar power supply. In this case, bubbles were attached to the top plane electrode Figure 4.2 show two examples of a bubble being driven by an A.C. voltage with amplitude 1.6 kV and frequency 50 Hz. Images of the deformed bubble were taken with a frame rate of 3000 frames s^{-1} and exposure time 330 μs. For the electrode geometry shown in Figure 4.2, the electric field acts primarily perpendicular to the bubble surface, which is approximately flat. This field will polarize the surface and push it downward. For an applied voltage of 2 kV, for example, the electric field in the bubble can be approximated as the voltage divided by the diameter of the bubble, which is 2.4 mm. This results in an electric field of approximately 8.3 kV cm^{-1}. The radius of curvature of the resting bubble is approximately 10 mm. This is larger than the actual radius of the bubble due to the cohesion of the bubble against the glass wall. The resulting Weber number for this field strength and radius of curvature is of order 1. Thus, deformation of the bubble surface should occur.

The oscillations observed in Figure 4.2 are reminiscent of dipole mode shape oscillations ($l = 2$), except with one tip of the bubble constrained to the electrode surface. Using equation 2.31, the $l = 2$ shape mode frequency, f_2, in this case is 52 Hz, which

matches the applied frequency well. For comparison, the volume mode frequency, f_0, is 920 Hz. The top example in Figure 4.2 shows the bubble at maximum and minimum deformation during the course of two oscillation cycles. As the voltage increases (between frames 1-2 and 3-4), the bubble expands under the action of the applied field. When the field amplitude decreases (between frames 2-3), the bubble boundary snaps back toward equilibrium under the restorative action of its surface tension. On average, the area expansion of the bubble is observed to be upwards of 5-10%. It is observed that increasing the frequency to the range 100-200 Hz results in a substantial decrease in the oscillation amplitude. As the driving field becomes much larger than the dipole mode frequency ($l = 2$), the fluid response becomes too slow to respond to the quickly alternating fields.

In some cases, bubble expansion was accompanied by the ignition of plasma streamers inside the bubble gas. The bottom set of images in Figure 4.2 shows a single expansion phase (half cycle) for a bubble driven at the same conditions, 1.6 kV and 50 Hz. In this case, the applied field ignites a series of plasma streamers, which propagate downward to the bottom of the bubble. An example of the voltage and current signal observed during such streamer ignition is shown in Figure 4.3. In this case, the applied frequency is 100 Hz. The current spikes represent streamer ignition, which occurs multiple times per cycle and primarily during the positive phase of the applied voltage. During excitation, the voltage signal undergoes severe distortion, caused in part by the dielectric breakdown resulting from each streamer pulse. An additional source of distortion is believed to be the high voltage transformer, which is not designed to operate below 400 Hz.

4.3 Properties of Streamers in Electrode Attached Bubbles

A clearer picture of plasma formation in electrode-attached bubbles was obtained using single pulses delivered by the Suematsu high voltage pulser. Using this method,

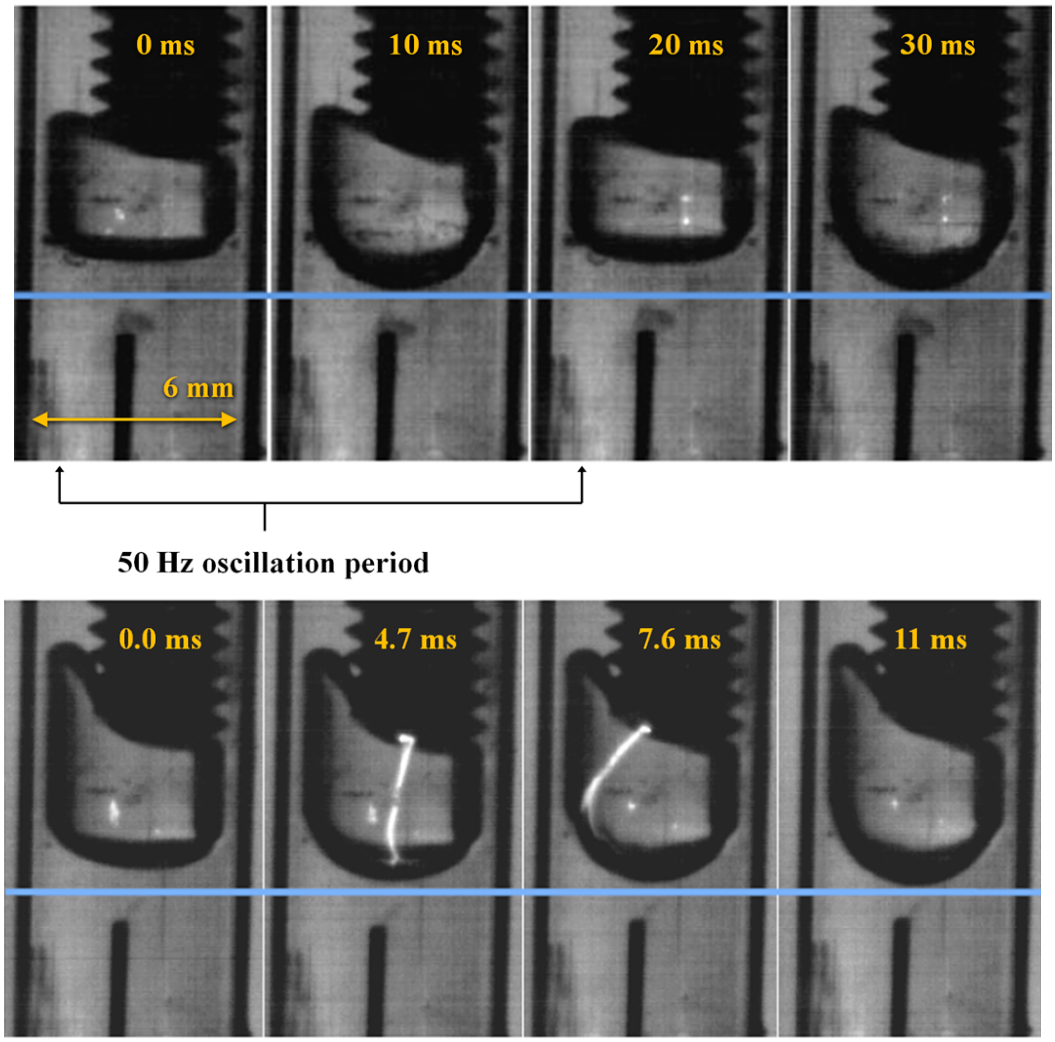

Figure 4.2: Periodic bubble driving at 50 Hz, 1.6 kV, illustrates the maximum and minimum deformation of the bubble (top) under the force of the applied field. Periodic bubble driving at the same conditions (bottom) can be accompanied by plasma streamers. These streamers occur predominantly in the positive phase of the applied voltage

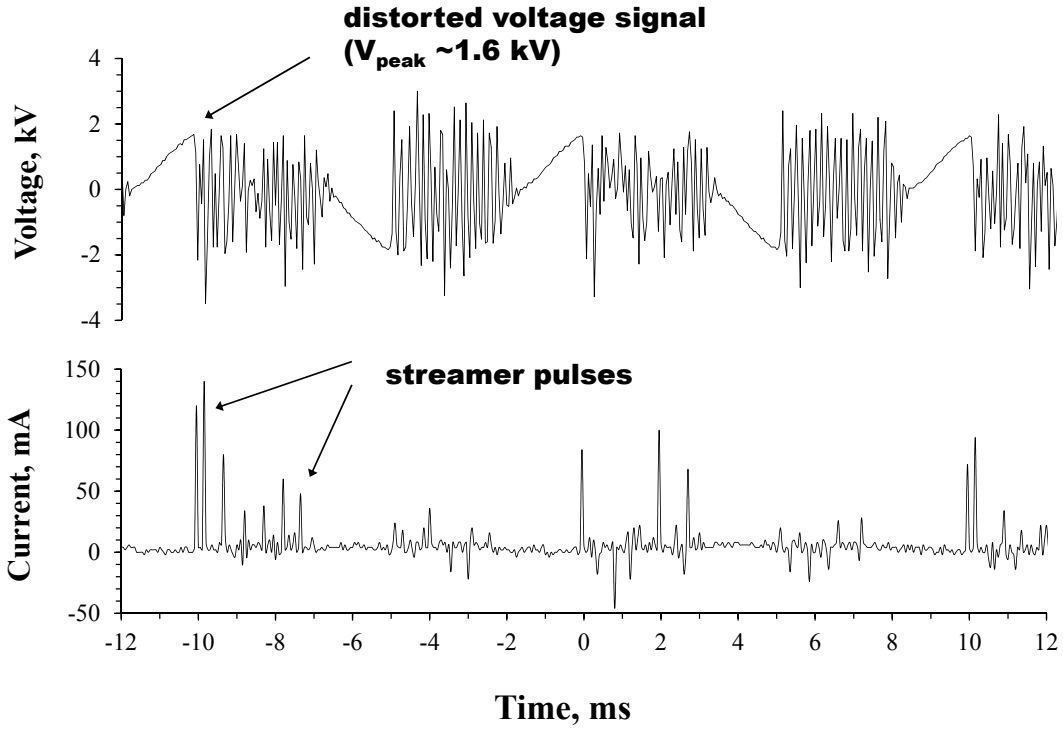

Figure 4.3: Discharge characteristics for a 100 Hz signal driving bubble deformation and igniting streamers. Distortion of the voltage signal is caused by both dielectric breakdown as well as the limitations of the high voltage transformer.

the voltage pulse occurs over much shorter times, (1 μs) than those produced by the Elgar supply ($\sim$5 ms). At such short pulse times, the total stress delivered to the bubble is too small to result in substantial deformation. This allows us to separate the fluid perturbations due to the plasma streamer from those due to the applied field pressure.

Bubble streamers were ignited by applying a positive 12 kV pulse to the top circular plate electrode. The needle electrode was held at ground. The pulse frequency was varied in the range 100-750 Hz. Bubble streamers were imaged using the Redlake camera at 5000 frames s^{-1}. Examples of the voltage and current signals for a single

pulse are shown in Figure 4.4. The rise in voltage is accompanied by a cluster of current spikes, indicating the excitation of one or more streamers. The positive 1 μs pulse is followed by a 1 μs reflection pulse of the same shape. As discussed in Chapter 3, this reflection is due to the impedance mismatch between the output of the pulser and the load (represented by the bubble and water). Streamers were also ignited at the peak of the negative pulse, but their current signatures were significantly smaller than peaks occurring during the positive cycle (see Figure 4.4). In general, streamers were observed to occur primarily at the positive cycle, often more than once per cycle. Streamers observed during the negative cycle did not display a noticeable difference, from a photographical standpoint, compared to the positive cycle streamers.

The predominance of streamers occurring during the positive cycle is consistent with the current polarity dependence first observed in Figure 4.3. The current variations observed in Figure 4.4 change in phase with the applied voltage, indicating the dominance of conduction current over displacement current. This is most likely due to the contamination of the water by electrode particulates, which raises the conductivity of the liquid. Since the total amount of water in the vicinity of the electrodes is so small (due to the small tube diameter), a small release of electrochemical products results in large increase in conductivity.

Figure 4.5 shows images of plasma streamers ignited at four different pulse frequencies, ranging from 100 Hz to 750 Hz. The peak voltage in each case is 12 kV. Accompanying these images is a 2-D simulation of streamer formation provided by the code *nonPDPSIM*, which is described in detail by Babaeva [86, 108]. This code solves Poisson's equations for the electric potential and a set of transport equations for the density of charged and neutral species. Radiation transport and photoionization are included by implementing a Greens function propagator. The numerical grid uses an unstructured mesh with triangular elements and refinement regions to resolve the details of the electrode tip and the bubble. The mesh consisted of 7400 nodes

of which 4300 were in the plasma zone with tight refinement along the water-bubble interface. The gas mixture was set at $N_2/O_2/H_2O = 79\%/18\%/3\%$ with an ambient pressure of 1 atm and a photon mean free path of 100 μm [108]. The discharge was initiated using a small cloud of seed electrons with a radius of 500 μm and a peak density of 10^8 cm^{-3} placed at the edge of the upper electrode. The bubble was static during the simulation. A detailed overview of these simulations can be found in [108]. In the present discussion, only results pertinent to the experimental data presented in this chapter will be discussed.

In both the experiment and model, the streamer appears to travel along the side of the bubble, terminating near the bottom tip of the bubble, often overshooting it. Results from the model indicate that the streamer traverses the bubble wall in about 8 ns with the electron density reaching a maximum of $7 \cdot 10^{15}$ cm^{-3}. The propagation of the streamer along the gas-water interface is analogous to a streamer impacting the

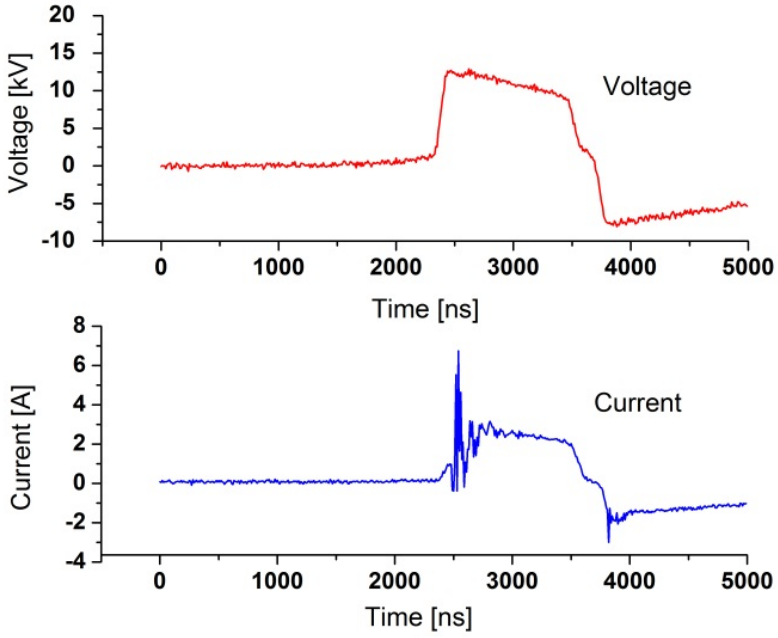

Figure 4.4: IV traces for bubble plasma produced by the Suematsu pulser with a 1 μs pulse length. Observation of the current spikes is accompanied by a slight voltage dip.

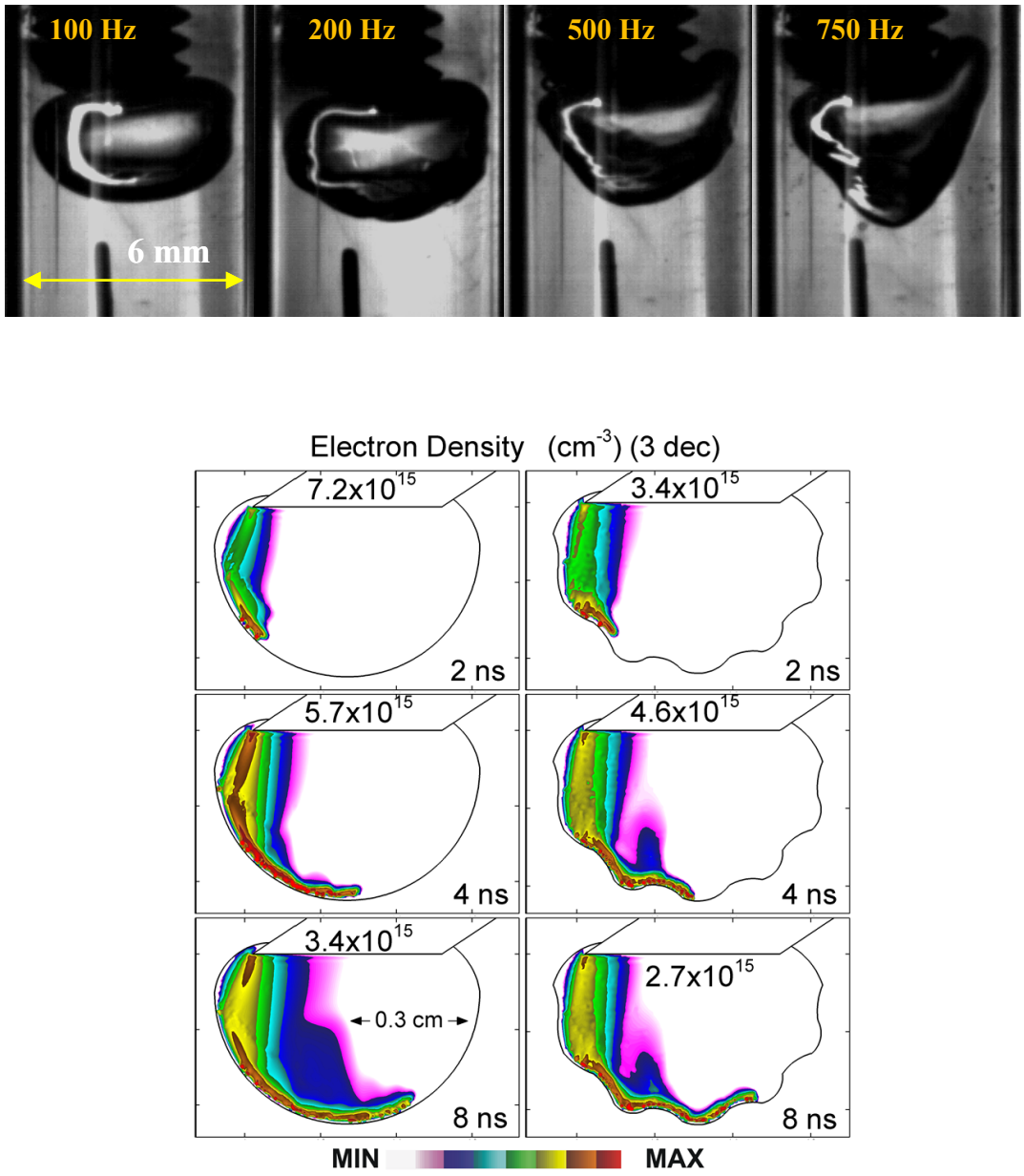

Figure 4.5: (Top) Plasma streamers ignited in bubbles at different pulse frequencies. The effect of higher pulse rate is to increase the average stress on the bubble, thus resulting in higher deflection of the bubble surface.(Bottom) Model of electron density growth of the streamer as its propagates along a smooth bubble surface and a perturbed bubble surface. Results are taken from Sommers [108].

dielectric in a dielectric barrier discharge. When the streamer strikes the boundary of the bubble, it deposits charge on the fluid surface, which generates a secondary electric field. This field subsequently "turns" or deflects the streamer parallel to the boundary. In this geometry, there are also components of the vacuum electric field that are directed parallel to the surface. The surface charging reinforces those parallel components. The gradient in permittivity across the bubble-water interface results in electric field enhancement, which further intensifies the avalanche.

As the pulse rate is increased, the perturbation of the bubble by the streamer impulses becomes evident. Each time the streamer impacts the fluid boundary, it transfers a net impulse to the fluid by virtue of the intense electric fields at its tip. This is the same mechanism as that observed in Figure 4.2, only now the field is applied for a very short time ($\sim$10 ns). Looking at the images in Figure 4.5, it is clear that the perturbations are excited along the side of the bubble but have the strongest effect at the bottom surface, which is the common meeting point for all streamers. Each streamer pushes down on the bottom at nearly the same point, while the sides are pushed in a largely random and incoherent manner due to the varying path of each streamer. The result of this continuing process is the permanent deflection of the bubble surface. This deflection increases with higher pulse rate. At a pulse frequency of 750 Hz, for example, the deflection is extreme and conical in shape. In contrast, the deformation at low frequency is quickly damped by the viscosity of the fluid, resulting in a smooth steady state fluid interface. The model indicates that the streamer hugs the contours of the surface even when the bubble exhibits surface distortions, which become increasingly more violent as the repetition rate is increased from 375 to 750 Hz. Images from Figure 4.5 corroborate this result. In the case of 500 Hz and 750 Hz, in particular, the streamer appears to bend with the perturbed surface as it propagates along the bubble wall.

A condition for the electrical stress to perturb the fluid boundary is that the

electrical pressure be larger than the local surface tension. This condition can be expressed, as discussed in Chapter 2, using the electrical Weber number,

$$W_e = \frac{\varepsilon_0 \left|\mathbf{E}\right|^2 R_0}{\gamma} \tag{4.1}$$

In reality, the actual mechanism by which a streamer distorts the bubble surface is a combination of electrostatic and fluid dynamic effects. In addition to electrical stress, the streamer may also produce local pressure effects, including heating of the surrounding gas [49, 99]. Thus, the condition $W_e = 1$ represents a sufficient condition but not a necessary one. The results of the *nonPDPSIM* model indicate that the electric field at the head of the streamer reaches 510 kV cm^{-1} at the time the streamer first impacts the side of the bubble. This corresponds to a reduced field, E/N, of 2100 Td and a Weber number, W_e, of 970. By the time it reaches the bottom surface of the bubble, the streamer field has been reduced to 185 kV cm $^{-1}$ (770 Td, W_e = 130). These values of W_e indicate that the field pressure is large enough to deform the fluid surface. In conventional dielectric barrier discharges, the surface is rigid, resisting distortion from the intense fields. In this case, the liquid is fluid and can be deflected by the applied stress. It is clear from this analysis that short pulse lengths can be used to excite bubble deformation, but only at a sufficiently high pulse rate.

Light emission from the streamer plasma was captured using an ocean optics USB spectrometer and is shown in Figure 4.6. The observation of OH, N, H_α lines is consistent with prior work investigating the spectral characteristics of bubble streamers in attached bubbles [85]. It is also consistent with results from the model, which predict OH concentrations up to $8 \cdot 10^{14}$ cm^{-3}.

Figure 4.7 shows the perturbing effect of a single streamer on the bubble wall. In this case, the streamer leaves behind a darkened track that diffuses outward from side to side over a time of 1-2 ms following the pulse. The darkened area represents the

perturbation of the fluid surface by the intense fields at the head of the propagating streamer. The deflection of the surface changes the trajectory of the back light, resulting in the darkened area. The relaxation of the surface perturbation is consistent with the frequency dependence observed in Figure 4.5. If the time between two pulses is sufficiently long (>10 ms), then the surface wave excitation due to the first pulse will not carry over to the second pulse.

4.4 Resonant Excitation of Surface Waves

4.4.1 Capillary Waves

The previous section illustrates that repeated streamer pulses can lead to significant perturbation of the bubble boundary. At large pulse frequencies, these perturbations are chaotic and incoherent, while at low frequency the perturbations tend to be damped out by viscosity. Between these two extremes, however, a very interesting result was obtained. Over a narrow range of frequencies, the periodic impact of the streamers gave rise to large amplitude waves on the bubble surface. Oscillations of this type are known as capillary waves, and are typically excited along the interface between a fluid and gas [145]. The propagation of capillary waves is influenced by the surface tension constant of the fluid γ, the acceleration due to gravity g, and the liquid density ρ. The dispersion relation for capillary waves, $\omega(k)$, is known as Kelvins equation and can be modified in the presence of a uniform electric field to yield the following viscosity free form [145],

$$\omega^2 = \frac{\gamma k^3}{\rho} + gk - \frac{\epsilon_0 E^2 k^2}{\rho} \tag{4.2}$$

The wave excitation mechanism in the case of bubble plasma arises from the local pinching of the surface by the streamer. Each pinch produces an outgoing perturbation in the same way a rock thrown into a pond produces a cylindrical wave front on

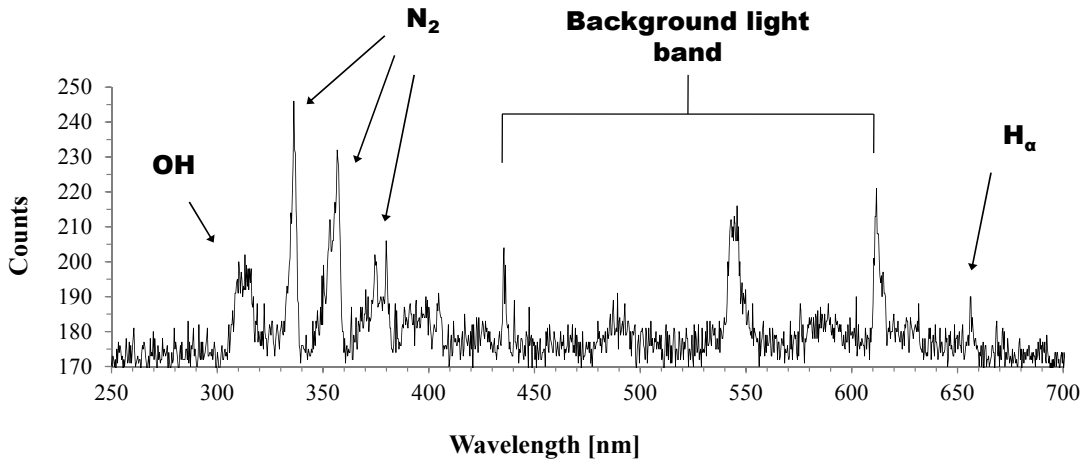

Figure 4.6: Spectra observed from plasma forming in the attached gas bubble confirms the production of reactive species such as OH.

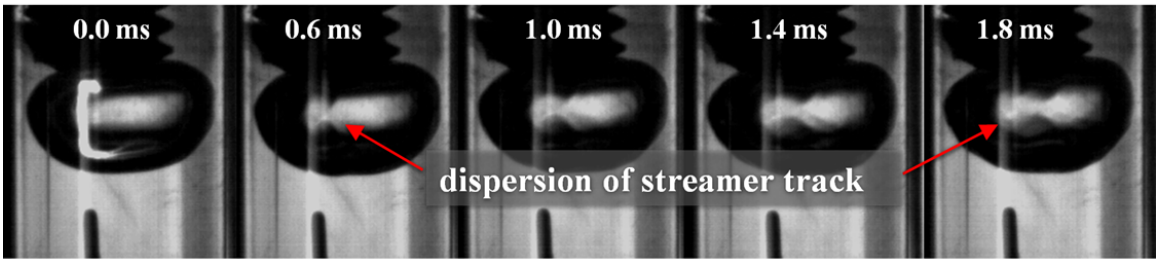

Figure 4.7: Relaxation of the perturbed bubble surface in the aftermath of a wall hugging streamer. Eventually, (t > 10 ms) the wave is damped by viscous forces in the water.

the surface of the water. If the fluid interface is closed and fixed at its boundary, then the outgoing and reflected waves will interfere with each other, resulting in a standing wave. This boundary condition will restrict the wave excitation to a discrete spectrum of wavelength conditions. It is possible to excite large wave growth on the bubble by pulsing or pinching the bubble surface at exactly these resonance conditions. One can estimate the resonance condition of an attached bubble by approximating the bubble cross section as a circle. In this case, the resonance condition is that the wavelength, λ satisfies a periodic boundary condition,

$$m\lambda = 2\pi R_0, \qquad m = 0, 1, 2... \tag{4.3}$$

Both the streamer transport time, ∼10 ns (see Figure 4.5), and the total pulse time, 1000 ns, are much shorter than typical fluid oscillation timescales, ∼1 ms. As a result, the electric field is relevant to the oscillation physics only for a very short time. In addition, charge relaxation by the conductivity of the water will eliminate residual surface charge on time scales shorter than the oscillation period [116]. In liquid water the charge relaxation time is determined by the permittivity, ϵ, and conductivity, κ,

$$\tau = \frac{\epsilon}{\kappa} \tag{4.4}$$

For the deionized water used in this experiment, τ ∼100 μs, so the charge relaxes much quicker than the period of oscillation. The electric field due to both the streamer and charge deposition, therefore, can be modeled as a delta function impulse that excites the bubble surface but is not present during the propagation of the wave. Therefore, during oscillation the electric field term in 4.2 can be neglected. In addition, for frequencies in the kHz range, the term gk is also small compared to surface tension term. Substituting the resonance condition from equation 4.3 into the dispersion

relation gives the simplified dispersion relation for constrained bubbles.

$$\omega = \sqrt{\frac{\gamma m^3}{\rho R_0^3}} \tag{4.5}$$

For a fixed frequency, this relation will give rise to a discrete spectrum of possible capillary wave modes excited on the bubble surface, each with a different wavelength.

4.4.2 Rayleigh-Taylor Instabilities at the Bubble Surface

The perturbation of the gas-liquid boundary can give rise to the Rayleigh-Taylor instability, which is an unstable wave growth excited at the boundary between two fluids when one is accelerated into the other [146]. One example of this effect is when a heavy fluid, such as water, is supported (via gravity) on top of the lighter fluid, such as in the case of an underwater gas bubble. For a fluid boundary exhibiting a sharp change in density, the growth rate of the perturbation is given by [146],

$$\gamma_{RT} = \sqrt{gk} \quad [\mathrm{s}^{-1}] \tag{4.6}$$

Here, k is the spatial wavenumber of the growing wave and g is the acceleration acting on the fluids. In the above example, g corresponds to the acceleration due to gravity. In general, g, can represent any source of acceleration acting on the two fluids such as a local pressure or force disturbance acting on the boundary.

In the case of a gas bubble, this condition is satisfied near the sides and the top of the underwater bubble. Although the bubble can achieve equilibrium in this geometry, it is not stable. Any perturbation will tend to excite wave growth with time. Another source of the Rayleigh-Taylor instability in a gas bubble may be due to the sudden pressure increase in the aftermath of a plasma streamer. The sudden expansion and acceleration of the gas at the head of the streamer is large enough to perturb the bubble surface. This excitation may also be enough to initiate the growth

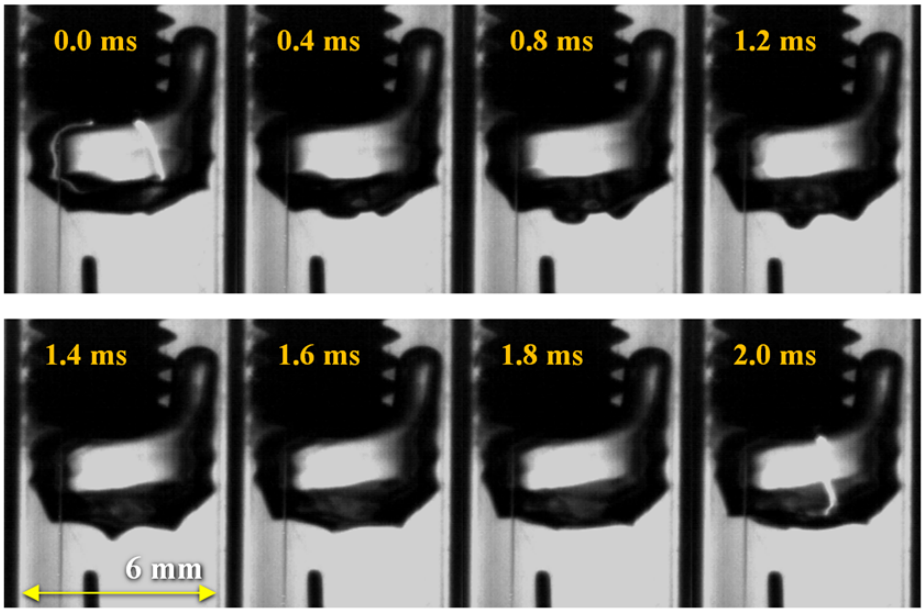

Figure 4.8: A single oscillation period illustrating the excitation of capillary waves on the surface of the bubble. Pulses are applied at 500 Hz and 12 kV.

of a Rayleigh-Taylor instability.

4.4.3 Capillary Waves Excited in the Point-to-Plane Geometry

An example of a surface capillary wave excited on the bubble surface is shown in Figure 4.9. In this case, the pulse frequency is 500 Hz and the peak voltage is 12 kV. The times noted in the figure are relative to the streamer impact. At $t = 0$ ms, the streamer terminates on the bottom of the bubble. This results in the growth of the capillary wave, which propagates outward around the side of the bubble. The wavelength of the surface oscillation is observed to be in the range 1.5-1.9 mm.

Kelvins equation predicts that for wavelengths in this range, the frequency should be in the range 250-350 Hz. The discrepancy between theory and experiment could be due to a number of factors. The primary reason is likely the three dimensional structure of the wave. This not only changes the form of the periodic resonance condition but also places a significant uncertainty in the measurement of the wavelength using 2-D photos. Another possible explanation is viscosity, which is not taken into

account in equation 4.2. The viscous forces acting on the exciting wave will not only damp the growth of the wave but also shift the resonance frequency.

A third explanation is that the streamer impact time is changing during each cycle. The point of the wave crest facing inward toward the electrode represents the shortest electrode gap for the streamer. This inverted crest could act as a "lightning rod" for the excited streamer. If the streamer always interacts with the inverted wave crest each cycle, then the effective driving frequency would need to be twice the resonant frequency. In the above case, this would correspond to twice the range 250-350 Hz, which is 500-700 Hz. Despite this disagreement, the resonant nature of the wave is quite evident from examining Figure 4.8. The relaxation of the wave amplitude in the last two images (1.8-2.0 ms) corresponds very closely to the exact time that the follow-up streamer pulse is ignited, indicating that the streamer is pinching the fluid boundary at just the right time.

The growth of the capillary wave to large amplitudes takes place over many cycles. Figure 4.9 shows the evolution of the wave amplitude after N cycles (N = 10, 17, 21, 25, and 33 cycles). It is only after 10-15 cycles that the wave structure becomes prominent. Over the next few cycles, the amplitude grows very quickly, reaching a maximum amplitude of approximately 0.8 mm. After approximately 30 cycles, the wave amplitude saturates at a steady state value. The observed limitation in the wave

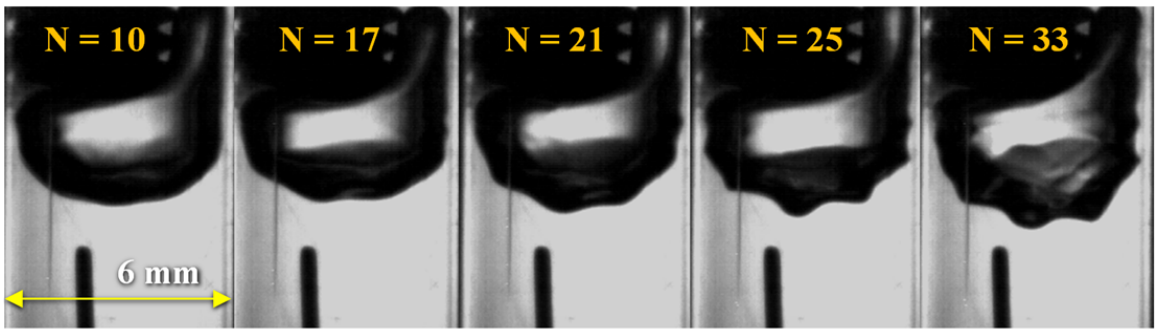

Figure 4.9: The evolution of capillary wave amplitude over N pulse cycles. Eventually the wave growth reaches a steady state amplitude.

growth is most likely due to a combination of factors. One source of attenuation is viscous damping. As the size of the wave front increases, so does the velocity of the fluid surface. The viscous force opposing this motion is proportional to the fluid velocity [122] and will eventually become strong enough to prevent further wave growth, as is the case in a damped harmonic oscillator [114]. Another contribution may be due to the variance in the streamer impact location. The impact site of the streamer appears to be somewhat random but still appears to preferentially strike the bubble during its expansion phase rather than during its contraction phase, presumably where E/N is maximum. This tendency may be caused by a feedback mechanism from the already distorted shape of the bubble and surface charge, which distorts the shape of the local field and creates a preferred path for the streamer. In general, a change in the pulse frequency is observed to cause a dramatic decrease in the steady state wave amplitude. At frequencies below 500 Hz, the wave growth is dampened by viscosity, while above 500 Hz, the surface is overdriven, resulting in the chaotic steady state perturbation observed in Figure 4.5.

Another possible contribution to the observed wave growth is a Rayleigh-Taylor instability, as discussed in Section 4.4.2. Using equation 4.6, the growth rate for excited waves with wavelength in the range 1-2 mm is 175-250 s^{-1}, which corresponds to a characteristic growth time in the range 4-6 ms. This time range corresponds to the duration of 2-3 wave cycles suggesting that Rayleigh-Taylor effects may play a role in wave growth. However, a number of things remain unclear. First, the wave growth is observed to be highly sensitive to the streamer pulsing frequency. If the wave growth were due solely to Rayleigh-Taylor, then it would occur over a wide range of frequencies. In addition, it is observed that the wave growth occurs over many cycles (N $\sim$ 20-25), which is much longer than the characteristic growth time calculated above (2-3 cycles). As discussed in Section 4.4.2, gravity may not be the only source of acceleration during this process. It is possible that the sudden

acceleration from the pressure at the streamer head may contribute to the onset of such an instability. Further investigation into the time evolution and frequency dependence of the observed wave growth is necessary.

4.4.4 Capillary Waves Excited on a Thin Needle Tip

The 3-D nature of capillary waves can be better demonstrated by placing the bubble on a thin needle tip electrode, as shown in Figure 3.6. In this arrangement, the needle puts less constraint on the possible wave modes that are allowed to propagate on the bubble surface. Figure 4.10 shows the excitation of a three dimensional capillary wave on a 1 mm bubble due to a single, positive 12 kV pulse. In this case, a sharp needle electrode is plunged directly into the bubble interior. The opposing electrode is the grounded circular plate electrode, held at distance of 4 mm away. The first frame shows the bubble in the immediate aftermath of a single streamer excitation. The faint afterglow of the plasma can be seen at the needle tip. After 70 μs, small amplitude wave structure can be observed forming on the bubble surface. After 600 μs, the capillary wave has reached its maximum peak-to-peak amplitude at $\Delta R = 0.2$ mm, which corresponds to a normalized amplitude of $\Delta R/R_0 = 20\%$. In these images, the three dimensional nature of the capillary waves becomes clear. At 1 ms, the perturbation of the capillary wave has returned to equilibrium. At 1.2 ms, the wave enters the next phase of its oscillation and the perturbations begin to grow again. In this case, the ability to excite large wave amplitude waves using only a single pulse stands in sharp contrast to the slowly evolving wave growth observed in threaded rod attached bubbles. As seen in figures 4.8 and 4.9, waves in those cases were not observed to reach full amplitude until 20 cycles after the initial streamer impact. This observation is unexpected considering that the bubbles attached to the thin needle are considerably smaller than those attached to the plate (by a factor of 10), which means that the surface tension force resisting deformation is up to 10

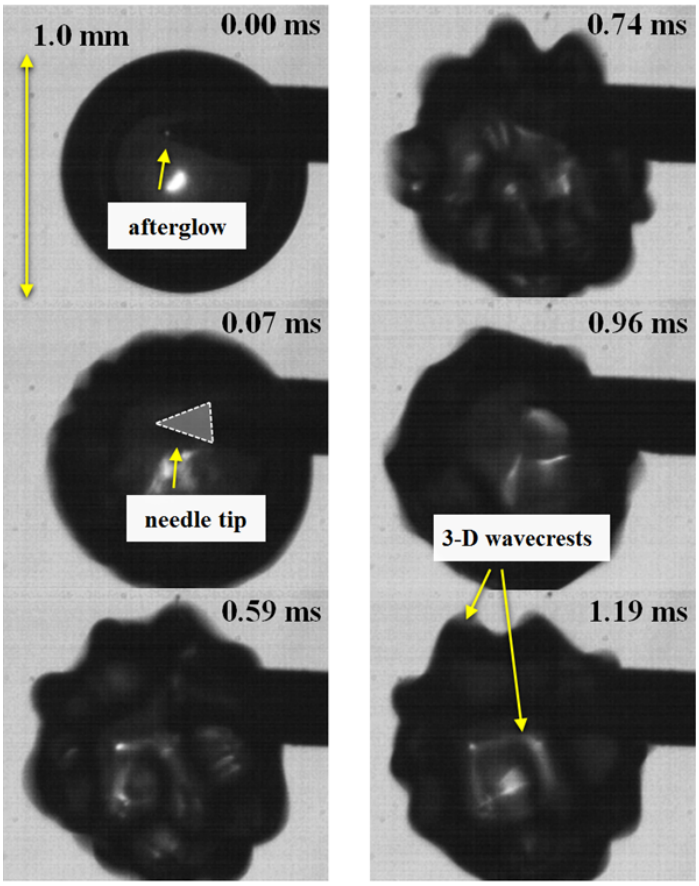

Figure 4.10: Capillary waves excited on a needle electrode using a single 1 μs, 12 kV pulse from the Suematsu supply.

times higher.

There are a number of observations that can explain this discrepancy. First, the small needle attached bubbles are more sensitive to any streamer induced pressure or temperature effects, due to the smaller gas volume available to absorb this energy. Second, the needle electrode produces a much larger electric field at its tip, most likely resulting in a higher field at the streamer tip. This is due to the high curvature of the needle compared to the flat plate. Another possible explanation is a change in the Rayleigh-Taylor growth rate. Since the wavelength of the capillary wave is smaller in the example of the needle ($\lambda \sim 0.4$ mm), the characteristic time for wave growth (see Equation 4.6) will also be shorter. As a result, the characteristic time for instability growth is 2.5 ms in the needle example compared to 4-6 ms for waves

observed in Section 4.4.3. Overall, this discussion indicates that Weber number alone does not determine the resulting wave excitation in the bubble. There may be several other contributing factors, including energy deposition by the streamer as well as Rayleigh-Taylor instabilities excited at the interface.

4.4.5 Wave Coupling Between Bubbles

It is possible to couple streamer induced capillary waves from one bubble to another. Two examples of this phenomena are shown in figures 4.11 and 4.12. In the first example, the attached bubble is excited by streamers pulsed at 500 Hz, 8.5 kV. Times are shown relative to the impact of the streamer. At 1.0 ms, the second bubble has risen up through the action of buoyancy. When it gets close to the attached bubble, it manifests capillary waves of its own. Although the nature of this energy transfer is not fully understood, it may be driven by the propagation of pressure disturbances from the attached bubble through the water. These pressure waves arrive at the second bubble and subsequently excite capillary wave oscillations on its surface. The two bubbles appear to oscillate 90 degrees out of phase from each other. This can be explained by the following argument. As a point on the first bubble extends outward, it pushes the point directly across from it (on the second bubble) inward, resulting in a phase shift between the two waves. The wavelength on the surface of each bubble is shorter than the case observed in figures 4.8 and 4.9 by a factor of about two (0.7-0.8 mm). This indicates the presence of a completely separate mode. The capillary oscillation frequencies for both bubbles, approximately 1000-1250 Hz, are well above the repetition rate of the pulsed discharge. These frequencies are also consistent with those predicted by Kelvins equation. From Kelvins equation, the oscillation frequency for the observed wavelengths should be in the range 950-1150 Hz.

A second example of wave coupling is shown in Figure 4.12. In this example, the

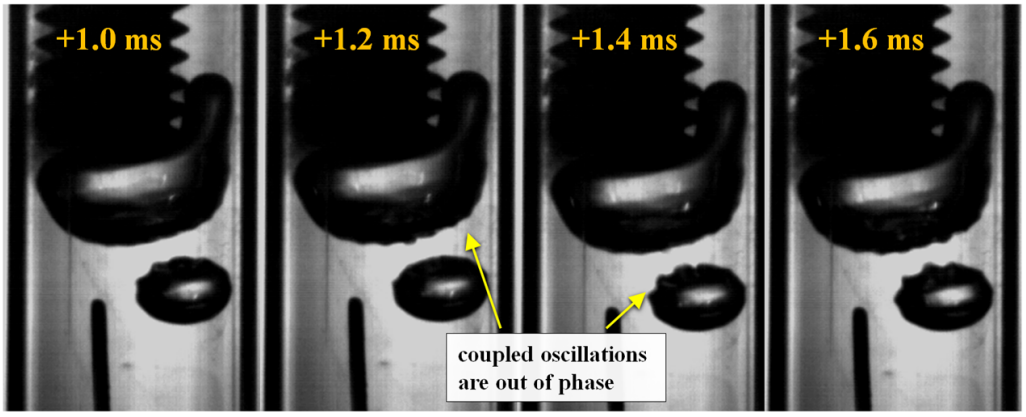

Figure 4.11: A nearby bubble undergoes capillary wave oscillations communicated by the attached bubble. Times are relative to streamer excitation.

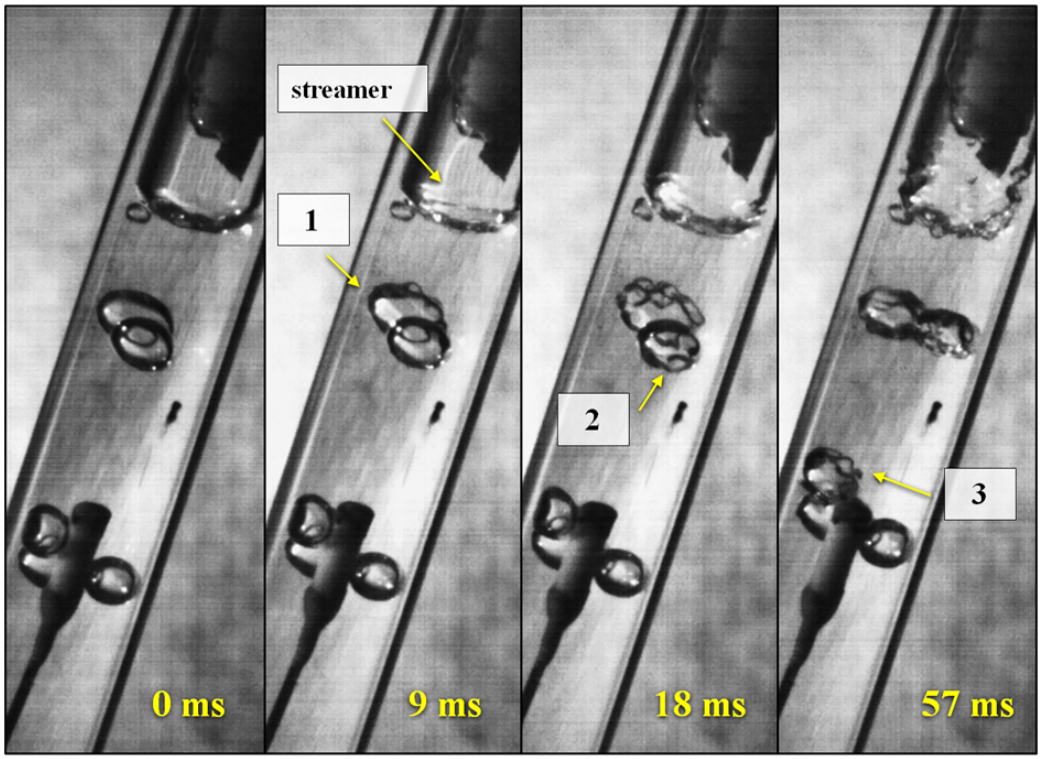

Figure 4.12: Wave coupling can be extended to bubbles up to 2 cm away from the original attached bubble. The excitation of nearby bubbles spreads in time, starting at bubble #1 and eventually reaching bubble #3.

secondary bubble is farther away from the primary attached bubble (3-4 mm). As the wave amplitude of the nearest bubble (labeled 1) increases, it eventually couples to a third bubble (labeled 2), located directly behind it. Eventually this wave excitation spreads all the way to a third bubble (labeled 3) nearly 2 cm away from the original electrode attached bubble. This demonstrates the long distance coupling possible with capillary wave excitation, all of which can be driven electrically vie formation of plasma streamers.

4.4.6 Evaluating the Shape Effect in Capillary Waves

The large wave amplitudes observed in Section 4.4.5 represent a substantial deformation in the curvature of the bubble surface. These deformations should give rise to an analogous distortion of the electric field within the interior of the bubble, according to the shape effect. The capillary wave oscillations observed throughout this chapter have been shown to be topologically complex and do not immediately lend themselves to a simple formula. One method of modeling a 3-D capillary wave is by assuming the wave excitation to be azimuthally symmetric. A wave of this type can be parameterized in spherical coordinates according to the relation,

$$R(\theta) = R_0\big(1 + a\cos(n\theta)\big), \quad n = \text{even} \tag{4.7}$$

In this case, the wave is excited along the direction of the polar angle, θ, with normalized amplitude, a. The wavenumber in this case is given by $k = n/R_0$. As the number of wave crests increases, the wavelength decreases. Accompanying the reduction in the wavelength is an increase in the local curvature of the surface. According to the discussion of Section 2.3.2, the electric field strength in the vicinity of this induced curvature should be highly distorted.

Although this parameterization does not fully capture the three dimensional na-

ture of capillary wave oscillations, it does provide a convenient analytical form for characterizing the effect of changing the bubble curvature on the distortion of the applied electric field. It is reasonable to expect that an increase in both the wave amplitude, a, and the wavenumber, n, will lead to an increase in the enhancement of the field. To prove this hypothesis, the electrostatic solver Maxwell 2-D was used to model the electric field inside an air bubble excited by the 2-D capillary wave parameterization given by equation 4.7. For a detailed description of the electrostatic simulations, see Section 3.6. In this simulation, the bubble was assumed to have permittivity $\epsilon = \epsilon_0$. It was placed inside a liquid medium with $\epsilon_2 = 80\epsilon_0$ and conductivity 20 μS m^1. For simplicity, the applied electric field, $\mathbf{E}_0$, was chosen to be uniform. In the vicinity of the distorted bubble, the electric field will become distorted from the applied field, $\mathbf{E}_0$.

In this simulation, the field is applied in the z direction and the bubble geometry is defined with R-Z symmetry. Figures 4.13 and 4.14 show the simulated field enhancement factor, $G(\mathbf{x})$, that results from independently varying both the wave amplitude, a, (top) and the wavenumber, n, (bottom). The contour map is shown in logscale. Shown at the top of each image is the maximum value of the field enhancement factor, G_{max}, measured inside the volume of the bubble. The wavenumber in the top figure is fixed at $n = 20$, while the amplitude in the bottom figure is fixed at $a = 0.10$. The amplitude was chosen to be consistent with wave amplitudes observed in experiment (see Figure 4.11).

The most immediate observation from the simulated field images is that in areas where the boundary curvature changes, so too does the magnitude of the electric field. This occurs not only at the crest of the excited waves, but also in the contracted gas cavities. This second effect occurs primarily in the cavities that are perpendicular to the field. From the discussion in Section 2.3.2, the applied field induces a surface charge, $\sigma_b = \mathbf{P} \cdot \mathbf{n}$, on the fluid boundary. This charge is maximized when the applied

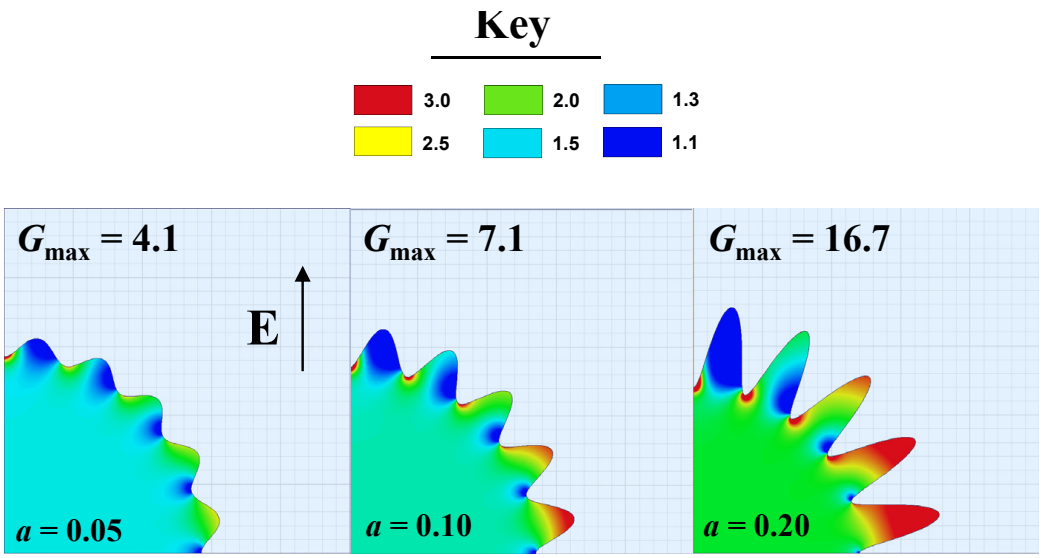

Figure 4.13: Simulation of the electric field enhancement factor, G, in cases where the wave amplitude is varied. The wavenumber is held constant at $n = 20$.

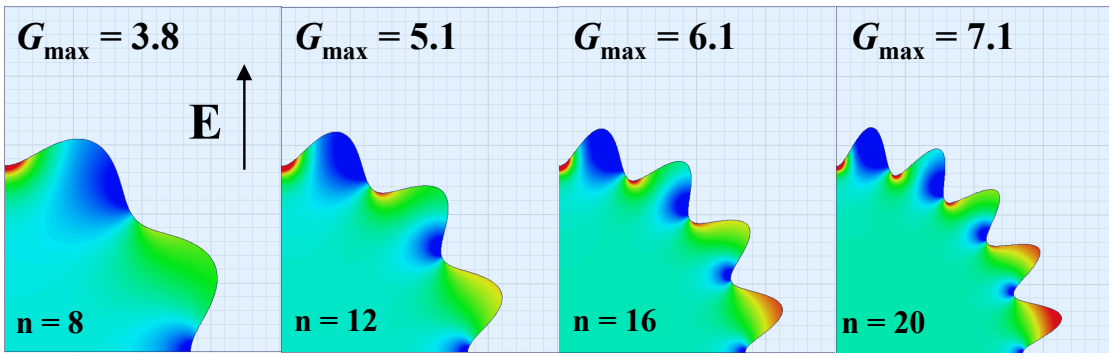

Figure 4.14: Simulation of the electric field enhancement factor, G, in cases where the wavenumber, n is varied. The amplitude is held constant at $a = 0.10$.

field acts normal to the liquid surface. Furthermore, the closer the opposing surfaces are together, the more intense the secondary field will be resulting from the induced charge σ_b. From this perspective, the contracted cavities can be considered individual electrode gaps. As the distance between these gaps decreases, the interior electric field is increased.

Another observation from these simulations is that for constant amplitude, an increase in the wavenumber can still be used to increase the field enhancement. In changing from $n = 8$ to $n = 20$, for example, the maximum field enhancement increases from 3.8 to 7.1. Furthermore, an increase in wavenumber increases the number of cavities exhibiting field enhancement. These properties indicate that substantial field enhancement can be accomplished without achieving impractically large wave amplitudes. The ability to change the wavenumber, as discussed in Section 4.4.3, is dependent on achieving the appropriate resonance condition and hence frequency. Thus one can maximize the field enhancement by choosing the appropriate wave mode.

One disadvantage in obtaining more extreme degrees of curvature is the decreasing scale length over which the field is enhanced. As the wavenumber, n, is increased, the effective electrode gap, d, forming in the gas cavities becomes smaller. The small scale lengths in the these cavities may be too small to realize a useful value of the ionization product, $M \sim \lambda d$. For a bubble of radius 1 mm, the size of these cavities is approximately 0.3 mm. If the original applied field were 10 kV cm^{-1} ($E/N = 180$ Td), for example, the apparent ionization coefficient, λ would be 75 cm^{-1} and the ionization product $M =$ would be 2.25. However, if the applied field is increased to 20 kV cm^{-1} ($E/N = 400$ Td), then the value of λ jumps to over 1000 cm^{-1} and the ionization product in the cavity becomes $M = 30$. Thus it is clear that for the excitation of such high amplitude waves, the critical field for streamer formation becomes more practically realizable. This ionization product can be increased even further if the

same waves can be excited in larger bubbles (>1 mm). From the previous discussion, this would increase the integration path of the growing avalanche and thus increase the ionization product, M. Overall, it is clear that for a given shape and value of the applied field, there is a minimum bubble diameter, d for which the condition $M = 20$ can be satisfied. As the bubble size is decreased, one of two things must change, either the field must be increased, or the enhancement factor must be increased via shape distortion.

As stated in Chapter 2, the use of M as a measure of plasma formation is only an approximation. There are a number of other factors that influence the probability of streamer formation in the bubble. One factor that has not been discussed is the population of seed electrons present in the bubble prior to pulsing. A larger seed population would decrease the necessary avalanche amplification required to achieve the streamer criterion and thus lower the required value of M to below 20. In the case of an underwater bubble, this seed electron population could be provided by the conductivity of the water at the bubble surface. Early avalanche growth could also be affected by the presence of UV radiation.

CHAPTER V

Nonlinear Distortion of Free Standing Gas Bubbles

The results of Chapter 4 demonstrate the viability of using electric fields to excite significant deformation in the shape of the bubble. In these electrode-attached bubbles, plasma formation was achieved at low voltages ($\leq$5 kV). In an ideal device, however, it would be preferable to ignite plasma in bubbles that are isolated from the electrodes. This would not only increase the exposure of the liquid to the reactive species but also reduce energy deposition, and hence erosion, at the surface of the electrode [62].

Having demonstrated the basic principles of bubble distortion–while also reviewing the limitations of the electrode attached geometry–let us now return to the primary focus of this dissertation, *the investigation of plasma formation in bubbles that are isolated from the electrode.* In chapter 3, we introduced the ultrasonic levitation cell, capable of trapping bubbles and generating intense electric fields through the use of underwater electrodes. In this chapter, we will utilize this setup to excite a variety of shape deformations, including the spherical harmonic modes introduced in chapter 2. In this work, analysis of modes will be limited to even shape modes ($l = 0,2,4\ldots$), which are symmetric about the equatorial plane ($\theta = \pi/2$). It will be shown that these modes can be excited by fields that lead to zero net drift, lending them to stable continuous oscillations.

The primary advantage of exciting shape deformations is to demonstrate the shape effect, which is the distortion of the applied electric field resulting from a deformation in the bubble's dielectric boundary. As discussed in Chapter 2, this phenomenon can be exploited to facilitate plasma breakdown in the gas bubble, particularly when it is isolated from the electrode. According to the discussion of Section 2.4.3, this deformation can be maximized by exciting the bubble at any one of the shape mode resonance frequencies, f_l. In order to efficiently couple to these modes, it is also necessary tailor the geometry of the applied electric field, which acts as the source of pressure. It was shown in Section 2.7, that a uniform field is optimal for exciting the dipole mode ($l = 2$). In this chapter, we will use the dipole mode as a starting point, both because a uniform field is straightforward to create in practice and because we know (from Figure 5.9) that the dipole mode is capable of undergoing extreme changes in curvature. It will further be shown that nonuniformity in the applied field will result in the excitation of higher order contributions to the $\ell = 2$ mode, resulting in a host of complex shapes.

In this chapter, the applied field will be provided by a sinusoidally varying voltage, both because it is simple to produce in practice (via the Elgar A.C. power system) and also because it couples naturally to the shape mode oscillations. It was shown in Chapter 2 that the scale of the electrical pressure acting on the boundary of the bubble is proportional to the square of the electric field magnitude ($p_e \sim \epsilon\left|\mathbf{E}\right|^2/2$) [116]. For the case of a uniform A.C. field pointing in the $\mathbf{z}$ direction, the field can be written,

$$\mathbf{E} = E_0 \cos(\omega t)\mathbf{z} \tag{5.1}$$

The scale of the electrostatic pressure is then given by,

$$p_e \sim \frac{1}{2}\epsilon\left|E_0 \cos\omega t\mathbf{z}\right|^2 \sim \cos^2\omega t \sim 1 + \cos(2\omega t) \tag{5.2}$$

Hence, the field pressure, p_e, oscillates at twice the frequency of the applied field. It is also independent of the sign of the electric field, which means that the positive and negative cycle of the applied field give rise to the same stress. Thus, it is important to distinguish between the field frequency f_E and the pressure frequency, $f_p = 2f_E$. Unless stated otherwise, the pressure frequency will simply be referred to as f. This notation will prove to be ideal since it is the pressure tensor, $\mathbf{T}$ (rather than the field) that determines the resulting bubble dynamics.

5.1 Operating Conditions

The modular design of the electrode stage, described in Section 3.2.1, allows a multitude of electrode geometries. The primary geometry chosen to drive bubble distortions was the planar mesh electrodes, shown in Figure 5.1. The mesh wire was 0.25 mm thick with 0.75 mm spacing between each wire, yielding an open air fraction of 0.56. Both mesh electrodes were 1 cm x 1 cm. The electrode gap was varied between 2.5 and 3.4 mm. The use of mesh electrodes served three purposes: (1) the planar geometry provided an approximately uniform electric field within the gap, (2) the reduced surface area minimized conduction current and (3) the high physical trans-

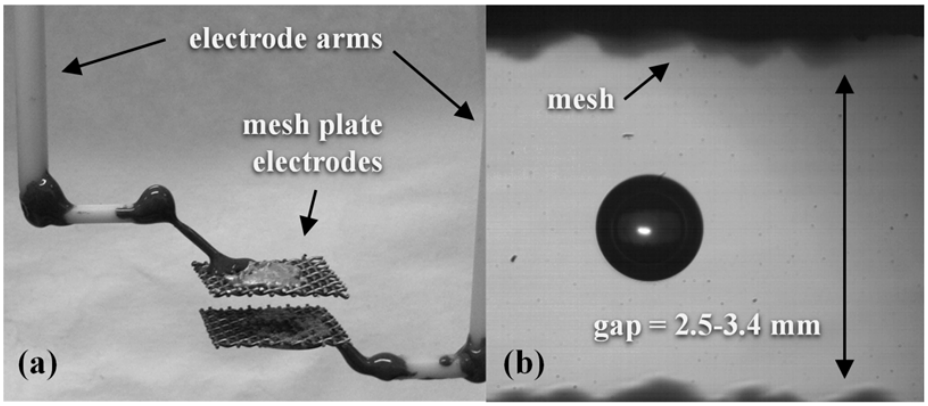

Figure 5.1: (a) Mesh plate electrodes provide an approximately uniform field to drive the suspended gas bubbles. (b) A bubble levitating in between the mesh electrodes. The cross hatching on the mesh is visible.

parency prevented acoustic disruption of the standing wave. The electrode voltage was produced by the Elgar A.C. power system, described in Section 3.3.1. Applied voltages were 3-9 kV peak to peak with frequencies in the range 100-1000 Hz.

All experiments were performed in deionized water in order to minimize the flow of electrical current through the system. The conductivity was measured at the beginning of every experiment and was always less than 10 μS m $^{-1}$. The conductivity was monitored during testing and remained below 20 μS m^{-1} throughout. Bubble oscillations were captured using the Redlake high-speed camera with a nominal frame rate of 5000 frames s^{-1} and an exposure time of 100 μs. The long range telescope lens was maintained in the zoom range of 2-3. Typical bubble diameters documented ranged between 0.2-0.8 mm.

5.2 Excitation of the $\ell = 2$ Mode

We begin with an example illustrating the excitation of the first even shape mode, the $\ell = 2$ mode. It was shown in Chapter 2 that the dipole mode can be specifically isolated by driving the bubble with a uniform electric field, hence the decision to use the parallel plate electrode geometry. Because the mesh grids are not solid, the electric field generated in such geometry has significant nonuniformity. This is primarily due to the finite spacing of the mesh, which at 0.75 mm is comparable to the typical bubble diameter. The vertical misalignment caused by the cross hatching of the mesh, visible in Figure 5.1, also contributes to this nonuniformity. The applied field will consequently vary over the length of the bubble, giving rise to a complex mode structure. Another factor that complicates the mode structure arises from the nonlinearity of the shape distortions, which can cause energy exchange between modes, allowing one mode to grow from another [147].

In this first example, a bubble of radius 0.22 mm is driven by a voltage of amplitude 4.7 kV and frequency of 500 Hz. This corresponds to a pressure frequency, f, of 1000

Hz and a Weber number, W_e of 4.3 ($E_0 = 14$ kV cm^{-1}). The $l = 2$ resonance frequency for a bubble this size is 1550 Hz, which results in the ratio $f/f_2 = 0.66$. Figure 5.2 shows the voltage, current, and Weber number for case 1. The plot of W_e provides an estimate of the time dependent electrical stress relative to the equilibrium surface tension stress ($\gamma/2R_0$). The electric field is estimated as the voltage, V, divided by the electrode gap, d. This estimate provides an upper bound on the possible value of the field acting on the bubble. The overarching goal of this work is to distort the bubble with the minimum possible energy, and hence field strength. This estimate therefore serves as a worst case scenario. The resistance of the water gap was measured to be approximately 50 kOhm. This is an order of magnitude lower than that expected for a parallel plate geometry, indicating an error in the assumption that the fields are uniform. This nonuniformity may be a result of the higher electric fields near the thin wire surface of the mesh as well as lower fields in the gap between the electrodes. The increased field at the electrode surface would lead to higher ohmic currents delivered to the surface and thus a lower resistance than would be measured in a parallel plate geometry. This discussion also neglects the effects of electrolysis, which might cause further deviation from Ohm's law.

The fields at the surface of the thin mesh wire are most likely higher than that of the hypothetical uniform field (V/d) and therefore collect a higher current density. It is also likely that the backside of each mesh, being uncovered, participates significantly in current collection. The observed deviation of the voltage and current signals from sinusoidal dependece is due to the diminished performance of the high voltage transformer when operated near the lower limit of its frequency range (400 Hz). This distortion generates a pressure signal possessing a sharper rise time than an A.C. signal.

Figure 5.3 shows images of a typical oscillation cycle for the $l = 2$ mode, beginning at t = 12.48 ms. As the field amplitude increases, the bubble is stretched along the

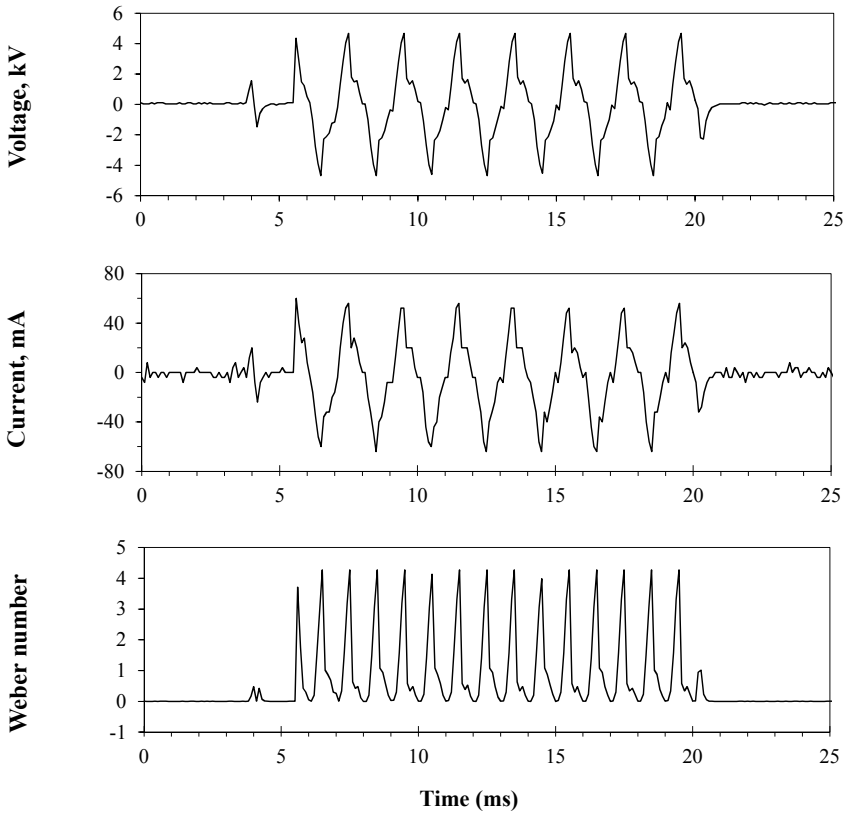

Figure 5.2: The applied voltage, current and normalized electric field pressure used to drive $\ell = 2$ mode oscillations of the levitated bubble in case 1.

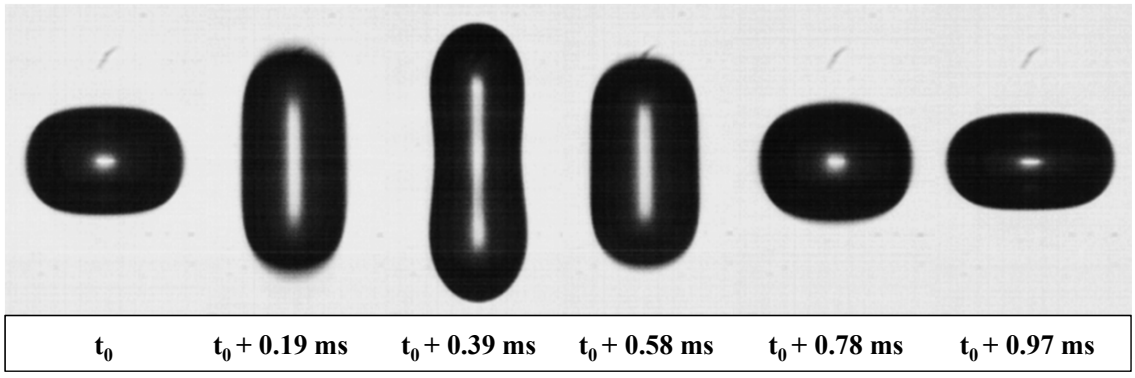

Figure 5.3: A typical cycle of the $\ell = 2$ mode beginning at t = 12.48 ms. The equilibrium bubble diameter is 0.43 mm.

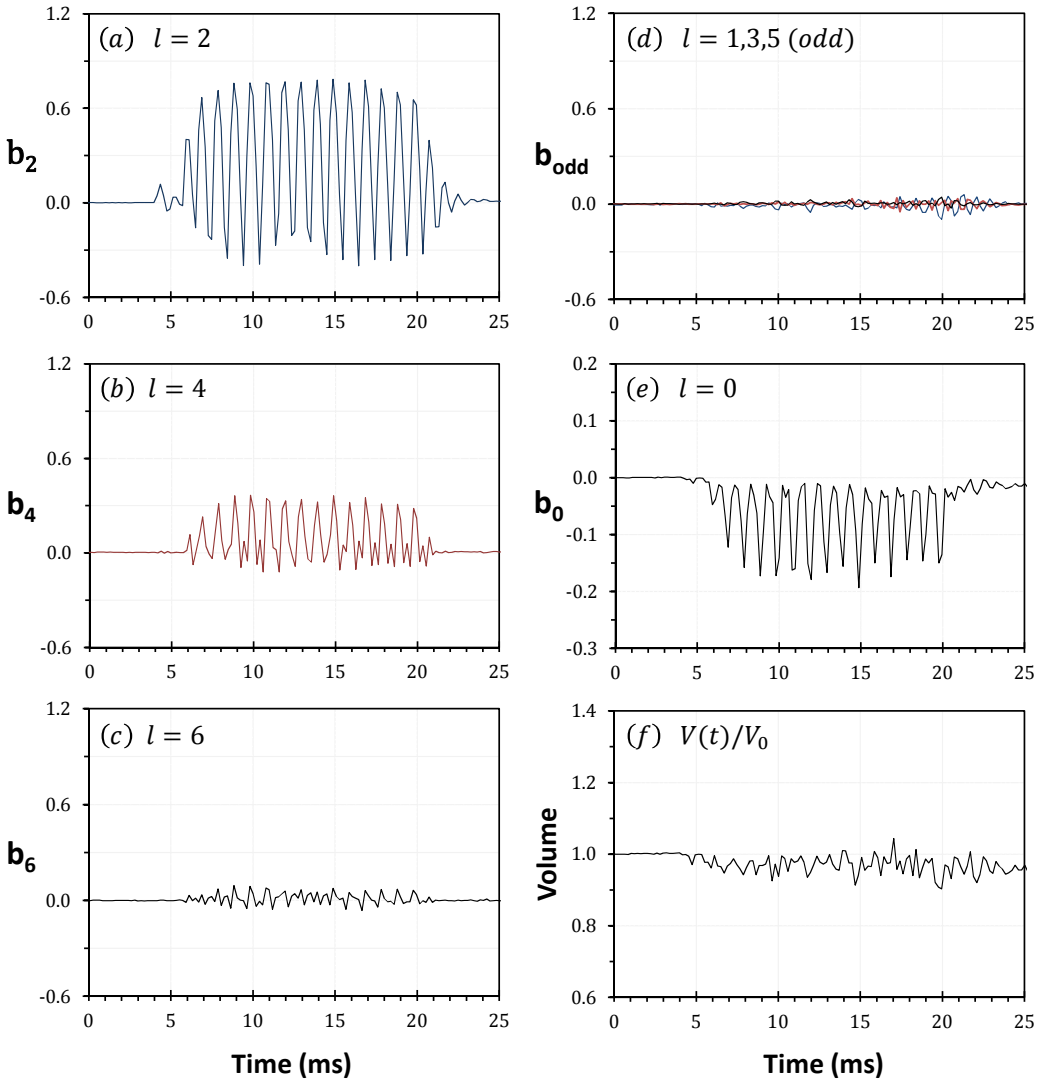

Figure 5.4: Shape mode analysis for a bubble oscillating in the $l = 2$ mode. The left column shows even coefficients, from top to bottom, (a) b_2, (b) b_4, and (c) b_6. The right column shows (d) odd coefficients b_1, b_3, b_5, (e) volume mode coefficient b_0 and (f) the normalized volume.

direction of the field. As it stretches vertically, the bubble's sides contract inward, as is consistent with the $\ell = 2$ mode when $b_2 > 0$ (see Figure 5.9). As the pressure subsides, the bubble relaxes, eventually overshooting its equilibrium position. The inertia gained from this relaxation causes the bubble to compress inward, which is consistent with $b_2 < 0$. This compression is not the result of the field pressure, which is unipolar and can only stretch the bubble. Instead, it results from inertia gained by the bubble as its surface tension forces it back to equilibrium. The shape mode analysis for case 1 is shown in Figure 5.4. The plots in the left column show the first three even modes (a) b_2, (b) b_4, and (c) b_6 while part (d) shows the odd modes b_1 , b_3, and b_5 . The mode b_0 is shown in (e) while the bubble volume, calculated with equation 3.12, is shown in (f).

It is apparent that only the even modes are nonzero. This is due to the shape of the applied field and resulting pressure, which are symmetric (even) about the equatorial plane ($\theta = \pi/2$). The deformation resulting from this pressure will also be symmetric. It can be shown that modes corresponding to symmetry about the equatorial plane are exactly the even shape modes ($\ell = 0, 2, 4, 6...$) [119]. Parts (a)-(c) indicate that multiple even modes are present, with the dominant contribution coming from $\ell = 2$. The prominent modes, b_2 and b_4 oscillate at the same phase and frequency. Fourier analysis indicates that this frequency is near 1000 Hz, the frequency of the applied pressure. Overall, strong excitation of the $\ell = 2$ mode was observed for a wide range of, f, with b_2 always in sync with the applied pressure. The strongest excitation of b_2 was observed not at $f/f_2 = 1$, the expected resonance, but instead over the range $f/f_2 = 0.5$-0.7. This is consistent with previous work on nonlinear bubble oscillations [148], which reported a similar mismatch between linear and nonlinear resonance phenomena. One possible contribution to this discrepancy is the effect of viscosity, which will tend to alter the true resonance frequency from that given in equation 2.31.

The volume mode, b_0, shown in Figure 5.4(e), also oscillates at the applied frequency, but is negative. Figure 5.4(f) shows that the volume is approximately constant throughout the oscillation, indicating that the growth of the even modes (b_2, b_4, b_6) is exactly countered by the contraction of the volume mode, b_0. From this result, one can speculate that the field strength is too small to provide the thermodynamic work necessary to expand the bubble. Further discussion of this effect follows in Section 5.6

5.3 Excitation of the $\ell = 4$ Mode

As observed in Section 5.2, the $\ell = 2$ mode is dominant over a broad range of frequencies and can be strongly excited even when $f/f_2 \neq 1$. The nonuniformity of the applied field allows the possibility of higher order modes, which should appear when the pressure frequency, f, approaches the higher order values of f_l. In particular, as the frequency is increased well above f_2 and approaches f_4, visual evidence of the $\ell = 4$ mode should emerge. In the next example, the applied frequency remains the same (500 Hz) but the bubble radius is increased to 0.32 mm, resulting in higher relative frequencies, $f/f_2 = 1.25$ and $f/f_4 = 0.45$. Figure 5.5 shows the applied voltage, current, and normalized pressure.

The driving pressure signals are very similar to Figure 5.2, except that the Weber number is now lower. Figures 5.6 and 5.7 show, respectively, a typical oscillation cycle for case 2 and the accompanying shape mode analysis. A close look at Figure 5.6 reveals that the $\ell = 4$ mode is present but is superimposed over the still dominant $\ell = 2$ mode. It was observed that neither an increase in the frequency (such that $f/f_4 \sim 1$) nor an increase in the electric field pressure were capable of generating oscillations dominated by the $\ell = 4$ mode. This indicates the strong role that field geometry and symmetry play in the excitation of these modes. In this case, the approximately uniform field will always excite the $\ell = 2$ mode to some degree. To

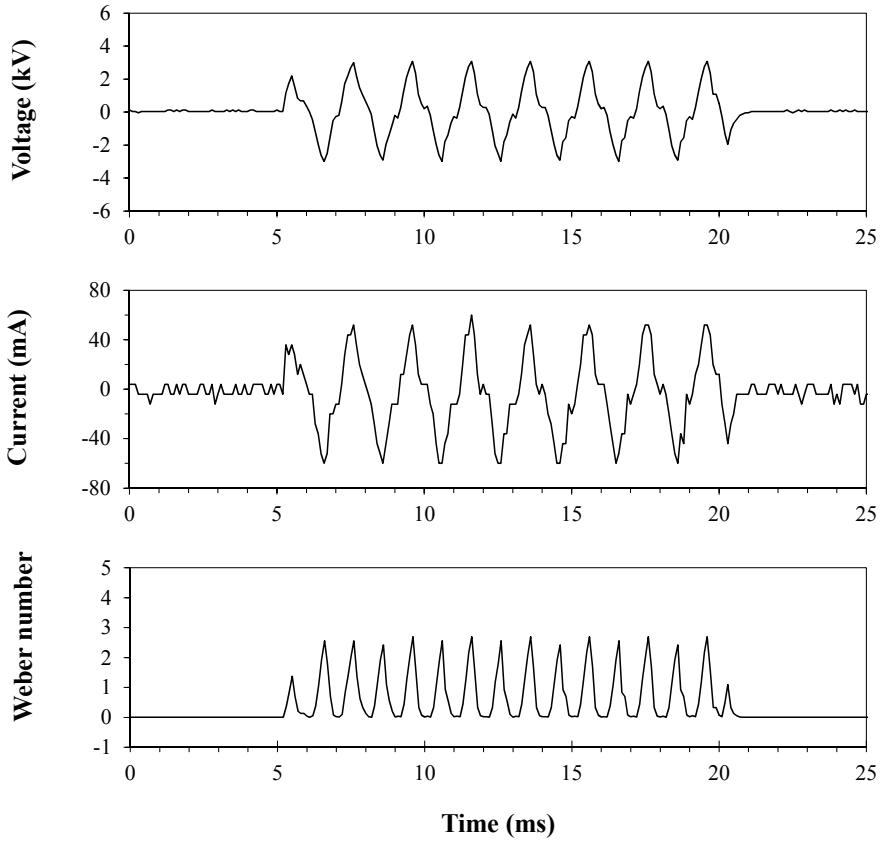

Figure 5.5: The applied voltage, current and normalized electric field pressure used to drive $\ell = 4$ mode oscillations of the levitated bubble in case 2.

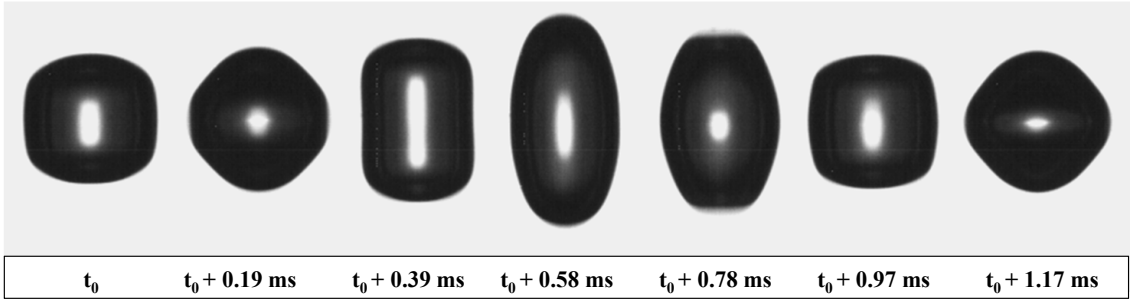

Figure 5.6: A typical cycle of the $\ell = 4$ mode beginning at t = 15.40 ms. The equilibrium bubble diameter is 0.65 mm.

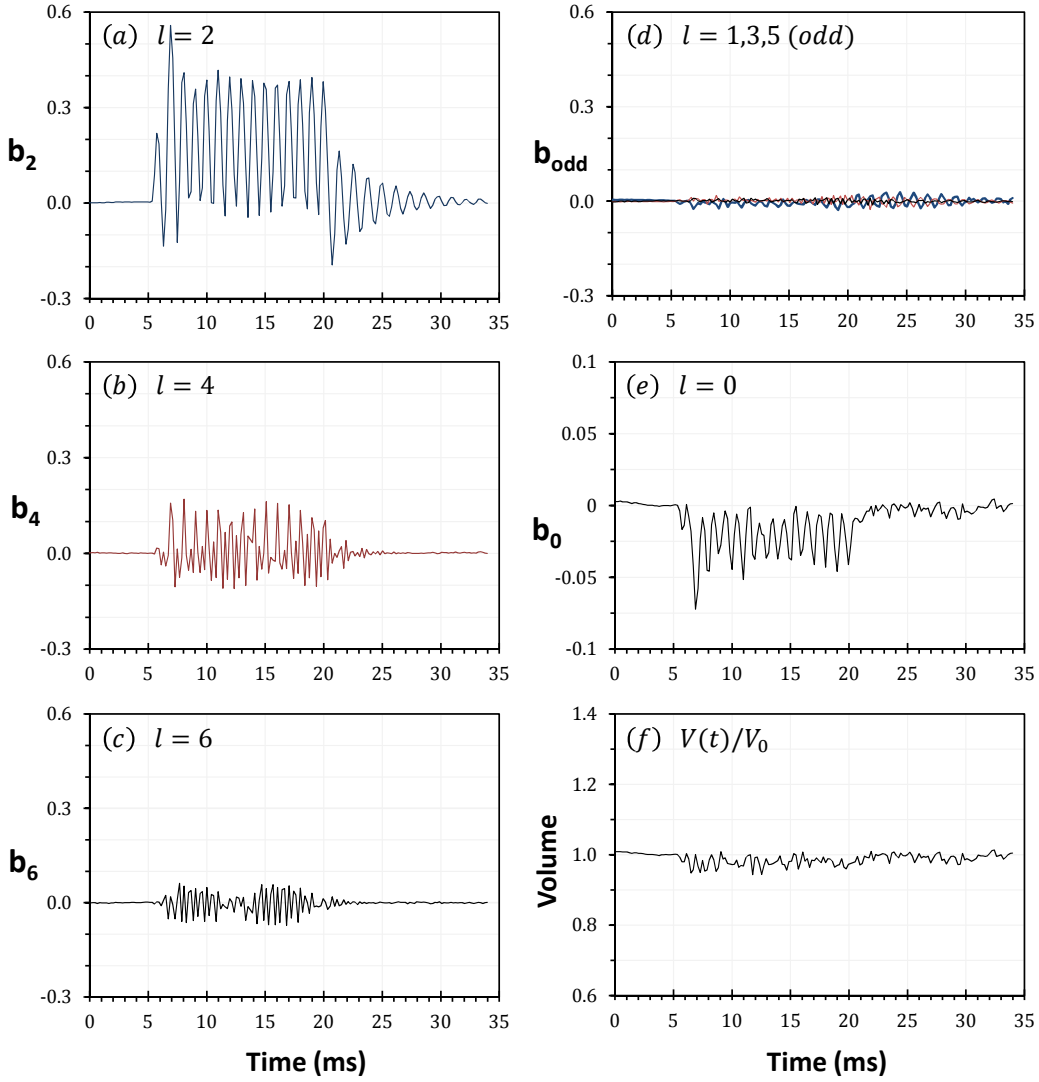

Figure 5.7: Shape mode analysis for a bubble oscillating in the $l = 4$ mode. The left column shows even coefficients, from top to bottom, (a) b_2, (b) b_4, and (c) b_6. The right column shows (d) odd coefficients b_1, b_3, b_5, (e) volume mode coefficient b_0 and (f) the normalized volume.

isolate the $\ell = 4$ mode, a different field geometry is required. Work by Bellini [120] indicates that a quadrapole field configuration would be optimal due to its particular form of symmetry.

5.4 Evaluating the Field Enhancement in Spherical Harmonic Deformations

In Chapter 4, it was shown that the intense curvature generated by high amplitude capillary wave oscillations gave rise to field enhancement inside the bubble. This was demonstrated by simulating the electrostatic field inside a deformed gas bubble. We now perform the same analysis on gas bubbles deformed by the spherical harmonics. As with the approach taken in Section 4.4.6, the shape effect is evaluated by the simulating the distortion of a uniform field electric field applied across the body of the deformed bubble. In this case, the axisymmetric spherical harmonic modes fit naturally into the R-Z symmetry used in the Maxwell model. Due to the slow timescales associated with the fluid motion of the bubble ($\sim$1 kHz), the evolution of the electric field can be considered quasistatic [116]. Thus, to good approximation, one can estimate the field enhancement occurring at any instant as that due to a D.C. electric field. This approximation provides a simple, tractable way of evaluating the shape effect in bubble shapes observed by experiment. Before examining field simulations in such bubbles, it will be helpful to consider the example of a dielectric ellipsoid, which is an extension of the dielectric sphere example discussed in Chapter 2.

5.4.1 The Dielectric Ellipsoid: A Guide to Field Enhancement

In Chapter 2, the dielectric sphere served as a basic example for computing the electric field in the bubble along with the stress acting on its boundary. In that

discussion, no mention was made of how the internal bubble field would evolve under a perturbation of the bubble surface. A convenient starting point to address this question is the example of the dielectric ellipsoid, which itself represents a stretching and a compression of the sphere according to a tractable parameterization. More importantly, as will be shown next, the electric field inside the ellipsoid is completely solvable when the applied field is uniform, just like in the case of a sphere. In the following analysis, the ellipsoid will be defined as follows. Let the ellipsoid's major axis (along z) coincide with the applied field, $\mathbf{E}_0$, and let the two perpendicular axes be equal. The resulting ellipsoid is axisymmetric about the applied field and its surface is defined by the following equation [119],

$$\frac{x^2 + y^2}{a^2} + \frac{z^2}{c^2} = 1 \tag{5.3}$$

Just as in the case of the axisymmetric shape modes, the ellipsoid shape is reduced to two dimensions. It can also be written in symmetric spherical coordinates [119],

$$R(\theta) = \sqrt{a^2 \cos^2\theta + c^2 \sin^2\theta} \tag{5.4}$$

It can be shown that the ellipsoid is equivalent to the first even spherical harmonic mode, $l = 2$, up to 1st order. To prove this, define the eccentricity, ε, of the ellipsoid by the equation $\varepsilon^2 = 1 - c^2/a^2$. Next, expand equation 5.4 to 1st order in ε^2 using a

Taylor expansion and substitute for the appropriate Legendre polynomials.

$$\begin{aligned} R(\theta)/a &= \sqrt{\cos^2\theta + (c^2/a^2)\sin^2\theta} \\ &= \sqrt{\cos^2\theta + (c^2/a^2)(1-\cos^2\theta)} \\ &= \sqrt{1+\varepsilon^2\big(\cos^2\theta - 1\big)} \\ &= \Big(1 + \frac{\varepsilon^2}{2}\big(\cos^2\theta - 1\big)\Big) + O(\varepsilon^4) \\ &= \Big(1 - \frac{\varepsilon^2}{3}\Big)P_0(\theta) + \Big(\frac{\varepsilon^2}{3}\Big)P_2(\theta) + O(\varepsilon^4) \end{aligned} \tag{5.5}$$

Understanding the electric field in an ellipsoid, therefore, should provide a good starting point for the investigation of field distortion in experimentally excited bubble modes. For an ellipsoid of permittivity, ϵ_1, resting in a dielectric medium, ϵ_2, it can be shown that the electric field inside the bubble is uniform and proportional to the applied field, $\mathbf{E}_0$ [128],

$$\mathbf{E}_1 = \Big(\frac{1}{1+sL_{z0}}\Big)\mathbf{E}_0 \tag{5.6}$$

The quantities s and L_{z0}, which are independent of position, can be written in closed form [128],

$$s = \frac{\epsilon_1 - \epsilon_2}{\epsilon_2} \tag{5.7}$$

$$\begin{aligned} L_z(e) &= \Big(\frac{1}{e^2} - 1\Big)\cdot\Big(\frac{1}{2e}\ln\frac{1+e}{1-e} - 1\Big), \qquad e = \sqrt{1-a^2/c^2},\ (a<c) \\ L_z(\delta) &= \frac{1}{\delta^2} - \frac{\sqrt{1-\delta^2}}{\delta^3}\arcsin\delta, \qquad \delta = \sqrt{1-c^2/a^2},\ (a>c) \end{aligned} \tag{5.8}$$

The quantity, L_{z0} is called the depolarization integral and provides a geometric indication of how distorted the curvature of the ellipsoid surface has become. The quantity, s, on the other hand, is a material property that describes the difference in permittivity between the two media. Upon examining equation 2.13, it is clear that, s, should be considered a measure of the net surface charge induced on the deformed surface. From equation 5.6, it is clear that $G(\mathbf{x})$ is constant throughout the volume

of the ellipsoid,

$$G(\mathbf{x}) = \frac{\left|\mathbf{E}_1(\mathbf{x})\right|}{\left|\mathbf{E}_0\right|} = \left(\frac{1}{1 + sL_{z0}}\right) \tag{5.9}$$

In the case of a gas bubble submerged in water, G can be plotted solely as a function of the aspect ratio, c/a. Figure 5.8 shows the resulting values of the enhancement factor, G, for $0.01 \leq c/a \leq 10$. For large values of c/a, the bubble resembles a long thin needle aligned with the field. In this case, the enhancement factor approaches unity, and the internal field approaches the value of the applied field. For $c/a = 1$, the bubble is a sphere and $G \approx 3/2$, as predicted by the dielectric sphere example from Section 2.6. For small values of c/a, the bubble is compressed into a thin flat, "pancake" shaped disk. As $c/a \to 0$, the enhancement factor asymptotically approaches ϵ_2/ϵ_1 [128], which for a bubble in water is 80. This optimal enhancement, however, is only achieved at an extreme aspect ratio. An enhancement of 70, for example, requires $c/a = 0.001$. For an aspect ratio that is more in line with distortion documented in literature [124], such as $c/a \sim 0.1$, the enhancement is reduced to $G = 6.7$. It is clear that the distortions of the ellipsoid give rise to a significant enhancement of the internal electric field, but one that comes at the cost of extreme deformation. The spherical harmonics, on the other hand, provide a source of much more exotic curvature, as observed in Section 2.4.3. Let us now examine the electric field distortion occurring in the spherical harmonic deformations, starting with those observed in experiment.

5.4.2 Electrostatic Simulation of the Field in Observed Bubbles

The simulation of experimental data was first performed on four characteristic bubble shapes, shown in Figure 5.9. These shapes represent the most extreme excitation of the two dominant modes achieved experimentally, using the techniques of Sections 5.2 and 5.3. The first two frames show the $\ell = 2$ mode at (a) maximum negative distortion (b_2 = -0.424) and (b) maximum positive distortion (b_2 = 0.683)

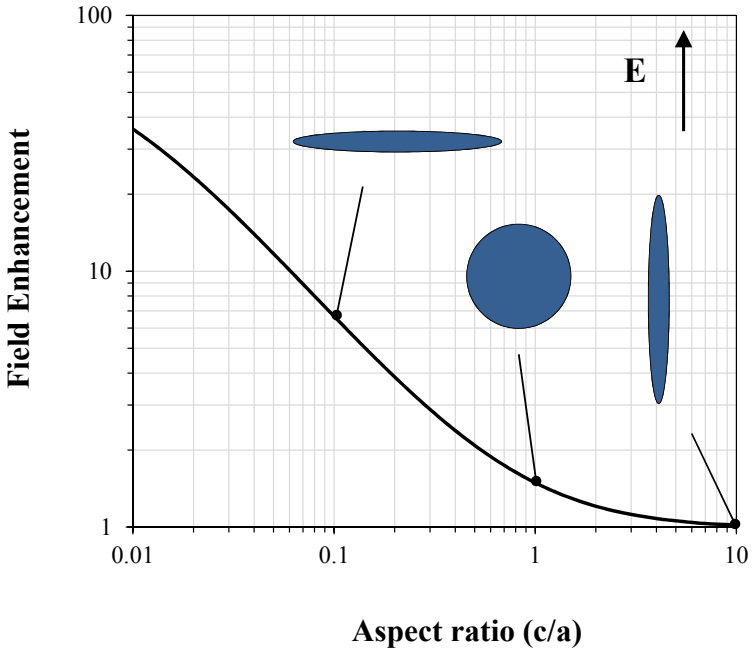

Figure 5.8: The electric field enhancement inside an axisymmetric ellipsoid air bubble. The quantities c and a represent the dimensions parallel and perpendicular to the field respectively. From left to right, the displayed shapes represent $c/a = 0.1, 1, 10$.

while the next two frames show the $\ell = 4$ mode at (c) maximum negative distortion (b_4 = -0.101) and (d) maximum positive distortion (b_4 = 0.067). As described in Section 5.3, the $\ell = 4$ mode was difficult to excite in isolation, and therefore exhibited less severe distortion. In each of the four cases, the discrete spherical harmonic

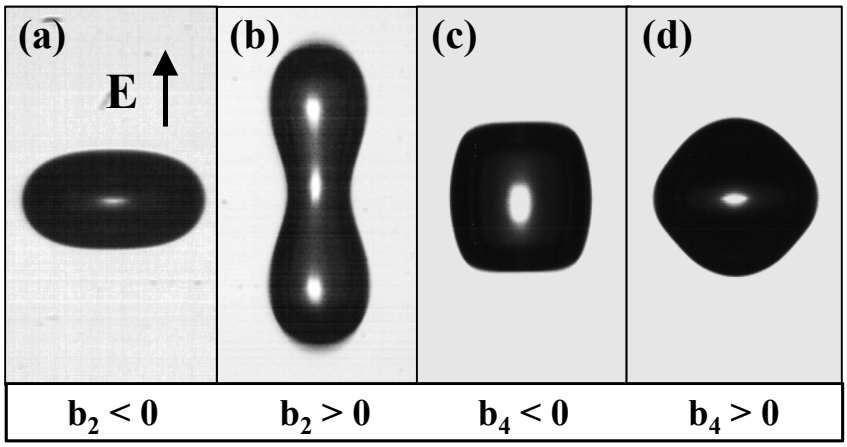

Figure 5.9: Four examples illustrating large excitation of the two dominant modes, (a) b_2 = -0.424, (b) b_2 = 0.683, (c) b_4= -0.101 and (d) b_4= 0.067. The simulated field was oriented as shown.

fit obtained through equation 3.11 was used to specify the shape boundary. The air bubble was modeled with a permittivity equal to vacuum. The water was assumed to be deionized water with conductivity and relative permittivity set at 20 μS m^1 and 80 respectively. Both were chosen to replicate the experimental conditions. Solutions were achieved with an energy error of less than 0.005% within 20−22 iterations. The computed electric field distributions are shown in Figure 5.10, with all values normalized to the external applied field. These values represent the position dependent enhancement factor inside the bubble, namely, $G(\mathbf{x}) = \left|\mathbf{E}(\mathbf{x})\right| / \left|\mathbf{E}_0\right|$. As a reference point, define G_0 to be 1.5, the enhancement for an unperturbed sphere.

In both examples of the $\ell = 2$ distortion, the electric field was observed to deviate from the undeformed equilibrium G_0. For $b_2 < 0$, the field magnitude was enhanced above G_0, with a maximum of 2.3 at the top axial ends. In contrast, for $b_2 > 0$, the

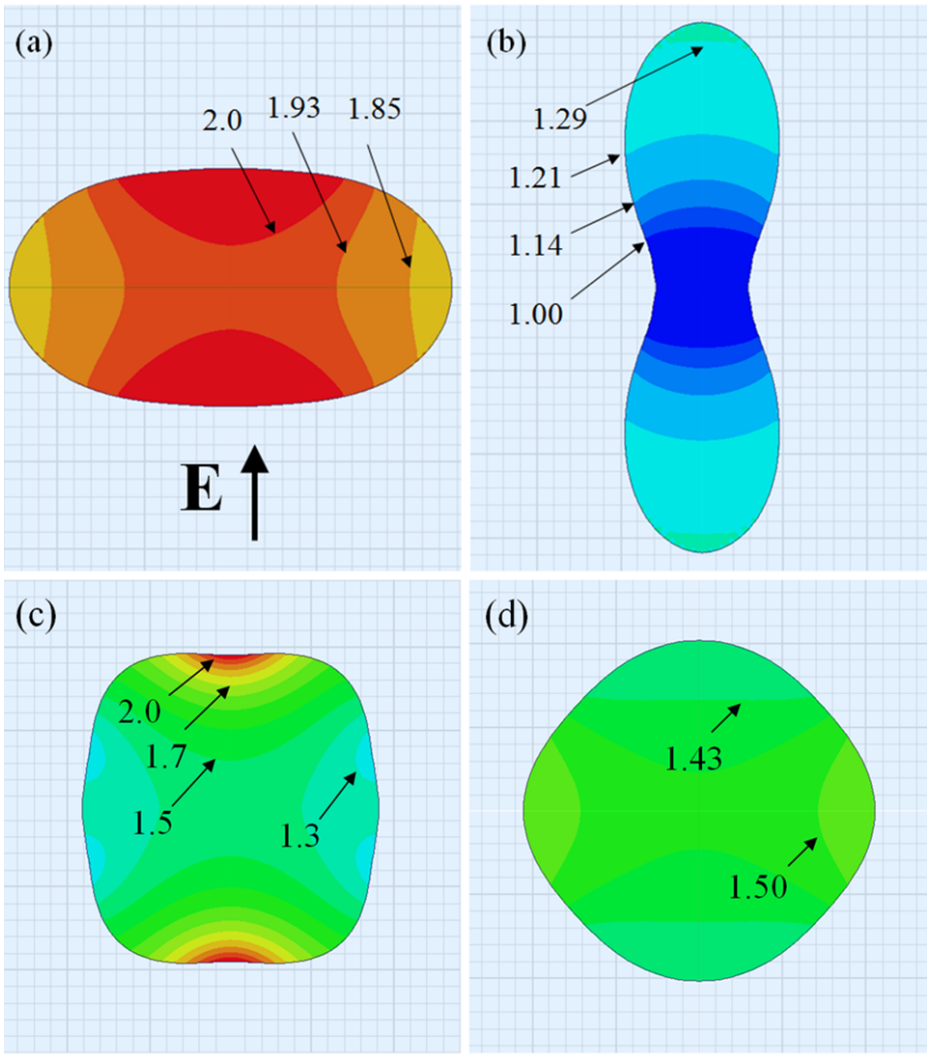

Figure 5.10: The enhancement factor G calculated for the four characteristic images in Figure 5.9. The value $G_0 = 1.5$ (in green) corresponds to the enhancement in an unperturbed sphere. Labels indicate the value of G at the boundary between two colors.

field was depressed below G_0, with a maximum field of 1.3 at the axial ends and a minimum field of 1.0 at the center of the bubble. If the two shapes are viewed as deformed ellipsoids, then the results are logically consistent with Figure 5.8. Case (a) is similar to a flattened ellipsoid, which results in field enhancement, while case (b) resembles a stretched needle, which results in field depression. The primary deviation from the ellipsoidal shape is the localized contraction of the bubbles sides in a manner characteristic of $b_2 > 0$. However, this local contraction does not appear to produce any appreciable distortion of the field.

The cases of (c) $b_4 < 0$ and (d) $b_4 > 0$ are shown in the bottom row of Figure 5.10. The smaller deviation of G in these cases can be attributed to the small values of b_4. Nonetheless, these results indicate a pattern that is similar to the case of $\ell = 2$; the negative coefficient results in field enhancement while the positive coefficient results in field depression. The largest field enhancement, for $b_4 < 0$, occurs at the axial ends and is 2.1. The lowest magnitude occurs for $b_4 > 0$ and is 1.4. Despite the experimental observation of significant mode excitation for both $\ell = 2$ and $\ell = 4$, the resulting field distortion does not appear to be enhanced more than 53% above the baseline value of the sphere, G_0. Overall, the highest enhancement occurs when the bubble diameter contracts in the direction of the applied field. Extrapolating from this observation, one can speculate that for large negative values of the mode coefficients (see Figure 5.9), the field enhancement might be more extreme.

5.4.3 Electrostatic Simulations in Pure Spherical Harmonic Modes

It is possible to simulate the field enhancement for extreme spherical harmonic perturbations using the same electrostatic model. Consider now stationary bubbles in a uniform field, deformed into individual spherical harmonic modes. One can alter both b_2 and b_4 separately to determine the field enhancement in the limit of severe distortion. To simulate deformations that are physically consistent, each shape was

deformed at constant volume. This required that the volume mode coefficient, b_0, be altered slightly. In all such cases, it was altered no more than to the value b_0 = -0.22. This constraint is consistent with the shape analysis in figures 5.4 and 5.7, in which b_0 exhibited negative values when b_2 or b_4 were nonzero.

Figure 5.11 shows contour maps of the field enhancement in the bubble for the $l = 2$ and $l = 4$ mode respectively. On the following page, Figure 5.12 shows the corresponding 1-D field profiles along the axial centerline of the bubble, with the coefficient b_2 or b_4 labeled beside each curve. As discussed in section 5, the symmetry of the applied field allows one to reduce the problem to a quarter of the bubble. In Figure 5.12, each case begins at $z = 0$, the center of the bubble, and extends out axially along the centerline up to the bubble boundary, where the field experiences a sudden drop-off due to the large permittivity jump from gas to liquid. The field immediately outside the bubble is substantially below the applied value, 1.0, but increases with distance away from the bubble and approaches 1.0 asymptotically. The dotted line represents the case of the sphere, in which b_2 and b_4 are zero. In these cases the field enhancement inside the sphere is uniform and given by $G_0 = 1.5$, as expected from theory.

The simulations in Figure 5.12 appear to be consistent with those in Figure 5.10. When either coefficient b_2 or b_4 is positive, the field is predominantly lower than G_0. As both coefficients become more negative, the air gap within the bubble contracts and the field becomes amplified much higher than G_0. In the extreme case of b_2 = -0.8, for example, the bubble contracts to 20% of its original radius and has a maximum field enhancement of $G = 50$ near the edge of the bubble. From this perspective, the bubble can be thought of as a flexible electrode gap. As we decrease the electrode gap spacing, the voltage drop per unit length decreases. The relationship holds because the electric field in the water (in the vicinity of the bubble) is depressed far below its value at infinity. This is due to the induced dipole moment of the distorted bubble,

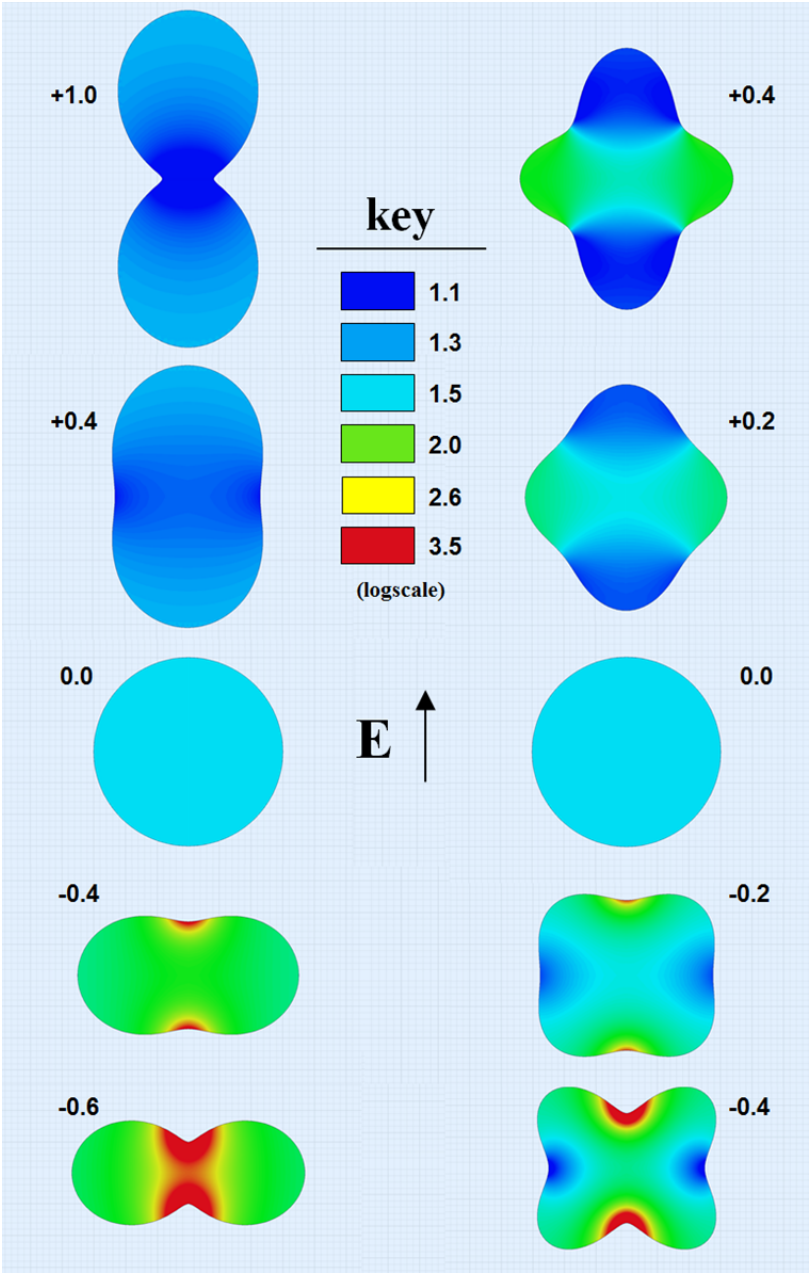

Figure 5.11: Contour maps showing the enhancement factor of the applied electric field in log scale. The field is enhanced substantially in areas where the bubble is compressed in the direction of the applied field.

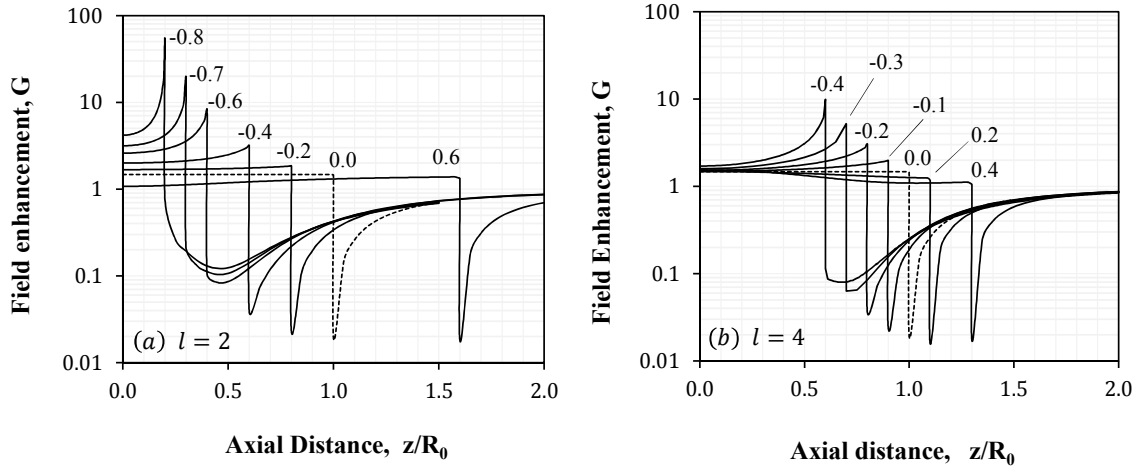

Figure 5.12: Axial profile of the field enhancement factor, G, inside a gas bubble subjected to excitations of the (a) $\ell = 2$ mode and (b) $\ell = 4$ mode. The coefficient value, b_2 or b_4, is labeled beside each curve.

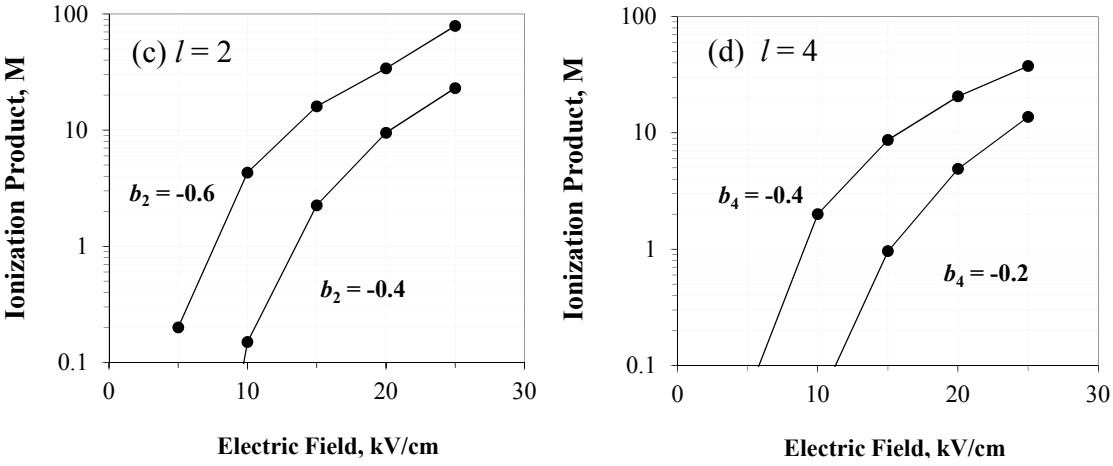

Figure 5.13: The ionization product, M calculated in 1 mm air bubbles for hypothetical values of the electric field strength. The integral is taken along the centerline of bubbles deformed by the $l = 2$ mode (left) and $l = 4$ mode (right). The mode coefficient is labeled beside each line.

which enhances the field inside but decreases the field outside. Thus, the majority of the voltage drop occurs in the bubble and the condition $E_{avg} \cdot d$ can be assumed to be approximately constant. If we decrease d, the average field, E_{avg} must increase.

Overall, Figure 5.12 shows that for an electric field aligned with the bubbles axis of symmetry, large negative mode coefficients result in the strongest enhancement of the applied field. This enhancement is local and confined to regions where the bubbles shape undergoes extreme contraction. This contraction can result in the complete inversion of the water surface into a conic structure, closely resembling a thin conducting tip. Such localized behavior can be contrasted with the ellipsoids presented at the beginning of section 5.1, which require elongation or compression of the entire bubble shape in order to achieve comparable values of G. It is also clear that the orientation between the direction of bubble contraction and the applied field is important in obtaining field enhancement.

The normalized enhancement factors calculated in Figure 5.12 can be used to estimate the integrated ionization coefficient inside the deformed bubbles. In Chapter 2, this was termed the ionization product, M, defined as,

$$M = \int_{\ell} \lambda(\mathbf{x})\ d\mathbf{x} = \int_{\ell} (\alpha - \eta)\ d\mathbf{x} \tag{5.10}$$

The models of λ presented in Chapter 2 were used to estimate the ionization product, M, along the centerline of the bubble interior. The bubble radius was chosen to be 1 mm, which is typical of experimentally observed bubbles. Figure 5.13 shows the ionization product for the two most negative coefficients for the $l = 2$ mode (left) and the $l = 4$ mode (right). The coefficients are labeled beside each curve. In both cases, the extreme field enhancement observed in the most highly compressed modes results in the highest ionization product. In addition, a dramatic change in the ionization product occurs when the applied field is varied from 10 kV cm^{-1} to 20 kV cm^{-1}. The

results are quite similar to those observed in capillary wave simulations presented from Chapter 4. For bubbles in the mm range, and enhancement factors obtained from simulation ($G = 2$ - 10), the ionization product increases dramatically over the range 10-20 kV cm^{-1}. It is only at the highest level of deformation and largest field that M approaches the Meek condition for streamer formation given in Chapter 2 ($M \sim 20$). In the case of spherical harmonic modes, however, the degree of deformation required to satisfy the streamer criterion is extremely high. The value of the mode coefficients required to accomplish this is much larger than anything achieved in practice thus far (see Section 5.9). In smaller bubbles ($R_0 < 1$ mm), the degree of deformation required would be even more extreme due to the increasingly small bubble path length over which M is calculated. Thus, for bubble sizes below 1 mm, an even larger applied electric field would be required.

Despite these issues, the electrostatic simulations presented in this chapter indicate that distortion of the bubble shape may be capable of substantially increasing the value of the ionization product in the bubble. For comparison, the calculated value of M for an unperturbed sphere in the range 10-20 kV cm^{-1} results in values of M approximately in the range 0.1-1. These values are considerably lower than those displayed in Figure 5.13 for the case of distorted bubbles.

5.5 Bubble Deformation Under Extreme Electric Fields

Electrostatic simulations indicate that highly distorted bubble shapes give rise to substantial enhancement of the applied electric field inside the bubble. It is unclear if such extreme deformation can be achieved in practice, particularly with electric fields as the driving source. Ultimately, the goal of this research is to provide guidance for the development of a practical plasma reactor. The largest field enhancement observed in Section 5.4.3 occurs in cases where the bubble undergoes extreme contraction. The main difficulty in achieving this in practice is the tendency of the electric field

to stretch the bubble rather than compress it. In fact, as we showed in Section 5.2, compression arises not from the stress of the field but from the inertia gained during the bubble's relaxation back to equilibrium. One could imagine that a larger compression could be achieved by simply inducing a larger expansion, thus giving the bubble more inertia during its relaxation. However, this approach is limited by the nonlinear effects of bubble deformation. We have already seen that a sufficiently large electric field will destabilize the bubble and in some cases cause it to break apart.

We have also seen that extreme curvature can be created in the dipole mode ($\ell = 2$) by way of contracting the bubbles sides. It is unfortunate that this contraction is not in the direction of the applied field, but it still may be of interest in demonstrating the principle of the shape effect. In particular, if a secondary electric field were applied perpendicular to the driving field, at the exact time that the sides of the bubble contract, then we may expect to see field enhancement similar to that observed in highly compressed bubbles. From this discussion, it is desirable to gain a greater understanding of the behavior of the bubble under the action of intense electric fields, specifically those large enough to induce complete destabilization of the bubble shape.

5.5.1 Bubble Breakup

We turn now to the example of a bubble being driven by intense electric fields. Figure 5.14 shows the time resolved extension of a bubble in response to a uniform field. In this case, two parallel plate electrodes are positioned above and below the bubble, with an electrode gap of 3.0 mm. The TREK high voltage amplifier system is used to apply a 7.5 kV, 500 μs pulse to the electrodes, resulting in an electric field of 25 kV cm^{-1}. The bubble diameter is 0.6 mm, giving rise to a Weber number of 15. The Redlake camera was set to 25,000 frames s^{-1} with an exposure time of 38 us. As the field is turned on, the bubble begins to stretch vertically, its shape closely resembling the dipole mode. After 100 μs, we begin to see the effects of the nonlinear

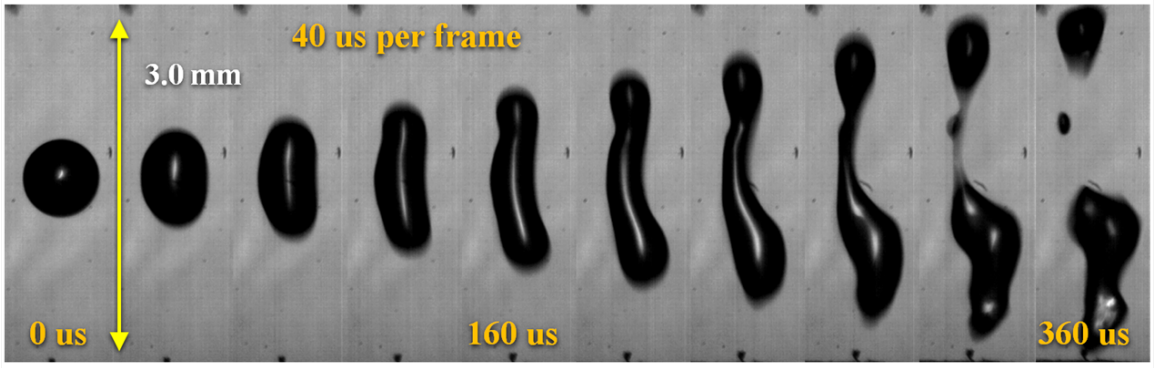

Figure 5.14: A bubble stretches under the action of a uniform electric field, with amplitude 25 kV/cm. The field is generated by a pair parallel plate electrodes placed above and below the levitated bubble.

deformation. The boundary of the bubble begins to bend. This is an example of the nonuniformity of the field. Areas of larger field pressure (higher E) push harder on the fluid boundary, leading to localized indentations on the surface. Eventually, the contracted zone begins to cover a larger area of the bubble. The thin capillary tube keeping the bubble together continues to contract until finally breaking apart, allowing the two pieces of the bubble to separate. This detachment process occurs quickly (10-20 μs) relative to the camera capture rate. During this temporary window, the contraction of the bubble's midpoint is reminiscent of the compression predicted during the extreme contraction of the $\ell = 2$ and $\ell = 4$ modes in Section 5.11. We can indeed reimagine this as a mechanism for the shape effect by superimposing a secondary electric field perpendicular to the original uniform field. If such a field were applied, the Maxwell simulations of Figure 5.11 indicate that we should expect considerable enhancement of the electric field. An experimental investigation of this exact geometry is described in Chapter 7.

5.5.2 Dependence of the Field Strength on Distortion

The tendency of the bubble to destabilize or break up is directly related to the applied field pressure, or more specifically to the magnitude of the electrical Weber

number, W_e. It is reasonable to expect that a critical value of W_e exists, above which bubble breakup will occur. Figures 5.15 and 5.16 show analysis of bubble deformation for 12 different cases, including bubbles of varying radius and electric field. In Figure 5.15, the deformation of the bubble is defined as the percentage increase in the bubble diameter in the direction of the field, given as,

$$\Delta\%d = \frac{d_{final} - d_{initial}}{d_{initial}} \tag{5.11}$$

For each case, the maximum deformation, $\Delta\%d$, during each expansion was measured and plotted against the Weber number, W_e. The Weber number is an appropriate comparison since it takes into account the strength of the surface tension fighting against deformation. In Figure 5.15, all cases where bubble breakup (fission) was observed are highlighted in red. From this graph, it appears that the approximate threshold for breakup is a Weber number in the range 17-20. Figure 5.16 shows images for four particular cases (also labeled on Figure 5.15), each with increasing Weber number. Case (c), in particular, provides an example of the field strength just weak enough to preserve the shape of the bubble. Overall, the normalized distortion is linearly proportional to the applied Weber number. For large Weber numbers this relationship begins to fail. This behavior agrees with previous investigations of fluid drop behavior as well as basic linear models predicting deformation behavior [149].

These results indicate that for a given bubble radius, R_0, there is maximum applied field that can be used to excite resonant mode oscillations. Electric fields above this threshold will not yield the desired curvature associated with spherical harmonic modes but instead merely lead to the stretching of the bubble. This does not necessarily hold true in nonuniform field geometry where the field is not directly pulling on the bubble, but still presents a limitation in the design of a practical device. One way to avoid this issue may be to effectively decrease the duty cycle of the applied field.

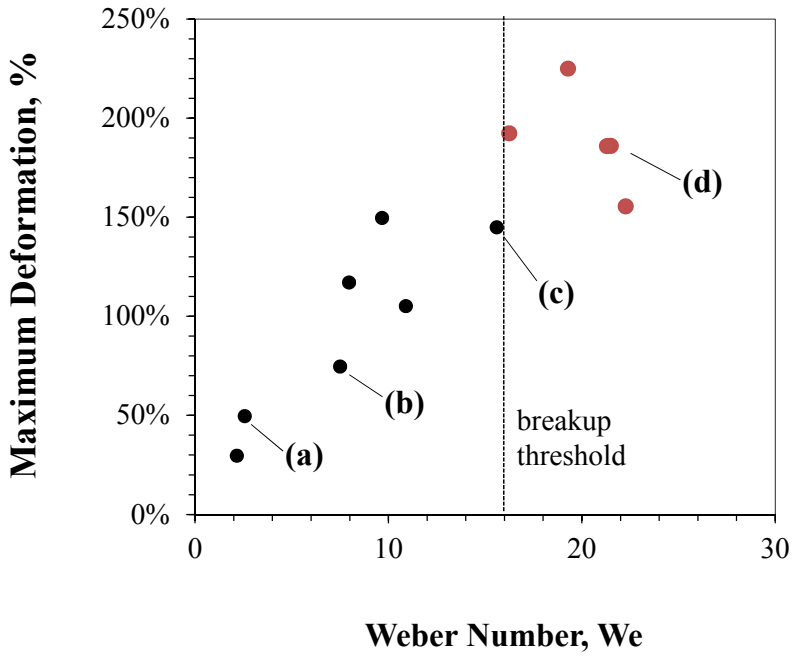

Figure 5.15: The normalized deformation in the direction of the applied electric field as a function of the Weber number

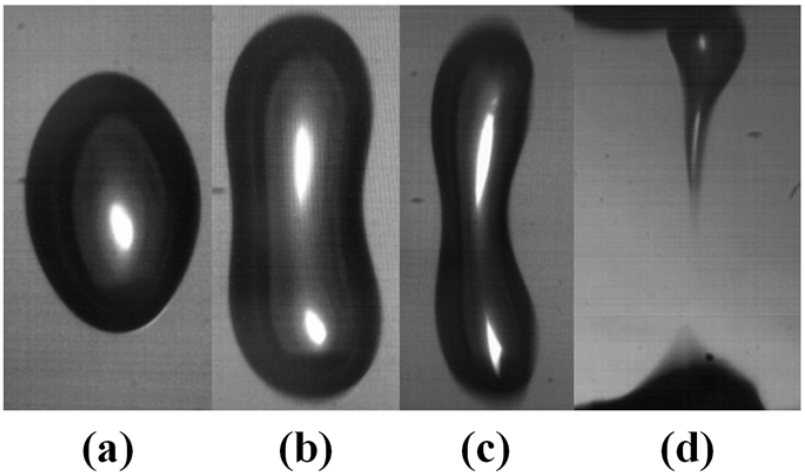

Figure 5.16: The effect of increasing the strength of the electric field acting on a levitated bubble. As the amplitude increases, the bubble's sides narrow up to a critical point beyond which it is separated into two fragments.

If it is applied in short pulses, the D.C. component of the field may not be activated long enough to rip the bubble apart. In this work, we chose the driving frequency based on the linear behavior of the bubble, namely by matching it to a set of discrete modes. But as noted before, the nonlinear frequency response can differ substantially from the linear response. A better understanding of this nonlinear response could improve the degree of mode excitation for a given voltage. These effects together could be used to produce more extreme excitation of the spherical harmonics at lower field intensities. Overall, it is not necessarily true that bubble break up is undesirable when it comes to the design of a real device. The transient curvature experienced during fission is yet another potential source of field enhancement.

5.6 Evaluating the Volume Effect

The results from Sections 5.2 and 5.3 suggest that the electrode geometry and accompanying field range investigated in this work were not capable of achieving volume mode excitation. Further insight into this issue can be obtained by considering the pressure balance of the bubble surface at equilibrium, as introduced in Chapter 2. In Section 2.4.1, it was shown that at equilibrium, the gas pressure, p_g and vapor pressure p_v act outward against the surface tension, p_s and ambient liquid pressure p_0. When the applied field acts to change the volume of the bubble it must not only overcome the surface tension pressure but also the gas pressure. As the field begins to stretch the bubble, it must be able to sustain any pressure difference resulting from the volume change. Thus, in the case of achieving the volume effect, the Weber number alone is not a sufficient measure of the tendency to change the bubble volume. The ratio of the gas pressure to the surface tension pressure has been shown to be an important parameter in determining the response of the bubble. It has been

designated according to Shaw [149], by the letter Π,

$$\Pi = \frac{p_g}{p_s} = \frac{2R_0 p_g}{\gamma} \tag{5.12}$$

For a bubble of radius 1 mm at a gas pressure of 1 atm, $\Pi = 2800$. This indicates that the gas pressure is a much larger contribution to the overall pressure balance than surface tension. Indeed, the pressure balance is often approximated by the condition $p_g = p_0$ [111], which simply says that the gas pressure is in equilibrium with the ambient liquid pressure. This condition also implies that a much larger electrostatic pressure is required to equal the gas pressure than is required to equal the surface tension pressure. As an example, suppose that the internal gas pressure is changed by 10%. Assuming that the bulk liquid is incompressible, the resulting pressure difference is $0.1p_g$. The electrostatic pressure required to sustain this volume change can be calculated by equating the electrostatic pressure and acoustic pressure at this condition.

$$p_e = \frac{\epsilon_0 E^2}{2} = 0.1 p_g \tag{5.13}$$

In order to sustain a 10% differential, the electric field would have to be at least 50 kV cm^{-1}. This value is larger than the maximum field strengths used in this work, which were approximately 25 kV cm^{-1}. This is consistent with the absence of volume changes observed in shape mode analysis. Another factor that may have contributed to the absence of volume change was the electric field geometry, which was primarily designed to be uniform. In Section 2.6.2, it was shown that for a purely uniform field, the net integral of the electrostatic pressure over the surface of the bubble was zero, indicating that a uniform field does not tend to compress the bubble inward. The use of a nonuniform field, on the other hand, could be used to create a net compression or rarefaction of the bubble volume. Finally, the applied fields in this chapter were driven at frequencies designed to match the shape modes (100-600 Hz). No attempt

was made to match the volume mode frequency, ω_0, which was of order 1-5 kHz. Driving the bubble at this resonance has been shown to produce large amplitude oscillations [124, 125].

The above discussion indicates that demonstration of the volume effect requires an approach more specifically tailored to the excitation of volume mode oscillations. Although the shape effect has been the major focus of this work, it appears that the volume effect should be investigated further and that the above changes may be implemented in a realistic manner.

CHAPTER VI

Fundamental Discharge Processes in Gas Bubbles

Chapters 4 and 5 established several methods of inducing extreme shape deformation in gas bubbles. Simulations of the electric field strength and ionization product, M, within these deformed bubbles indicates that such shape deformation provides a substantial improvement in the probability of plasma formation. It appears that with proper shape distortion, the electric field strength necessary to achieve streamer ignition in isolated bubbles is on the order of 10-20 kV cm^{-1} for bubbles of radius 1 mm. This is in contrast to the case of an undeformed bubble, which for the same size would need nearly 50 kV cm^{-1} across its entire body to achieve the Meek streamer criteria. The above estimates provide a starting point for the practical design of a reactor based on plasma formation in bubbles. Unfortunately, very little is known about the actual discharge mechanisms that drive plasma formation in isolated bubbles. In this chapter, we focus on a fundamental investigation of the physical process of achieving plasma ignition of isolated bubbles with the goal of achieving, experimentally the first known example of ignition in an isolated bubble.

A better understanding of bubble discharge physics would provide insight into a wide variety of physical phenomena central to the study of plasma formation in liquids. The ignition of plasma in small gas bubbles distributed throughout the liquid, for example, has been proposed as a fundamental process in the explanation

of breakdown in liquids [49]. Understanding how plasma forms in these bubbles may aid in the development of a fundamental model of breakdown in liquids. Most importantly, though, a fundamental characterization of plasma formation in bubble-filled liquids would be an enabling step toward the development of a practical liquid based plasma reactor. In such devices, the ignition and transport of plasma through the bubble gas and liquid ultimately determines the energy efficiency of the device and the production rate of chemically reactive species.

The discussion of indirect discharges in Chapter 1 indicates that plasma ignition in bubbles is preferable to that in liquids. This is due to the lower breakdown strength and lower energy input required to form plasma in the gas. It was also proposed that ignition in distributed bubbles is preferable to electrode-attached bubbles due to the farther reach of the isolated bubble plasma deeper into the volume of the liquid. Together, these factors suggest that plasma should be confined solely to the interior of isolated gas bubbles while minimizing excitation in the liquid. However, as discussed in Section 2.2.4, achieving isolated bubble ignition is difficult. This is due not only to the attenuation of the electric field in the volume of the liquid, but also to the absence of secondary electrode effects.

Figure 6.1 shows two hypothetical mechanisms by which plasma can be ignited in a bubble filled liquid. In the top case, a streamer is ignited at the needle tip and travels through the distributed gas bubbles. In this case, the bubbles represent areas of high reduced field (E/N) that are capable of reigniting or sustaining the streamer. In the bottom case, plasma is ignited only inside the isolated bubble. This discharge may propagate by transmitting plasma into a nearby bubble. This streamer "hopping" phenomenon is achieved through two possible mechanisms (1) the emission of resonant photons from one bubble are absorbed in an adjacent bubble causing ionization, and (2) the intense electric field at the head of a streamer in the first bubble couples to the second bubble, resulting in ionization. This type of bubble

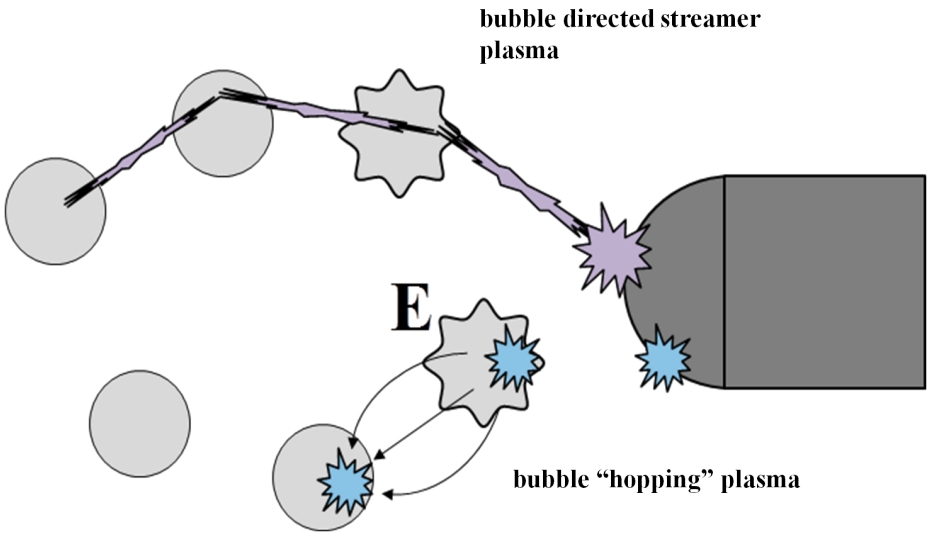

Figure 6.1: Submerged gas bubbles can extend the plasma deep into the liquid via two different mechanisms: (1) A liquid streamer is sustained by passing through a chain of gas bubbles (2) The plasma is ignited solely in the volume of the gas. This plasma can hop to other bubbles through either the release of resonant photons or the coupling of the streamer field to a nearby bubble.

hopping phenomenon has been predicted numerically by Kushner and Babeava [88]. For both discharge mechanisms, the bubbles influence the trajectory of the streamer in order to extend the reach of the reactive species into the volume of the liquid.

6.1 Experimental Approach

In this experiment, we investigated the mechanism for discharge initiation in an unperturbed underwater gas bubble. All testing was performed in the piezoelectric levitation cell described in Chapter 3. In contrast to the shape deformation study presented in Chapter 5, the translatable electrode stage in this case was used to precisely control the conditions leading to electrical breakdown. The goal of this approach was to not only determine the necessary bubble-electrode separation necessary to ignite plasma but more importantly to determine what form this plasma would take. In particular, we address the question, under what conditions would the plasma form in

the bubble and under what conditions would it form in the liquid?

6.1.1 Electrode Design

Figure 6.2 shows the electrode geometry chosen for this experiment. For a detailed description of the electrode dimensions, see Section 3.2.1. The top electrode is the circular plate electrode originally shown in Figure 3.6(b) while the bottom electrode is the syringe needle electrode shown in Figure 3.6(a). In all experiments, the top electrode was grounded and the needle electrode was biased at positive voltage. The sharp geometry of the needle was chosen to maximize the electric field at the tip of the electrode ($\sim$0.1-1 MV cm^{-1} and hence maximize the strength of the field present at the surface of the bubble. The translation stage was used to finely tune the position of the electrodes and the bubble to within approximately 0.1 mm. On average, the needle was positioned at a distance of $0.5-2$ mm from the bubble. A photograph of the typical orientation is shown in Figure 6.2. The ground electrode was positioned typically 3 mm relative to the bubble resulting in an electrode gap of 4 mm. For a detailed overview of the translatable electrode stage, see Section 3.2.1.

The voltage pulse was provided by the Suematsu pulser. A detailed account of the pulse transmission line and IV properties can be found in Section 3.4.1. The pulser was used to generate voltage pulses with amplitude, V, in the range $10-14$ kV. The radius of curvature at the needle tip, R_c was measured using a microscope and was found to be approximately 100 μm. The approximate electric field strength at the needle tip (V/R_c), is of order $\sim$1 MV cm^{-1}. This field strength provided the capability to generate a direct liquid discharge at the needle tip if desired [49]. Reliable breakdown was further assured by consistently replacing the syringe at the tip of the needle electrode, which eroded after continued use.

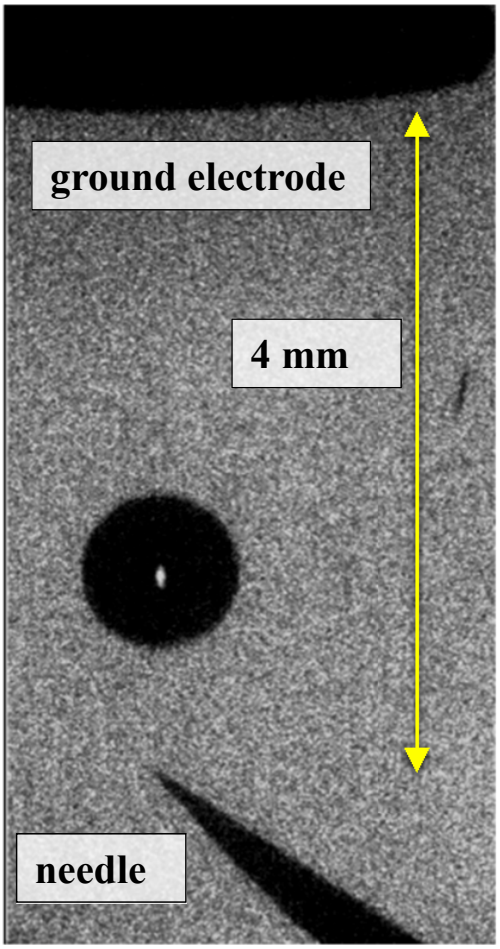

Figure 6.2: The electrode geometry as observed by a 500 nsec gated ICCD image. A faint backlight brings the geometry just above the ICCD noise level but not too high to drown out plasma emission resulting from the pulse. The small light spot at the center of the bubble represents the focused image of the backlight.

6.1.2 Gas Types

In this experiment, plasma formation was investigated for two gas types, ambient air and helium. As discussed in Section 2.2.4, helium has a much higher ionization coefficient than air over moderate ranges of the reduced field, $E/N = 50 - 100$ Td. Since the applied voltage pulses are limited to 13.6 kV, the use of helium bubbles was expected to increase the probability of forming plasma in bubbles that were isolated from the electrode. The primary disadvantage of using helium is its high molecular diffusion coefficient, [113], which at $D = 0.9$ cm^2 s^{-1} is five times higher than air. As discussed in Section 2.4.5, very little of the gas in the bubble during ignition will be helium. Gas bubbles in this case are more accurately considered air bubbles contaminated with helium and water vapor. Despite this limitation, it is expected that the small amount of helium left in the bubble will still have a substantial effect on breakdown conditions due to the high ionization coefficient of helium. Air bubbles were injected using the 30 gauge syringe introduced in Section 3.1.4 while helium bubbles were injected using the solenoid valve injection system (see again Section 3.1.4). Typical diameters were 0.5-2.5 mm. The operating conditions of the piezo-cell were similar to those used in Chapter 4, with deionized water (10-20 μS m^{-1}).

6.1.3 Imaging

The PIMAX ICCD camera was the primary camera used to image both fluid and plasma phenomena. A full description of the ICCD characteristics can be found in Chapter 3. In this experiment, exposure times were chosen to be in the range 30-1000 ns. As described in Section 3.5.2, the ICCD was only capable of capturing a single exposure each time it was triggered. This property limited the ability to exactly resolve the time evolution of all phenomena. A straightforward way to overcome this limitation was to simply trigger the ICCD at a variable delay time, which was controlled using a delay generator. This necessitated the careful control of experimental

conditions in order to achieve highly repeatable results. The ICCD intensifier gain was set to 6 and the telescoping lens zoom ranged from 2-4X. On this gain setting, the noise level, without any backlight, was of order 600 counts per pixel. This provided a lower limit on the level of plasma emission that the camera could detect. With the backlight on, the typical light level was in the range 590-700 counts. This allowed the boundary of the bubble and the electrode to be imaged without overwhelming the emission produced by plasma.

6.2 Summary of Observed Plasma Phenomena

The Suematsu pulser was used to deliver 1 μs pulses to the point-to-plane geometry while varying both the needle-bubble separation and the total electrode separation. Overall, it was observed that the resulting plasma excitation could be split into three categories. In the first category were cases in which both the needle-bubble and needle-plate separation were large. In such cases, a streamer was ignited in the liquid. Typically these streamers were observed to have minimal branching and a small degree of emission. Two examples of a liquid streamer are shown in Figure 6.3, both taken with 500 ns exposure. Part (a) shows the streamer shortly after the beginning of the pulse (360 ns), emitting light along its path. The intensity level of this streamer was observed to be in the range 800-1000 counts, not far above the noise level of the ICCD (600 counts). Part (b) shows the aftermath of a separate liquid streamer, 2500 ns after the pulse. In this image, the emission from the plasma channel has decayed below the sensitivity of the ICCD, resulting in a low density channel that appears as a shadow against the backlight. This shadow may be due to refraction of the backlight, which is scattered by the change in refractive index occurring in the streamer channel. The change in the refractive index could also be due to the formation of low density water in the streamer channel, a result commonly predicted in liquid streamer phenomena [49, 48]. In general, the dark tracks observed in Figure

6.3(b) are observed to dissolve on the order of 10 μs. It is difficult to measure the voltage and current characteristic of liquid streamers due to the small signal strength. Any transient current pulses resulting from the streamer excitation are drowned out by the large displacement currents ($\sim$1 A) associated with the applied pulse. It is difficult, therefore, to determine the exact ignition time and current signature for these liquid streamers.

The second category of phenomena was observed at small needle-plate separation. In this case, full breakdown of the interelectrode gap was observed, resulting in the formation of a spark. Figures 6.4(a) and 6.4(b) show the two phases of spark formation. In the first phase, a pre-spark streamer traverses the electrode gap over timescales of $<$100 ns. After traversing the gap, it bridges the two electrodes resulting in a spike in current ($\sim$5 A) and a sudden drop in voltage. Accompanying these effects is a large increase in the emission from the plasma channel. In the aftermath of the spark, (0.5-1 ms), a residual cluster of vapor bubbles is observed. Any bubble levitating in the vicinity of the spark is completely destabilized and ejected from its levitation point. In some cases, the initial spark can travel through the bubble, as shown in Figure 6.4)(c). In this image, the bubble is not attached to the electrode but is levitating between the needle and the ground plate, which is behind the bubble. For a given voltage, the spark is easier to initiate when a bubble is present than when it is not. The typical ICCD intensity for a spark captured using a 500 ns gate is 50,000 counts, approximately 50 times more intense than the liquid streamer shown in Figure 6.3. In general, most plasma events discussed in this chapter occurred during the positive cycle of the pulse. With all other variables fixed, the position of the ground electrode did not significantly affect the discharge produced. This was true for electrode gaps larger than 2 mm. When the gap was decreased below 2 mm, a spark was ignited on a regular basis.

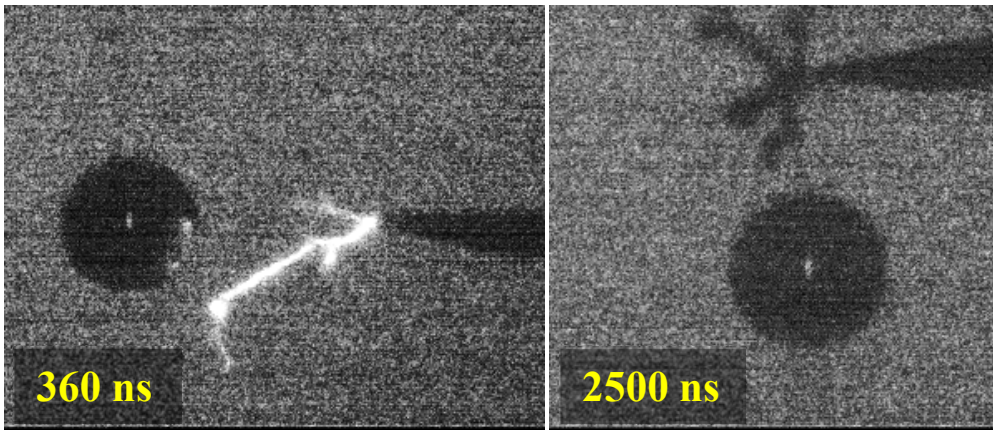

Figure 6.3: The liquid streamer appears at small voltages and large gap separation. Both images are shown in the ICCD intensity scale 590-700 counts

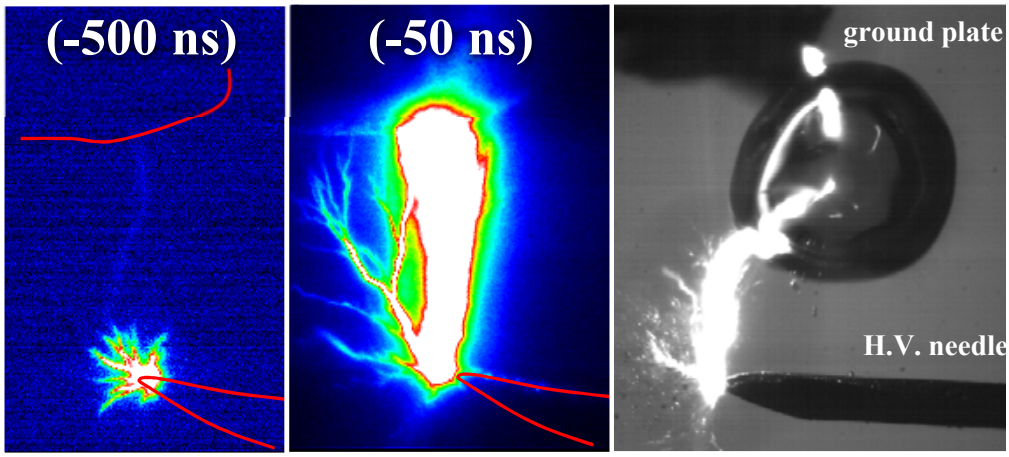

Figure 6.4: The spark appears at large voltages and small gap separation. It is marked by a (a) characteristic prestreamer channel that forms before the spark. When the spark is ignited, (b) the emission is up to 50 times more intense than the liquid streamer. (c) In cases where the bubble is in the electrode gap, the spark is easier to ignite and can travel through the bubble.

6.2.1 The Multiphase Streamer

A third category of plasma phenomena was observed to occur at intermediate electrode separation ($>$ 2 mm), particularly when the needle was within 1 mm of the bubble. In this case, a liquid streamer, initiated at the high voltage needle, was observed to make contact with the bubble. At this point, two things were observed: (1) a secondary plasma was ignited within the interior of the bubble and (2) the fluid boundary of the bubble was observed to explode outward. Images of this multiphase streamer phenomenon were first captured using the Redlake high speed camera. An example is shown in Figure 6.5. The high voltage needle, seen in the lower right corner, is pulsed at 11.7 kV. The needle-plate separation was set at 3 mm. Images were captured at 6280 frames s^{-1} with a 100 μs exposure time. These timescales provide a clear view of the combined plasma-fluid interactions. In the first frame, the streamer makes contact with the bubble, entering perpendicular to the surface. During the next 100 μs, the opposite side of the bubble surface explodes outward. This perturbation is highly anisotropic and parallel to the original impact trajectory of the streamer. The third and fourth picture illustrate the aftermath of the streamer's interaction with the bubble. The surface of the bubble undergoes a large perturbation, resulting in highly nonlinear shape deformation.

In the 4th picture (t = 480 μs), a track-like abscess appears on the side of the bubble. This track most likely corresponds to the physical path that the streamer takes as it travels to the bubble. Recall from the discussion of the shape effect in Chapter 2 that streamers ignited in bubbles tend to travel along the surface due to the strong refraction of the electric field in these areas. As the streamer propagates along the surface it transmits stress to the fluid boundary in three different ways: (1) an electric stress arising from the intense fields ($\sim$500 kV cm^{-1}) at the head of the streamer (2) an acoustic force, resulting from the pressure wave created in the wake of the streamer and (3) a thermal force, resulting from the expanding, heated gas in

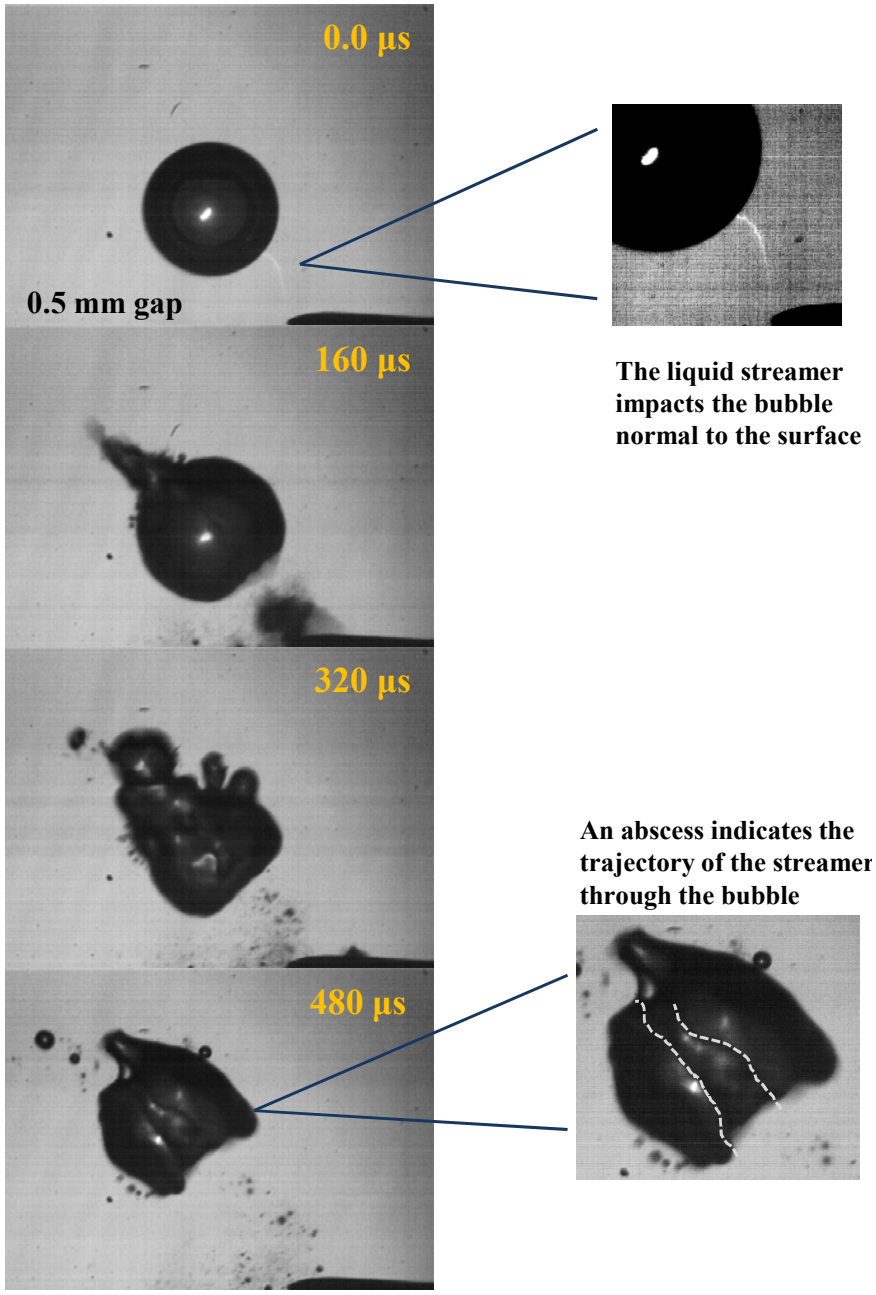

Figure 6.5: The streamer bubble interaction, as captured by the high speed camera at 5000 frames s^{-1}. Upon making contact, the streamer imparts energy to the bubble, resulting in extreme destabilization of the bubble's shape.

the plasma. The streamer is expected, therefore, to perturb the surface of the bubble as it propagates.

A more compelling view of this streamer track can be found in an early experiment performed in the attached bubble geometry, similar to that presented in Chapter 4. Figure 6.6 shows an attached bubble being pulsed by the Suematsu pulser at 12 kV and 750 Hz. In the first frame, the large 6 mm diameter bubble rests on the surface of the threaded rod, as is typical of the attached bubble experiments (see Chapter 4). In the second frame, a full spark is ignited across the electrode gap. Soon after the spark, a darkened channel is observed in the original path of the spark. A second arc is ignited soon after in the same channel indicating that the local dielectric geometry has an influence on streamer propagation. These tracks are characteristic of streamer propagation through the bubble and often persist in the bubble up to 10 ms following streamer ignition.

Looking back at the streamer in Figure 6.5, the bubble begins to drift away from the electrode at 500 μs. This drift is driven by the net momentum accumulated by the bubble as it undergoes electrical, acoustic, and thermal interactions with the streamer. Superimposed on this drift is a series of large shape oscillations, which are damped out by the viscosity of the water on the order of 500 μs. The only residual effects observed long after the interaction are a net decrease in bubble radius. The change in radius is most likely due to shape oscillations undergone by the bubble following its interaction with the streamer. These oscillations agitate the oxygen in the bubble, causing it to dissolve into the water. In cases when the bubble is not directly in front of the needle, the streamer can still bend and connect with the bubble. This phenomenon is demonstrated in Figure 6.7.

In this case, the streamer curves upward to impact the bubble. At 56 μs, the long exposure time reveals both the thin filament of plasma emission from the streamer during its early evolution as well as the subsequent expansion of the liquid channel.

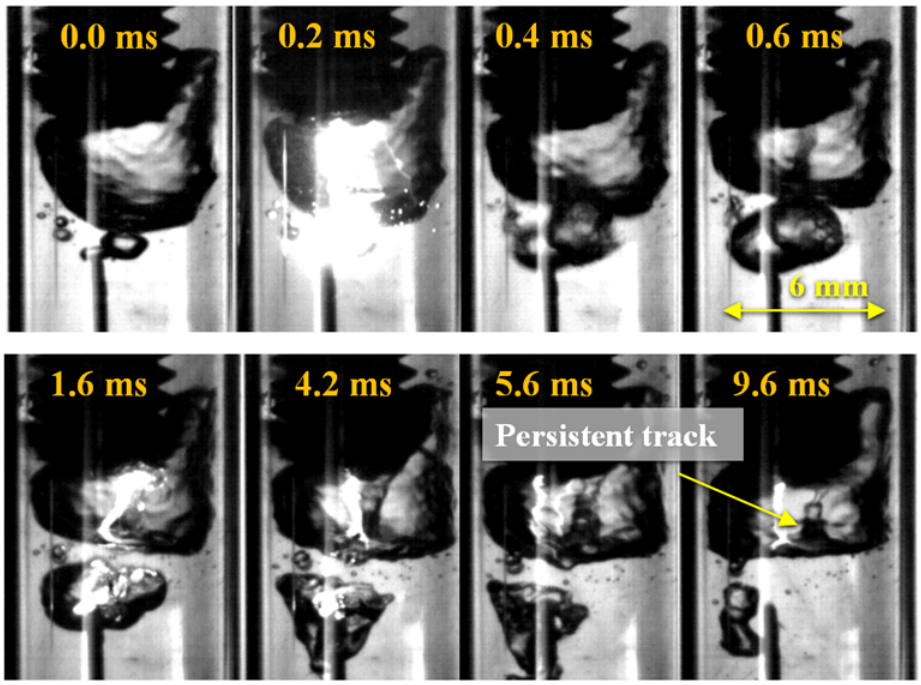

Figure 6.6: A spark ignited between the two electrodes travels through the attached bubble. In the aftermath, a distinct track mark is left on the bubble surface. The Suematsu is pulsed at 12 kV, 750 Hz. The capture rate is 5000 frames s^{-1}.

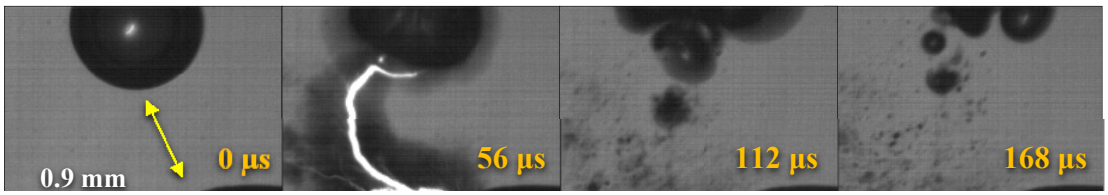

Figure 6.7: Another example of the streamer bubble interaction more clearly shows the streamer channel evolution over time as well as the tendency of the streamer to find the bubble. The camera frame rate is 5000 frames s^{-1}.

As suggested previously, this channel is due to either a gradient in the liquid density or a phase change from liquid to vapor. Following the streamer impact, the bubble is pushed upward and out of the frame. Its trajectory is aligned with the entrance direction of the streamer, just as in the case of the bubble in Figure 6.5.

6.2.2 IV Characteristic of the Multiphase Streamer

Figure 6.8 shows the voltage and current across the electrode gap for the case of a multiphase streamer. The time axis shown is relative to the oscilloscope trigger and shows the positive cycle of the pulse. The ignition of the streamer is marked by a voltage drop (1-2 kV), which is accompanied by a wave of current pulses (0.2-1 A). These current spikes should be distinguished from the large amplitude displacement current oscillations, which are caused by the fast rise time (100 ns) of the Suematsu pulser. Both the voltage drop and current spikes occur approximately at the same time, 420 ns into the pulse. It should be noted that the small voltage drop in Figure 6.8 closely resembles the voltage drop resulting from plasma excitation in electrode attached bubbles, as discussed in Chapter 4. In such cases, the attached bubble plasma is essentially a dielectric barrier discharge, with the liquid medium functioning as the dielectric barrier. In the case of a multiphase streamer, the voltage drop appears to be delayed until the streamer makes contact with the bubble. At this point, the observation of multiple current spikes could indicate the excitation of multiple plasma

streamers in the bubble. To determine this, further imaging of the plasma in the bubble is required.

6.3 ICCD Imaging of the Multiphase Streamer

The images presented in Section 6.2.1 provide a wide angle view of the complex processes that occur during the evolution of the multiphase streamer. However, many questions concerning the nature and origin of the discharge remain unanswered: what is the extent of plasma formation in the bubble? Can the streamer plasma be initiated in the bubble instead of the electrode tip? What is the physical mechanism of the fluid instability? Further insight into these issues can be obtained using the PIMAX ICCD camera to resolve the time evolution of plasma both in the liquid streamer and in the gas bubble. The PIMAX ICCD was used to take single images of the multiphase streamer with exposure times ranging from 30 ns to 1 μs. This provided the capability of resolving fast processes like streamer propagation but also slower processes such as fluid motion.

As stated in Section 3.5.2, the resolution of any time dependent process using the ICCD must be taken across multiple shots. Obtaining an accurate picture of plasma evolution in such cases requires the design of a highly repeatable experimental setup. ICCD images can be taken at different times by triggering the ICCD relative to an event that is easily recognizable. In this case, the voltage drop observed in Figure 6.8 was used as a point of reference. In the following section, it will be shown that the time of the voltage drop corresponds to the time at which the streamer makes contact with the bubble. The delay of the ICCD was set using the Stanford delay generator (see Section 3.5.2). This provided an estimate of the absolute timeline of plasma evolution. One difficulty with this approach was the variability of the breakdown event, which occurred at different times during the applied pulse. This problem was partially overcome by cleaning the electrode and taking care to keep the

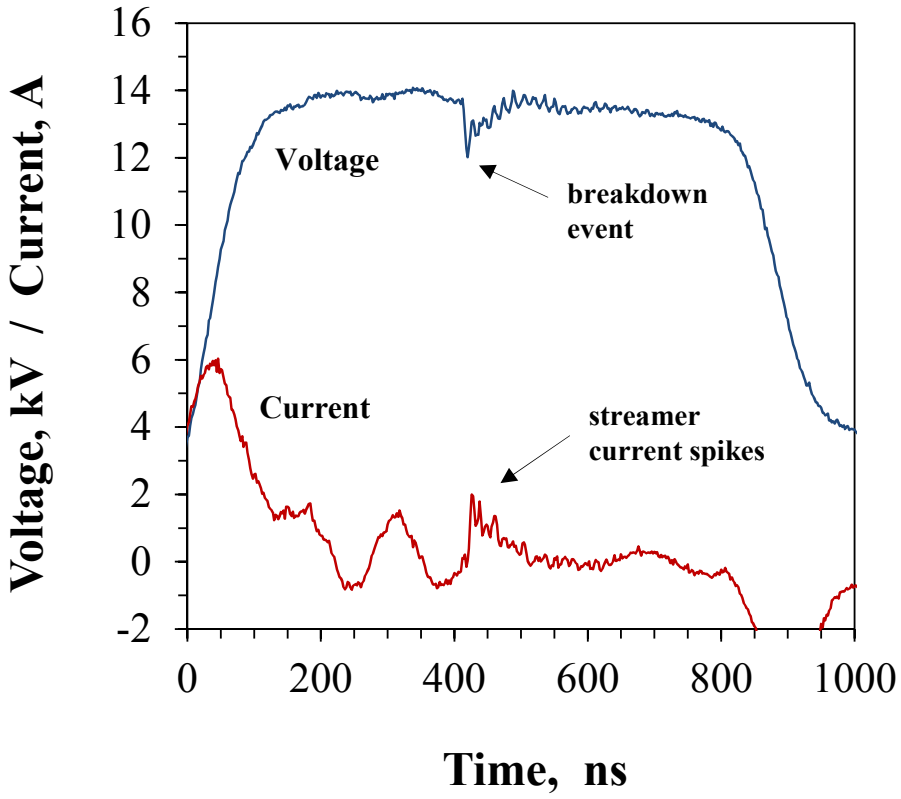

Figure 6.8: Typical voltage and current traces for the streamer bubble interaction. The voltage drop is characteristic of a dielectric barrier discharge. The time scale displayed is relative to the oscilloscope trigger.

alignment of the bubble and electrodes constant, thus producing a breakdown event at approximately the same time. The exposure time was set at 500 ns. The delay time, t_d, was defined as the difference between the beginning of the ICCD exposure and the time corresponding to the breakdown event (see Figure 6.8). Thus, when t_d was between -500 ns and 0 ns, the ICCD exposure was able to capture the breakdown event. At all other times, the exposure captured pre-breakdown phenomena ($t_d <$ -500 ns) or post-breakdown phenomena ($t_d > 0$ ns).

6.3.1 Early Timescales: Streamer Formation and Bubble Impact

Figure 6.9 illustrates the early evolution of the streamer as it makes contact with the bubble. Times range from prebreakdown ($t_d \leq 500$ ns) up to $t_d = 2$ μs. In the first image, at $t_d = -650$ ns, the exposure occurs entirely before the streamer makes contact with the bubble. In its infancy, the plasma is confined to the high voltage

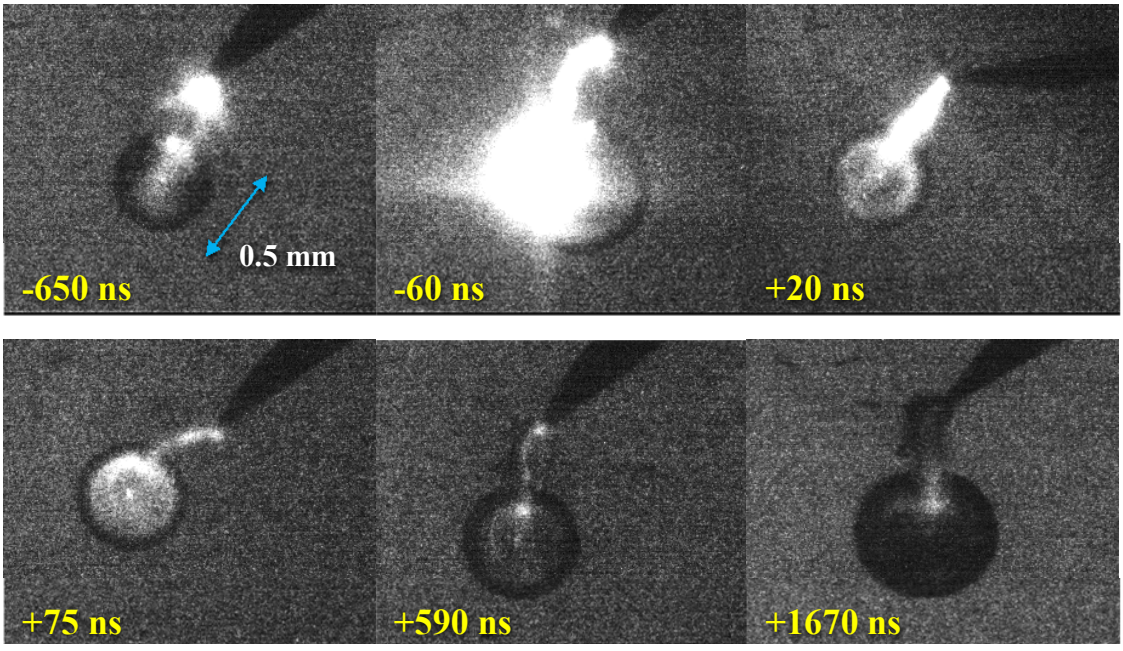

Figure 6.9: Evolution of the multiphase streamer within 2 μs of the breakdown event. The bubble glow becomes visible following the relaxation of the streamer channel. All images are shown in the ICCD intensity scale 590-700 counts.

needle, at the point where the electric field is most intense. In the next image, the streamer has made contact with the bubble, resulting in a dramatic increase in light emission. The majority of the light emission takes place over the first 100 ns, which correlates well with the timescale of the current spikes observed on the IV trace in Figure 6.8. Over the next 400 ns, the glow of the plasma relaxes. At this point, plasma forming in the bubble is now visible. As expected, the plasma is concentrated at the fluid boundary, where the field is most intensely refracted. When the streamer makes contact with the bubble, the peak emission reaches approximately 5,000-10,000 counts for a 500 ns gate, which is much larger than the emission from the liquid streamer (<1000 counts). The bubble glow in the aftermath of impact, for comparison, is much lower, typically of order 800 counts.

The streamer impact was investigated in greater detail by reducing the exposure time of the ICCD gate to 50 ns. Figure 6.10 shows three examples illustrating the evolution of the streamer from its formation at the needle to the growth of the plasma channel upon making contact with the bubble. In all three images, the bubble is set at a similar position relative to the electrode. Observation of the characteristic breakdown event on each IV trace was used to confirm the initiation of the multiphase streamer. The first image indicates that the streamer formation has not yet occurred 200 ns before the breakdown event. The second picture is consistent with this view. Between 120 ns and 70 ns before impact, the streamer initiates at the needle tip and propagates toward the bubble. In the third frame, the streamer has made contact with the bubble and the breakdown event has occurred. Below each frame is a line profile of the light emission of the streamer channel. The dashed lines over each image indicate the path over which the line profile is taken. In the second frame, the line profile is taken over the streamer front, where maximum emission occurs. These line profiles indicate that the streamer undergoes a dramatic increase in emission upon making contact with the bubble, resulting in an increase by a factor of 5. This

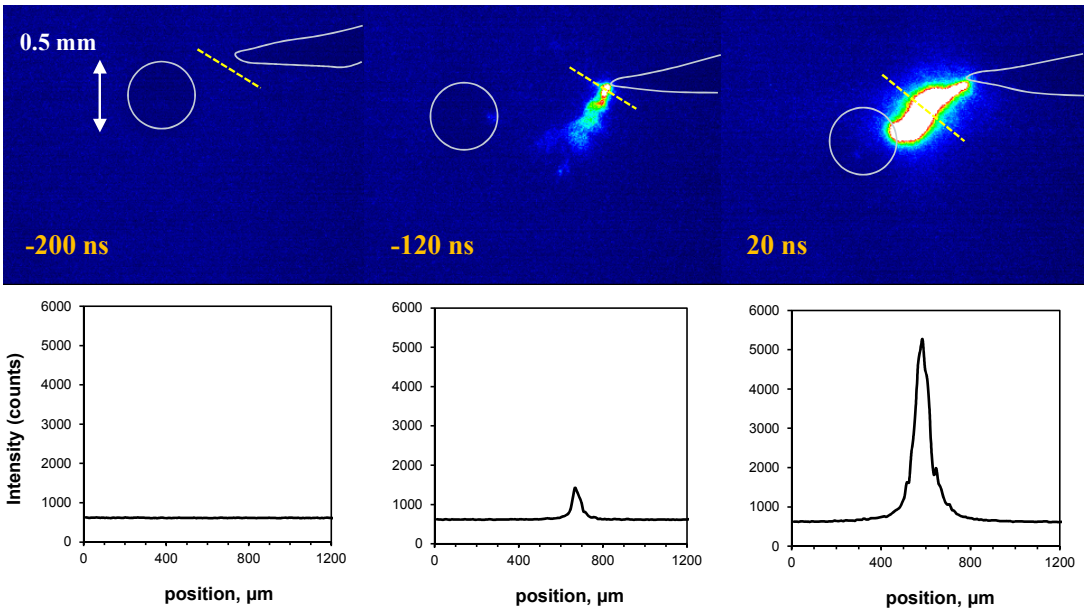

Figure 6.10: ICCD images of the streamer making contact with the bubble, with 50 ns exposure. Below each image is a line profile of the emission intensity captured by the ICCD. The connection of the streamer to the bubble is marked by a dramatic increase in emission.

transition may be due to the conduction of charge through the streamer channel, which would result in an increase in the collision rate and hence also in the excitation rate. The origin of the charge transfer is far less clear. One possible explanation is that charge is built up on the surface of the bubble at the beginning of the pulse. This charge could be deposited on the bubble surface by the finite conductivity of the liquid. When the streamer makes contact with the bubble, this charge is suddenly transported through the highly conductive plasma in the streamer channel. Another possible explanation is that the enhanced excitation (and emission) is the result of multiple gas streamers being reignited inside the bubble, as indicated by Figure 6.9. Overall, it is clear from the time resolved images in Figure 6.9 and 6.10 that the breakdown event corresponds to the point at which the streamer makes contact with the bubble.

As a simple sanity check, one can compute the speed of the streamer as it travels

to the bubble. Figure 6.10 (b) indicates that the streamer has traveled approximately 200 μm at a time 75 ns before contact. Since the bubble needs to travel an additional 1100 μm in the next 78 ns, so that it makes contact at $t_d = 0$, the approximate velocity of the streamer must be at least 16 km s^{-1}. This calculation likely underestimates the streamer speed due to the fact that there is a delay between the impact of the streamer and the drop in voltage. Streamer speeds in water have been reported in the range 10-100 km s^{-1} depending on the conductivity of the water [49, 48].

6.3.2 Characterization of Bubble Plasma

In Figure 6.9, the extent of plasma formation in the bubble is obscured by the intense emission observed during streamer impact. The clearest view of the bubble plasma occurs during relaxation of the liquid plasma channel for $t_d > 50$ ns. Figure 6.11 shows ICCD images of six cases each illustrating the excitation of plasma in the bubble. The top row shows a comparison between plasma excited in air bubbles (left, $t_d = 150$ ns) and helium bubbles (right, $t_d = 166$ ns). In this case, the helium bubble is pulsed within 10 seconds of injection. Both images were obtained at the same voltage, 13.6 kV, and similar distance to the needle. To more accurately capture the bubble glow, each image was taken with the backlight turned off. For each case, the size of the bubble is shown in the upper right corner while the gas in the bubble is shown in the lower left hand corner. The most immediate difference between the two gases is the filamentary nature of the air plasma compared to helium plasma. Although the streamer nature is apparent in the helium bubble, it exhibits a more diffuse character. This observation is consistent with imaging taken of streamers in electrode-attached bubbles by Tachibana [85]. It is difficult to discern whether this plasma fills the volume or is still constrained to the surface. Another change observed when using helium is a decrease in the voltage required to produce the bridging streamer (by 1-2 kV) as well as the consistency of ignition. This could be a result of the diffusion of

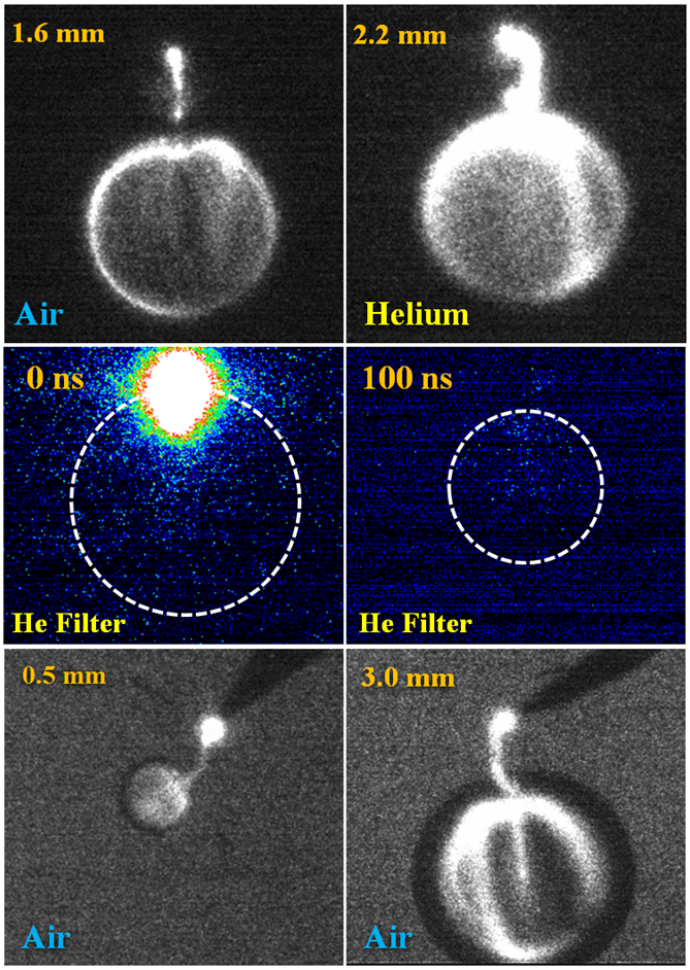

Figure 6.11: Bubble plasma in the aftermath of the streamer. The top row shows a comparison between air bubbles (left) and helium bubbles (right). The second row shows images taken with the He filter (590 nm), indicating the presence of helium in the bubbles. The bottom row shows plasma excitation in small bubbles (left) and large bubbles (right). All cases were taken at 13.6 kV and 500 ns exposure.

helium into the liquid barrier between the bubble and the electrode tip. The presence of dissolved helium would presumably increase the degree of ionization occurring at the electrode tip and thus be more likely to ignite a streamer.

To further investigate the extent of helium in both the gas and liquid, an optical bandpass filter was attached to the front of the ICCD camera. The filter was designed to allow passage of light near the strong helium line at 587.6 nm. The filter was centered at 590 nm with a 50% transmission coefficient and a bandwidth of ± 10 nm. Images taken with the filter are shown in the second row of Figure 6.11. The delay time, t_d, of the ICCD exposure is shown in the upper left corner of each image. The first image shows the streamer making contact with the bubble boundary, which is indicated by the dashed line. From this image, it is clear that helium gas is present in the liquid streamer. This supports the hypothesis made above that helium is diffusing out into the electrode-bubble gap and being ionized by the multiphase streamer as it passes by. The second image shows the afterglow of the bridging streamer in the bubble. A faint signal is seen within the interior of the bubble, confirming that some amount of helium is in the bubble and being ionized. As first stated in Chapter 3, the helium bubble is, in reality, strongly contaminated by air diffusing in from the surrounding water. As a result, the helium plasma will retain properties characteristic of bubble streamers formed in air. It is further observed that if the helium bubble is allowed to sit for up to 10 minutes before applying the pulse, it is indistinguishable from the air plasma.

The third row shows plasma ignition in bubbles of two very different sizes (0.5 mm vs. 3.0 mm). In the case of the large bubble (right), it is quite clear that the plasma, which occurs in both the liquid and gas, takes the form of a streamer. The gas phase plasma appears to branch out into multiple tracks as is often observed in electrode attached bubbles [85, 108]. These tracks bend around the bubble surface and converge at the tip of the bubble opposite of the streamer entrance point. We have

seen already that this point is the nucleus for a variety interesting fluid dynamical effects occurring in the aftermath of the plasma formation. The fact that this is also a focal point for plasma in the bubble may offer a possible physical explanation for the fluid explosions observed in Figure 6.5. In the case of the small bubble (left), the spatial extent of the plasma is more difficult to infer. Although the plasma appears to more uniformly cover the boundary of the bubble, the diffuse nature of the plasma may be simply due to the spatial resolution of the ICCD.

The mechanism behind the transition from liquid plasma to gas plasma is still unclear. One possible explanation is the following: the liquid streamer propagates out from the needle tip with intense electric fields at its tip. When this streamer reaches the bubble boundary, the intense fields immediately ionize the gas in the bubble. The field at the liquid tip must persist long enough for the avalanches in the bubble to satisfy the streamer criterion ($\lambda x \sim 20$). Another possibility, is that the streamer channel in the liquid is a hollow cavity, composed of vapor or dissolved gas. This has been proposed as a mechanism for streamer propagation in cases where the liquid has a dissolved gas, such as oxygen [49]. When the streamer impacts the bubble, this channel empties its contents into the bubble and the streamer continues to propagate. This hollow channel could be produced via the method proposed by Lewis [55]. In this model, the intense electromagnetic stress at the tip of the streamer peels or unzips the liquid as the streamer propagates, resulting in a hollow cavity along the path of the streamer. This low density channel could be used to transport electrical charge and hot gas into the bubble, both of which could initiate the fluid explosion observed at later times.

6.3.3 Late Timescales: Fluid Motion and Instability

For times later than 2 μs following the impact of the streamer on the bubble, the primary physical mechanism transitions from plasma formation to fluid motion.

Characterization of these late timescales may lend insight into the nature of the destabilization of the fluid boundary. Figure 6.12 shows the evolution of the fluid boundary following the streamer bubble interaction. At this time, plasma emission has disappeared and the streamer channel has begun expanding radially outward. As the channel expands, the bubble boundary becomes strongly perturbed. This is supported by the fact that the image of the backlight at the center of the bubble has disappeared. The surface perturbations act to refract the backlight, causing it to be scattered rather than focused. The continued action of the streamer channel, at $t_d = 17$ μs, appears to compress the bubble inward at the point of contact, distorting it into a shape that resembles an apple. At the opposite end of the bubble, the surface sharpens, indicating the early formation of the exploding surface. After 20 μs, the explosion emerges from the bubble, forming a conical wave front. This disturbance propagates outward, eventually reaching a distance comparable to the bubble diam-

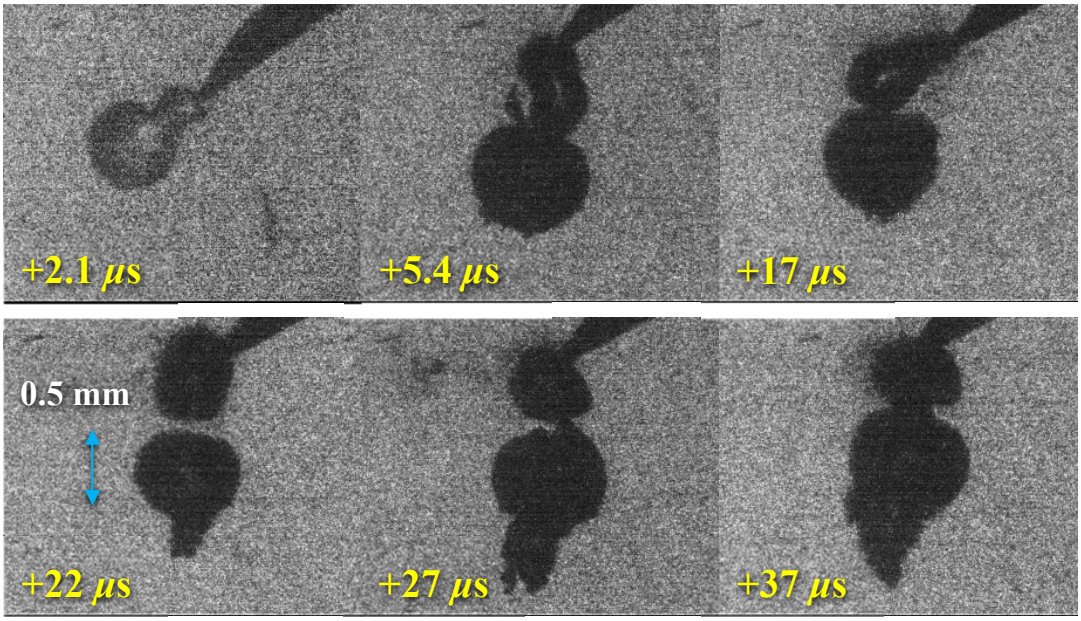

Figure 6.12: Evolution of the fluid boundary in the aftermath of the streamer impact. The conical wave front expands outward from a point that is directly across from the streamer impact location.

eter, ∼0.5 mm, after approximately 40 μs. As the conical wave front grows outward, the streamer channel becomes detached from the bubble. Eventually the channel cavitates, forming a separate residual bubble. This observation may explain the tendency of the bubble to decrease in radius after being impacted by the streamer. The cavitating streamer channel may absorb gas, thus allowing the bubble to stabilize on its own.

In general, the size of the bubble was observed to have a substantial impact on the dynamics of the exploding fluid surface. The time dependence of the fluid expansion was further investigated for four different bubble sizes. Due to the difficulty in injecting bubbles of constant size, each data set was compiled from bubbles of similar sizes. The average diameters of the bubbles in the four groups were, 0.5, 1.3, 1.8, and 2.4 mm. The standard deviation of bubble diameter in each group was kept under 10%. The expansion length was measured using the image processing software ImageJ. The fluid explosion length, Δx was defined as the difference between the tip of the explosion wave front and the diameter of the bubble at equilibrium,d_0, as illustrated in Figure 6.13. The equilibrium shape was calculated using an image of the bubble taken before the pulsed was applied and then superimposing it onto the exploding image to determine the distance between the tail and the surface. The results for the four sets of radii are shown in Figure 6.14. The primary uncertainty in these measurements was the projection of the boundary expansion on the 2-D photograph. Although care was taken to keep the needle in the same plane as the bubble (perpendicular to the camera), the streamer often would strike the bubble at an unknown angle. This would cause the camera to measure an expansion front distorted by a factor of $cos\ \Theta$, where Θ is the angle between the plane of the photograph and the entrance vector of the streamer.

Figure 6.14 indicates that the primary difference between bubbles of different size is the effective start time of the explosion growth. In practice, this corresponds to

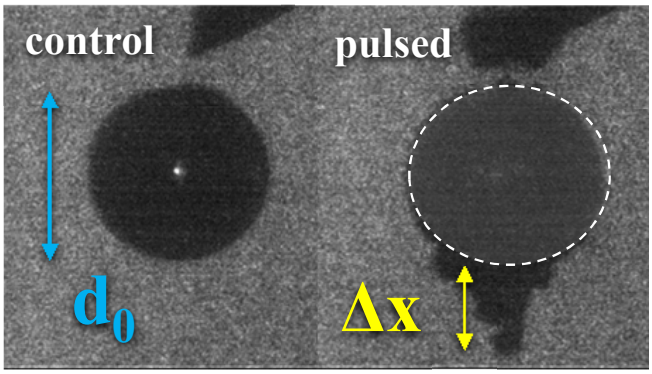

Figure 6.13: The fluid explosion length,Δx, was measured relative to the equilibrium diameter of the bubble, d_0.

the minimum time at which one can distinguish between the exploding boundary and the bubble. This is the reason so few data points exist for early expansion. One can quantify the effective explosion start time by extrapolating the expansion data backward to its intersection with the horizontal axis. This was done using basic regression analysis on each data set, using a least squares fit to construct each line. The linear fits are shown in Figure 6.14 beside each data set, along with an estimate of the explosion velocity beside each fit.

The average velocity obtained by the least squares fit gives values in the range 15-25 m/s. These average velocities are much slower than the acoustic timescales of either the gas or liquid [122]. One explanation could be that the expansion is driven by a phase instability at the interface between the fluid and the gas [131]. The spread in the length measurements obscures any size dependence, if any, that exists for the velocity. In reality, these calculations represent a lower limit on the velocity of the fluid boundary. More importantly, the transient behavior of the fluid surface at early timescales has not been resolved. The velocity of the fluid could be much larger at times immediately following the streamer impact. Higher time resolution of the fluid explosion is required to determine the true velocity. One indication provided by

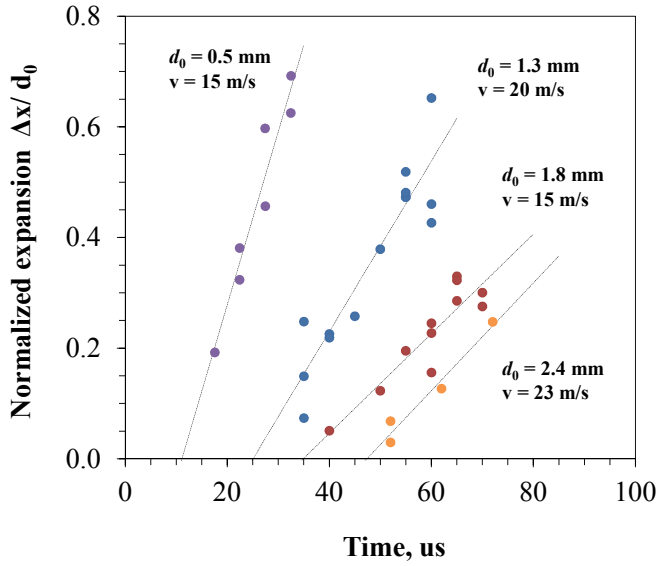

Figure 6.14: The extent of the exploding boundary as a function of time following the breakdown event. Average bubble diameters were 0.5 mm, 1.3 mm, 1.8 mm, and 2.4 mm.

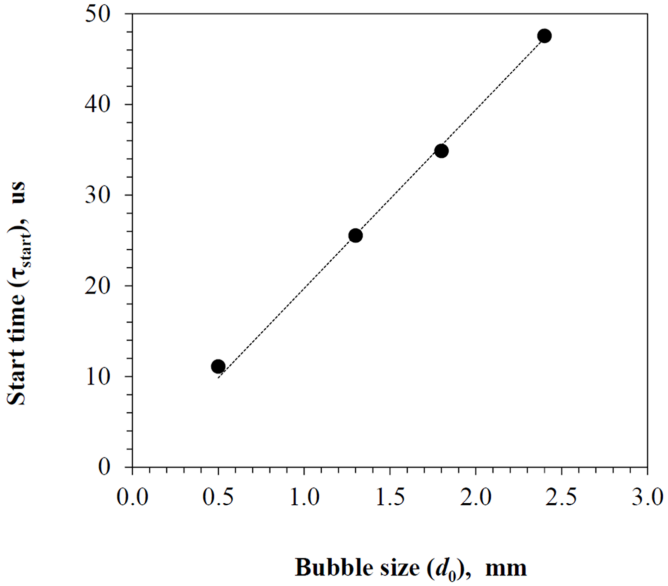

Figure 6.15: The explosion start time as a function of the equilibrium diameter. The larger the bubble, the longer the delay until the fluid boundary begins to explode outward.

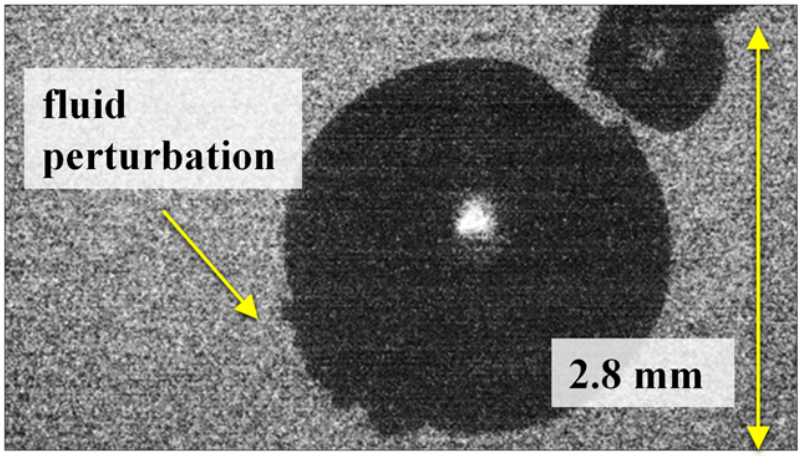

Figure 6.16: The response of the bubble boundary at early times closely resembles a surface wave, which is distinct from the conical wave front observed at later times.

Figure 6.14 is that the explosion start time appears to be sensitive to bubble size. The size dependence could be due to a number of factors. One explanation is that smaller bubbles have higher energy densities associated with the streamer interaction occurring at the streamer focal point. This would cause the explosion to be initiated at earlier times.

One final point that should be addressed is the lack in the current understanding of the early fluid instability. It is not only evident that such displacements are difficult to measure via image processing, but it is unclear if this timescale can even be considered as simply an early boundary expansion. Indeed, at times well before the explosion cone becomes visible, the surface physics of the bubble instability appear very complicated. Figure 6.16 shows what appears to be the early onset of a Rayleigh-Taylor instability on the bubble 60 μs after the streamer has made contact with the bubble. As discussed in Section 6.2.2, streamer related pressure waves may be at the heart of the observed instability.

6.4 Plasma Ignition in Isolated Bubbles

The multiphase streamer offers the first recorded example of plasma excitation in a bubble isolated from the electrode surface. In this case, however, the bubble plasma relies on a preexisting liquid streamer to transfer plasma excitation from the electrode tip to the bubble surface. It remains to be seen if a plasma can be excited solely in the volume of the bubble gas. Confining the plasma to the bubble requires that the ratio of the field at the needle tip to the field in the gas not be too large. One way to confine plasma formation to the bubble, therefore, may be to simply reduce the field at the electrode tip. If it is possible to ignite plasma in an isolated bubble using the wire-plane geometry from Figure 6.2, then not only would it be the first known occurrence of such phenomena, but it would also provide an initial estimate of the reduced electric field (E/N) necessary to produce plasma in a bubble. Of the two gases investigated in this work, air and helium, helium has a much larger ionization coefficient, α, for low to moderate values of the reduced field (10-100 Td). As a result, helium bubbles should be easier to ignite than those with air.

6.4.1 ICCD Imaging of Ignition in Isolated Bubbles

ICCD images were taken of levitating bubbles pulsed by the Suematsu supply. The geometry was kept the same, as seen in Figure 6.2. In each case, the ICCD camera was set to a 500 ns gate and the telescoping lens was set at 2.4X zoom. The applied voltage and electrode gap were carefully adjusted to prevent a liquid streamer from forming at the electrode tip. It was observed that reducing the voltage to approximately 12 kV was in some cases sufficient to observe plasma formation in the bubble without a streamer bridging the gap. However, this procedure was quite chaotic and not entirely repeatable. In general, it was easier to ignite plasma in helium bubbles compared to air bubbles. In the case of helium, the probability of plasma formation was also sensitive to the residence time of the helium bubble. For

bubbles that were pulsed within 30 seconds of injection, plasma formation was much more likely than those cases that were allowed to sit for up to 10 minutes. Igniting recently injected bubbles was also observed to result in a more widespread glow in the bubble. These time dependent effects are primarily due to the diffusion of the helium gas out of the bubble and into the water. Even for helium bubbles submerged for only 30 seconds, the discussion of Section 6.1.2 indicates that most of the helium has mixed with the water. However, looking at the vast difference in the ionization coefficient in Figure 2.3, it is clear that a small amount of helium will still have a large effect on the formation of plasma in the bubble.

Figure 6.17 shows several examples of plasma being excited in an isolated bubble filled with helium. Part (a) shows a control bubble (without any voltage applied) for reference. In this case, a small glow is observed at the center of the bubble. As discussed in Chapter 3, this does not correspond to plasma formation, but instead to the focused image of the backlight on the bubble. In parts (b) and (c), the plasma forms in two distinct locations; a gas plasma that occurs on the inner walls of the bubble and a liquid streamer that occurs at the tip of the needle. The electrode gap in these cases is approximately 0.25 mm with bubble diameters in the 1.5 mm range. In part (c), we see the effect of slightly decreasing the applied voltage. The liquid streamer is significantly less intense as is the bubble plasma. At the very top of the bubble, one can see the reflection of the liquid streamer on the bubble surface. This reflection is quite distinct from the more diffuse glow occurring within the volume. To obtain a clearer picture of the plasma in the bubble, the backlight was turned off. Part (d) shows plasma in the formation without any backlight. From this view, the bubble plasma appears brighter and more diffuse, covering the entire surface of the bubble. A reflection of the branched streamer can be seen on the top of the bubble.

The excitation of plasma in bubbles composed only of air was possible, but required the bubble to be extremely close to the electrode tip. In Figure 6.18, the

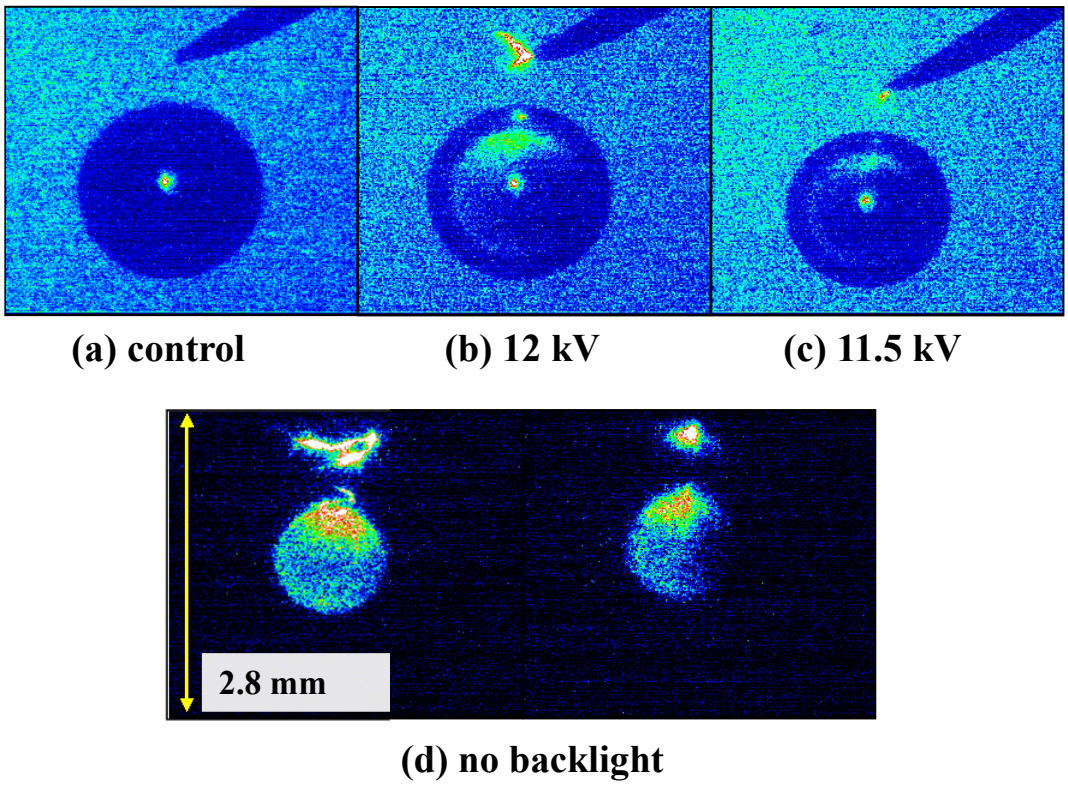

Figure 6.17: The excitation of plasma in a helium bubble contaminated with air for five cases: (a) a control bubble not driven by any pulse, (b) A 12 kV pulse, (c) a 11.5 kV pulse (d) two examples of plasma excitation at 13.6 kV with the backlight turned off.

bubble appears to be nearly in contact with the electrode but is actually at a distance of 150 μm. In this case, we see the benefit of using the acoustic levitation field. The needle tip is small enough that it does not disrupt the bubble from levitation. Instead, the reflection of the sound field off of the electrode, as discussed in Chapter 3, keeps the bubble separated from the needle, allowing one to get extremely close to the bubble without touching it. The image of the bubble was captured at 500 ns exposure.

It was observed that better coupling of the plasma to the interior of the bubble could be accomplished by using repetitive pulses from the Suematsu supply. Figure 6.19 shows the effect of pulsing a helium filled bubble at 50 Hz and 12 kV. In this case, the bubble is 0.25 mm from the needle tip and the ICCD was set at 500 ns exposure. The first frame shows an image of the bubble before any pulse is applied. As the number of pulses increases, after approximately 1 second, a faint plasma can be observed in the bubble. After 5 seconds, the plasma becomes more intense filling a large fraction of the bubble volume. It is clear in these frames that the most intense plasma forms at the bubble surface at the point closest to the needle electrode. More importantly, the plasma excitation appears to be completely confined to the interior of the bubble. A similar test was performed with the pulse frequency increased to 200 Hz. However, this generated liquid streamers at the electrode tip and in some cases caused spark formation across the electrode gap.

It is unclear what effect the repetitive nature of the applied pulses had on improving plasma formation in the bubble. At 50 Hz, the time between pulses is 20 ms. This is much longer than the lifetime of any plasma species formed during the pulse [89]. One possible explanation is that the plasma formation results in a local energy deposition inside the bubble gas. This effect would be compounded over the course of many cycles leading to a gradual increase in temperature. Such a temperature change would increase the vapor pressure in the bubble, leading to a higher con-

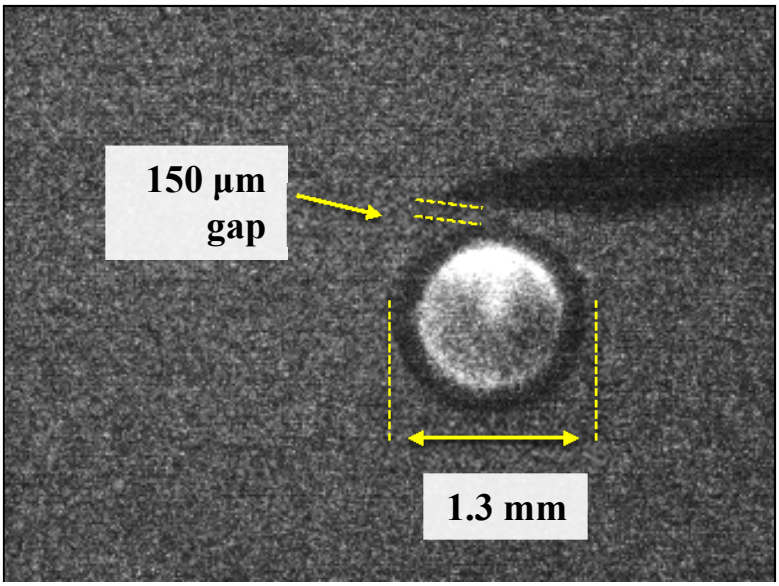

Figure 6.18: The excitation of plasma in an air bubble. In this case, plasma is excited only when the bubble is extremely close to the electrode tip.

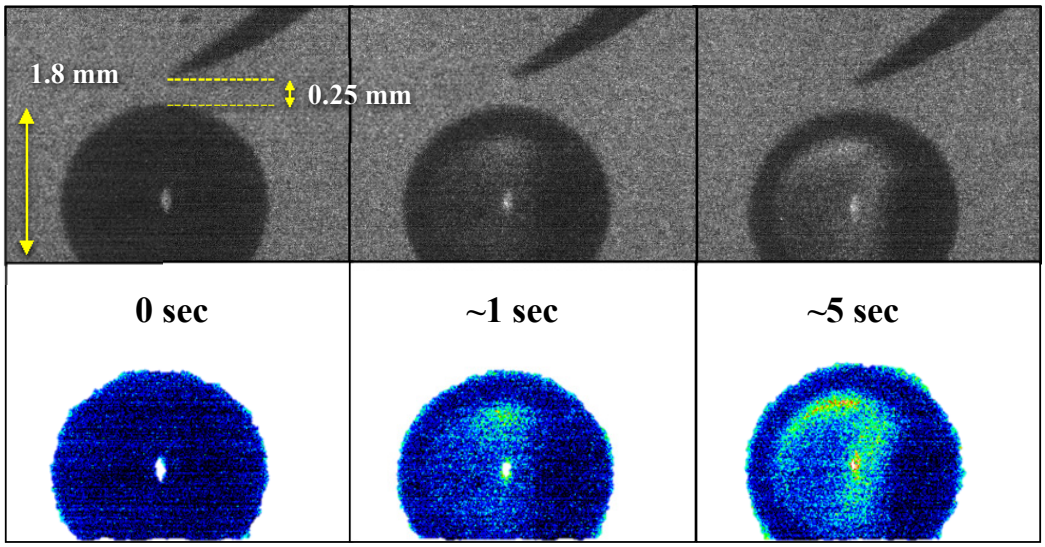

Figure 6.19: The excitation of plasma in a detached helium bubble under a 50 Hz, 12 kV pulsed voltage signal. Both rows are displayed in the ICCD intensity scale 590-700 counts.

centration of water vapor. Looking at Figure 2.1, the ionization coefficient of water vapor is significantly higher than that of air. Thus, an increase in temperature would tend to facilitate plasma formation. A temperature increase might also increase the conductivity of the surrounding water, leading to greater charge injection at the surface of the bubble and therefore provide a larger population of seed electrons for the discharge.

In general, the ability to excite plasma in isolated bubbles was observed to be extremely unreliable and was very sensitive to the cleanliness of the electrode. Despite this difficulty, it is clear that full wall hugging streamers were ignited in a bubble without any contact from the electrode. These images provide a basic foundation for estimating the actual breakdown conditions in an isolated bubble. Once these breakdown conditions are better understood, it may be possible to determine the necessary distortion of the bubble required to achieve plasma formation in bubbles that are farther away from the electrode.

6.4.2 Estimating the Electric Field and Ionization Coefficient in an Isolated Bubble

The breakdown conditions for streamers forming in the isolated bubbles observed in Section 6.3.2 can be computed if one has knowledge of the electric field inside the bubble. The electric fields in these cases can be estimated using electrostatic simulation of the field in the bubble. The 2D electrostatic solver, Maxwell, was used to replicate the electrode geometry shown in Figure 6.2 and compute the electric field inside the levitated gas bubble. A similar wire to plane geometry was created using an electrode gap of 5 mm. To simplify analysis, the wire electrode was aligned with the central axis, which reduced the problem to a 2-D solution with R-Z symmetry. The wire electrode was modeled as a thin rod with a half circle arc forming the electrode tip. The tip was chosen to have comparable radius of curvature to the needle electrode

(∼0.2 mm). The needle electrode was biased at a positive 10 kV voltage to obtain similar conditions to experiment. The bubble diameter was varied in the range 0.1-0.5 mm in radius and bubble-electrode gap was varied in the range 0.25-1.0 mm.

The apparent ionization coefficient, λ, was computed as a function of the electric field, E, using the semiempirical fit presented in Figure 2.3. The position dependent knowledge of λ was used to calculate the ionization product, M, inside the bubble using equation 2.12. The integration path chosen for this calculation was along the centerline of the bubble. Although this is not the typical path traveled by the streamer (most streamers in bubbles are wall hugging), it still provides a figure of merit to estimate the probability of plasma formation. In all cases, the pressure in the bubbles was assumed to be 1 atm. At this pressure, values of λ in air of 300, 100, and 10 cm6−1 correspond to electric field strengths of approximately 70, 50, and 30 kV cm^{-1} respectively. This illustrates the high sensitivity of λ to the applied field in the range of 30-70 kV cm^{-1}.

Figure 6.20 shows simulations of the apparent ionization coefficient, λ, for 0.75 mm sized bubbles composed of air and helium respectively. The calculated value of M is displayed inside each bubble. In addition, Figure 6.21 shows the effect of changing the bubble size on the ionization product M. The calculated values of M, as well as the voltage drop across the bubble, are plotted in 6.22.

As the bubble position is changed from 0.25 mm to 1.0 mm, the value of λ inside the bubble drops off dramatically. This drop-off is due to the high sensitivity λ in moving to regions of lower electric field strength. At the closest distance, λ grows to well over 100 cm^{-1} while dropping off to below 0.1 cm^{-1} at the farthest point. The ionization product, M, was calculated using equation 2.12 for each bubble size. The calculated value is displayed inside each bubble. It is also plotted in Figure 6.18. In the case of air bubbles, M does not exceed a value of 20 (the Meek condition) until the bubble is within 0.25 mm of the electrode. This explains the observations in

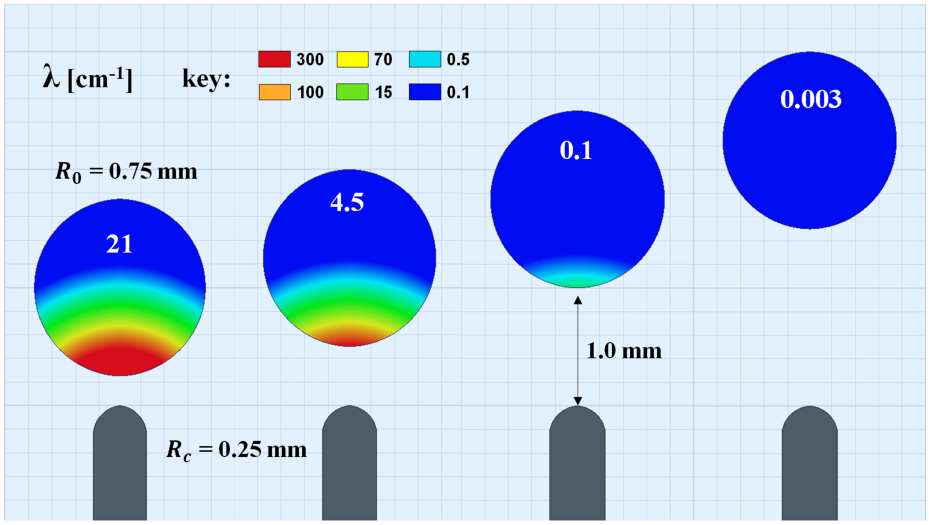

(a) Air

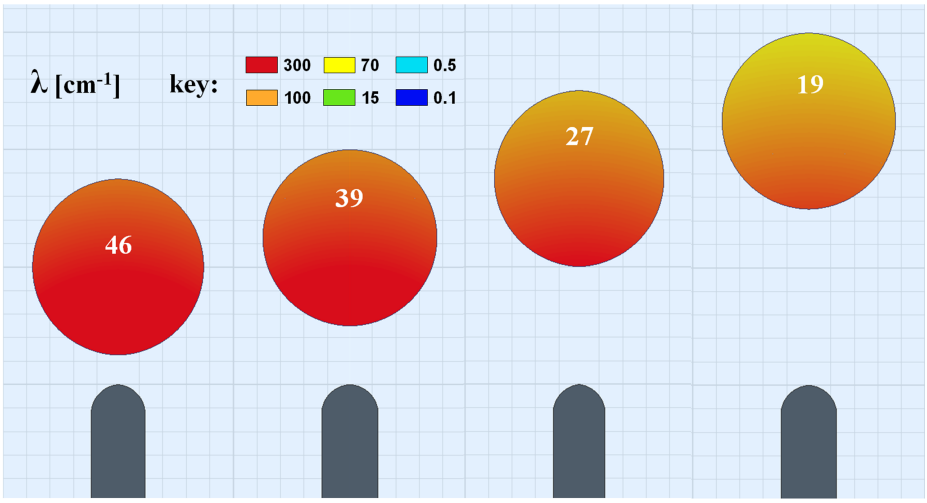

(b) Helium

Figure 6.20: 2-D maps of the apparent ionization coefficient, λ, for (a) air bubbles and (b) helium bubbles. All values are shown in units of cm^{-1}. The ionization product, M, calculated using equation 2.12, is displayed in each bubble.

Figure 6.18, which indicate that plasma is only formed in bubbles in the immediate vicinity of the electrode.

The sharp attenuation of M in air bubbles can also be explained by the sensitivity of $\alpha - \eta$ to the reduced field in the region near 100 Td (27 kV cm^{-1}). In this range, λ is very low and dominated by attachment. It is not until the reduced field is increased to the range 150-200 Td (40-50 kV cm^{-1}) does the value of λ increase far above the 1 cm^{-1} mark. Helium, on the other hand, has a significantly higher value of λ at lower values of E/N, which explains the considerably larger values of the ionization product, even at the largest distance of 1.5 mm. For comparison, at $E/N = 100$ Td (27 kV cm^{-1}), the value of λ is well above 300 cm^{-1}.

The simulations of helium suggest that one should be able to ignite helium plasma bubbles at significantly larger distances than those observed. There are, however, a number of reasons to explain the disparity between this model and the experimental observations in this work. The primary reason is most likely the immediate diffusion of helium out of the bubble when it is injected, as discussed in Chapter 3. Not only would this cause the helium content to decrease but it would also lead to the inward diffusion of water vapor and dissolved oxygen from the water, two sources of attachment. For example, at a reduced field of 100 Td (27 kV cm^{-1}), the attachment coefficient, η, for both gases is of order 100 cm^{-1} [92].

In reality, the actual ionization product lies somewhere between the curves for air and helium shown in Figure 6.22. Another possible contribution to ionization in the bubble is the electric field produced by the liquid streamer. Figure 6.17, for example, shows an example of a liquid streamer excited in the liquid accompanying the excitation of a gas streamer in the bubble. As discussed in Chapter 2, the electric field strength at the tip of the streamer is very large, ($\sim$100-500 kV cm^{-1}). If the streamer is ignited in the vicinity of the bubble boundary, the intense field strength may have an influence on the excitation of plasma in the bubble gas.

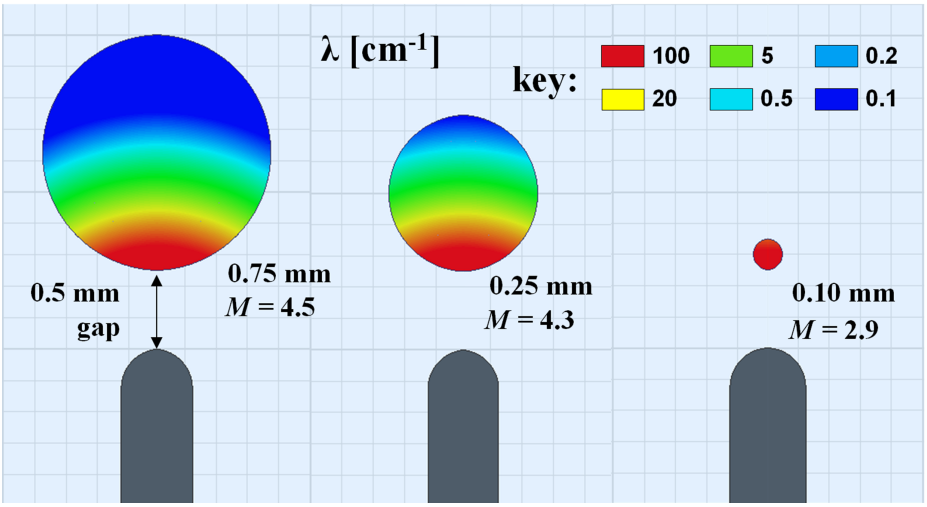

Figure 6.21: The dependence of λ on the size of the bubble for three different air bubbles. The total ionization product becomes sensitive to the bubble diameter, d when the attenuation length of λ is comparable to the size of the bubble.

Figure 6.21 shows the effect of changing the bubble size on the ionization product. From left to right, the bubble radius is 0.75 mm, 0.25 mm, and 0.1 mm. The bubbles are positioned such that the gap between the electrode tip and the bubble boundary stays constant at 0.5 mm. In decreasing the bubble diameter from 0.75 mm to 0.25 mm, the ionization product does not change appreciably. This is due to the fact that λ decreases drastically over a distance smaller than the bubble radius. Thus, the value of the ionization product should not change until the bubble diameter becomes comparable to the distance over which λ changes. In the third case, this condition is met with a bubble that is 0.1 mm in radius. In this case, the value of λ is large over the entire span of the bubble. For bubbles smaller than this size, M should dramatically decrease as the value of λ remains approximately the same but the effective gap d decreases. This observation suggests that there is a minimum bubble size required to achieve breakdown. Another way to view the changing breakdown conditions in both figures is to consider the voltage drop across the bubble diameter, which is shown in Figure 6.22. Each curve corresponds to one of three different bubble sizes, 0.1, 0.25, and 0.75 mm while the x-axis (bubble distance) corresponds to the value of

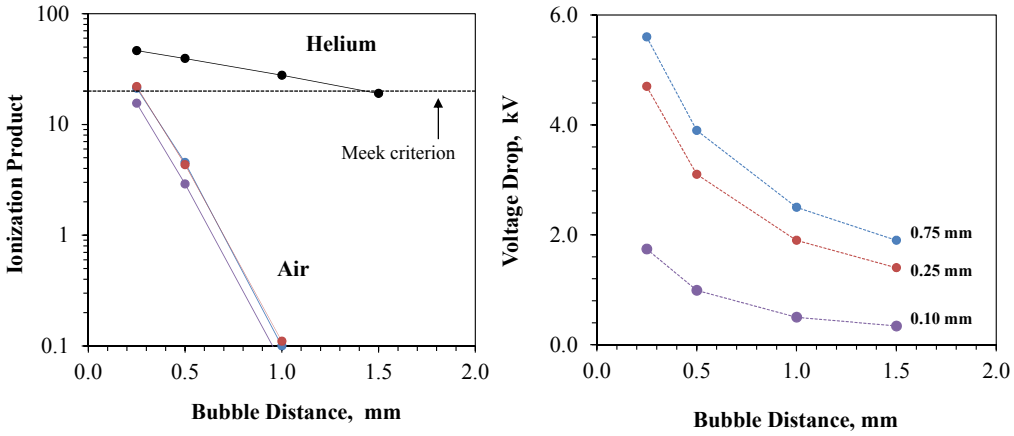

Figure 6.22: The ionization product, M and the voltage drop across the bubble for different bubble sizes of air bubbles along with the single case for helium. In the case of helium, the bubble radius is 0.75 mm.

the electrode-gap spacing. At the closest distance, the point at which the streamer criterion is met corresponds to a voltage drop of 5.6 kV. When the bubble size is decreased to 0.1 mm, the voltage drop decreases to 1.9 kV. In general, the minimum diameter, d_{min} (bubble diameter) can be increased by increasing the field, E, or decreasing the neutral density N. These two improvements could be accomplished by utilizing the shape effect.

This chapter has presented a broad overview of discharge mechanisms occurring in bubble filled liquids. This characterization has yielded a wealth of new phenomena, including the observation of a multiphase streamer as well as the formation of plasma in an isolated bubble. It is clear that careful design of electrode geometry and the applied voltage pulse can be utilized to confine plasma to the interior of the bubble. Although this achievement has been limited to bubbles that are close to the electrode, it is clear from the capillary wave deformations in Chapter 4 and the shape mode deformations in Chapter 5 that the shape effect may play an instrumental role in extending the reach of the plasma farther into the volume of the liquid.

CHAPTER VII

Plasma Ignition in Deformed Gas Bubbles

7.1 Experimental Overview

The previous two chapters have introduced two crucial but separate areas in the understanding of discharge physics in bubbles. In Chapter 5, the application of electric fields was used to induce extreme shape deformation while in Chapter 6, the application of electric fields was used to ignite plasma in unperturbed bubbles. In this chapter, we combine these two elements to investigate plasma formation in gas bubbles that are deformed by an electric field. This is accomplished using two different approaches: (1) a single field driving scheme, in which electric fields generated by a single voltage supply are used to both deform the bubble and excite plasma ignition, and (2) a dual field driving scheme, featuring two separate voltage sources, one used to deform the bubble (the drive voltage) and one used to ignite plasma (the pulse voltage). It is clear from the last two chapters that the voltage required to deform the bubble and the one used to ignite plasma have fundamentally different requirements.

The resonance frequencies required to drive bubble oscillations are on the order of 100-1000 Hz. These frequencies are determined by the time required to overcome the resting inertia of the fluid and deform it against the force of the local surface tension. Any drive field must be sufficiently long to achieve substantial distortion of the fluid boundary. However, as seen in Chapter 5, the voltages required to create substantial

distortion (5-10 kV) are not as large as those required to ignite plasma in the bubble (12 kV). Plasma timescales on the other hand are much shorter, occurring on the order of 1-100 ns. An igniting pulse that is too long can lead to excessive energy deposition and in some cases spark formation across the liquid gap [48]. Hence, the voltage required to ignite the plasma should be ideally a fast pulse. In contrast, a single field scheme will have to have both large duration ($\sim$1 ms) and large amplitude (12 kV).

7.2 Plasma Ignition Using a Single Source

Using a single voltage source to drive and ignite the bubble is perhaps the most straightforward approach to igniting plasma in an isolated, deformed bubble. This approach was accomplished using the TREK high voltage amplifier. The arbitrary waveform generator was used to produce a D.C. voltage pulse of arbitrary duration and amplitude. In these experiments, the pulses ranged from 300-1000 μs with voltages in the range 10-15 kV. Figure 7.1 shows the typical geometry used to drive and ignite bubbles. It very closely resembles the electrode geometry from Chapter 6, but the syringe needle has been replaced with a molybdenum wire with larger radius of curvature. The coarser tip was chosen to suppress ignition of the liquid near the electrode tip. This issue is especially important for long pulse times, which can lead to heating of the water and eventual spark formation. The use of the wire, on the other hand, still maintains the field intensity required to achieve nonlinear deformation of the bubble.

7.2.1 Experimental Results

Figure 7.2 shows an example of a long pulse applied to stretch and ignite the bubble. In this case, a 0.6 mm diameter bubble is driven by a 1 ms pulse with a peak voltage of 11.2 kV. During the first 300 μs of the applied pulse, the bubble is stretched

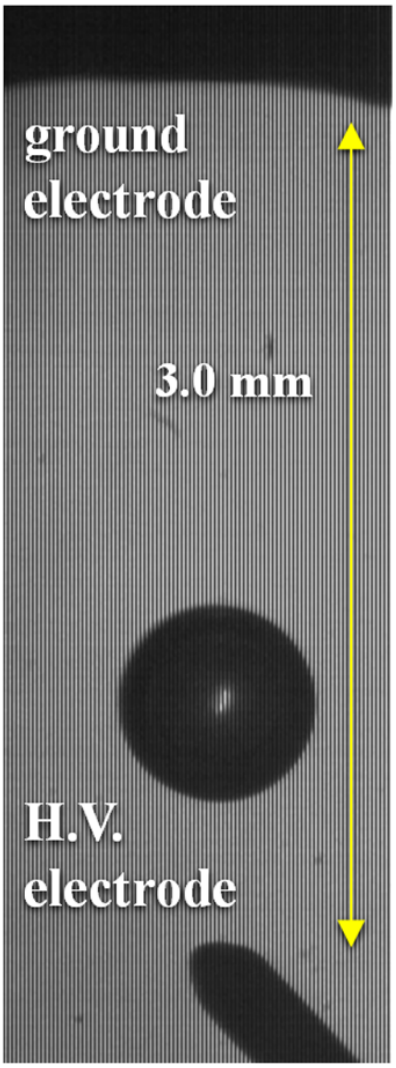

Figure 7.1: The modified wire-plane geometry used to drive and ignite a single bubble. The molybdenum wire electrode tip is not nearly as sharp as the syringe needle.

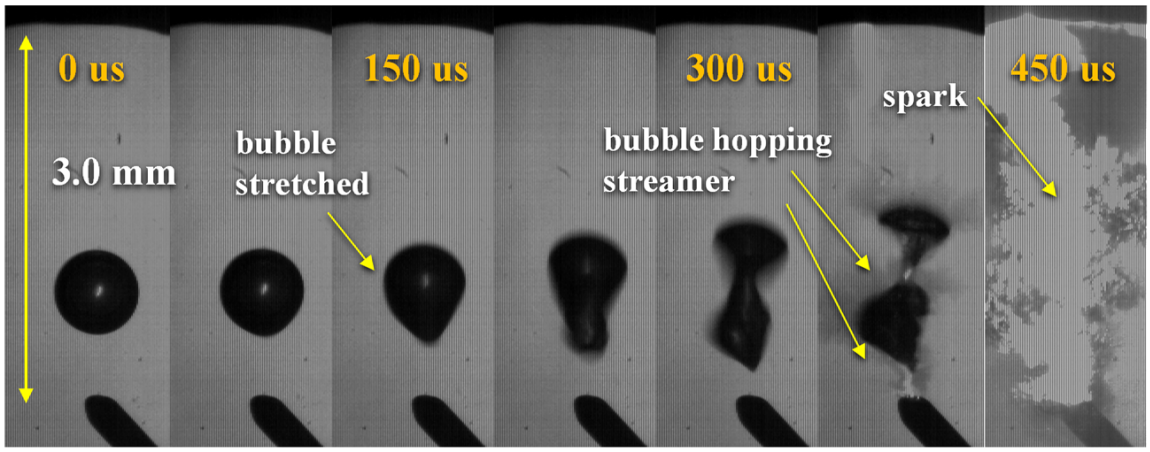

Figure 7.2: A single 1 ms electric pulse is applied to a levitated bubble. The bubble first distorts in response to the field and then aids in the ignition of an arc. The applied +voltage is 11.2 kV.

and deformed. Due to the extreme nonuniformity in the applied field, the bottom half of the bubble is perturbed severely, resulting in the balloon like shape observed at 150 μs. Eventually, the bubble's sides begin to contract. In Chapter 2, this effect was illustrated in the context of a uniform field, which tended to squeeze the sides of the bubble inward and stretch the tips axially. At 300 μs, the bubble begins to break apart. In this case, however, the top half of the bubble is deformed to a significantly different shape than the bottom half. This is due to the nonuniformity in the field, which results in a gradient in the electric pressure. As a result, the bottom portion of the bubble is pulled downward with more force than the top part. This force gradient actually results in a vertical contraction of the top fragment. This contraction is similar to the contraction of the even spherical modes, observed in Figure 5.11. In that case, a contraction in the direction of the field resulted in extreme enhancement of the electric field, by a factor of 5-10. In this case, such field enhancement may be responsible for the ensuing ignition of a streamer, which travels between the two bubble fragments and eventually ignites a full spark. This case constitutes an example of a liquid streamer traveling from bubble to bubble, a concept proposed by Babaeva

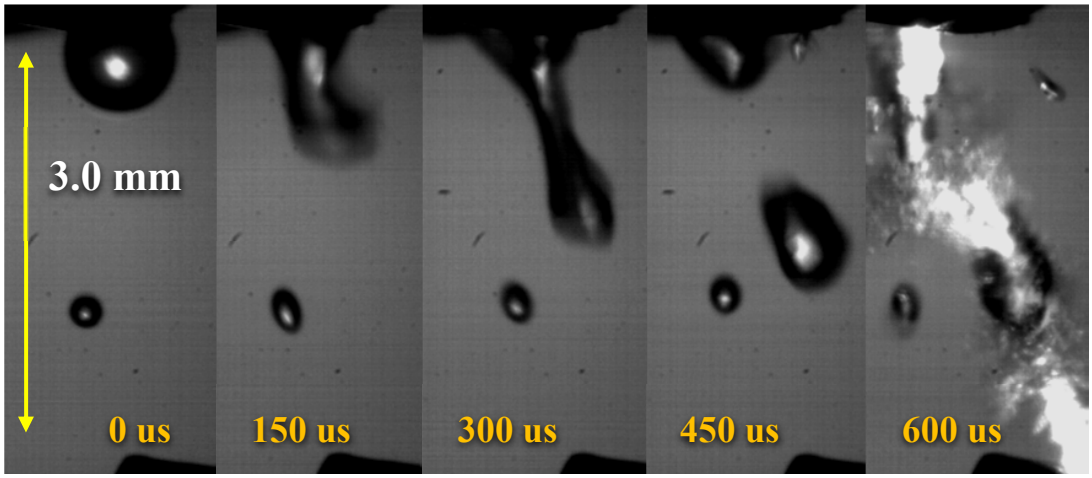

Figure 7.3: An initially attached bubble is pulled off the electrode, eventually aiding in the ignition of a spark across the electrodes. The applied voltage is 11.2 kV.

and Kushner [88] and described in Chapter 6 as a possible propagation model for plasma ignited in bubble filled liquids. In general it was observed that, with this electrode gap (3 mm), the same voltage applied in the absence of a bubble would not result in a spark. This indicates that the presence of the bubble, more specifically the deformed bubble, may be important in determining the formation of plasma in the gap. Figure 7.3 shows another example of this phenomenon. In this case, the bubble is initially attached to the top electrode. Following the application of the electric field, the bubble stretches downward eventually detaching from the electrode. The detached fragment, having just snapped off from the attached bubble, subsequently undergoes oscillations of a very complicated nature. At a certain point, this distorted bubble fragment provides the necessary bridge to, once again, initialize a spark between the electrodes. The resulting spark appears to be influenced by the bubble geometry as it is observed to travel directly through both the detached bubble fragment as well as the residual attached bubble on the top electrode.

In certain cases, the 1 ms pulse was not sufficient to ignite a spark between the

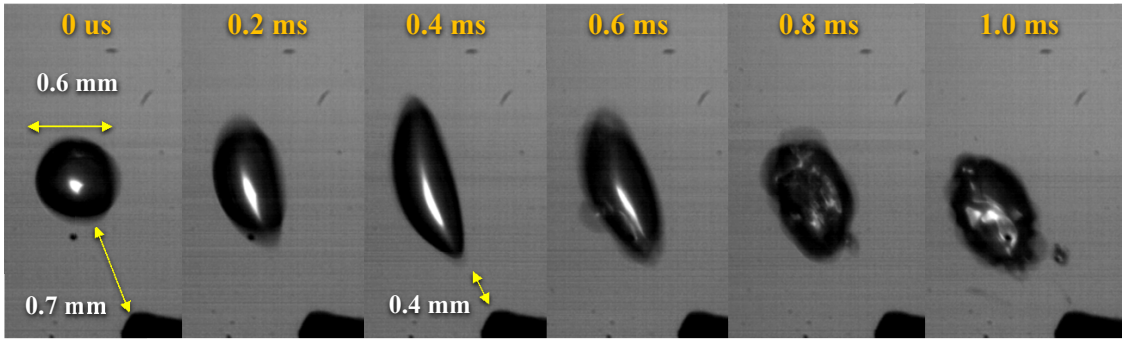

Figure 7.4: Following the elongation of the bubble by the applied field, small amplitude waves are spontaneously excited on the bubble surface. This phenomenon could be a result of plasma ignition in the bubble.

electrodes but still resulted in considerable deformation of the bubble. In Figure 7.4, a bubble is stretched under the action of the electric field. In this case, however, the tip of the bubble becomes quite sharp in the vicinity of the pulsed electrode. At approximately 800 μs. the bubble undergoes spontaneous and violent capillary wave oscillations, without any sign of a bridging streamer. As observed in Chapter 4, these oscillations are an indicative of a plasma streamer propagating along the walls of the fluid boundary. It is possible that the large value of the electric field produced at the sharp tip of the elongated bubble resulted not in a spark between the electrodes but a plasma streamer isolated in the free standing bubble. It is difficult to know for certain if a plasma streamer was ignited in the bubble. There are a number other possible explanations for the observed phenomena. In particular, it has been predicted that sufficiently high electric fields are capable of destabilizing the fluid boundary of the bubble [130, 132]. However, this type of destabilization typically results in bubble breakup or droplet ejection. Another possible cause of the observed perturbations is the excitation of a Rayleigh-Taylor instability, as discussed in Chapter 4. In this case, the instability could arise during the expansion of the bubble surface moving downward toward the pulsed electrode. However, it could also be excited (as

speculated in Chapter 4) by the pressure at the tip of the plasma streamer inside the bubble. Overall, the exact source of the perturbations is ambiguous. Insight into the extent of plasma formation could be obtained by imaging similar phenomena with the ICCD camera. This could be used to determine if any light were emitted (due to plasma formation) from the bubble prior to wave excitation.

7.3 Plasma Ignition Using a Dual Source

Greater control of plasma ignition can be achieved by using two separate voltage sources, one source to drive distortion and another to ignite plasma. This optimal configuration would allow one to excite deformation over long timescales using moderate voltages ($\sim$ 5 k) while igniting plasma with the use of a secondary short, high voltage (12 kV) pulsed supply. To provide a simple demonstration of this principle, let us return to the example of the $l = 2$ mode. In this case, it was observed that an A.C. field could easily stretch the bubble. However, the extension of the bubble in the direction of the field was not conducive to field enhancement. Rather, it was speculated that a second field would need to be applied perpendicular to the original field to exploit the extreme contraction occurring during the fission of the bubble. In the following experiments, such a secondary source is generated using the Suematsu supply to ignite plasma in the bubble once it has been deformed.

7.3.1 Experimental Approach

Figure 7.5 shows the orientation for a simple two stage driving system. The driving electrodes are formed by a pair of circular, parallel plate electrodes. This generates a uniform field capable of deforming the bubble over fluid timescales of $\sim$ 1 ms. The second electrode, a 30 gauge syringe needle, is positioned at the side of the bubble. Using the delay generator, this needle was pulsed by the Suematsu pulser at a specified delay relative to the driving voltage. This approach can be used to ignite

plasma in the bubble at different degrees of deformation.

The driving voltage was generated by first creating a D.C. voltage waveform with the Agilent arbitrary waveform generator. This waveform was delivered to the TREK high voltage amplifier to produce signals with amplitude up to ± 20 kV with pulse lengths in the range 50-500 μs. Typical waveforms for both the driving voltage (TREK) and pulse voltage (Suematsu) are shown in Figure 7.5. The bottom electrode is grounded relative to both the needle and the top driving electrode. As discussed in Section 3.4.1, the 1 μs pulse delivered by the Suematsu pulser has a 1 μs negative overshoot due to the impedance mismatch with the load. Images were captured using the Redlake high speed camera with capture rates in the range 5000-13000 frames s^{-1}. The parallel plate electrode gap was set to 3 mm.

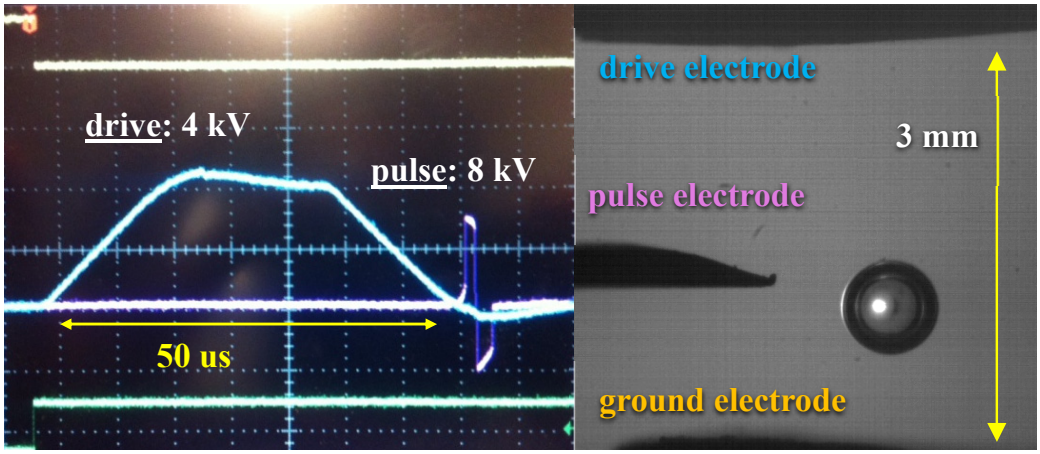

Figure 7.5: Dual voltage traces for the drive voltage (provided by the TREK) and the pulse voltage (provided by the Suematsu). The drive electrode stretches the bubble into the $l = 2$ mode, while the needle electrode pulses the bubble.

7.3.2 Results

Figure 7.6 illustrates the simultaneous stretching and ignition of the levitated bubble. When the driving field is applied, the bubble stretches vertically. This

deformation is asymmetric due to the nonuniformity of the applied driving field. Around 700 μs, the pulse voltage is triggered. At this point, the plasma ignition takes the form of a bridging streamer connecting the needle and bubble. The primary difference between this case and those observed in Chapter 6 is that the bubble is now deformed. The streamer can be seen entering the side of the bubble, but there is also an excitation at the top of the bubble, at the point closest to the driving electrode. This may be correspond to a secondary plasma ignited by the vertically aligned driving field. The next frame shows the fluid destabilization that is characteristic of the interaction between the streamer and bubble. In this case, the streamer derived pressure not only drives an explosion trail parallel to the bridging streamer, but also at the top of the bubble. This occurs at the same point where the anomalous excitation is observed at time 700 us. In the last two frames, one can see the clear expulsion of droplets from the "head" of the bubble indicating the complicated nature of the plasma fluid interaction.

A question that naturally arises is whether the plasma observed in Figure 7.6 can be confined to or initially generated in the bubble. ICCD imaging presented in the previous chapter indicates that even in the case of an undeformed bubble, it is possible to ignite plasma solely within the volume of the bubble gas. Considering the additional deformation introduced in these cases, it is quite reasonable to assume that some plasma may originate in the bubble itself. Figure 7.7 shows an example of, what appears to be, a specific case of bubble originated plasma. In this case, the bubble is deformed in a similar manner. After 600 μs, a streamer is ignited between the bubble and needle. However, in this example, the multiphase streamer (seen evolving in frame 3) appears to originate at the surface of the bubble. In later frames, the streamer has bridged the electrode gap and subsequently destabilizes the bubble. In 7.8, a similar result is observed. In this case, it is interesting to note that the streamer originates from a point on the bubble that corresponds to the largest contraction in

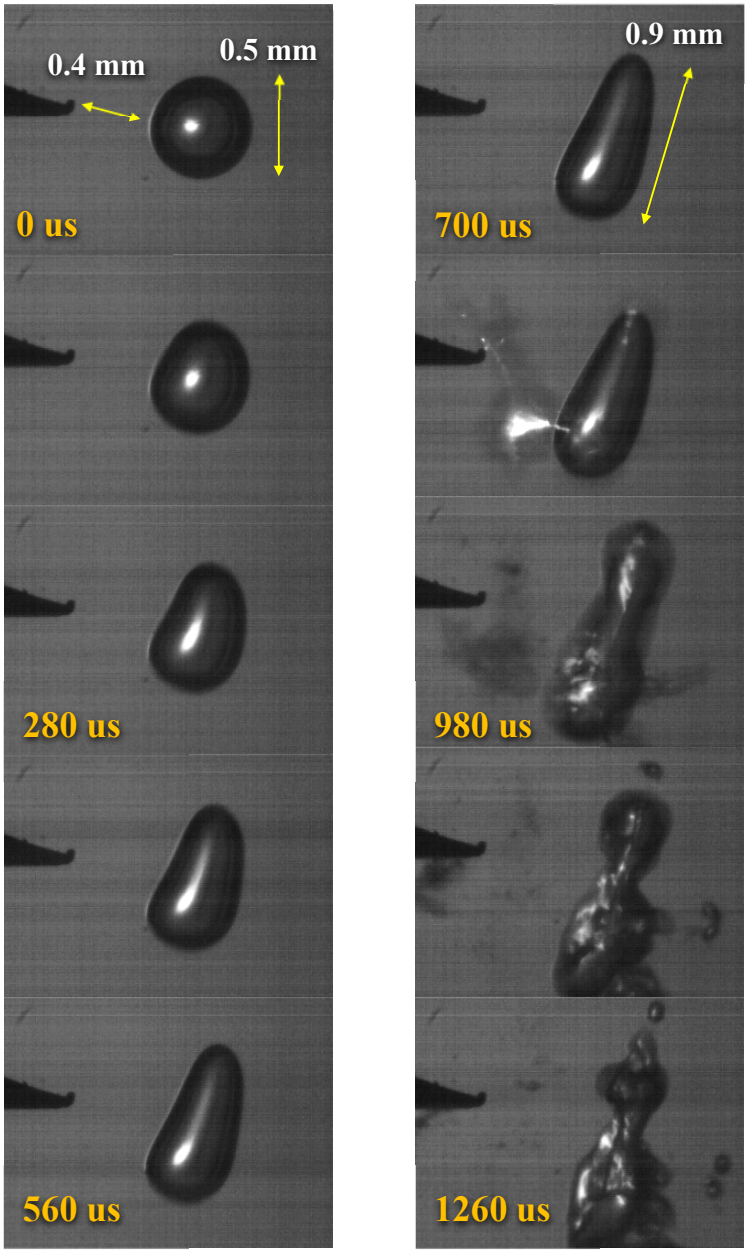

Figure 7.6: The bubble is stretched in response to the drive field. At 700 us, the pulse voltage is triggered, resulting a bridging streamer.

the direction of the applied pulse field. The resulting fluid destabilization appears to split the bubble at exactly this same point.

Figure 7.9 illustrates another way of viewing the influence of the bubble on the formation of plasma in the liquid. In this case, a spark is formed between the needle and the ground electrode. However, a small cluster of streamers, labeled (1) and (2) are observed to branch out from this spark and make contact with the bubble. In this case, the streamers appear to make contact with the bubble and then continue propagating on the ground electrode. This image indicates that streamers may be able to renter the liquid after making impact with the bubble. This has important implications in the design of a liquid processing reactor, as it is desirable to extend the plasma formation as far as possible into the liquid volume. As suggested in Chapter 6, one way to accomplish this may be to force streamers to jump between bubbles.

7.4 Simulation of the Electric Field Inside Deformed Bubbles

It is unclear from these images alone, whether the deformation achieved in Section 7.3.2 is sufficiently extreme to influence the breakdown conditions inside the bubble. It is clear that substantial field enhancement can result from stretching and contracting of the sides of the bubble. In these examples, however, the deformation is not nearly as extreme as the shape mode oscillations observed in Chapter 5. Let us now obtain an estimate of the field enhancement in these stretched bubbles to determine if deformation of the bubbles plays an important role in the formation of plasma. An estimate of the electric field was performed using Maxwell 2D. In this case the electrode-bubble system was approximated as a 2-D geometry of the X-Y type. In this case, the electrodes and bubble are imagined to extend out infinitely into the plane of the image. The needle electrode is set at 1.28 mm and the bubble diameter is set at 0.6 mm in order to simulate the experimental conditions from Figure 7.7. The deformed bubble is modeled as a rotated ellipsoid, with major and minor axis

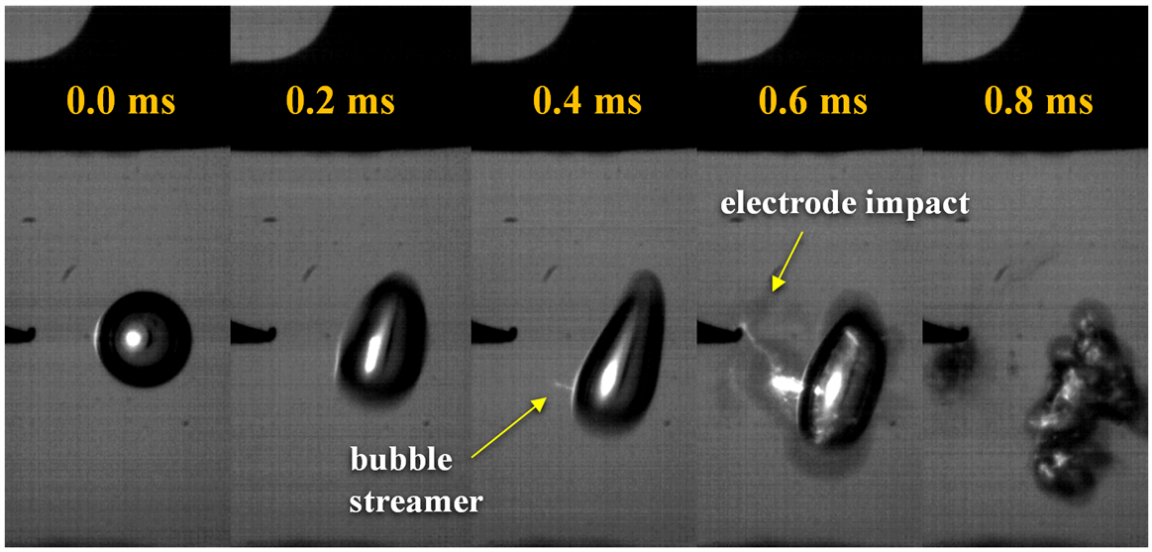

Figure 7.7: In certain cases, the bridging streamer appears to originate from the bubble, rather than from the needle electrode.

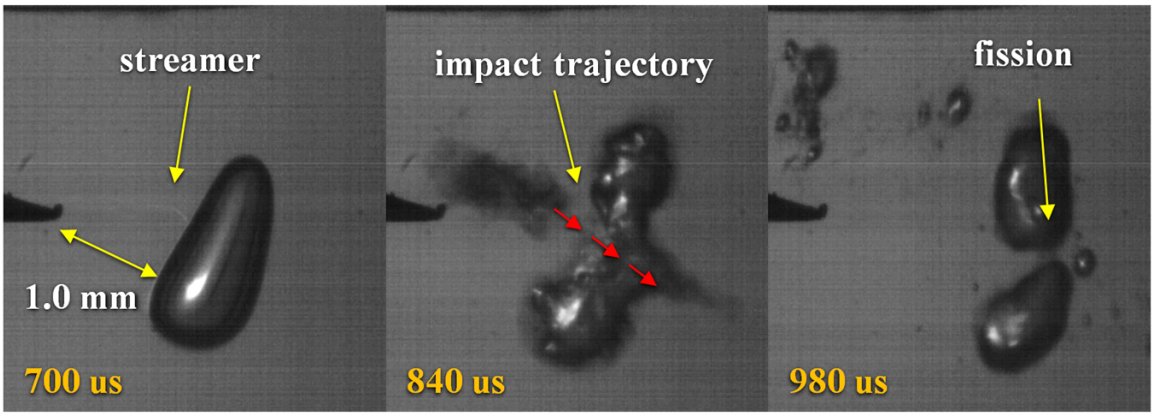

Figure 7.8: The bridging streamer splits the bubble into two separate fragments.

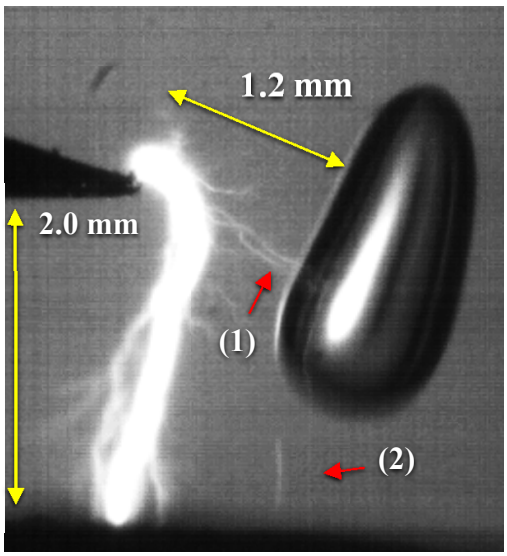

Figure 7.9: An arc bridges the needle and ground plate. Secondary streamers travel instead to the bubble (or vice versa).

set to 1.0 mm and 0.45 m respectively. The ellipsoid dimensions and the angle of rotation were computed using an image processing algorithm to fit the shape of an ellipsoid to the imaged bubble.

The simulated bubble does not reproduce the asymmetry of the experimentally observed bubble. However, from the electrostatic models generated in Chapter 5, it is clear that critical parameter in predicting field enhancement is the contraction of the bubble in the direction of the applied field. This dimension is matched between experiment and model. The magnitude of the electric field is simulated both in the deformed ellipsoid and in a control case, the spherical bubble at equilibrium. Figure 7.10 shows the geometry, field magnitude, and vector field for each case. One interesting observation from the plot of the field magnitude is the effective dipole moment that forms along the vertical axis of the ellipsoid. One consequence is that the maximum electric field is formed at the lower left corner of the deformed bubble. Looking back at the photograph of the bubble, this point corresponds exactly to the location where the streamer emerges from the bubble. This observation supports

the hypothesis that the streamer originates first in the interior of the bubble. It is immediately clear that the strength of the electric field is larger in the case of the elongated bubble. The maximum value, for example, in the deformed bubble is 150 kV cm^{-1} (558 Td) compared to 130 kV cm^{-1} (483 Td) in the spherical case, corresponding to an increase of 15 %. However, as discussed throughout this work, the maximum electric field is not the best indicator of plasma formation. A more accurate measure of plasma formation is the ionization product, M [92],

$$M = \int_{\ell} \alpha(\mathbf{x}) - \eta(\mathbf{x})\ d\mathbf{x} \tag{7.1}$$

Here ℓ is the path of integration. The dashed lines in Figure 7.10 indicate the integration path chosen. These correspond approximately to the direction of the field lines in the bubble. In the case of the spherical bubble, the ionization product is measured to be $M = 40$ while in the case of the ellipsoid, $M = 85$. This corresponds to an increase in the ionization product by nearly a factor of 2. In reality, both of these field simulations overestimate the electric field in the bubble due to the fact that they are treated as infinite in one dimension [107]. The finite extent of the dielectric boundary will tend to decrease the field enhancement in the bubble. Nonetheless, this calculation demonstrates the important principle that in the range of applied fields (10-50 kV cm^{-1}), a small increase in the field can give rise to a dramatic increase in the ionization product. This is especially important when evaluating the shape effect. Even if the field is increase by a factor of 2-3, as has been observed in many of the examples in this dissertation, the proportional increase in the ionization product M will be even larger.

Despite the limited degree of distortion achieved in these experiments, it is clear that the evolution of the multiphase streamer is directly affected by the elongated bubble. Images of the streamer originating at the surface of the bubble are exclusively

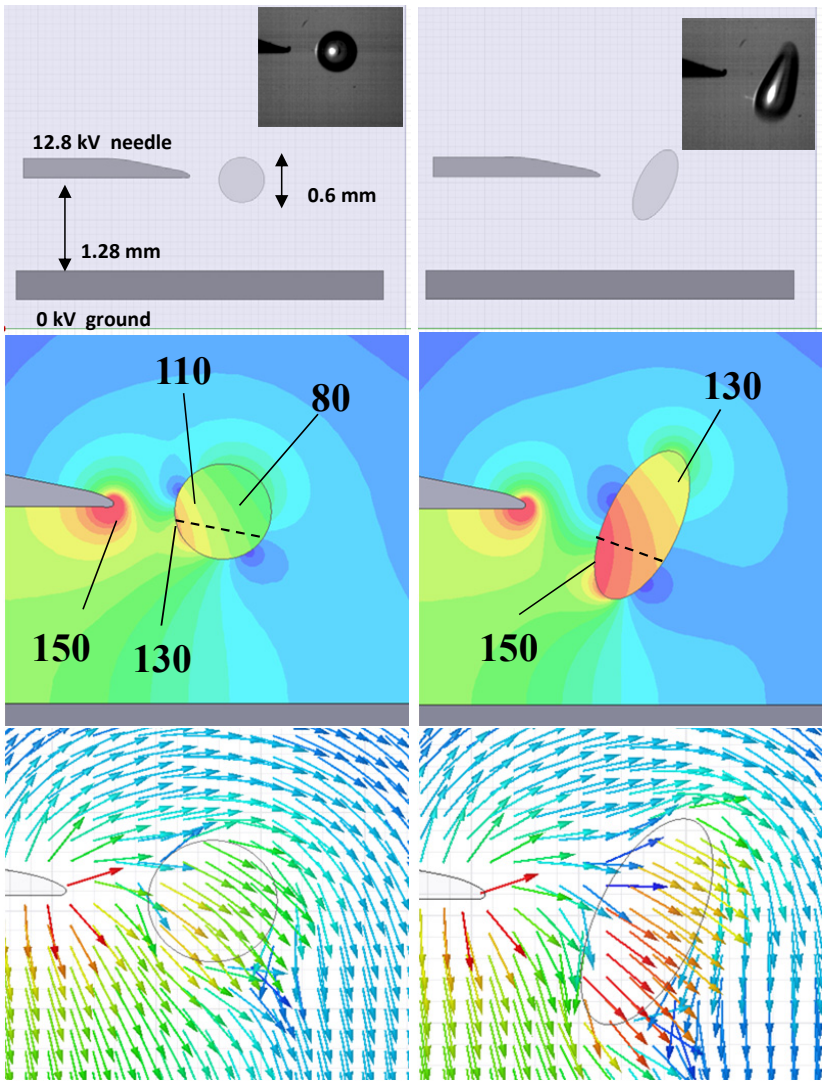

Figure 7.10: 2D Maxwell simulations of the electric field for both the spherical control bubble and the deformed ellipsoid bubble. (Top row): the simulated geometry along with the image that each is modeled after. (Middle row): the magnitude of the electric field shown in kV cm^{-1}. Dashed lines correspond to the integration path used to calculate M. (Bottom row): the electric field vectors in and around each bubble.

observed in cases where the bubble is distorted. It remains to be seen if the plasma can be confined solely to the bubble, as was observed in unperturbed bubbles in Chapter 6. Ultimately, the application of a dual driving system to more extreme bubble deformation, such as that achieved in Chapter 5, would further clarify the results observed in this chapter. The apparent excitation in Figure 7.4 is promising but does not constitute solid proof of plasma excitation. Overall, the trend is clear, distortion of the bubble shape will lead to significant enhancement of the internal electric field.

CHAPTER VIII

Conclusion

8.1 Overview of Research

The goal of this dissertation was to present a multifaceted investigation of plasma formation in underwater gas bubbles. This was motivated both by the potential use of bubble based plasmas for applications in environmental remediation as well as the desire to discover the fundamental processes involved in the excitation of plasma in underwater bubbles. It was proposed that plasma could be ignited in isolated bubbles by first exciting them into extreme deformation. One of the primary goals of this work, therefore, was to demonstrate this concept in an isolated underwater bubble. To accomplish this goal, a unique apparatus was developed to study underwater bubbles in a stable and controlled manner. This device is based on the use of ultrasonic acoustic standing waves to trap the bubble at a fixed position underwater. This device also included a modular electrode feed system mounted on a 3-D translation stage, capable of delivering intense electric fields to the surface of the bubble. Together these features were utilized to both deform the shape of the bubble and ignite plasma within its interior.

Early experiments were focused on understanding the basic properties of plasma formation in electrode attached bubbles. High speed imaging of a bubble driven by a 12 kV, 1 μs pulse, confirmed that streamers tend to follow the contours of the bubble

surface even in cases where the surface was deformed. The bubble streamers were also observed to cause significant perturbations of the bubble surface, illustrating the strong electric and acoustic pressure at the streamer tip. For a special set of conditions, the periodic impact of the streamer on the bubble surface was observed to excite resonant capillary waves, reaching amplitude up to 20 % of the equilibrium radius. The wavelength of these waves was observed to be 1-2 mm with a frequency of 500 Hz. It was further observed that these resonant waves could transmit similar oscillations to nearby floating bubbles up to 2 cm away.

Next, bubble deformation in isolated bubbles was investigated using the ultrasonic levitation cell. It was shown that a careful choice of driving frequency and electrode geometry was capable of exciting a wide variety of nonlinear, spherical harmonic perturbations of the bubble shape. Simulation of the electric field in these deformed shapes indicates moderate levels of field enhancement, on the order of 2-3. It was shown that this field evolution was similar to that observed in the case of a dielectric ellipsoid. Further simulations were used to prescribe the required shape distortions to achieve enhancement factors of 10-50, with the ability to reach large levels of the ionization coefficient, λ within the bubbles. Under the most extreme deformation it was predicted that an applied field of 20 kV cm^{-1} would provide the necessary ionization to satisfy the Meek streamer criterion $\lambda x \sim 20$. In general, the volume of the bubbles was observed to stay constant. Further analysis indicated that the applied field strength, frequency, and geometry in these experiments were all unoptimized for the achievement of volume mode oscillations. A number of possible changes were suggested to improve volume mode excitation in future experiments. The behavior of bubbles under the action of very intense electric fields ($>$ 20 kV cm^{-1}) was also investigated. It was determined that violent bubble breakup could be achieved at Weber numbers of approximately 16, corresponding to an electric field of 25 kV cm^{-1}.

The ultrasonic levitation cell was also used to perform an investigation of fundamental discharge mechanisms in bubble filled liquids. For a specific range of voltage and electrode geometry, a unique type of streamer discharge was observed that propagated through both the liquid and gaseous interior of the bubble. The impact of the streamer on the surface of the bubble was observed to result in an outward explosion of the fluid interface in the same direction as the impact trajectory of the streamer. This explosion formed 10-40 μs following streamer impact and its evolution was sensitive to the size of the bubble. ICCD imaging of this phenomenon indicates that the streamer channel undergoes a large increase in emission after the streamer makes contact with the bubble, closely resembling the charge relaxation commonly associated with dielectric barrier discharges. Following streamer impact, ICCD images confirm that plasma streamers are reignited in the interior of the bubble and travel predominantly along the bubble wall, just as in the case of an electrode attached bubble. Together these results indicate the observation of a new multiphase streamer that can travel through both gas and liquid.

Another significant result was that under careful adjustment of the operating conditions, the plasma could be confined to the interior of the bubble without the excitation of a bridging streamer. Electrostatic simulations of the applied electric field in the bubble indicate that the experimental conditions for this phenomenon are consistent with the Meek streamer criterion being satisfied inside the bubble. It was observed that this isolated bubble plasma could be ignited much easier using a repetitively pulsed voltage source.

Finally, an investigation was performed of plasma formation in deformed gas bubbles. This was accomplished using two different approaches: (1) a single source driving, in which one electric field signal was used to distort and ignite the bubble, and (2) a dual source driving scheme, in which one source was used to drive deformations of the bubble and another used to ignite plasma. Results indicate that deformation of

the bubble had a substantial effect on igniting arcs between the electrode gaps as well as initiating multiphase streamers that, for the first time, were observed to originate at the bubble rather than the electrode. Overall, this dissertation has presented three different new examples of plasma excited in an isolated, underwater gas bubble: (1) a liquid streamer that is initiated at the electrode and travels to the bubble, (2) a streamer that is initiated at the bubble and travels to the electrode, and (3) a gas streamer that is excited purely in the interior of the bubble.

8.2 Towards a Practical Plasma Reactor

The techniques utilized in this work have been focused on the fundamental physics of both bubble dynamics and plasma formation in dielectric liquids. It is an entirely different process to transform these techniques into a practical device that can be used for environmental remediation. Indeed, a separate dissertation could be written on the optimization of these techniques to develop and test such a device. In the spirit of guiding such efforts in the future, the following sections have been included to discuss the important factors that will influence the design of a practical device.

8.2.1 Source of Bubble Deformation

In this work, bubble distortion was achieved using electric fields. This approach provided precise control over the driving force used to excite the bubble. The use of high speed voltage supplies in particular, allowed one to control the frequency, duration, and strength of the applied fields, which directly determined the level of stress ($p_e \sim 1/2\epsilon_0 E^2$) acting on the bubble. There are a number of difficulties expected, however, in transforming an electric field based driving source into a practical reactor.

One reason, as explained in chapter 7, is that the field shape and pulse length required to deform the bubble are different than that required to efficiently ignite plasma. This necessitates the use of two separate voltage sources, which may compli-

cate the electrical design and space requirements of the device. Another issue is the large conductivity of liquids that would likely be processed in a reactor. Applying the shape driving fields on the order of ∼1 ms periods would increase the joule heating of the liquid medium [8], which would reduce the energy efficiency of the device. To determine if these issues can be overcome, further examination of shape deformation using electric fields is required. It may be possible to optimize the oscillation amplitude of the bubble through more efficient design of the electrode geometry and driving pulse shape, neither of which was pursued in this work. Furthermore, insulation of the driving electrodes by a high permittivity material may also be used to limit the joule heating of the liquid medium.

One possible alternative to electric field shape driving is to use pressure waves created by an ultrasonic transducer [110, 134] (much like the device described in Chapter 3) to excite shape deformations. Multiple studies have been undertaken to demonstrate both volume and shape modes distortions using pressure waves [124, 125]. Furthermore, transducers can be engineered to a wide variety of shapes and sizes to fit both the geometry of the device and the requirements for bubble shape driving [117]. These systems are also very simple, typically powered by something resembling car radio amplifier and can typically be run on 1-10 Watts absorbed power [117]. The power required for plasma production, for comparison, could reach up to kilowatts [59].

8.2.2 Optimal Deformation Type

Another design consideration is to determine the optimal deformation type for bubbles in a practical reactor. In this dissertation we have considered spherical harmonics, capillary waves, and even stretched bubbles. Spherical harmonics provide a source of extreme curvature change that can be exploited to achieve intense field amplification. However, as shown in Chapter 5, the conditions required to achieve

these deformations are contrived, requiring the bubble to become compressed in just the right direction and only undergoing resonant excitation using a carefully designed electrode geometry.

Capillary waves on the other hand seem to fit the design requirements quite well. We have already seen that large amplitude waves ($\Delta R_0/R_0 \sim 20\%$) can be excited in both electrode attached bubbles and isolated bubbles (via wave coupling). Excitation of Rayleigh-Taylor modes in these bubbles would also not present a limitation as the extreme shape deformation created during the instability would only help enhance the applied electric field further. Moreover, capillary wave excitations achieved in this work were observed to cover the entire portion of the bubble body, allowing the ignition field to be applied from any direction. One unexpected advantage of these excitations is the bubble to bubble wave coupling observed in Chapter 4. In a real device, this would allow a synergistic effect whereby excited bubbles would reinforce the applied pressure waves and increase the excitation of adjacent bubbles.

8.2.3 Geometry

In a practical device, gas bubbles must be constantly injected, distorted, and ignited to sustain the necessary concentration of reactive species required to process the target liquid. Figure 8.1 shows a straightforward application of the ideas discussed thus far with pressure waves, for example, as the shape driving source. The presence of buoyancy suggests that bubbles should be injected near the bottom of the device and allowed to float upward. At a specified height, pressure transducers are attached to the walls of the reactor and used to excite shape distortions on the stream of rising bubbles. In the same region, a pair of electrodes is used to ignite plasma in the bubbles at regular intervals. In Chapter 4, it was shown that if a bubble of radius 1 mm were deformed by capillary waves, an electric field of approximately 20 kV cm^{-1} would be sufficient to satisfy the streamer criterion. An electrode gap of 2 cm for

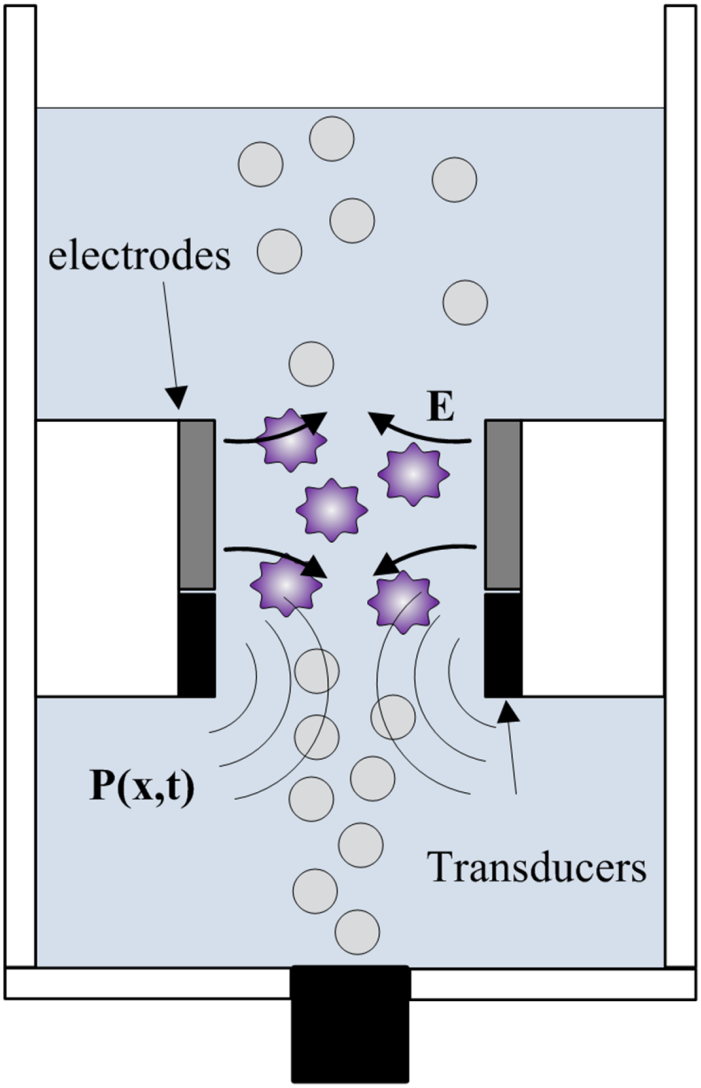

Figure 8.1: A simplified diagram illustrating the practical application of the shape effect. The injected bubbles float upward into the acoustic sound field, which excites capillary wave oscillations. The electrodes are then pulsed to ignite plasma in the volume of the bubble.

example, would require a voltage pulse of 40 kV.

8.3 Future Work

This dissertation has presented a variety of new phenomena related to formation of plasma in underwater bubbles, and perhaps an even greater amount of questions. The following is an overview of future work that would provide further insight into the area of bubble discharge physics.

1.) Investigation of the volume effect. The focus of this dissertation has been in demonstrating the shape effect. Another possible method of altering the breakdown conditions in the bubble is by actively changing the volume. The volume effect could be demonstrated by driving the bubble at the volume mode resonance, ω_0. Bubble deformation can also be accomplished in this case using pressure waves, as discussed in Section 8.2.1.

2.) ICCD imaging of plasma ignition in deformed bubbles. In Chapter 6, we demonstrated plasma excitation in isolated bubbles that were undeformed. It remains to demonstrate such excitation in deformed bubbles. The results of Chapter 7 provide multiple indications of such plasma formation but ICCD imaging of plasma evolution in these deformed bubbles has not yet been attempted. More importantly, a comparison between the conditions required to achieve plasma in a deformed bubble versus those required in an undeformed bubble could provide the first experimental validation of the shape effect.

3.) Development of a model for the multiphase streamer. Among the most significant results in this work was the observation of a streamer that propagates through both liquid and gas. The physical mechanism underlying this multiphase

streamer is still poorly understood. Many questions remain: what is the mechanism by which the plasma transitions from liquid to gas? What causes the explosive fluid behavior in the aftermath of the streamer?

4.) Development of a general model for plasma excitation in an isolated bubble. The presence of the liquid electrode-bubble barrier makes ignition in an isolated bubble a unique and complicated process. In this dissertation, plasma formation was modeled as a simple balance between ionization and attachment. This analysis ignored many of the important processes occurring in the electron swarm as it grows the under the action of the applied field. The next step is to develop a time dependent model that includes other important processes such as diffusion, recombination, excitation, and photoionization. This model would also need to take into account the presence of water vapor in the bubble, which was largely ignored in this work.

BIBLIOGRAPHY

BIBLIOGRAPHY

[1] A.M. et al. Anpilov. *J. Phys. D: Appl. Phys.*, 34:993–9, 2001.

[2] B.R. Locke, M. Sato, M.R. Hoffman, and J.S. Chang. *Indust. Eng. Chem. Res.*, 45:882–905, 2006.

[3] M. Malik and A. Ghaffar. *Plasma Sources Sci. Technol.*, 10:82–91, 2001.

[4] J.H. Carey. *Water Pollut. Res. J. Canada*, 27:21, 1992.

[5] R. Munter. *Proc. Eston. Acad. Sci. Chem.*, 50(2):59, 2001.

[6] W. Glaze, J. Kang, and D. Chaplin. *Ozone Sci. Eng.*, 9:335–52, 1987.

[7] B. Eliasson and U. Kogelschatz. *IEEE Trans. Plasma. Sci.*, 19:1063–77, 1991.

[8] J.E. Foster, B.S. Sommers, S.N. Gucker, I. Blankson, and G. Adamovsky. *IEEE Trans. Plas. Sci.*, 40(5):1311–23, 2011.

[9] L.A. Yutkin. *Electrohydraulic Effect and its Industrial Application.* Mashinostroenie, Leningrad, USSR, 1986.

[10] G. Gambus, P. Patino, and J. Navea. *Energy Fuels*, 16:172, 2002.

[11] S.K. Sengupta, U. Sandhir, and N. Misra. *J. Polym. Sci. Part A.*, 39:1584, 2001.

[12] H. Lange, M. Sioda, A. Huczko, Y. Zhu, H.W. Kroto, and D.R. Walton. *Carbon*, 41:1617, 2003.

[13] P.C. Vandeivere, R. Bianchi, and W. Verstraete. *J. Chem. Technol. Biotechnol.*, 72(4):289–302, 1998.

[14] E. Klimiuk, K. Kabardo, Z. Gusiatin, and U. Flipkowska. *Polish J. Environ Studies*, 14(6):771–80, 2005.

[15] Y.C. Wong, Y.S. Szeto, W.H. Cheung, and G. McKay. *J. Appl. Polym. Sci.*, 92(3):1633–45, 2004.

[16] E. Forgacs, T. Cserhati, and G. Oros. *Environ. Int.*, 30(7):953–71, 2004.

[17] W.G. Kuo. *Water Res.*, 26(7):881–86, 1992.

[18] A.T. Sugiarto, S. Ito, T. Ohshima, M. Sato, and J.D. Skalny. *J. Electrost.*, 58(1):135–45, 2003.

[19] F. Jin, X. Bai, X. Wang, F. Wang, and H. Ren. *IEEE Trans. Plasma Sci.*, 39(4):1099–1103, 2011.

[20] H. Aoki, K. Katsuhisa, and S. Hamaguchi. *Plasma Sources Sci. Technol.*, 17(2):025006, 2008.

[21] L.R. Grabowski, M. Van Veldhuizen, A.J. Pemen, and W.R. Rutgers. *Plasma Sources Sci. Technol.*, 16(2):226–32, 2007.

[22] H. Wang, J. Li, and X. Quan. *J. Electrost.*, 64(6):416–21, 2006.

[23] M. Magureanu, D. Piroi, F. Gherendi, B. Mandache, and V. Parvulescu. *Plasma Chem. Plasma Process.*, 28(6):677–88, 2008.

[24] J.S. Clements, M. Sato, and R. Davis. *IEEE Trans. Ind. Appl.*, IA-23(2):224–35, 1987.

[25] Development Alternatives Inc. USAID/Indonesia. Action research on point of use drinking water treatment alternatives. 497-M-00-05-00005-00.

[26] A.H. Smith, E.O. Lingas, and M. Rahman. *Bulletin of the World Health Organization*, 78(9):1103, 2000.

[27] A. Hricko. *Environ. Health Perspect.(NIH)*, 102(2), 1994.

[28] P. Payment. *Can. Jour. of Microbio.*, 35:1065, 1989.

[29] J.W. Synder. *Appl. and Environ. Microbio.*, 61(12):4291, 1995.

[30] A.M. Driedger, J.L. Rennecker, and B. Marinas. *Water Res.*, 34(14):3591–97, 2000.

[31] A. Latifoglu. *Indoor Built. Environ.*, 12(6), 2003.

[32] K.P. Cantor. *Environ. Health Perspect.*, 46:187–95, 1982.

[33] J.C. Hoff and E.W. Akin. *Environ. Health Perspect.*, 69:7–13, 1986.

[34] B.R. Locke and K.Y. Shih. *Plasma Sources Sci. Technol.*, 20(3), 2011.

[35] A.J. Sale and W.A. Hamilton. *Biochem. Biophys. Acta.*, 148:781–89, 1967.

[36] A. Mizuno, T. Inoue, S. Yamaguchi, K. Sakamoto, T. Saeki, Y. Matsumoto, and K. Minamiyama. *IEEE0-IAS Annual Meeting*, page 77, 1990.

[37] A.K. Sharma, G.B. Josephson, D.M. Camaioni, and S.C. Goheen. *Environ. Sci. Technol.*, 34:2267, 2000.

[38] D.M. Willberg, P.S. Lang, R.H. Hochemer, A. Kratel, and M.R. Hoffman. *Environ. Sci. Technol.*, 30:2526–34, 1996.

[39] S. Suarez, C.F. Carball, F. Omil, and J.M. Lema. *Rev. Environ. Sci. Biotechnol.*, 7:125–8, 2008.

[40] M. Sato, D. Kon-no, T. Oshima, and A Sugiarto. *J. Adv. Oxid. Technol.*, 8:198, 2005.

[41] P. Bruggeman and C. Leys. *J. Phys. D: Appl. Phys.*, 42:053001, 2009.

[42] K. Kitano, H. Aoki, and S. Hamaguchi. *Japan. Jour. Appl. Phys.*, 45(10B):8294–97, 2006.

[43] W.J. Murphy. *U.S. Patent*, 5,277,773, 1994.

[44] A.K. Sharma, B.R. Locke, P. Arce, and W. Finney. *Hazard. Waste Hazard. Matter*, 10:209–19, 1993.

[45] P. Sunka. *Phys Plasmas*, 8:2587, 2001.

[46] H.Z. Zastawny, H. Romat, N. Karpel Vel Leitner, and J.S Chang. *Phys Plasmas*, 137:325, 2003.

[47] R.P. Joshi, J.F. Kolb, S. Xiao, and K.H. Schoenbach. *Plasma Proess. Polym.*, 6:763–77, 2009.

[48] J.F. Kolb, R.P. Josh, S. Xiao, and K.H. Schoenbach. *J. Phys. D: Appl. Phys.*, 41:234007, 2008.

[49] R.P. Joshi, J. Qian, and K.H. Schoenbach. *J. Appl. Phys.*, 96:5129, 2004.

[50] J.W. Chase and J.W. Hunt. *J. Phys. Chem.*, 79(26):2835–45, 1975.

[51] N.F. Bunkin and A.V. Lobeev. *Quantum Electronics*, 24:297, 1994.

[52] S.M. Korobeinikov and A.V. Melekhov. *High Temp.*, 39(3):368–72, 2002.

[53] S.M. Korobeinikov and A.V. Melekhov. *High Temp.*, 40(5):652–9, 2002.

[54] A. Starikovskiy, Y. Yang, Y.I. Cho, and A. Fridman. *Plasma Sources Sci. Technol.*, 20:024003, 2011.

[55] T.J. Lewis. *IEEE Trans. Diel. and Elec. Insul.*, 5(3):306–15, 1998.

[56] J.S Chang, K. Urashima, and Y. Uchida. *Res. Rep. Tokyo Denki. Univ.*, 50:1, 2002.

[57] S.C. Goheen, D.E. Durham, M. McCulloch, and W.O. Heath. *Chem. Oxid. Tech. for the Nineties*, page 356, 1994.

[58] A.L. Bozic, N. Koprivanac, P. Sunka, M. Clupek, and V. Babicky. *Czech J. Phys.*, 54:C958, 2004.

[59] M. Malik. *Plasma Chem. Plasma Process.*, 30:21–31, 2010.

[60] M. Dors, E. Metel, J. Mizeraczyk, and E. Marott. *Proc. IEEE Int. Conf. Dielectr. Liquids*, pages 1–3, 2008.

[61] V. Blokhin, F. Vysikailo, K.I. Dmitriev, and N.M. Efremov. *High Temp.*, 37:963, 1999.

[62] V.L. Goryachev, A.A. Ufimstev, and A. M. Khodakovskii. *Technol. Phys. Lett.*, 23:386–7, 1997.

[63] J.Y. Park, J.D. Lee, and S.B. Han. *J. Adv. Oxid. Technol.*, 8:205, 2005.

[64] J. Velikonja, M.A. Bergougnou, G.S. Castle, W. Cairns, and I.I. Inculet. *Ozone Sci. Eng.*, 23:467, 2001.

[65] T. Hammer. *SAE Tech. Pap. Ser.*, 19:2894, 2000.

[66] F. Liu et al. *Plasma Process. Polym.*, 7(3):231–36, 2010.

[67] J.E. Foster, B.W. Weatherford, E. Gillman, and B. Yee. *Plasma Sources Sci. Technol.*, 19:025001, 2010.

[68] J.E. Foster, B.S. Sommers, B.W. Weatherford, , B. Yee, and M. Gupta. *Plasma Sources Sci. Technol.*, 20:034018, 2011.

[69] A. Hickling and M.D. Ingram. *J. Electroanalyt. Chem.*, 8:65, 1964.

[70] S.K. Sengupta and O.P. Singh. *J. Electroanal. Chem.*, 369:113, 1994.

[71] S.K. Sengupta, A.K. Srivastava, and O.P. Singh. *J. Electroanal. Chem.*, 427:23, 1997.

[72] S.L. Miller. *J. Am. Chem. Soc.*, 77:2351, 1955.

[73] K. Harada and S. Suzuki. *Nature*, 266:275, 1977.

[74] K. Kobayashi, Y. Tomita, and M. Sanmyo. *J. Phys. Chem.*, 1049:6318–26, 2000.

[75] R. Burlica and B.R. Locke. *IEEE Trans. Ind. Appl.*, 44:482, 2008.

[76] A. Czernichowski. *Pure and Appl. Chem.*, 66(2):291–310, 1994.

[77] B. Benstaali, D. Moussa, A. Addou, and J.L. Brisset. *Eur. Phys. J.: Appl. Phys.*, 4:171, 1998.

[78] A. Fridman, S. Nester, A. Kennedy, A. Saveliev, and O. Mutaf-Yardimci. *Prog. Energy Combust. Sci.*, 25:211, 1999.

[79] D. Moussa and J.L. Brisset. *J. Haz. Mater.*, 102:189, 2003.

[80] M. Moreau, M.G.J. Feuilloley, N. Orange, and J.L. Brisset. *J. Appl. Microbiol.*, 98:1039, 2005.

[81] K.Y. Shih and B.R. Locke. *Plasma Chem. Plasma Process.*, 30:1–20, 2010.

[82] S. Gershman, O. Mozgina, A. Belkind, K. Becker, and E. Kunhardt. *Contrib. Plasma Phys.*, 47:19–25, 2007.

[83] T. Miichi, S. Ihara, S. Satoh, and C. Yamabe. *Vacuum*, 59:236–43, 2000.

[84] T. Miichi, N. Hayashi, S. Ihara, S. Satoh, and C. Yamabe. *Reports of Faculty of Sci. and Eng.*, 31(1), 2002.

[85] K. Tachibana and Y. Takekata. *Plas. Sources Sci. Technol.*, 20:034005, 2011.

[86] N.Y. Babaeva and M.J. Kushner. *J. Phys. D: Appl. Phys.*, 42:132003, 2009.

[87] N.Y. Babaeva, A.N. Bhoj, and M.J. Kushner. *Plasma Sources Sci. Technol.*, 15(4):591, 2006.

[88] N.Y. Babaeva and M.J. Kushner. *Plasma Sources Sci. Technol.*, 18:035010, 2009.

[89] A. Fridman, A. Chirokov, and A. Gutsol. *J. Phys. D: Appl. Phys.*, 38:R1–R24, 2005.

[90] P. Bruggeman, J. Degroote, J. Vierendeels, and C. Leys. *Plasma Sources Sci. Technol.*, 17:025008, 2008.

[91] M. Lieberman and A. Lichtenberg. *Principles of Plasma Discharges and Materials Processing*. Wiley and Sons, New York City, USA, 1994.

[92] J. Dutton. *J. Phys. Chem. Ref. Data*, 4(3), 1975.

[93] A.N. Prasad and J.D. Craggs. *Proc. Royal Soc.*, 77:385–98, 1961.

[94] M.S. Naidu and A.N. Prasad. *J. Phys. D: Appl. Phys.*, 3:957–64, 1970.

[95] D.A. Price, J. Lucas, and J.L. Moruzzi. *J. Phys. D: Appl. Phys.*, 5:1249–59, 1972.

[96] M.A. Harrison and R. Geballe. *Phys. Rev.*, 91:1–7, 1953.

[97] A.A. Kruithof and F.M. Penning. *Physica*, 3:515, 1936.

[98] G.G. Raju. *Gaseous Electronics: Theory and Practice*. CRC Press, Boca Raton, FL, USA, 2006.

[99] M.S. Naidu and V. Kamaraju. *High Voltage Engineering*. McGraw-Hill, New York City, USA, 1995.

[100] J.S. Townsend. *Electrons in Gases*. Hutchinson, London, UK, 1947.

[101] K.T.A.L. Burm. *Contrib. Plasma Phys.*, 47(3):177–82, 2007.

[102] A. Bernas and D. Grand. *J. Phys. Chem.*, 98:3440–43, 1994.

[103] T. Goulet, A. Bernas, C. Ferradini, and J.P. Jay-Gerin. *Chem. Phys. Lett.*, 170(5):492–6, 1990.

[104] J.M. Meek. *Phys. Rev.*, 57:722–8, 1940.

[105] J.J. Lowke and F. D'Alessandro. *J. Phys. D: Appl. Phys.*, 36:2673, 2003.

[106] W.M. Hayes. *The CRC Handbook of Chemistry and Physics*. CRC Press, New York, USA, 2013.

[107] T. Takuma and B. Techaumnat. *Electric Fields in Composite Dielectrics and Their Applications*. Springer, New York, USA, 2010.

[108] B.S. Sommers, J.E. Foster, N.Y. Babaeva, and M.J. Kushner. *J. Phys. D: Appl. Phys.*, 44:082001, 2011.

[109] C.T. Phelps and R.F. Griffiths. *J. Appl. Phys.*, 47:2929–34, 1976.

[110] P.L. Marston and R.E. Apfel. *J. Colloid Interface Sci.*, 68(2):280–6, 1979.

[111] A. Prosperetti. *J. Acoust. Soc. Am.*, 56(3):878–85, 1974.

[112] E.L. Cussler. *Diffusion: Mass Transfer in Fluid Systems*. Cambridge University Press, Cambridge, UK, 2009.

[113] H.A. Bolz. *CRC Handbook of Tables For Applied Engineering Science*. CRC Press, Boca Raton, USA, 1973.

[114] T.G. Leighton. *The Acoustic Bubble*. Academic Press, London, UK, 1994.

[115] S.J. Shaw and P.D.M. Spelt. *Proc. R. Soc. A*, 465:3127–42, 2009.

[116] D.A. Saville. *Annu. Rev. Fluid Mech.*, 29:27–64, 1997.

[117] Antonio Arnau. *Piezo Transducers and Applications*. Springer, Berlin, Germany, 2008.

[118] M.S. Plesset and A. Prosperetti. *Ann. Rev. Fluid Mech.*, 9:145–85, 1977.

[119] R. Courant and D. Hilbert. *Methods of Mathematical Physics, Vol 1*. Interscience, New York City, USA, 1953.

[120] T. Bellini, M. Corti, A. Gelmetti, and P. Largo. *Europhys. Lett.*, 38:521–6, 1997.

[121] E.A. Theisen, M.J. Vogel, C.A. Lopez, A.H. Hirsa, and P.H. Steen. *J. Fluid. Mech.*, 580:495–505, 2007.

[122] H. Lamb. *Hydrodynamics*. Cambridge Press, Cambridge, UK, 1897.

[123] J. Crank. *Mathematics of Diffusion*. Oxford University Press, London, UK, 1956.

[124] Z.C. Feng and L.G. Leal. *Annu. Rev. Fluid Mech.*, 29:201–43, 1997.

[125] W.L. Lauterborn. *J. Acoust. Soc. Am.*, 59:283–93, 1976.

[126] J.R. Melcher and G.I. Taylor. *Annu. Rev. Mech.*, 1:111–46, 1969.

[127] L.D. Landau and E.M. Lifshitz. *Electrodynamics of Continuous Media*. Pergamon Press, Oxford, UK, 1984.

[128] J.A. Stratton. *Electromagnetic Theory*. McGraw-Hill, New York, USA, 1941.

[129] J.D. Jackson. *Classical Electrodynamics*. Wiley and Sons, New York, USA, 1999.

[130] C.G. Garton and Z. Krasucki. *Proc. R. Soc. Lond. A*, 280:211–26, 1964.

[131] S. Torza, R.G. Cox, and S.G. Mason. *Phil. Trans. Roy. Soc. Lond. A*, 269:1412–17, 1971.

[132] P.L. Marston and G. Goosby. *Phys. Fluids*, 28:1233–42, 1985.

[133] H.A. Pohl, K. Pollock, and J.S. Crane. *J. Biol. Phys.*, 6:133–60, 1978.

[134] L.A. Crum. *J. Acoustic. Soc. Am.*, 68:203–11, 1980.

[135] A.J. Walton and G.T. Reynolds. *Adv. Phys.*, 33:595–660, 1984.

[136] D.F. Gaitan, L.A. Crum, C.C. Church, and R.A. Roy. *J. Acoust. Soc. Am.*, 91:3166–83, 1992.

[137] B.P. Barber, R.A. Hiller, R. Lofstedt, S.J. Putterman, and K.R. Weninger. *Phys. Reports*, 281:65–143, 1997.

[138] K. Baxter, R.E. Apfel, and P.L. Marston. *Rev. Sci. Instrum.*, 49(2), 1978.

[139] T.J. Asaki, P.L. Marston, and E.H. Trinh. *J. Acoust. Soc. Am.*, 93(2):706–13, 1993.

[140] T.G. Leighton, A.J. Walton, and M.J.W. Pickworth. *Eur. J. Phys.*, 11:47–50, 1990.

[141] A. Eller. *J. Acoust. Soc. Amer.*, 43(1):170–171, 1968.

[142] MathWorks. *Image Processing Toolbox Users Guide*, 1998.

[143] M. Kline. *Calculus: An Intuitive and Physical Approach.* John Wiley and Sons, New York, 1998.

[144] Ansys. *Maxwell 2D Users Guide*, 2012.

[145] C.F. Hayes. *Journ. Phys. Chem.*, 79:1689, 1979.

[146] P.G. Drazin. *Introduction to Hydrodynamic Instability.* Cambridge University Press, Cambridge, UK, 2002.

[147] E.H. Trinh, D.B. Thiessen, and R.G. Holt. *J. Fluid Mech.*, 364:253–72, 1998.

[148] H. Azuma and S.J. Yoshihara. *J. Fluid Mech.*, 393:309–32, 1999.

[149] S.J. Shaw, P.D.M. Spelt, and O.K. Mater. *J. Eng. Math.*, 65:291–310, 2009.